UNIVERSITY OF SOUTHAMPTON

FACULTY OF ENGINEERING AND PHYSICAL SCIENCES

Engineering Materials, Mechanical Engineering

Process variation effects linked to feature size on fatigue performance in additively manufactured 316L stainless steel

by:

KHANDOKAR ABU TALHA

https://orcid.org/0000-0003-1569-2460

Thesis for the degree of Doctor of Philosophy

September 2024

University of Southampton

Abstract

FACULTY OF ENGINEERING AND PHYSICAL SCIENCES

SCHOOL OF ENGINEERING

DOCTOR OF PHILOSOPHY

Process variation effects linked to feature size on fatigue performance in additively manufactured 316L stainless steel

by

Khandokar Abu Talha

Metal-based additive manufacturing provides a substantial degree of design flexibility for metal parts, garnering interest from various industries, including Vestas Aircoil, a project partner. The focus is on utilising this technology to design innovative heat exchangers aimed at reducing vibration-induced fatigue and enhancing heat transfer. Laser-based powder bed fusion (LPBF) technology, in particular, has gained prominence for manufacturing high-strength, intricate parts. However, inherent challenges such as poor surface quality, defects, microstructure inhomogeneity, and material anisotropy limit its application. The influence of part geometry size and scale on crystallographic and porosity microstructural features, crucial in early-stage fatigue crack initiation, necessitates a comprehensive investigation. This study aims to examine the size scale effect on microstructure and fatigue behaviour, contributing to the development of a lifing technique applicable to generic heat exchanger structures.

Despite the design freedom offered by LPBF, it presents unique challenges. A thorough analysis was conducted to explore the impact of process parameters, including build direction, energy density, build location, and geometry size scale, on average grain size, boundary distribution, preferred crystallographic orientation, and recrystallization within grains. The study revealed a robust crystallographic orientation in rectangular bend bar specimens with the longest dimension oriented in the LPBF build direction (Z builds), accompanied by larger grains and lower recrystallization compared to their counterparts, indicating high material anisotropy across all batches of specimens. Subsequent analysis of area size scale effects on microstructure using two batches of micro tensile specimens consistently showed a large grain size in heat-restricted zones, along with a high percentage of recrystallized grains in critical gauge areas. These findings underscore the interplay of LPBF laser parameters, orientation, and specimen geometry in shaping microstructures and properties. Generally, higher strength and ductility result from orientations with larger layer areas and lower energy density,

while restricted heat flow can impact the recrystallization process, potentially weakening material strength.

In the context of high cycle fatigue (HCF) behaviour, this study focused on LPBF-processed 316L stainless steel (SS) rectangular bend bars. Employing a three-point bending setup, specimens underwent cyclic loading at two stress levels with a frequency of 10 Hz and a stress ratio (R) of 0.1. The study particularly emphasized early-stage crack initiation and coalescence mechanisms, monitored through a silicone replication technique. Scanning electron microscopy (SEM) and surface roughness profilometry were employed to examine fracture surfaces, sub-surface defects, porosities, and material surfaces after etching.

Specimens built in horizontal (X and Y), and vertical (Z) directions were investigated to assess the influence of material defects on crack initiation and subsequent effects on fatigue lifetime. Additionally, the study explored the impact of various stress states and the influence of yield strength on fatigue behaviour. Generally, Z build specimens exhibited the highest number and percentage of porosity compared to X and Y build specimens. Lower yield strength was associated with smaller fatigue life due to persistent slip band-induced early-stage crack initiation.

Fatigue behaviour evaluation for LPBF-processed material proved to be complicated. Porosity and defects played a pivotal role in initiation, with crack coalescence and initiation events dominating overall fatigue lifetime, leading to multiple coalescences. The study also observed stress shielding and anti-shielding behaviours of cracks across all specimens. Coalescence between two cracks significantly influenced the stress state of other surface cracks, generally shielding parallel cracks and anti-shielding aligned cracks. These results underscore the significance of investigating surface defect distribution and coalescence mechanisms in controlling fatigue behaviour.

A finite element (FE) model was developed using a constitutive model of 316L SS to simulate tension-tension fatigue tests of micro tensile specimens. The model, validated against elastic-plastic responses obtained from micro tensile fatigue tests, revealed an overestimation of fatigue lifetime. Fractography of micro tensile specimens identified surface roughness as the predominant factor controlling fatigue, with process-induced defects and porosity often initiating or interacting with cracks, accelerating propagation behaviour. The final failure stress calculated from the fracture surface was nearly twice the ultimate tensile strength (UTS) for all the specimens.

In conclusion, this study provides valuable insights into the intricate relationship between LPBF process parameters, specimen geometry, and resulting microstructures and properties. The findings contribute to the development of lifing techniques for generic heat exchanger structures and enhance the understanding of the high cycle fatigue behaviour of LPBF-processed 316L stainless steel.

Table of Contents

List of Figures

Table of Tables

Research Thesis: Declaration of Authorship

Print name: Khandokar Abu Talha

Title of thesis: Process variation effects linked to feature size on fatigue performance in additively manufactured 316L stainless steel.

I declare that this thesis and the work presented in it are my own and has been generated by me as the result of my own original research.

I confirm that:

1. This work was done wholly or mainly while in candidature for a research degree at this University;
2. Where any part of this thesis has previously been submitted for a degree or any other qualification at this University or any other institution, this has been clearly stated;
3. Where I have consulted the published work of others, this is always clearly attributed;
4. Where I have quoted from the work of others, the source is always given. With the exception of such quotations, this thesis is entirely my own work;
5. I have acknowledged all main sources of help;
6. Where the thesis is based on work done by myself jointly with others, I have made clear exactly what was done by others and what I have contributed myself;
7. None of this work has been published before submission

Signature: KHANDOKAR ABU TALHA Date: 13-09-2024

Acknowledgements

I express my gratitude to the Horizon 2020 programme for funding this project, with special appreciation to my incredible supervisors, Professor Philippa Reed and Dr Andrew Hamilton, who went above and beyond to support my PhD journey, even during their holidays. Their unwavering dedication has left an indelible mark on my heart and played a pivotal role in the success of my PhD.

To my family, especially my father, thank you for being my pillar of strength and for the mental and financial support system that has been instrumental in guiding me through this journey. My heartfelt appreciation goes to my future wife, Shamma Khan, for being my source of encouragement, motivation, and academic cheerleader during the final months of my PhD journey. A special shout-out to my fellow researcher and dear colleague, Sandeep Sahu, and Deepak Kumar, for their constructive criticism and tireless efforts during our evening EBSD sessions.

I extend my sincere gratitude to all my colleagues for their support, listed in random order - Benjamin Cunningham, Donghyuk Kim, Anqi Liang, Alvaro Sanchez, Ara Masis Khodavirdi, and Diego Martinez Luca. A warm and special thanks to Dr Claus Hessler Ibsen and Dr Michal Kazimierz Budzik. Your support has been the driving force behind the success of this project, and I am forever grateful.

Definitions and Abbreviations

2D: two Dimensional

3D: three Dimensional

AB: As-Built

AM: Additive Manufacturing

BCC: Body Centre Cubic

CAD: Computer Assisted Design

DLD: Direct Laser Deposition

EBM: Electron Beam Melting

EBSD: Electron Backscattered Diffraction

EDS: Energy Dispersive Spectroscopy

EPFM: Elastic-plastic fracture mechanics

FCC: Face Centre Cubic

HAGB: High Angle Grain Boundary

HAZ: Heat Affected Zone

HCF: High Cycle Fatigue

HIP: Hot Isostatic Pressing

IPF: Inverse Pole Figure

LCF: Low Cycle Fatigue

LEFM: Linear Elastic Fracture Mechanics

LOF: Lack-of-fusion

L-PBF: Laser Powder Bed Fusion

LRO: Long Range Order

NDT: Non-destructive Detection Technique

OM: Optical Microscopy

PSB: Persistent Slip Band

RS: Residual stresses

SE: Secondary Electron

SEM: Scanning Electron Microscopy

SFE: Stacking Fault Energy

SLM: Selective Laser Melting

SLS: Selective Laser Sintering

SSS: Solid Solution Strengthening

SSY: Small Scale Yielding

VED: Volumetric Energy Density

VHCF: Very High Cycle Fatigue

XRD: X-ray Diffraction

Nomenclature

2c : surface crack length

2θ: X-ray diffraction peak position

a : Depth of te fatigue crack (in sample width direction)

a/c : crack aspect ratio

a/W : ratio of the crack length to specimen width

da/dN: Fatigue crack growth rate

E: Young's Modulus (MPa)

K: Stress intensity factor (MPa√m)

K_I: Stress intensity factor in mode I fatigue

K_{IC} : Plane strain fracture toughness

L_c : Profile filter value

L_r : Required evaluation length

n : An integer

N_f : Number of Cycles to Failure

P: Power (Watt, Mega Watt or Joules)

R_a : Arithmetical mean of vertical deviation of the linear roughness

R_z : Maximum height of the linear roughness profile

S_a : Arithmetical mean of vertical deviation of the roughness of a surface

S_z : Maximum height of the roughness f a surface

T: Temperature (°C or K)

$\Delta\varepsilon_p$: Plastic strain range

Nomenclature

ΔK: Stress intensity factor range (MPa$\sqrt{m}$)

$\Delta\varepsilon$: Strain range

$\Delta\sigma$: Stress range

ε_a : Strain Amplitude

θ : Diffraction angle

λ : Wave length

σ_a : Stress Amplitude (MPa or Pascal)

σ_{uts} :Ultimate Tensile Strength (MPa)

$\sigma_{y:}$ Yield Strength (MPa)

$\sigma_{y\,0.2\%}$: 0.2% Yield Strength (MPa)

Chapter 1 Introduction

1.1 Motivation

This doctoral project is part of a multi-disciplinary doctoral program funded by Horizon 2020. The program aims to develop a next-generation heat exchanger with a novel structure. A major focus for the industrial project partner Vestas Aircoil is the design of a novel heat exchanger but also to avoid fatigue failure due to complex vibrational loading and thermal cycles. This program aims to improve heat exchanger design against fatigue by reducing vibration and enhancing heat transfer efficiency by implementing additively manufactured novel metamaterial structure within the heat exchanger design. Due to the multi-disciplinary nature of this program, four early-stage researchers worked simultaneously to develop this technology. While other early-stage researchers worked on developing novel heat exchanger designs, this project is focused on investigating the effect of process variation linked to feature size on subsequent fatigue performance in additively manufactured 316L stainless steel.

1.2 Background

Additive manufacturing (AM) is a relatively new technology that is of interest to many industries due to its potential to offer exceptional design freedom and also to retain good mechanical properties of the material. This technology can potentially enhance heat transfer efficiency and reduce vibration by enabling fabrication of complex designed parts, which is of great interest to the project partner Vestas Aircoil. In fact, many optimised heat exchanger structures reported recently have parts as small as millimetre long [1]. AM technology can be used to design these near net complex structures with tailor made material properties which could potentially contain small geometric features. However, fatigue behaviour investigation of AM processed heat exchangers can be challenging as AM technology also has many limitations, including poor surface finish and material defects in the processed part. Material defects and surface finish can play a crucial role in early-stage crack initiation, often dominating fatigue life [2]. In addition, material anisotropy and microstructure inhomogeneity due to processing parameters affects mechanical properties, ultimately influencing overall fatigue life. Thus, it is important to identify frequently encountered defects in additively manufactured parts, characterise AM microstructures, understand defect formation mechanisms during processing, and develop the relationship between processing parameters, part geometry size and scale with subsequent microstructure and material properties [3][4].

316L stainless steel (SS) is a commonly used material in heat exchangers by the project partner Vestas Aircoil. It has excellent mechanical properties and corrosion resistance, making it suitable for many

industrial applications. It is usually produced by casting, forging and often by hot pressing, but the laser powder bed fusion (LPBF) process, a type of AM, opens up many possibilities. LPBF is desirable as it can produce high strength material [5]. However, parts produced with LPBF contain several types of defects. Numerous studies have been conducted to optimise the processing parameters of LPBF for 316L SS to reduce defects. However, these frequently encountered microstructural defects cannot be entirely eliminated.

Material defects, surface roughness and mechanical properties are reported to be linked to fatigue life. The investigation of fatigue behaviour of novel heat exchangers requires understanding or at least correlating geometry size-scale with defect distribution and mechanical properties. This requires knowledge of various standard fatigue lifing techniques and fundamental theories of fatigue behaviour of metals. This European Industrial Doctorate aims to investigate the fatigue behaviour of additively manufactured 316L SS material and to implement this knowledge to understand crack initiation and propagation behaviour to develop a fatigue lifing model that can be used in the design of a complex additively manufactured structure such as a heat exchanger.

1.3 Aim and objectives

This project therefore aims to understand the effects of LPBF processing on fatigue failure processes in 316L SS alloy by investigating the impact of small-scale feature sizes expected in a complex heat exchanger structure on fatigue. Furthermore, developing fatigue lifing models that can be used for the design of other engineering applications is a focus. A reasonable approach is to investigate the short fatigue crack behaviour of LPBF processed 316L SS. The resulting experimental data can aid computational models for designing and fatigue lifing of a more complex heat exchanger design associated with the European Industrial Doctorate programme funded by Horizon 2020. The aims of this project were pursued via the following objectives.

Objective 1: Investigating the role of process parameters

- Explore the role of process parameters (e.g., power density and build direction) on the microstructure of the LPBF processed 316L SS.
- Examine the impact of thermal history associated with processing parameters and geometry size and scale on the microstructure of 316L SS specimens.

Objective 2: Understanding constitutive and overall short crack fatigue behaviour

- Use macroscale bend bar specimens (60×10×10 mm) to analyse constitutive materials and fatigue response behaviour.
- Investigate the relationship between microstructural features, mechanical properties, and fatigue events (initiation and coalescence) affecting total fatigue life.

Objective 3: Developing finite element and material models

- Create a finite element (FE) model of micro tensile specimens to validate constitutive material behaviour from LPBF-produced bend bars.
- Analyse constitutive and fatigue behaviour of micro tensile specimens (6.32 mm length, 0.9×0.9 mm² cross-section).
- Explore the relationship of microstructural features (defects and porosity) with fatigue behaviour in 316L SS and compare with macroscale bend bar specimens.

Altogether, the project aims to devise a fatigue lifing approach for a complex structure such as heat exchanger geometry containing small-scale features based on the knowledge generated from the investigations mentioned above.

Chapter 2 Literature review

2.1 Introduction

Additive manufacturing (AM) has gained widespread popularity for its ability to provide design freedom, facilitate near-net shape production, and accommodate complex geometries. However, this manufacturing process presents its own set of challenges, prompting extensive research to optimize its various facets [6], [7]. Recent findings indicate that processing parameters, including energy density, scanning strategy, spot size, hatch distance, layer thickness, and rotation, significantly impact the microstructure of additively manufactured materials. Numerous studies have independently explored the role of each process parameter, employing a parametric approach for optimization [8], [9], [10], [11].

However, understanding the intricate interplay between these process parameters can be complex and necessitates a comprehensive grasp of their effects on thermal heating/cooling and heat flow conditions. This chapter aims to describe a specific AM process, namely laser powder bed fusion (LPBF), and delve into the optimisation of its process parameters. It will elaborate the influence of thermal heating/cooling on microstructure, establishing a link between the process, microstructure, and resulting material properties in the LPBF process. Additionally, the chapter will examine the impact of geometry size scale on microstructure and mechanical properties.

The subsequent sections will provide an in-depth review of the relationship between process parameters, geometry size scale, microstructure, and mechanical properties, with a focus on their influence on fatigue failure induced by LPBF processing. In summary, this chapter aims to comprehensively elucidate the effects of process and geometry size scale on microstructure and mechanical properties and their consequential impact on fatigue failure.

2.2 Laser powder bed fusion (LPBF) process

Laser powder bed fusion (LPBF) is a type of AM process that works with numerically sliced 3D computer-aided design (CAD) models converted into multiple 2D layers. The process works by devising a laser scan path for each layer which determines a fill sequence and boundary contour. During scanning, a single-track laser melts the powder particles and creates a molten pool (see Figure 2-1 (b)), and the process is repeated until an entire layer is completely melted. Once a layer is melted, another layer of powder is spread on top of it, making it a discrete rather than a continuous process. The powder material is supplied by a hopper and then it is uniformly spread on the build platform of the powder bed by a blade or roller. The layer thickness is generally in the range between 25 to 100 µm and dependent on numerous factors such as materials and other processing parameters [11].

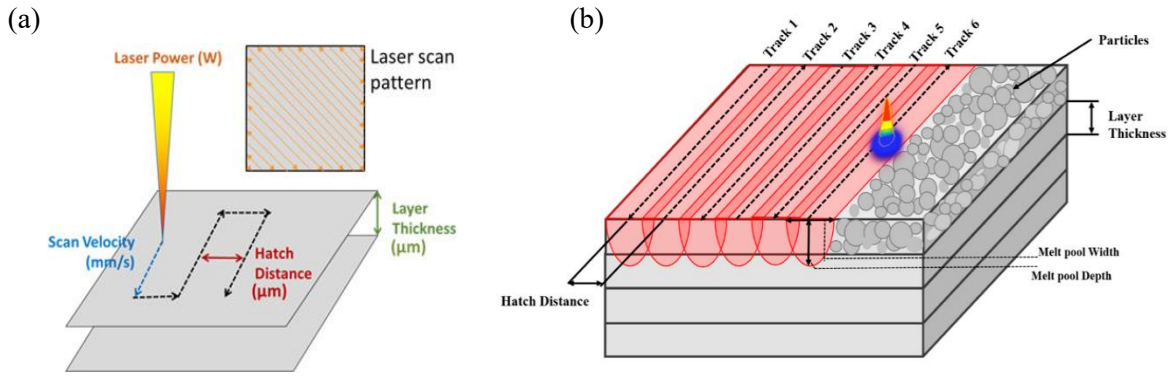

Figure 2-1: (a) Schematic of the process parameter of powder bed fusion (b) laser track creating melt pools until a complete layer is melted. [7], [10]

LPBF process parameters include laser scan speed, layer thickness, scanning strategy, laser power, and hatch distance (distance between two laser passes), shown in Figure 2-1 (a). These parameters are usually derived from parametric studies to minimise defects, increase build rate, maximise material density, reduce surface roughness and produce parts with tailor-made material properties [11]. These parameters can provide an estimation of the energy delivered by the laser during the LPBF process using Equation 2-1[7].

$$E_A = \frac{P_L}{v_s \times H} \qquad \text{Equation 2-1}$$

Here v_s is the scan speed, P_L is the laser power, and H is the hatch distance. E_A is the nominal power per unit area applied on the surface of the powder bed. E_A can be further extended as energy density by considering the layer thickness, shown in Equation 2-2.

$$E_V = \frac{P_L}{v_s \times H \times d_{layer}} \qquad \text{Equation 2-2}$$

Here E_V is volume-based energy density, and d_{layer} is the powder layer thickness. However, this approach is limited as it does not consider the laser energy absorbance throughout the powder layer. [7]

The combined effect of volumetric energy density with scanning strategy can control the solidification rate and thermal gradient of LPBF processed part, which will be discussed in the following section.

2.2.1 Microstructure of LPBF processed materials

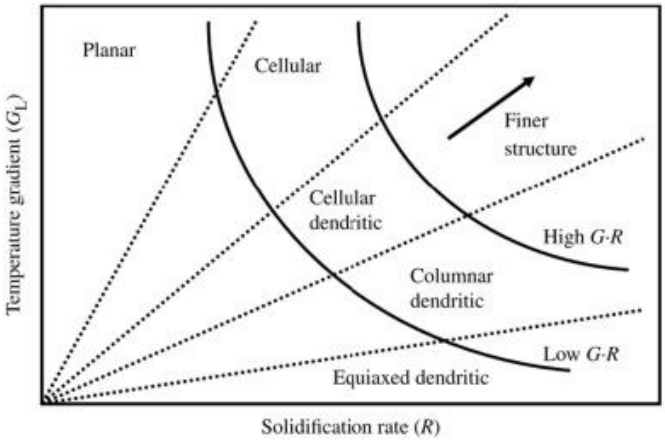

Figure 2-2: Effect of the temperature gradient (G) and solidification rate (R) on developed microstructures.[7]

LPBF products usually have more refined microstructures than cast or wrought materials. This is due to the accelerated solidification of laser-melted metal caused by the high heat conduction from the molten region to the surrounding material [8]. If process defects like porosity and cracking can be prevented, the refined microstructure usually results in stronger yet less ductile LPBF products [7].

In the LPBF process, the solidification microstructure is affected mainly by the temperature gradient (G), solidification rate (R), undercooling (ΔT), and material-related parameters such as composition and liquid diffusivity [12]. The LPBF process has a fast solidification rate (R) and high temperature gradient (G), and the most frequently found structures are the equiaxed dendritic, columnar dendritic and cellular dendritic (as in Figure 2-2 at relatively low G/R and high G-R), formed by constitutional segregation during solidification. Depending on the processing parameters, the size of cellular structures in the LPBF processed parts usually are in the range of 0.1–1 μm. Besides the above-mentioned microstructural features, columnar grains are also observed, which are typically greater than 10 μm in diameter, and can be up to several mm in length, usually for high-power-high-scanning speed conditions. [7]

Processing parameters such as power and scanning velocity can be correlated to G and R to create a process diagram (see Figure 2-2). Higher scanning speeds, for example, increase R and G; and are responsible for the formation of highly textured columnar grains (crystallographic texture is a term used, to describe the statistical distribution of grain orientation. A highly textured material would have a significant fraction of grains with preferred crystallographic orientation), whereas lower scanning speeds favour equiaxed grains with a random texture [12]. Alternatively, rising power from the energy source tends to increase the temperature gradient, G. It is worth noting that the melt pool's G and R values are not constant within the melt pool. In one study [7], Oliviera et al. reported that R is high towards the top of the melt pool while G is low; R is small towards the bottom of the melt pool, and G is high. The difference in R and G within the melt pool can in fact vary by an order of magnitude.

2.3 Defects formed during the LPBF process

Alloys produced by the LPBF process usually have defects (e.g., pores) in material parts produced in the as-built condition. These defects are worth discussing as they have been reported to be cause early-stage fatigue crack initiation [13], which is an important topic of this project. The parts also contain residual stress due to thermal gradients and inhomogeneous contraction/expansion in the material. Details about residual stress would be discussed in the section 2.3.3 [7].

These defects are mainly categorised into two different types: lack of fusion defects and keyhole porosity. Lack of fusion defect is related to small melt pool and low melting, caused by low energy input, and causing incomplete overlap between melt pool boundaries; while the high input energy can cause powder particles to vaporise resulting in another type of porosity. High energy input produces gas bubbles that can often get trapped because of keyhole instability, known as keyhole porosity. For a specific set of parameters, these conditions can vary depending on the material, and the exact conditions can also be different for each material [7][14][15].

2.3.1 Keyhole porosity

The main factors influencing keyhole porosity are scanning rate, laser power, and localised energy density on the powder bed. By lowering the laser intensity or increasing the scanning speed, keyhole porosity can be reduced. The keyhole porosity is usually unaffected by hatch size or layer thickness since the dynamics of the melt pool influences it. The frequency of keyhole porosity is often affected by the scanning technique. It is usually visible in places where the laser direction creates longer local dwell periods, enhancing the power of the laser radiation. At higher energy intensity, reducing keyhole porosity is considerably difficult. For example, when scanning an L-shaped turn, the laser slows for a brief moment to shift course, resulting in slower scanning at the "L" elbow. As a result, most scanning methods are designed so that certain turns are not done while the laser is on [7].

2.3.2 Lack of fusion porosity

The shape of the melt pool and the scanning method affect the lack of fusion porosity. This type of porosity depends on the total melting of the component, which can only be obtained by the complete overlap of the melt pool. The processing parameters suitable for complete melting can be determined based on the shape and scale of the melt pool. Several approaches have been taken to simulate the melt pool overlap but notable research was done by Oliveira et al. [7], which defined a method, that can simulate a series of semi-circle or semi-oval melt pools. Oliveira et al. claimed that the method would satisfy the overlap criteria. As shown schematically in Figure 2-3, the minimum depth of overlap for a specific melt pool size is specified as M_d^0. It is influenced by the hatch distance of the melt pool and can be used to determine the optimum layer thickness. Oliveira et al. suggested an optimum layer thickness less than M_d^0 should be chosen to eliminate the lack of fusion porosity amongst successive layers [7].

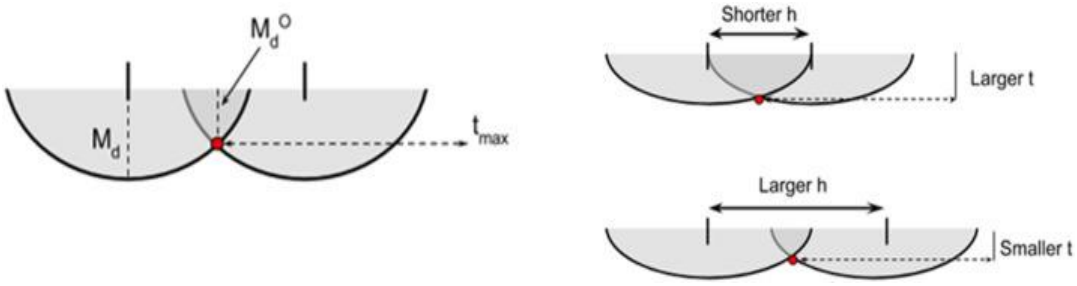

Figure 2-3: Influence of melt pool geometry for complete melting determined by layer thickness(t) and hatch distance (h). M_d and M_d^0 are melt pool depth and minimum layer thickness required for complete melting, respectively. [7]

2.3.3 Distortion due to residual stress

The LPBF process can lead to challenges beyond material defects, including residual stress within parts causing distortion. Residual stress arises due to high thermal gradients from localized heating during the process. When this stress exceeds material yield strength, it can distort the part, potentially compromising performance, and affecting build geometry. Distortion serves as a mechanism for the material to balance internal forces from melting and solidification, with significant distortion potentially rendering the component unusable. Despite efforts to understand and control residual stresses, achieving a completely stress-free part is difficult. When residual stresses surpass yield strength, it can often lead to dislocations and defects. The inhomogeneous residual stress distribution primarily responsible for distortion can be improved by preheating or post-manufacture heat treatments for stress relief. Also, strategies such as subdividing sections into smaller "islands" during scanning can effectively reduce residual stress by minimizing uninterrupted scanning lines [7].

Table 2-1 summarizes the defects found during the LPBF process and addresses the methods that can be taken to reduce these defects.

Table 2-1: Summary of approaches to reduce the build defects during the LPBF process [7].

Problem encountered	**Primary approach**	**Secondary approach**
Keyhole porosity	Reducing laser power.	Increasing laser velocity
Lack-of-fusion porosity	Reducing scan line spacing and layer thickness.	Reducing laser velocity, increasing laser power;
Reduce residual stress and distortion	Reducing scan vector length and using reheated substrate/chamber.	Reducing laser velocity.

In addition to the defect formation, microstructures are also dependent of the processing parameters, which essentially controls the mechanical properties of the material. This study will only focus on 316L stainless steel (SS) and thus, the effect of processing parameter on the microstructure and mechanical properties of 316L SS would be discussed at length in the following section.

2.4 Manufacturing processes and concomitant mechanical properties of 316L stainless steel

2.4.1 Microstructure of stainless steel (SS)

Grade 316L stainless steel (SS) is a molybdenum-containing austenitic stainless steel with less carbon than grade 316. It is more resistant to general corrosion and pitting than conventional nickel-chromium based stainless steels such as grades 302-304, making it suitable for various industrial applications [16][17][18].

2.4.1.1 Alloying elements

The alloying elements of 316L SS are listed in Table 2-2. These alloying elements are added to achieve specific materials properties. For instance, the primary effect of chromium is to impart resistance to corrosion. In fact, corrosion in the atmosphere is essentially negligible when Cr content exceeds 11-14 weight per cent. Then, Nickel improves the preservation of austenite and decreases the temperature at which it can be present. Molybdenum increases resistance to the localized corrosion phenomena, such as corrosion of the pitting and crevice. For special conditions, copper and silicon can also enhance corrosion resistance. Vanadium is used as a precipitate in creep-resistant alloys, to obtain high resistance to intergranular corrosion [16]. A detailed discussion on precipitation is given in the next section.

Table 2-2: Alloying element in 316L stainless steel [19].

Alloying elements	**C**	**Cr**	**Cu**	**Mn**	**M**	**Ni**	**P**	**S**	**Si**	**Fe**
Weight percentage	0.03	17.5-18	0.5	2	2.25-2.5	12.5-13	0.025	0.01	0.75	Balance

2.4.1.2 Precipitation in 316L stainless steel

The interstitial elements of carbon and nitrogen are found in almost all grades of austenitic stainless steels. Ti, Nb, V, and Cr have a high affinity to elements responsible for $M_{23}C_6$ / $M(NO_3)_3$ formation. These reactions can be helpful or harmful to mechanical properties, but most of the resultant products boost creep properties when their formulation is appropriately controlled. Bartova et al. [20] investigated 316L SS precipitate phases during annealing at 750° C, which is a standard high-temperature service state in the industry. They reported mainly three phases, including Sigma, Laves and $M_{23}C_6$ formation. Thus, only these phases are discussed in more details in this section [21].

C has low levels of Austenite supersaturation and a high affinity to Cr. In several grades of austenitic stainless steel, $M_{23}C_6$ is known as the secondary carbide. This phase is desired for high corrosion resistance and creep characteristics. Mo and Ni improve it by reducing Austenite's C solubility, while nitrogen raises carbon solubility and reduces $M_{23}C_6$ carbide formation. [22][23].

In most Fe-Cr alloy, the Sigma phase has a tetragonal atomic structure. In high alloyed austenitic stainless steel (SS), some elements such as Mo, Ni, Mn, and Si in the Sigma phase can substitute Fe and Cr atoms by dissolution. Sigma-phase precipitation typically occurs slowly and at long term ageing. Numerous studies suggest the nucleation sites for the Sigma phase may be $M_{23}C_6$ and δ ferrite [24].

Iron and other metallic elements such as Mo, Nb, and Ti form the Laves phase, an intermetallic with hexagonal unit cell and Fe_2Nb Laves phase is frequently recorded in niobium stabilized steels. Laves phase precipitation can be changed by adding specific alloys to improve the creep reinforcement effect. In an austenitic alloy of 20-30-2Nb, for example, the addition of Zr promotes fine dispersion of Fe_2Nb [25].

The LPBF-processed 316L stainless steel primarily contains nearly hundred percent austenite. Therefore, other phases or intermetallic compounds will not be a focus in the subsequent chapters.

2.4.2 Microstructure and mechanical property dependence on manufacturing process

316L stainless steels are conventionally manufactured by melting a charge in an electric arc furnace. The charge consists of alloy, high-carbon ferrochromium, Ni, steel scrap, stainless steel scrap, and Mo. After the metal melts, it is refined by reducing C content to an acceptable level. The molten metal is then processed using numerous metallurgical operations [26].

In one study, Bartolomeu et al. [27] compared the microstructure of samples manufactured by conventional casting, LPBF and hot pressing (HP). HP is a technique where heat and pressure are simultaneously applied to melt powder particles [28]. They found that the 316L stainless steel (SS) microstructure is highly affected by the method of processing. Figure 2-4 (e) shows the microstructure of a casting-generated 316L SS sample, showing rectangular grains with an average length of 91±17 μm. Figure 2-4 (f) shows the microstructure of an HP-produced sample, where equiaxed grains with an average size of 25 ± 4 μm are observed. In comparison to other samples, LPBF processed 316L SS showed the finest microstructure, the mean grain size being 13 ± 4 μm. [27]. Figure 2-4(a) shows an LPBF processed sample where the melt pools can be seen after etching. These melted and solidified zones are semi-circular in form, which agrees with the other research [26][29]. The effect of different processing routes on grain sizes can be clarified based on the significant cooling level variations. The HP technique cooling rate is 3 K/s, while for casting, it is 0.5 K/s. LPBF, on the contrary, has a very

high solidification rate of 103 to 108 K/s. Compared to casting and HP, a higher solidification rate in LPBF leads to significant grain refinement in the sample, as seen in Figure 2-4 (d), (e) and (f) [27].

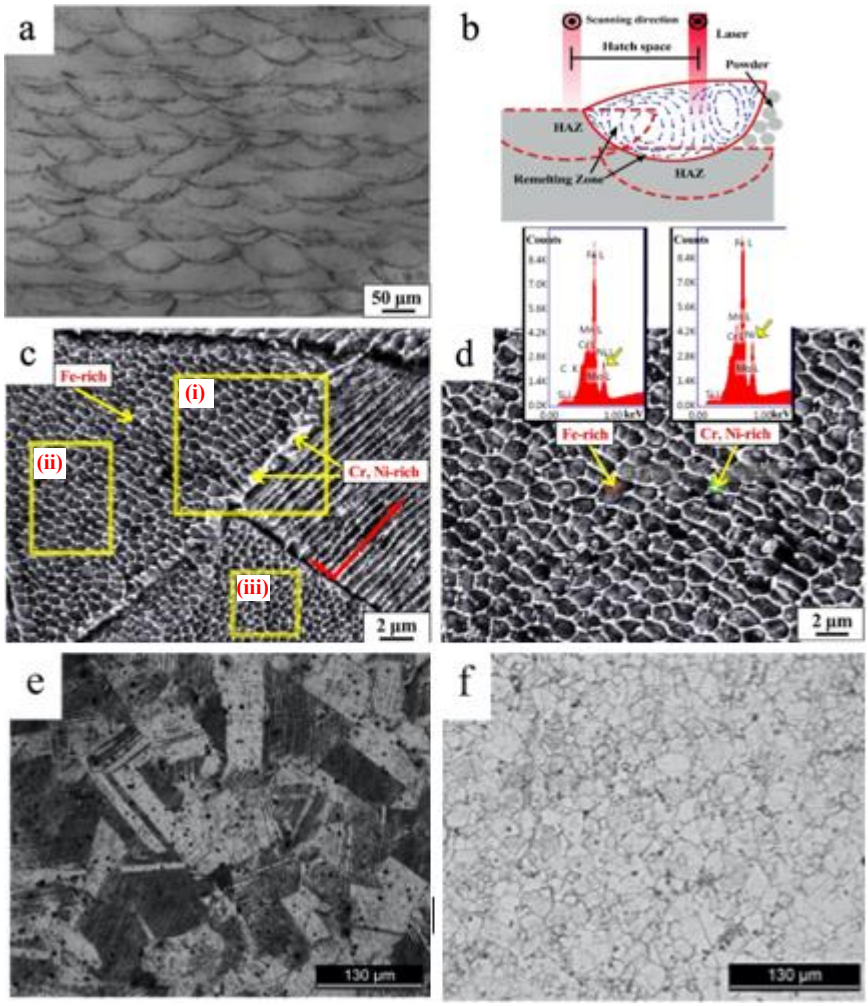

Figure 2-4: LPBF processed 316L SS (a) a cross-sectional view parallel to the building direction (b) High-magnification optical metallographic of the molten pools. The remelting zone was identified with the dimensional measurements of the molten pools (c) The morphology of subcellular structures. (d) Scanning electron microscopy (SEM) of cellular dendrites and solute segregation statistics in the white structure surrounding the dendrites. Sample optical micrograph images manufactured by (e) Cast, (f) HP [30][27].

Qu et al. [30] in Figure 2-4 (b) provided a schematic diagram to illustrate the LPBF process, where laser melts powder particles to form melt pool. While a single melt pool solidifies, laser moves to melt powder to form another neighbouring melt pool. In the process of melting powder particles, laser simultaneously remelts the previously solidified melt pool, forming a scaly pattern parallel to the build direction (see Figure 2-4 (a)). In the remelting zone (see Figure 2-4 (b)), the thermal gradient differs from that of the powder melting zone. This variation in thermal gradients leads to changes in the velocity

vectors of melt pool convection, consequently causing a shift in the direction of dendritic solidification. The morphology of microstructure on etched LPBF processed 316L SS displayed at high magnification clearly depicts these dendritic cellular structure (See Figure 2-4(c)). Columnar dendrites can be observed to grow directionally towards the centre of the molten pool from the boundary (indicated by the red arrow) inside the heat-affected zone (HAZ). The white substance surrounding the dendrites was reported to have a high concentration of Ni and Cr and the dark interior matrix is rich in Fe. This is portrayed in Figure 2-4 (d), where the peaks in the energy-dispersive X-ray spectroscopy (EDS) spectrum is attributed to Cr and Ni are noticeably sharp in the region of white segregation. This implies a high level of elemental segregation of Cr and Ni in 'Area (i)' in Figure 2-4 (c), especially at the top portion of the melt pool around the boundary. This elemental segregation is due to the low G/R and high G-R of solidification in the remelting zone mentioned previously (Section 2.2.1).

While comparing the subsequent mechanical properties, Casting and HP-produced samples had a mean hardness of 165 HV and 176 HV, respectively. As seen in Figure 2-5 (a), the calculated hardness value of 229 HV for SLM samples indicates a difference of between 40% and 30% increase compared to casting and HP samples respectively (The indentation was done on the build plane). Sun et al. [31] further confirmed the hardness value for LPBF processed 316L SS reported by Bartolomeu et al. [27] by SLM and casting technologies.

Figure 2-5 (b) shows that HP and SLM specimens have higher yield and ultimate tensile strength (UTS) than standard cast specimens. Moreover, compared with 316L SS cast samples, SLM samples had higher yield strength (+41%) and tensile strength (+144%). However, LPBF samples had lower ductility values than those reported by other methods [27], as measured by the percentage of tensile strain in Figure 2-5 (c). LPBF specimens have higher strength and lower ductility, consistent with other studies [32][33].

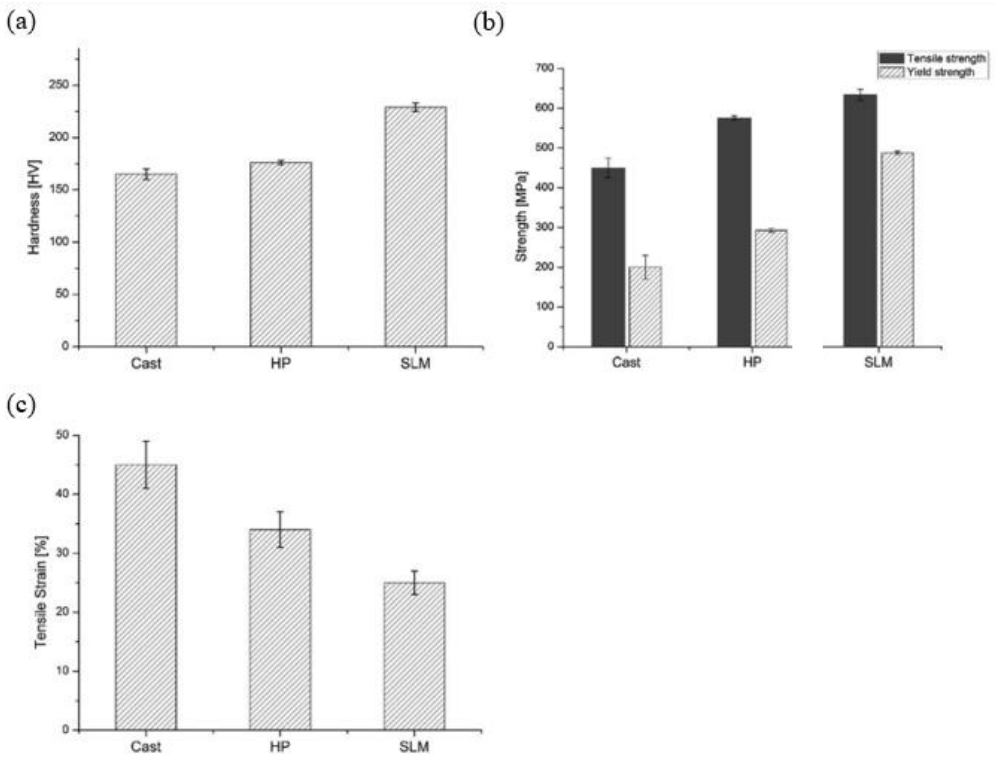

Figure 2-5: Comparison of the mechanical properties of 316L SS for three different manufacturing technique; casting, HP and LPBF. The graphs display (a) The Vickers hardness value (averaged from six indentation) (b) YS and UTS and (c) Tensile strain [27]. *Error bound to one standard deviation.*

The high strength of 316L SS for LPBF can be attributed to the development of high concentration of dislocations, low-angle grain boundaries and solidification-enabled cellular structures. Additionally, high uniform elongation is associated with a progressive and steady work-hardening process governed by a heterogeneous hierarchical microstructure. The role of microstructure in ductile behaviour can be further explained by earlier mentioned elemental segregation that occurs at the external boundary of the cellular substructure during rapid cooling [34]. This theory was confirmed by Pace et al. [35] and Wang et al. [36]. They reported the segregation of heavier elements such as Mo and Cr and a nano inclusion of Silicon Oxide at the cellular boundaries. Elemental segregation is connected to the dislocation structure at the external boundary of the cellular substructure. Due to the dislocation of cells that have already formed, the local stress field at the subcellular boundary promotes slip and homogenous deformation through shear allowing ductile behaviour. Another phenomenon, called twinning-induced plasticity of LPBF 316L material, as defined by Pham [41], appears to support shearing and plasticity between low-angle boundaries. Solute segregation along cell walls and low-angle grain boundaries can improve pinning dislocation and facilitate twinning, which illustrates LPBF's ability to produce alloys for structural applications with specific microstructures and high performance.

Hall-Petch strengthening [29][37] can explain another mechanism behind the high strength of LPBF specimens. It predicts that a higher strength is expected by reducing the grain size. According to this phenomenon, when there are several grain boundaries to travel through, a dislocation takes more energy to shift course and cross through the adjacent grain. The smaller grain size effectively limits dislocation pileups. In this sense and considering the microstructures in Figure 2-4, it can be inferred that the higher hardness and strength of LPBF specimens are linked to the observed finer microstructure [27]. The simple expression of Hall-Petch relationship between grain size and yield strength can be expressed with Equation 2-3.

$$\sigma = \sigma_0 + kd^{-0.5} \qquad \text{Equation 2-3}$$

In Equation 2-3, the σ is the yield strength; σ_0, k and d are the lattice friction stress, materials dependent constant named Hall-Petch slope and the average grain size respectively. The average grain size d is defined as the following.

$$d = \frac{1}{n}\sum_{i=1}^{n} n_i d_i \qquad \text{Equation 2-4}$$

In Equation 2-4, n is the total number of measurements; n_i and d_i are the number corresponding to the grain size respectively. The Equation 2-3 takes into consideration of only average grain size but Berbenni et al [38] developed a theoretical micromechanical model to account for the effect of grain size distribution for fine grained polycrystalline materials. The proposed theoretical model informs that, in addition to the average size, grain distribution plays an important role to determine a material's yield strength.

A later empirical study conducted by Lehto et al. has further confirmed that grain size distribution plays an important role in addition to average grain size in determination of yield strength of the polycrystalline materials. The extended Hall-Petch equation considering grain size distribution in the study was expressed with Equation 2-5 [39].

$$\sigma = \sigma_0 + kd^{-0.5}(1 + f\frac{\Delta d}{d}) \qquad \text{Equation 2-5}$$

The $\frac{\Delta d}{d}$ is relative grain size dispersion and f is constant derived empirically. This extended Hall-Petch model in Equation 2-5 describes the proportional relationship between the grain size distribution and materials yield strength.

Salman et al [40] conducted a study to compare the UTS, YS and corresponding microstructure for LPBF processed 316L SS, shown in Figure 2-6. A consistent trend is apparent from Figure 2-6, where

YS and UTS is inversely proportional to the average grain size. Subsequently, the grain dispersion appears to have a proportional relationship with the average grain size. The trend in Figure 2-6 confirms the extended empirical model described in Equation 2-5, as reported by Lehto et al. [39]. The next section will focus on the factors controlling the average grain size during the LPBF process.

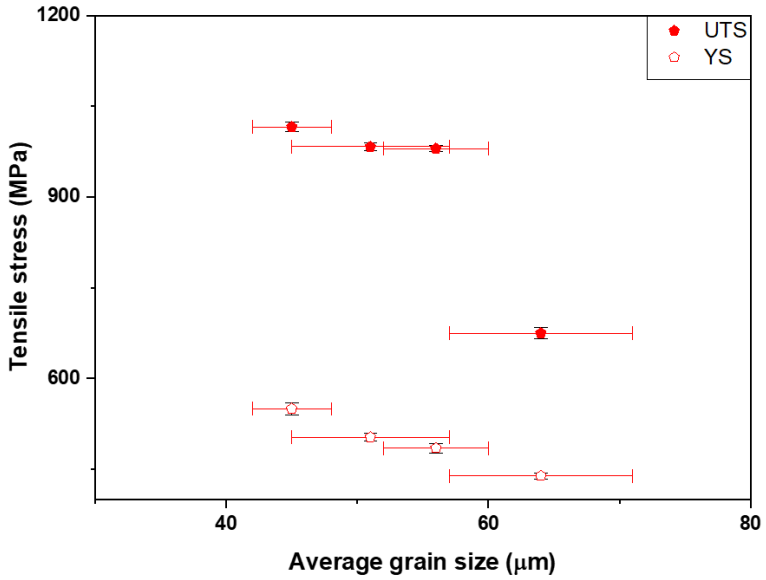

Figure 2-6: The effect of average grain size and their dispersion on UTS and YS of LPBF processed 316L SS. [40]

2.4.2.1 Role of scanning speed and laser power on the microstructure

Equation 2-1 and Equation 2-2 show that the delivered energy is significantly affected by scanning speed and laser power. In a study of LPBF of titanium alloy (Ti6Al4V), Hanzl et al. [8] reported different outcomes in different zones of laser power and scan speed combinations, which can be generalised to other material systems. They used laser power and scan speed to create a map and divided it into four zones (see Figure 2-7).

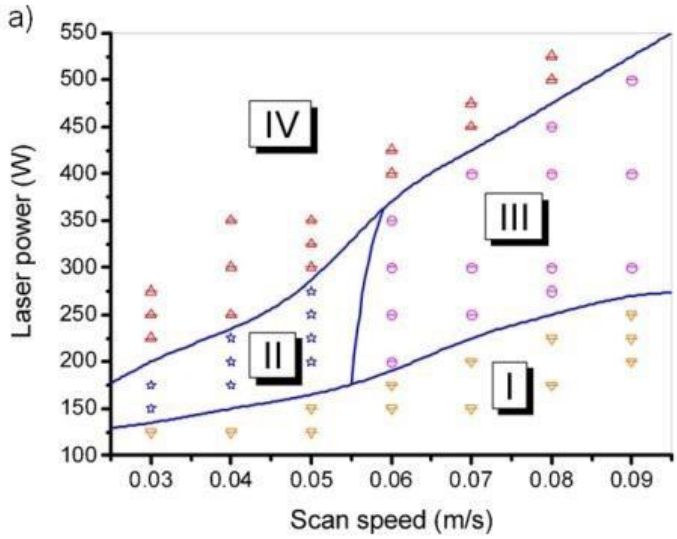

Figure 2-7: The effect of laser power and scan speed on material structure. I–IV represent four different zones based on energy input. [8]

The four zones based on power and laser speed are defined as follows:

I. No melting: At low laser power, energy is not sufficient to melt powder particles.
II. Partial melting: At moderate laser power and low scanning speed, the powder particles partially melt into coarser balls approximately the size of the laser beam diameter. [41]
III. Melting with the balling phenomenon: At high scanning speed and laser power, the melting track can form into rows of coarse beads. This phenomenon is caused by reduced surface tension.
IV. Complete melting: At sufficient laser energy, a molten metal track consists of completely melted powder is formed, which solidifies into a compact surface.

The representative surfaces for LPBF materials processed in zones II, III, and IV of laser power and scan velocity are shown in Figure 2-8.

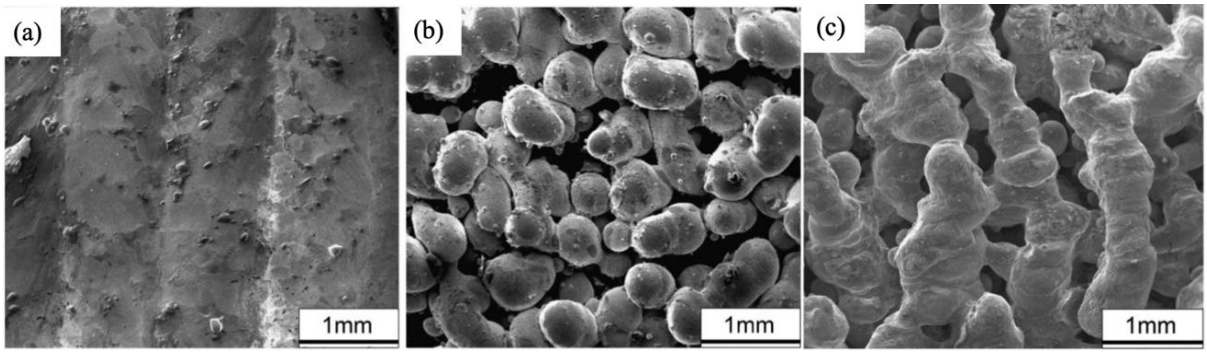

Figure 2-8: Surface morphology of LPBF processed materials; a) fully melted and compacted surface (zone IV); b) surface with the balling phenomenon (zone III); c) porous structure resulting from partial melting (zone II) [9].

Donik et al. further investigated the influence of laser power and scanning speed on the solidification by a parametric study. The study was conducted on various 316L SS specimens, manufactured with AconityMINI selective laser printing machine. The processing parameters include power ranging from 150-350 W, scanning speed within 400-800 mm/s range with a 45°-layer rotation. Also, two focus diameters were used to study its effect on specimen density. The chemical composition of the powder used for the specimen manufacturing is given in the Table 2-3 [42].

Table 2-3: Powder chemical composition reported of 316L SS using induced coupled plasma optical emission spectroscopy; reported by Donik et al.[42]

Elements	**C**	**Si**	**Mn**	**Cr**	**Ni**	**Mo**	**Fe**
wt %	0.006	0.22	1.6	17.7	13.6	2.8	balance

In total, twenty cubes with different processing parameters were qualitatively compared. The optical microscopy images of these cubes are shown in Figure 2-9. The following points can be drawn from their report [42].

- Spot diameter significantly affects the percentage of porosity, even at the same energy density. The comparison between specimen 19, 20 and 1,2 makes it very apparent in Figure 2-9.
- Large pores at low energy density (sample 19 and 17) and large number of small pores (sample 19 and 1) can be seen in Figure 2-9. The large pores are lack of fusion porosity, and the small circular pores are formed due to trapped gas. The first one indicates insufficient energy density resulting in unmelted powder particles left in the melt track and forming a defect, and the latter one is due the trapped gas during rapid solidification [7].

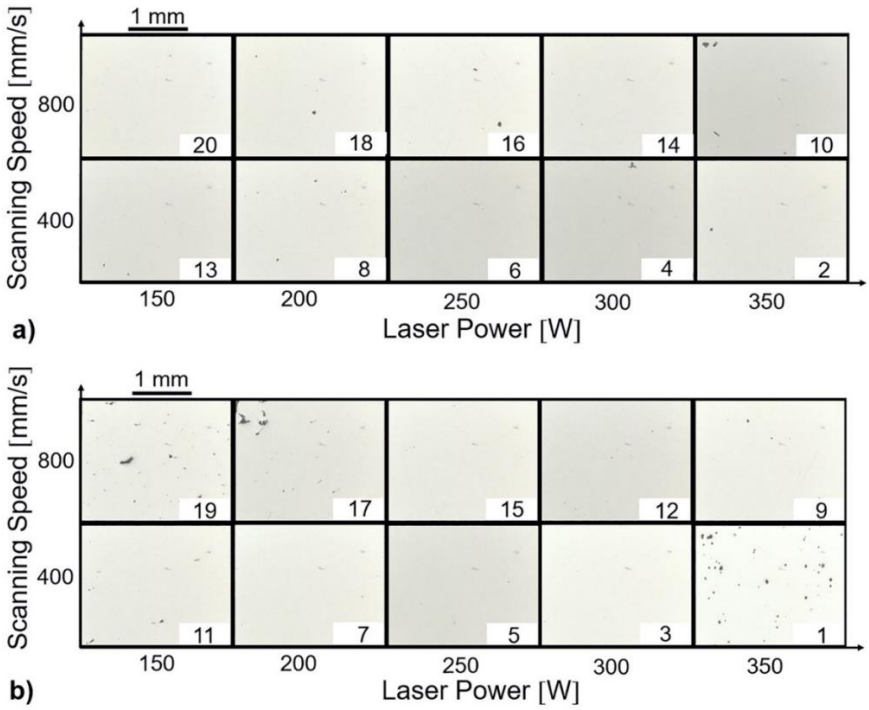

Figure 2-9: Optical microscopy images of 316L SS specimens fabricated with combination of different power and scan speed. The focus diameter used are (a) 60 µm (b) 80 µm [42]

In addition to the defect/pore distribution, energy density effect on microstructure was also investigated in the study by comparing the IPF maps and pole figures between specimens manufactured with different laser powers (see Figure 2-10). Figure 2-10 (b), (c) compares two microstructures manufactured with the same energy density but different laser powers. The average grain size was reported to get finer as the energy density decreases with decreasing laser power.

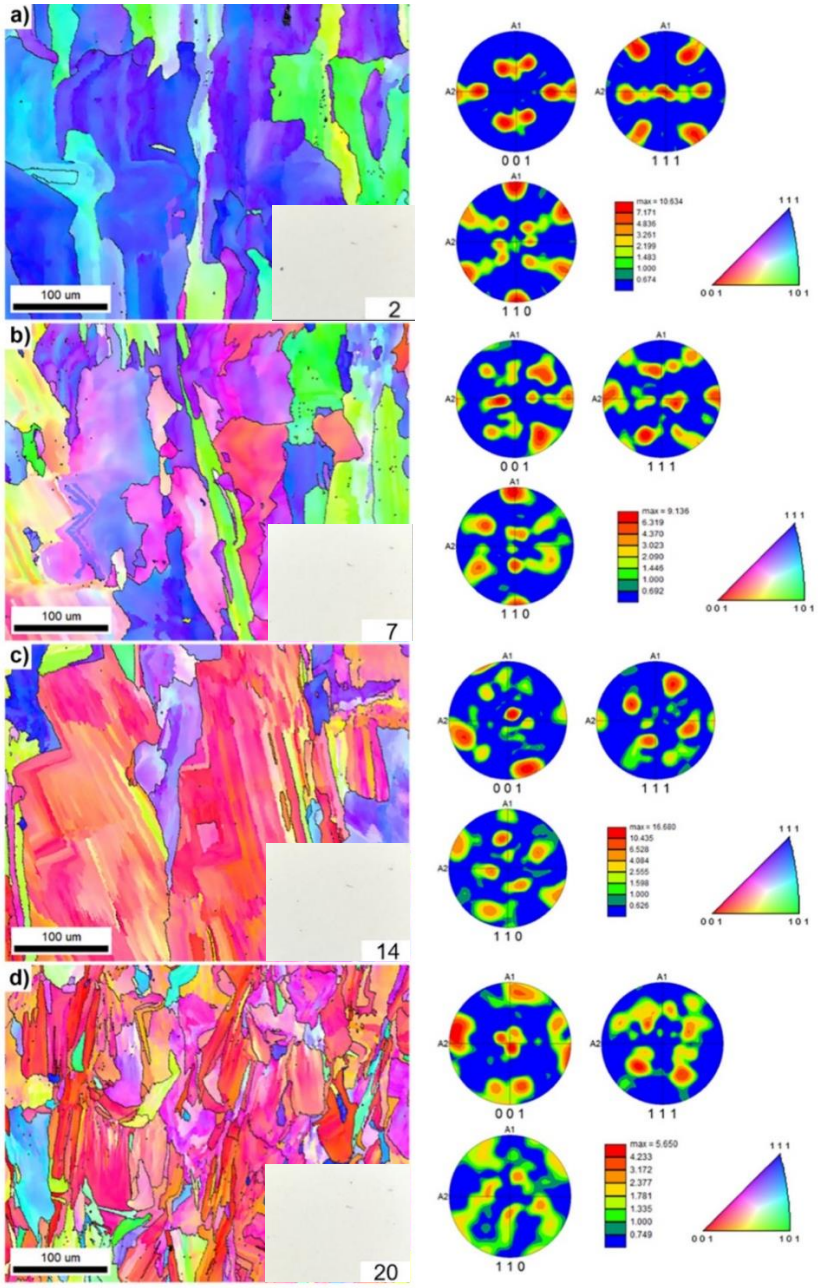

Figure 2-10: Electron-backscattered diffraction (EBSD) inverse pole figure (IPF) maps (left) for the 316L SS specimens built with different energy density (a) 486 J/mm^3 with 350 W (b) 208 J/mm^3 with 200W (c) 208 J/mm^3 with 300 W (d) 104 J/mm^3 with 150W. The pole figure (right) indicates preferred crystallographic orientation of the grains. [42]

The study further characterised the microstructure using the EBSD (Electron Back Scatter Diffraction) pole figure (PF) and inverse pole figure (IPF) maps and reported some insightful observations [42]. The key points are summarised below.

- Increase in input energy density resulted in a decreased number of low and high-angle grain boundary.

- LPBF process parameters had a minor impact on geometrical necessary dislocation density (GND).
- Higher energy density led to grain and sub-grain shapes resembling conventionally cast structures. Sample 2 in Figure 2-11 (a) shows columnar grain growth in the AM building direction, while sample 7 in Figure 2-11 (b) has zigzag growth with macro zigzag boundaries.

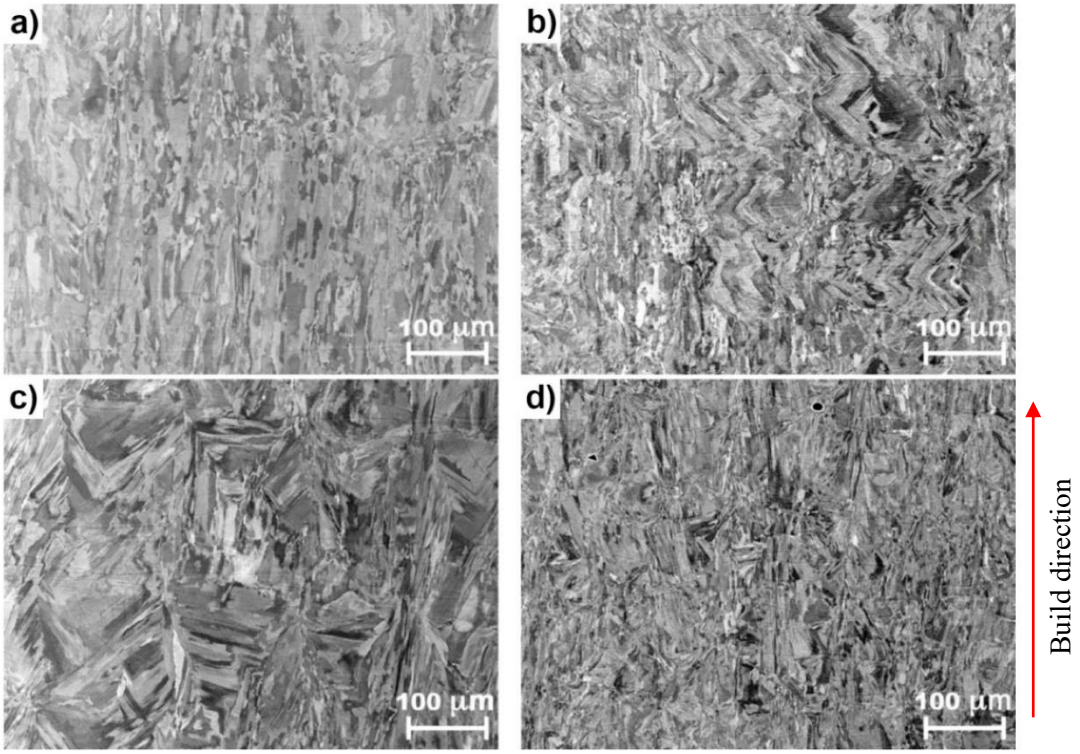

Figure 2-11:Backscatter image of (a) sample 2 (b) sample 7 (c) sample 14 and (d) sample 20 [42].

- Samples 7 and 14 in Figure 2-10 (b) and (c) respectively have the same energy density (208 J/mm³) but exhibit different grain sizes and grain area. This confirms that smaller power is associated with finer grains. Subsequently, energy density was reported to play an important role in controlling grain morphology; finer grain microstructures were associated with lower energy density due to higher cooling rates and shorter grain growth times [42].
- The average grain size and their dispersions was reported to be proportional to the energy density by many studies [43][44][45]. Donik et al. [42] and Agrawal et al. [45] in fact showed a relationship between grain size and energy density, with an upward trend of grain size with increasing energy density, displayed in Figure 2-12.

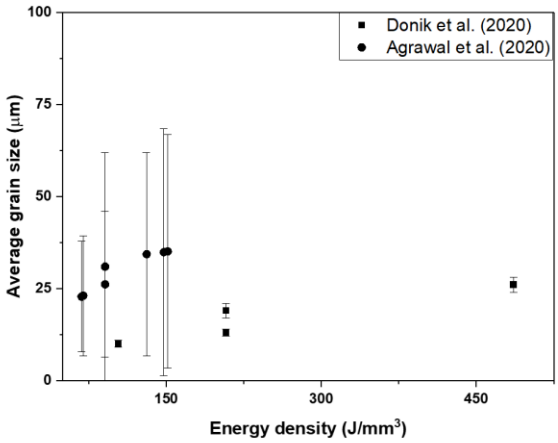

Figure 2-12: Effect of energy density on average grain size for LPBF processed 316L SS specimens[43][45]. Error bars bound one standard deviation.

- Donik et al. further reported the relationship between energy density and crystallographic texture with higher laser power of 300 W is finer and has weaker texture in Figure 2-10 (c) compared to the lower laser power of 200 W in Figure 2-10 (b). The observation was further supported by a general trend in Figure 2-10, indicating a strong relationship between energy density and texture (texture is measured by intensity in the pole figure).

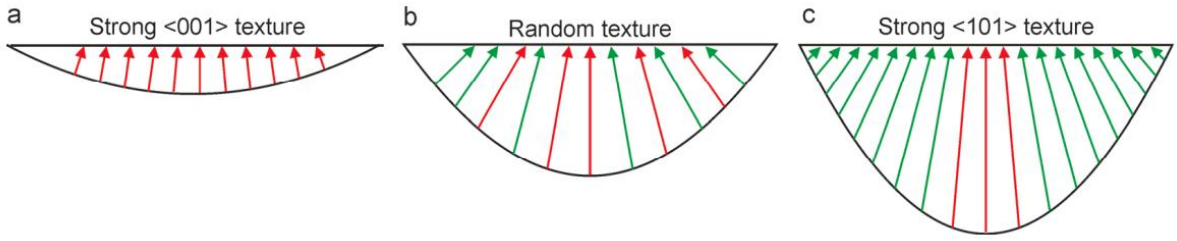

Figure 2-13: Schematic diagram depicting the formation of various textures based on melt pool depth, with red arrows denoting <001> orientation and green arrows denoting <101> orientation [46].

The crystallographic texture formation due to different volumetric energy density (VED) mentioned by Donik et al. [42] had been confirmed by several studies [46], [47], [48] and they also reported that strong crystallographic texture is associated with higher energy density. Leicht [46] explains the mechanism as following, the orientation of cells in a sample is linked to its texture, with cells growing parallel to the building direction corresponding to a <001> texture (see Figure 2-13 (a)). Also, melt pool boundary shape and radius significantly influence texture development, as cells grow normal to these boundaries. The texture becomes more random as the angle between the normal and building direction approaches 45°, forming a predominant <101> texture (see Figure 2-13 (c)). The transition between orientations, such as <001> and <101>, involves other orientations like <012>. Also, process parameters and scanning strategies can impact crystallographic orientations, ranging from strong <001>

to <101> textures to more random textures (see Figure 2-13 (b)). Thus, adjusting energy density affects texture strength, with larger melt pools from higher energy yielding a stronger <101> texture and lower energy resulting in a more random texture. The temperature gradient resulting from energy density and melt pool shape are crucial factors influencing crystallographic orientations.

2.4.2.2 Role of scanning strategy on the microstructure

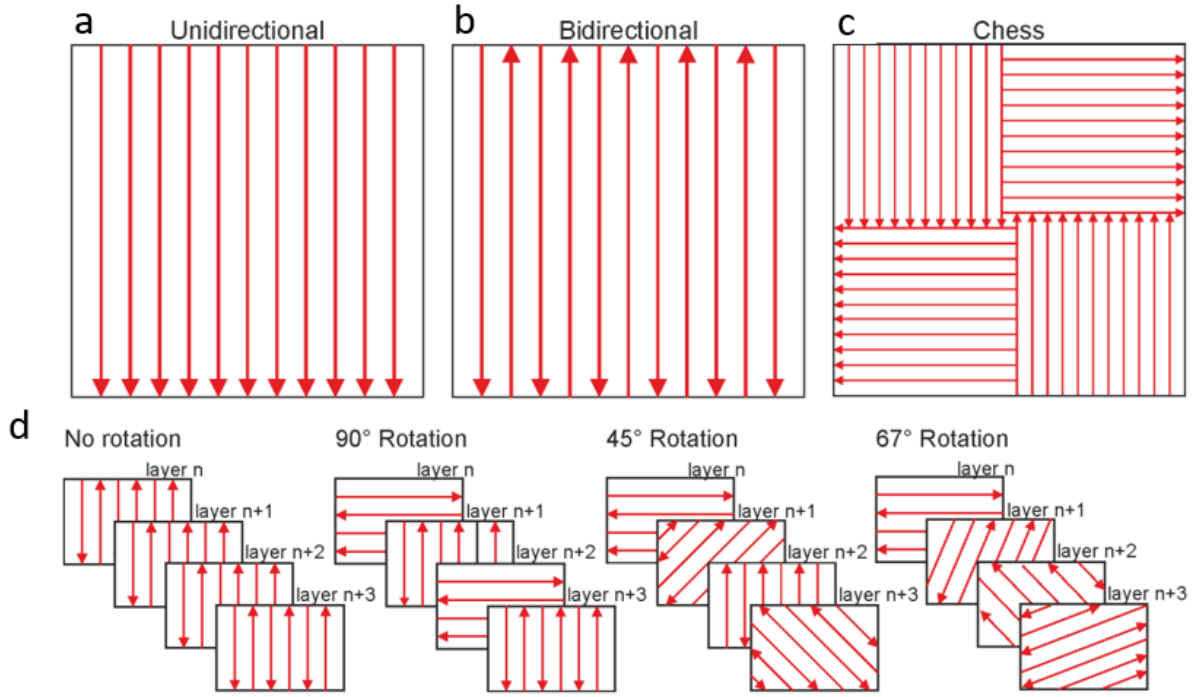

Figure 2-14: Schematic of different scanning strategies (a) unidirectional (b) bidirectional (c) Chess or island scanning. (d) layer rotation at various angles from 0° to 90° [46].

The scanning strategy is the path that the laser follows in order to scan and fuse the powder layer in the LPBF process. It is crucial for the final quality of a printed part, influencing defect types, microstructure, surface roughness, and residual stresses. Bidirectional and chess (island) scanning shown in Figure 2-14 are the most used strategies [41][49][50]. The island scanning technique is generally used to reduce temperature gradients, reducing potential distortion. Scanning strategy has been reported in a study to affect the roughness and density of LPBF materials, as shown for titanium alloy (Ti6Al4V) in Table 2-4 [14]. The island scanning strategy in the study reported a rougher surface in comparison to the line scanning specimens. The study further reported the degree of porosity in line and island scanned Ti6Al4V using X-ray computed tomography (XCT) technique. Line scanning was reported to achieve higher apparent density (~99.6 per cent), while island scanning was more porous (~98.6 per cent). Also, the island scanning was reported to have a larger number of pores compared to line scanning. On the other hand, a high-density spherical pore at the start of the build was reported for the line scan specimen.

The pore morphology for island scanned specimen was reported to be mostly irregular while line scanned specimen has mostly spherical pores.

Table 2-4: Material property comparison for Ti-6Al-4V specimens built with line and island scanning strategy.[14]

	Average roughness, R_a [µm]	**Maximum roughness, R_z [µm]**	**Density [%]**
Line scanning	48.4	678	99.60%
Island scanning	66.4	722	98.60%

The porosity distribution of these specimens was explained in a study conducted by Shrestha et al. [49] in terms of thermal condition during the LPBF process. They claimed that the local temperature gradient and solidification rate are linked to porosity distribution. Initially, the solidified component cools until a new layer is ready for scanning. Then, reheating occurs upon scanning the next layer. The longer the heat input from the laser persists in a given layer, the higher the overall sample temperature and the lower the local temperature gradients. Accordingly, the temperature gradient decreases as scanning within a layer takes a 90° turn. Consequently, the first scanned lines experience quicker cooling than the last scanned lines. Faster solidification imposes a higher risk of gas precipitation and pore formation [49]. It was suggested that changing the direction of printing between successive layers may reduce the porosity build-up on one side of the specimen. Also, a normalised thermal gradient often results in lower thermal stresses and thereby decreases the chance of directional distortion. The most significant distortion is, therefore, anticipated at the start of the scanning. Oliviera et al. reported that the distortion in the line scanning resulted from thermal stress [14].

In addition to affecting porosity, these variations in thermal conditions during the LPBF process also affect the metallurgical features of the microstructure, as reported in the section 2.4.2.1. The role of scanning strategy on these the microstructure can be summarised as following from the recent studies [14], [30], [40], [51], [52], [53].

- Unidirectional scanning involves scan vectors going from one side to another with the same direction in all layers, but it is rarely used due to increased residual stresses.
- Bidirectional scanning (meander scanning) is faster, with scan vectors turning back at the part edge.
- Chess strategy (island scanning) divides the cross-section into smaller boxes, using unidirectional or bidirectional scanning with rotated patterns to reduce residual stresses.

The variation of scanning strategy can significantly influence the average grain size. The differences in returning times (i.e., the time until the laser returns to a point of a melted scan track) associated with the scanning strategy, contributes to the observed variations in the grain size. Shorter returning times, as in island scanning, may result in higher overall temperatures, potentially affecting solidification conditions and, consequently, grain size. Moreover, the presence of a contour in the scanning strategy, which is a scan around the perimeter of the scan area in each layer, is suggested to contribute to smaller average grain size compared to the scanning without contour, possibly due to variations in grain size within the contour [40].

A subsequent factor affecting microstructure is the scan rotation. Scan vectors or stripe orientations are usually rotated at a certain angle after each layer, known as scan rotation. A common scan rotation angle is 67°, achieving optimal spacing between angles and reducing residual stresses [46]. Scan rotation is useful and are implemented to reduce the risk of distortions. Scan rotation angles, such as 67°, are chosen to maximize the number of layers before the same orientation occurs again, optimizing spacing and thus commercially available LPBF processes often use a 67° rotation angle as the standard.

Scan strategy and layer rotation not only affect part density, distortion, and residual stress but also the crystallographic texture. Numerous studies consistently reported a robust <100> crystallographic texture along the laser scan direction, a characteristic maintained even with a 180˚ rotation in bidirectional scanning [54], [55], [56]. On the other hand, bidirectional scanning without rotation results in a distinctive <110> texture along the build direction [46].

2.4.2.3 Effects of geometry size scale on microstructure and mechanical properties

In addition to the processing parameters, geometry size scale can also affect the microstructure of the LPBF process. In a recent study, the effects of specimen geometry and size on subsequent thermal conditions, microstructures, and resulting mechanical properties were investigated by Shrestha et al. [4] for 17-4 precipitation hardening (PH) SS. They used three separate geometries, including a dog-bone component (represents the specimen geometry) and two square rods of different initial cross-sectional measurements (smaller and larger), each of which were machined to the same final dog-bone geometry (as shown in Figure 2-15). They were manufactured utilising the same set of process parameters.

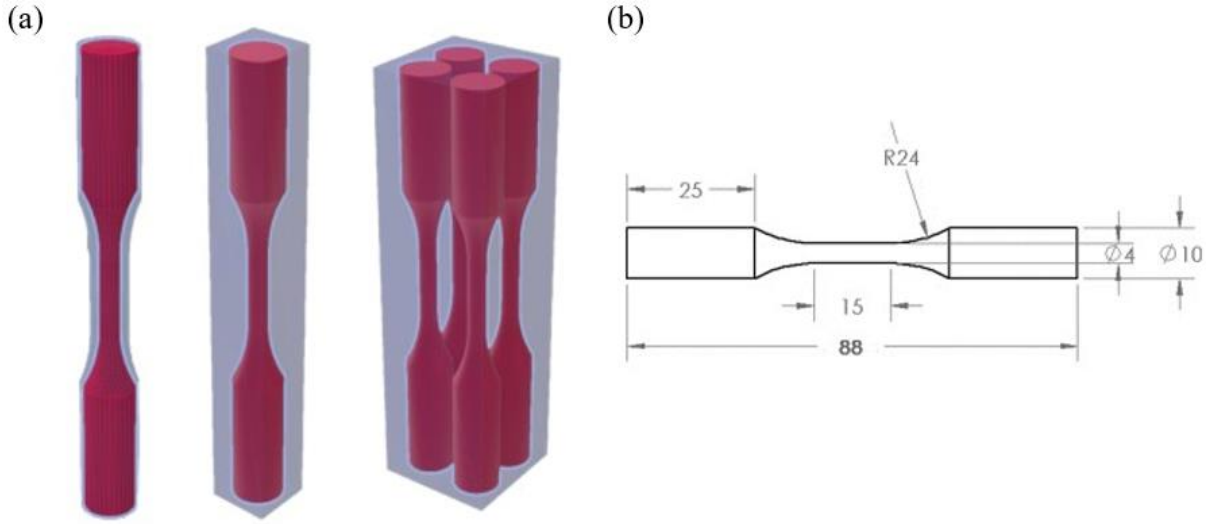

Figure 2-15: (a) Schematics of dog-bone parts, small blocks, and large blocks from which specimens were machined to the geometry and dimensions designed according to ASTM Standard E606 (b) Dimension of the dogbone specimen; all measurements are in millimetres.[4] [57]

A completely reversed uniaxial strain-controlled fatigue test and a quasi-static tensile test were used to determine these component's mechanical properties and there was a substantial variation in fatigue lifespan. According to the fractography study [4], the shorter lifespan of small block specimens was due to the entrapped gas pores causing crack initiation and eventual failure. As seen in Figure 2-16, a detailed defect distribution was conducted to assess the size and quantity of pores present within 100 µm of the outer surface.

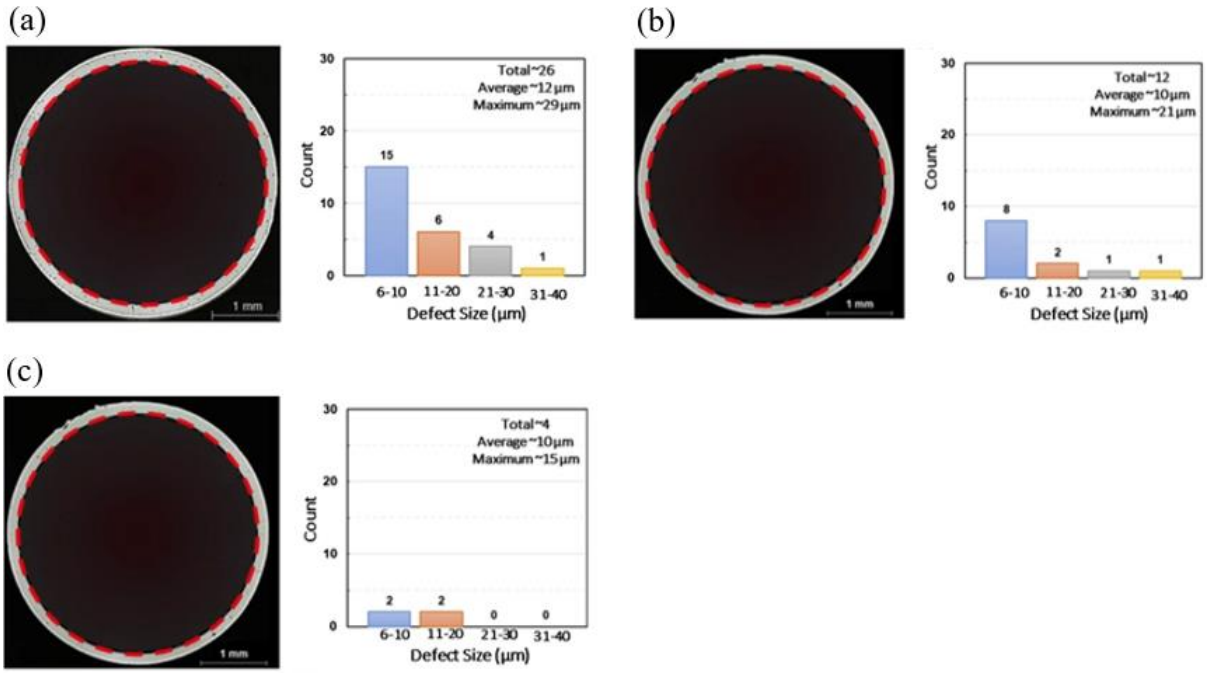

Figure 2-16: Optical micrographs of the porosity size distribution in the gauge section of (a) dog-bone, (b) small block, and (c) large block specimens, along with their respective histograms. [4]

According to Table 2-5, an increase in pores size and number was observed as the specimen geometry size gets smaller. Thus, big block specimens outperformed small block and dog-bone specimens in terms of fatigue performance.

Table 2-5: Comparison of microstructural features between specimens with different geometry [4]

Specimen	Number of pores	Maximum pore size	Average melt pool size
Large block	4	15 µm	162 µm
Small bock	12	21 µm	156 µm
Dog-bone	27	29 µm	142 µm

The study hypothesised that differences in thermal history affected by component geometry and size during the LPBF process resulted in variations in pore statistics. The melt pool characteristics was reported to be significantly influenced by the part's localised thermal history too [58].

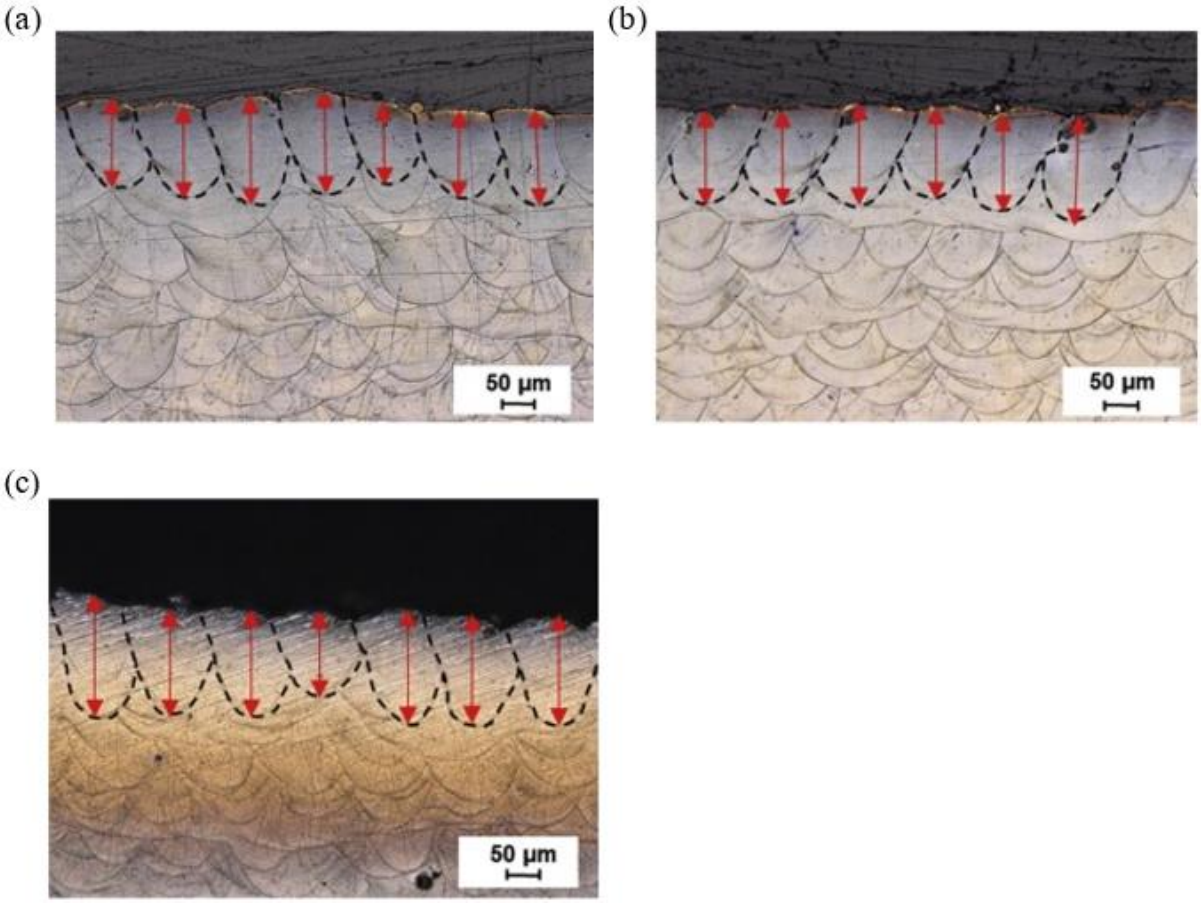

Figure 2-17: Optical micrographs of melt pool in their transverse position (i.e. perpendicular to the substrate plate) of (a) a dog-bone specimen (b) small-block specimen with, and (c) big-block specimen in non-heat treated condition [4].

Further investigation revealed, large block specimens had a deeper average melt pool. In contrast, small block and dog-bone specimens had shallower average melt pool, respectively (see Table 2-5). The variations in melt pool size between specimens in Figure 2-17 indicate that the dog-bone, small block, and large block specimens might have had different thermal histories, which can explain the differences in fatigue performance and porosity levels observed [4]. Dog-bone specimens had a faster cooling rate [59] due to high-temperature gradient compared to small and large block specimens, resulting in vertical grain growth and shorter melt pool depths. A quicker cooling rate in dog-bone specimens led to faster solidification, decreasing the period for gas bubbles to leave the melt pool, causing them to turn into entrapped gas pores [60]. This phenomenon explains why dog-bone specimens had many large pores, while large block specimens had fewer and smaller pores [4]. The study suggests a strong link between defects distribution, microstructure and geometry size. The findings imply the importance of the material defect distribution in fatigue lifing consideration. Further discussion on mapping defect distribution will be given in Chapter 4.

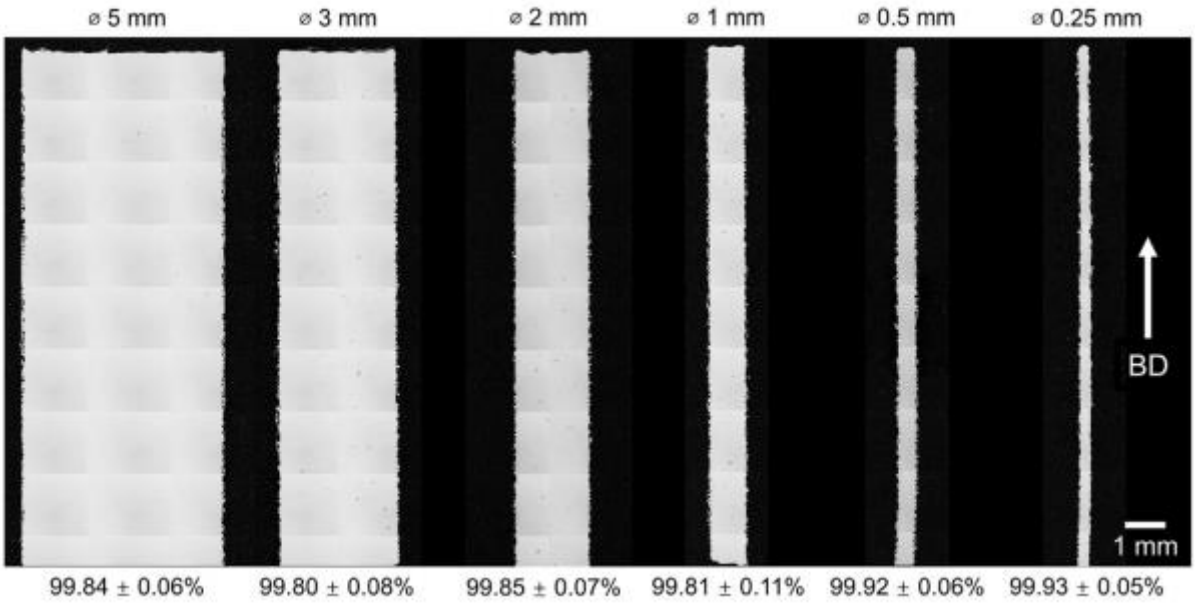

Figure 2-18: Longitudinal cross section area of 316L SS struts along with their diameter and density [48].

The effect of specimen size scale has further been investigated by several studies [48], [61]. Wang et al. [48] conducted a study on 316L SS struts of size ranging from 0.25 mm to 5 mm. They reported, as the strut size decreases, the part gets denser. In addition to that, the effect of specimen size scale on the microstructure has also been investigated in that study (See Figure 2-19). The study reported that the columnar grain width showed variance but did not follow a clear trend with strut diameter. A transition from < 110 > to < 100 > crystallographic texture along the BD was noted as the strut diameter decreased, with a critical threshold at 0.25 mm diameter strut. The strong texture of 0.25 mm diameter structure can be explained by shallow melt pool reported in Table 2-5 related to specimen size. Shallow melt pool was reported to have <100> preferred crystallographic orientation by Leicht [46], mentioned in the section 2.4.2.1. On the earlier mentioned study, Wang et al. [48] suggested that rapid solidification altered growth directions, leading to the observed texture changes and dismissed recrystallization as an influencing factor on crystallographic texture.

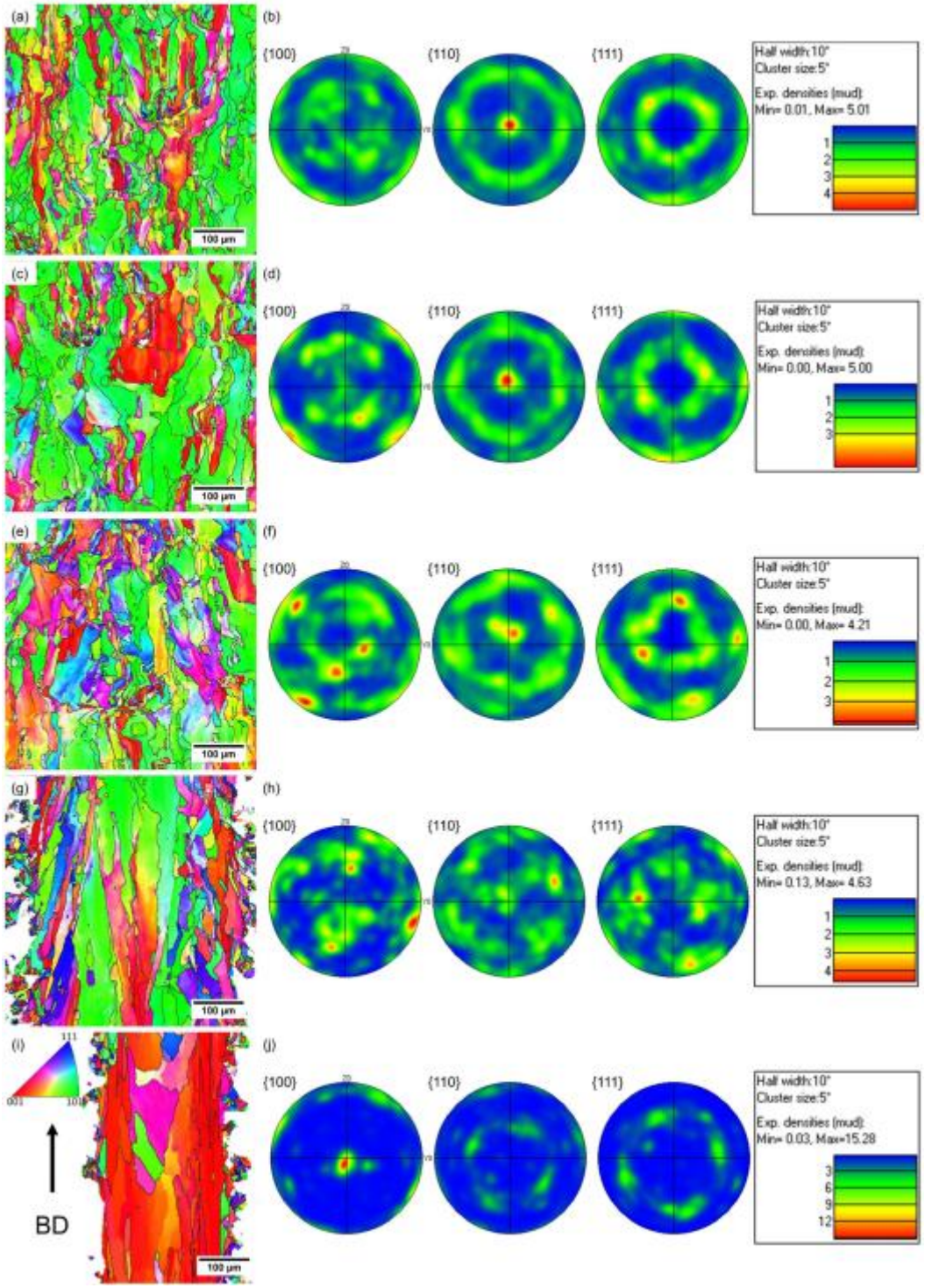

Figure 2-19: Comparison of IPF map (left) and pole figure (right) of 316L SS strut of different size (a)(b) 5 mm (c)(d) 2mm (e)(f) 1 mm (g)(h) 0.5 mm and (i)(j) 0.25 mm [48].

2.5 Fatigue performance of metallic materials

2.5.1 Introduction and definitions

Fatigue is generally defined as changes in metallic materials due to cyclic stress or strain. However, this definition typically refers primarily to changes that contribute to failure due to crack initiation and gradual growth. By definition, fatigue occurs when repetitive cyclic loading occurs below the loads that may cause a monotonic or static fracture. Suresh specifies various fatigue modes in his book such as mechanical fatigue, which will be the main focus of this study [62].

Fatigue typically results from damage accumulation in the material structure, caused by cyclic stress or strain, resulting in cracks that propagate and grow until they exceed the fatal size to cause final failure. In cyclic fatigue testing, the parameters typically used are defined in Equation 2-6 and Figure 2-20 [63]. Usually, materials that fail below 10^5 cycles are considered to suffer from low cycle fatigue (LCF) and above this is referred to as high cycle fatigue (HCF). The fatigue life of a material is usually presented by maximum stress (S) or stress amplitude against the number of cycles (N), known as stress life (S-N) data.

2.5.2 Mean stress effect on fatigue life

The definitions of fatigue loading often apply to completely reversed loads of fatigue where the mean stress σ_m is zero. Mean stress is considered to impact engineering material's fatigue behaviour significantly. A sinusoidal waveform fatigue cycle with the non-zero mean stress is shown schematically in Figure 2-20. Equation 2-6 determines the mean stress σ_m, stress amplitude σ_a and stress range $\Delta\sigma$ in this situation, respectively.

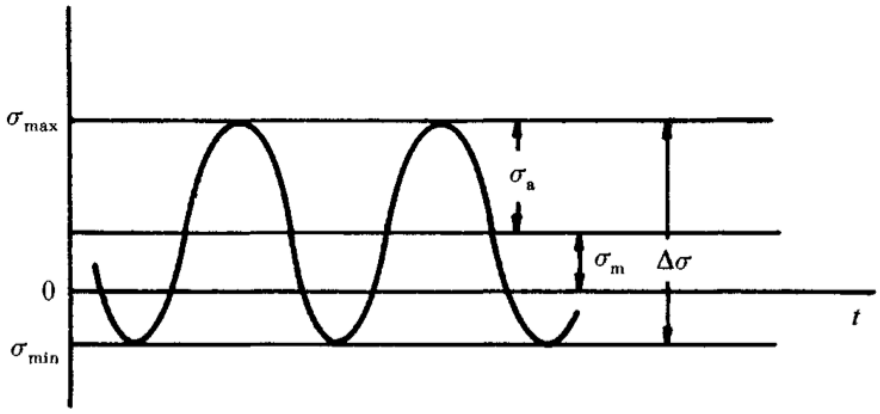

Figure 2-20: Nomenclature for the parameter of stress that affects the life of fatigue. With time t, the variance of stress σ is shown [62].

$$\Delta\sigma = \sigma_{max} - \sigma_{min}, \qquad \sigma_a = \frac{\sigma_{max} - \sigma_{min}}{2}, \qquad \sigma_m = \frac{\sigma_{max} + \sigma_{min}}{2} \qquad \text{Equation 2-6}$$

The load ratio, $R = \frac{Maximum\ stress}{Minimum\ stress}$, is often used to describe the mean stress. Load ratio R = -1 for fully reversed loading, R = 0 for zero-tension fatigue, and R = 1 for a static (noncyclic) load are used in this interpretation. Figure 2-21 (a) displays S-N diagrams for metallic materials as a result of four distinct levels of a mean stress, σ_{m1}, σ_{m2}, σ_{m3} and σ_{m4} [62]. Figure 2-21 (a) shows a standard stress life (S-N) plots for metallic materials as a function of four different levels of a mean stress, σ_{m1}, σ_{m2}, σ_{m3} and σ_{m4}. There is typically a declining fatigue life with an increasing mean stress value.

.

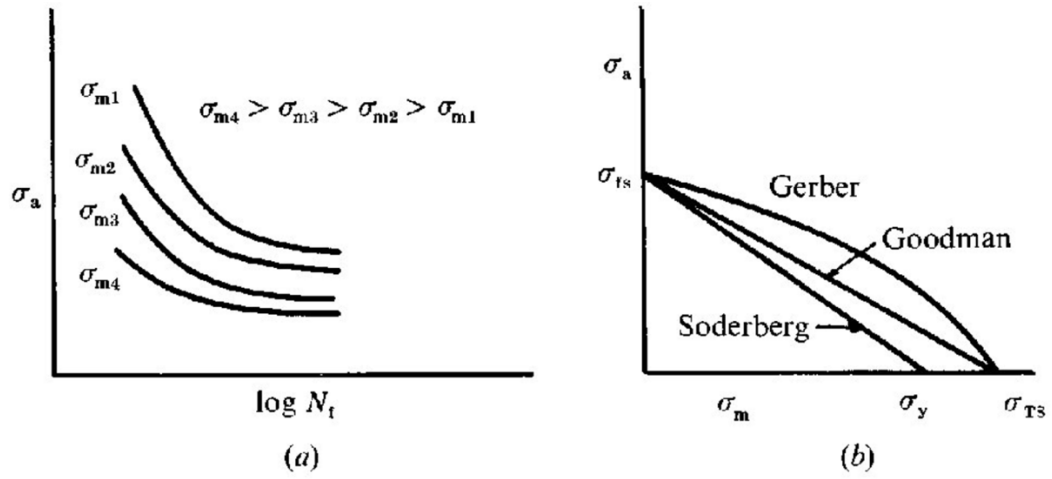

Figure 2-21: (a) Typical plots of stress amplitude-life for different mean stress values. (b) Constant life curves for non-zero mean stress loading fatigue [62].

Figure 2-21(b) shows a constant-life diagram that charts various combinations of stress amplitude and mean stress resulting in constant fatigue life. There had been numerous models, which described constant-life diagram data but the most well-known for high cycle fatigue are Gerber [64], Goodman [65] and Soderberg [66], depicted in Figure 2-21(b). As for low cycle fatigue, the most popular mean stress correction model is described by Smith-Watson-Topper (SWT) [67]. SWT mean stress correction is generally combined with the strain-life approach in most finite element modelling software (e.g., Ansys).

$$\text{Soderberg relation: } \sigma_a = \sigma_a|_{\sigma_{m=0}} \left\{1 - \frac{\sigma_m}{\sigma_y}\right\} \qquad \text{Equation 2-7}$$

Modified Goodman relation: $\sigma_a = \sigma_a|_{\sigma_{m=0}} \left\{1 - \frac{\sigma_m}{\sigma_{TS}}\right\}$ Equation 2-8

Gerber relation: $\sigma_a = \sigma_a|_{\sigma_{m=0}} \left\{1 - \left(\frac{\sigma_m}{\sigma_{TS}}\right)^2\right\}$ Equation 2-9

Smith Watson Topper relation: $\sigma_a = \sigma_{max}\sqrt{\frac{1-R}{2}}$ Equation 2-10

Here σ_a, σ_m, σ_{TS}, σ_{max} and R are stress amplitude, mean stress, tensile strength, maximum stress, and the ratio between minimum and maximum stress.

In most engineering alloys, Gerber gives a conservative estimate of fatigue life, while Goodman matches experimental observations for brittle metals closely but is conservative for ductile alloys. However, for compressive, mean stresses, it is typically nonconservative. Thus, an assumption is considered to avoid this problem that mean compressive stresses have no impact on fatigue life. On the other hand, the Soderberg model provides relatively accurate estimates for ductile alloys with mean tensile stresses. It does not, however, distinguish between fatigue life differences caused by compressive and tensile mean stresses [62].

2.5.3 Fatigue total life approach

2.5.3.1 Stress life (S-N) approach

A material's fatigue limit is typically calculated by plotting the stress amplitude σ_a against the number of fatigue cycles to failure for completely reversed loading (equal to one-half of the stress spectrum from maximum tension to maximum compression). Figure 2-22 shows a typical S-N curve, and the solid line represents mild steels and other materials that harden by strain-ageing. These alloys show a plateau in the stress-life plot, usually above 10^6 fatigue cycles under constant amplitude cyclic conditions. The materials can be cycled indefinitely below this plateau level without causing failure. This level of stress is known as the endurance limit σ_e. In most steels and copper alloys, the value of σ_e is 35 per cent to 50 per cent of the tensile strength σ_{TS} [62].

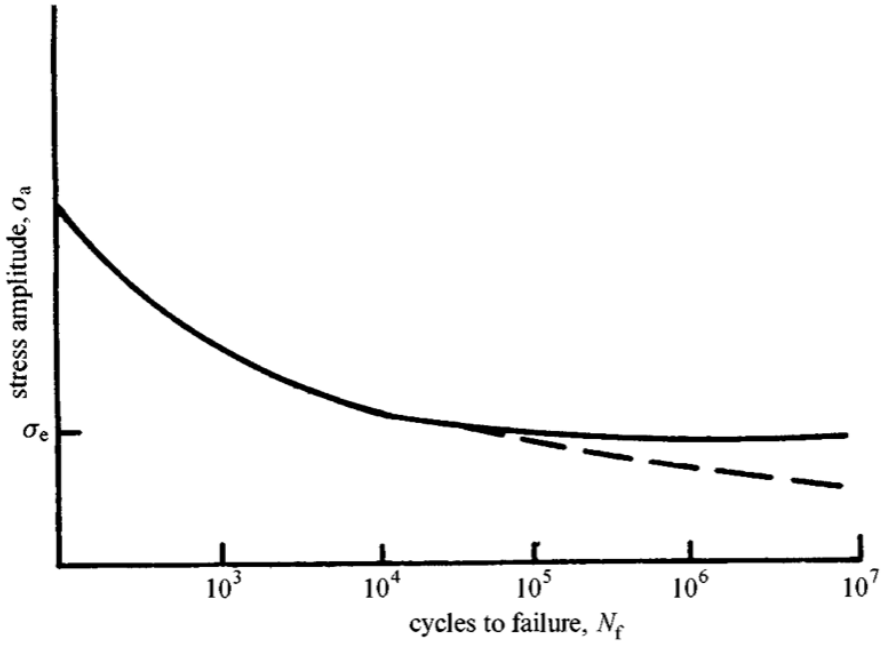

Figure 2-22: For ferrous and nonferrous alloys, a typical S-N diagram demonstrating the stress amplitude of nominally smooth specimens for fully reversed fatigue loading against the number of cycles to failure. The solid line indicates the fatigue limit exhibited by ferrous alloys, and the dotted line the endurance limit at 10^7 cycles for non-ferrous alloys [62].

As seen in Figure 2 20, several high-resistance steels, aluminium alloys, and other materials do not have an endurance limit (the dotted line). For such materials, with decreasing σ_a (or $\Delta\sigma$), the number of cycles increases. The degree of stress that the specimen can withstand for at least 10^7 cycles of fatigue loading is known as an endurance limit in these situations. When the S-N diagram in Figure 2-22 is represented on a log-log scale, a linear relationship is usually observed. The following equation relates the stress amplitude, $\sigma_a=\Delta\sigma/2$, to the number of cycles to failure, $2N_f$, in a fully reversed, constant-amplitude fatigue test [68].

$$\frac{\Delta\sigma}{2} = \sigma_a = \sigma_f'(2N_f)^b \qquad \text{Equation 2-11}$$

Where σ'_f is the fatigue strength coefficient, and b is defined as the fatigue strength exponent or Basquin exponent, between = 0.05 and -0.12 for most metals [62].

However, this method has numerous limitations, some of which are mentioned below. [69]

- The S-N approach is essentially empirical and does not provide the physical understanding shown by some other approaches into the mechanisms of fatigue.

- The actual stress-strain response of materials is overlooked, so it is impossible to model residual stresses from sequential loading effects. As a result, there might be significant error in life prediction when the loading condition does not have a constant amplitude.

While there are severe flaws in the S-N method, it is still used because many fatigue data is available [70].

2.5.3.2 Strain life (ε-N) approach

The strain life (ε-N) method calculates the fatigue life of a component subjected to variable amplitude loading. The ε-N method consists of four major steps:

- Notch strain and stress calculation
- Cycle counting
- Mean stress correction
- Damage calculation

The approach uses a cycle counting method to detect damaging events in the stress-strain response of the notch root. For each damage occurrence, an equivalent strain equation is used to account for the effect of the mean stress. The damage is then calculated for each occurrence using the material strain-life curve. The steps of the ε-N approach are described below [49], [70].

2.5.3.2.1 Notch stress and strain calculation

The initial step of the ε-N approach is to correlate the notch stress-strain range with the nominal stress range. The proposed approach includes utilising finite element methods (FEM) or experimentally using strain gauge readings. In general, both these methods are, deemed too complex. The most used method is the one suggested by Neuber because of its simplicity. It is known as the Neuber law, which states that the theoretical stress concentration factor is equal to the geometric mean stress and strain concentration factors. When linear elastic assumptions are assumed at the notch, this is usually represented in stress and strain ranges. The following equation is known as Neuber's equation [71]:

$$\Delta\sigma\,\Delta\varepsilon \cong \frac{(K_t \Delta S)^2}{E} \qquad \text{Equation 2-12}$$

ΔS is the nominal stress range of the net section, $\Delta\sigma$ and $\Delta\varepsilon$ are the notch root stress and strain ranges, the theoretical stress concentration factor is K_t, and E is the material's elastic modulus. The stress-strain curve of a material can then determines the notch root strain from the nominal stress, which can be used in Equation 2-12. Stress and strain amplitudes can be measured from the cyclic stress-strain curve obtained from the fatigue loading with an incremental step, while the hysteresis curve can measure strain and stress ranges. If the material's compressive and tensile responses are similar, the hysteresis

curve is double the cyclic curve, according to Massing [72]. If the cyclic strain-stress curve from experiments is not available, the Ramberg-Osgood [73] approximation can be used.

$$\Delta\varepsilon = \frac{\Delta\sigma}{E} + \left(\frac{\Delta\sigma}{K'}\right)^{\frac{1}{n'}} \qquad \text{Equation 2-13}$$

Here $\Delta\varepsilon$ and $\Delta\sigma$ are the notch root strain and stress ranges, E is the elastic modulus, n' and K' are the exponent and coefficient of cyclic hardening, respectively. A more detailed discussion on cyclic hardening is provided in the next section.

2.5.3.2.2 Cyclic hardening model

When a specimen is loaded in a one-dimensional (uniaxial testing) loading setup, it will deform until the yield point and then will harden beyond that point. Plastic deformation for an idealised case is shown in Figure 2-23. If the stress exceeds the yield point (A), perfectly plastic deformation occurs and continues to occur after A (the yield point) at the same stress level. Elastic unloading will occur if the sample is unloaded. In the hardening case, the stress needs to be constantly increased once yield occurs to continue the plastic deformation.

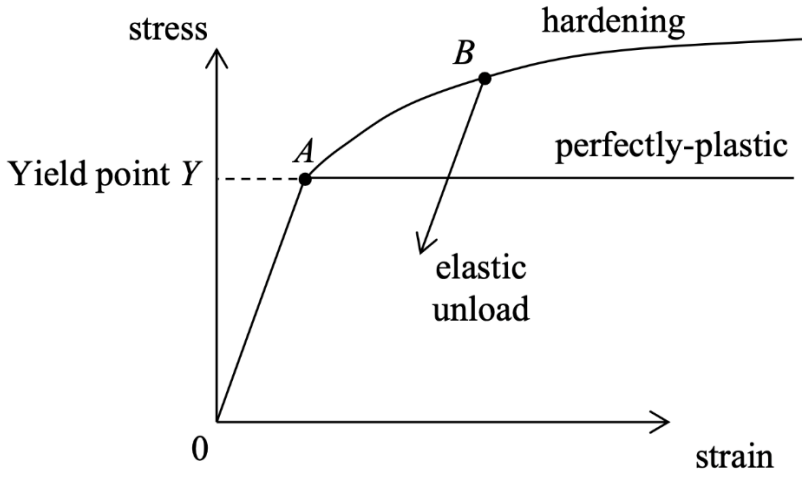

Figure 2-23: One dimensional (uniaxial) stress-strain relationship for an ideal case [74].

Such concepts can be extended to the multiaxial case, in which the initial yield would be of the following form.

$$f(\sigma_{ij}) = 0 \qquad \text{Equation 2-14}$$

The yield surface remains unchanged in the perfectly plastic situation. However, the yield surface can change size, shape and position in the more realistic hardening case and can be defined by

$$f(\sigma_{ij},\ K_i) = 0 \qquad \text{Equation 2-15}$$

K_i indicates one or more hardening parameters here, which change during plastic deformation and define the yield surface evolution. They may be higher-order tensors or scalars. The hardening parameters are null at the first yield, therefore.

$$f(\sigma_{ij}, 0) = f(\sigma_{ij}) \qquad \text{Equation 2-16}$$

The definition of how plastic deformation affects this yield surface is known as the hardening rules [74].

2.5.3.2.2.1 Isotropic hardening model

Isotropic hardening is where the yield surface maintains the same shape but expands with increasing tension, Figure 2-24. The yield function, in particular, takes the form of Equation 2-17 [1].

$$f(\sigma_{ij},\ K_i) = f(\sigma_{ij}) - K = 0 \qquad \text{Equation 2-17}$$

As the hardening parameter K changes, the size of the yield function changes, and its shape is determined by the initial yield function [74].

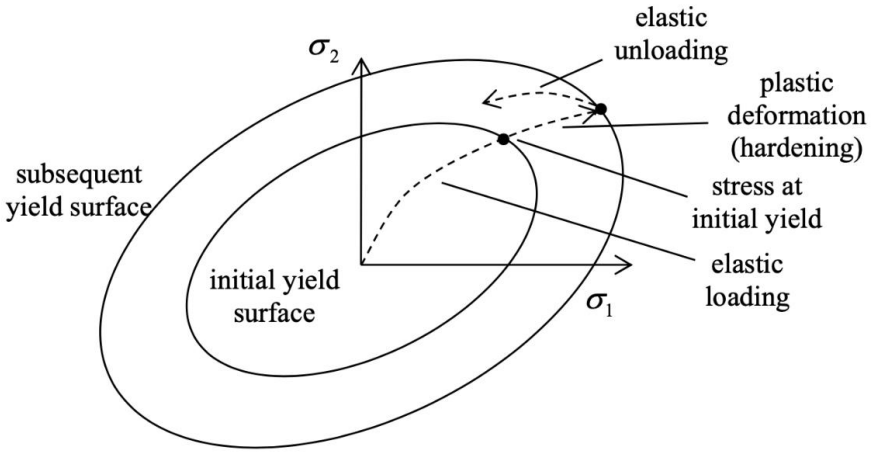

Figure 2-24: Isotropic hardening model [74].

For instance, the von Mises yield surface at initial yield can be defined as

$$f(\sigma_{ij}) = 0.707\sqrt{(\sigma_1 - \sigma_2)^2 + (\sigma_2 - \sigma_3)^2 + (\sigma_3 - \sigma_1)^2} - Y \qquad \text{Equation 2-18}$$

$$= \sqrt{3J_2} - Y$$

$$= \sqrt{\frac{3}{2} s_{ij} s_{ij}} - Y$$

In uniaxial tension, where Y is the yield stress in uniaxial tension, s is the deviatoric stress and J is the principal scalar invariants of the deviatoric stress matrix. Following that, one has [74]

$$f(\sigma_{ij},\, K_i) = \sqrt{3J_2} - Y - K = 0 \qquad \text{Equation 2-19}$$

2.5.3.2.2.1.1 Ramberg-Osgood isotropic hardening model

The Ramberg-Osgood equation was developed to determine the non-linear stress-strain relationship near yield points of the material. It is especially useful for metals that harden due to plasticity and have a seamless elastic-plastic transition. Since it is a phenomenological model, it is essential to check the model's fit with real experimental evidence for a specific material. The equation for strain (deformation) in its original form is [73].

$$\varepsilon = \frac{\sigma}{E} + K\left(\frac{\sigma}{E}\right)^{1/n} \qquad \text{Equation 2-20}$$

Here E is Young's modulus, K and n are constants related to material property, ε is strain, σ is stress. The equation implies that the elastic strain portion of the stress-strain curve can be represented by a straight-line gradient, whereas the plastic component, ε_p can be represented by a power law. The cumulative strain is calculated by including the elastic and plastic elements.

For the first part on the right hand in Equation 2-20, σ is proportional to the elastic component of the strain. In contrast, $K\left(\frac{\sigma}{E}\right)^{1/n}$ is the plastic part, representing parameters K and n that describe the material's hardening behaviour. Because of the power-law relationship between plastic strain and stress, the Ramberg-Osgood model assumes that plastic strain is non-zero even at very low stress. Additionally, the plastic strain stays marginal relative to the elastic strain at low stress. However, for stress levels greater than σ_0, the plastic strain gradually grows considerably higher than the elastic strain [73].

2.5.3.2.2.2 Kinematic hardening model

According to the isotropic model, if the yield strength in compression and tension are initially symmetrical relative to stress axes, they would remain equal as the yield surface increases with applied plastic strain. However, the kinematic hardening law could model the well-known Bauschinger effect and subsequent responses, under which a hardening in tension can contribute to a relative softening in

subsequent compression unloading. As a result, the yield surface maintains its form but shifts relative to the tension axes (see Figure 2-25) [74].

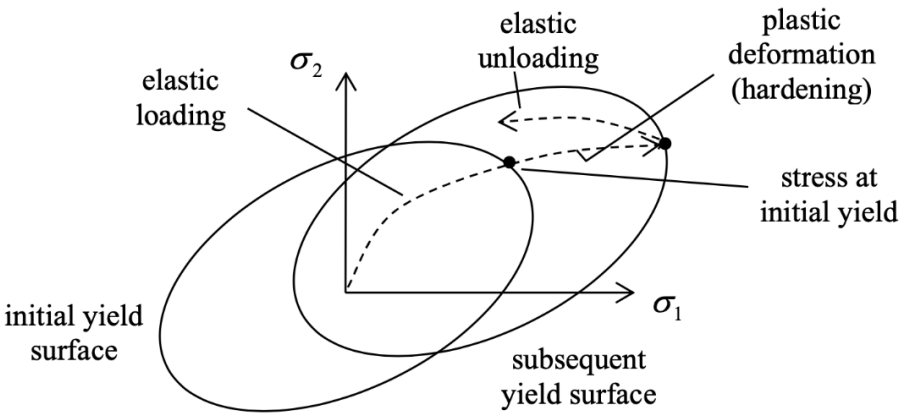

Figure 2-25: Description of kinematic hardening model. The solid line defines the yield surface, and the dotted line represents the shift of the yield surface [74].

The yield function now takes the general form of yield functionality.

$$f(\sigma_{ij},\, K_i) = f_0(\sigma_{ij} - \alpha_{ij}) - K = 0 \qquad \text{Equation 2-21}$$

The hardening parameter here is the stress α_{ij}, referred to as the back-stress or shift- stress; The yield surface relative to the stress-space axes is shifted by α_{ij} and the K is zero.

According to the Von Mises criterion again, deviatoric part of σ-α instead of the deviatoric part of σ,

$$f(\sigma_{ij},\, K_i) = \sqrt{\frac{3}{2}(s_{ij} - \alpha_{ij}^d)(s_{ij} - \alpha_{ij}^d)} - Y = 0 \qquad \text{Equation 2-22}$$

Where α^d is the deviatoric component of α.

The purpose of these models is to represent the actual stress-strain response of the material under repeated cyclic loading. An isotropic hardening model is usually sufficient to explain a monotonic response. A more complex combined isotropic and kinematic model is often used to represent the cyclic stress-strain response [49].

2.5.3.2.3 Cycle counting

Cycle count is a method, which can account for damaging events during cyclic loading. ASTM Standard E 1049-855 outlines standard procedures for cycle counting in fatigue analysis [75]. Counting processes such as the Rainflow technique and its derivatives are the most used technique and are often chosen due to their simplicity and ease of implementation. Generally, the stress-strain estimation at the notch root and the cycle counting is carried out in parallel. Neuber's law [71] uses the nominal load and stress-strain curve of material to determine stress and strain at the notch root. The cumulative damaging impact is then calculated using the Rainflow method derivative [70].

2.5.3.2.4 Damage calculation

In the final step, the number of cycles to failure is calculated for a smooth sample using an experimentally collected strain-life curve (at R=-1) for each closed hysteresis loop. If the mean stress is corrected suing the SWT equation, the SWT compatible strain-life curve is used. When the strain-life curve is not available from the experiment, the following Manson-Coffin relation can be used [76]:

$$\frac{\Delta\varepsilon}{2} = \frac{\sigma_f'}{E}\left(2N_f\right)^b + \varepsilon_f'\left(2N_f\right)^c \qquad \text{Equation 2-23}$$

Here $\frac{\Delta\varepsilon}{2}$, σ_f' and N_f are strain amplitude, number of cycles to failure and fatigue strength coefficient of the smooth specimen, c and b are the ductility exponent and fatigue strength exponent, respectively; ε_f' is the fatigue ductility coefficient. [76]

The total cycle to failure ($N_{f,i}$) is inverse to the damage from each loop (D_i) for a smooth specimen:

$$D_i = \frac{1}{N_{f,i}} \qquad \text{Equation 2-24}$$

The total damage (D) is then computed from Miner's linear damage rule [70].

$$D = \sum_{i=1}^{n} D_i \qquad \text{Equation 2-25}$$

2.5.4 The damage tolerant approach

Mechanical components will frequently contain internal defects, microstructural flaws, or inclusions. The damage tolerant approach consists of predicting crack propagation life based on empirical crack growth measurement laws. Usually, crack tip stress condition is defined by the stress intensity factor K for Mode I, II or III loading, combining linear elastic fracture mechanics (LEFM with the small-scale yielding (SSY) criterion. Although elastic loading conditions prevail in the system, the crack tip plastic region is considered minimal compared to the size of the specimen and the dimensions of the crack [63].

Understanding the different fracture modes is essential before considering the various stress and deformation fields due to external loading in the cracked body. In Figure 2-26, the surface displacements mechanism of the crack in the three basic modes of separation are shown schematically.

- **Mode I:** The tensile opening mode is when the crack faces split in a direction perpendicular to the crack plane, and the crack wall displacements are symmetric in the xz and xy planes.
- **Mode II:** The crack faces are simultaneously sheared perpendicular to the crack front in the in-plane sliding mode. In this situation, the crack walls' displacements are symmetric in the xy plane but anti-symmetric in the xz plane.
- **Mode III:** The crack faces shearing parallel to the crack front is known as tearing or anti-plane shear mode. In this scenario, the crack walls' displacements are anti-symmetric in the xy and xz planes.

Edge and screw dislocation motions, respectively, are analogous to the crack face displacements in modes I and III [63].

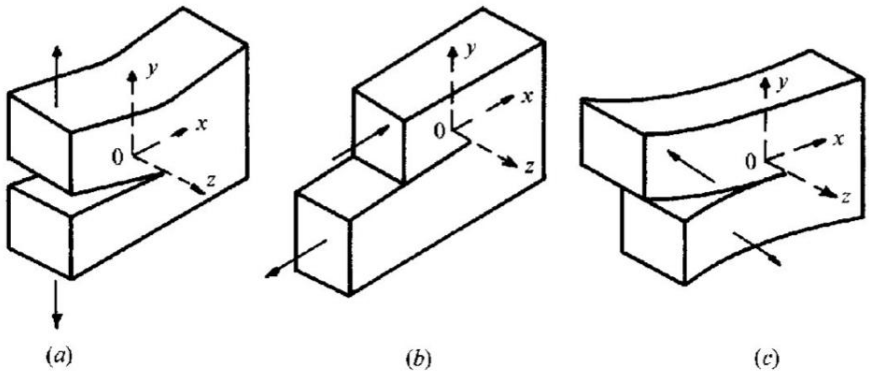

Figure 2-26: The three basic modes of separation. (a) Tensile opening (mode I). (b) In-plane sliding (mode II). (c) Anti-plane shear (mode III) [63].

2.5.4.1 Fracture mechanics description of crack growth behaviour

The stress field ahead of the crack tip can be written as Equation 2-26 in Cartesian coordinates for loading mode I [63]:

$$\begin{bmatrix}\sigma_{xx}\\ \sigma_{yy}\\ \sigma_{zz}\end{bmatrix} = \frac{K_I}{\sqrt{2\pi r}}\cos\left(\frac{\theta}{2}\right)\begin{bmatrix}1-\sin\left(\frac{\theta}{2}\right)\sin\left(\frac{3\theta}{2}\right)\\ 1+\sin\left(\frac{\theta}{2}\right)\sin\left(\frac{3\theta}{2}\right)\\ \sin\left(\frac{\theta}{2}\right)\cos\left(\frac{3\theta}{2}\right)\end{bmatrix} \quad \text{Equation 2-26}$$

K_I is the stress intensity factor for mode I loading r and θ are respectively the distance from crack tip and the angle between crack plane and any location on the plastic zone ahead of the crack tip. Since the concept of K is based on the consideration of LEFM and SSY, plasticity is expected to have a limited contribution; For plane strain condition (the specimen thickness is greater than $2.5(K/\sigma_y)^2$), the material stress intensity factor K can be defined as follows:

$$K = f\left(\frac{a}{W}\right)\sigma_{app}\sqrt{\pi a} \quad \text{Equation 2-27}$$

The $f\left(\frac{a}{W}\right)$ is geometrical compliance term, σ_{app} is the applied stress and a is crack length.

$$K_{max} = Y\sigma_{max}\sqrt{\pi a}, \qquad K_{min} = Y\sigma_{min}\sqrt{\pi a}$$
$$\Delta K = Y\Delta\sigma\sqrt{\pi a}, \ \Delta\sigma = \sigma_{max} - \sigma_{min}, \quad \text{Equation 2-28}$$

$\Delta K = K_{max} - K_{min}$ is the range of stress intensity factor, which controls the growth rate of cracks of different sizes under mode I loading and here, Y is referred to as the compliance function, which is a function of crack depth and component width. The concept of similitude should mean that if ΔK truly describes the crack tip stress state, then it can be used to compare crack growth behaviour assuming that two cracks of different sizes will have identical crack tip stress, strains and plastic zone size when loaded under different conditions, but which yield the same K values [63].

The stress intensity factor ΔK at the local stress field ahead of the crack tip is known to be the key driving force for crack propagation. ΔK is mostly used to explain crack growth behaviour by plotting its development on a log-log scale versus crack growth per cycle da/dN (crack growth rate evolution). The regular fatigue crack growth rate per cycle versus stress intensity factor is shown in Figure 2-27. In the lower portion of the graph, microcracks nucleate grow by the Stage I fatigue growth mechanism.

Stage I cracks are sensitive to microstructure, whereas the key linear portion of the plot is attributed to stage II long crack growth, which is microstructure insensitive. Finally, the third and fastest portion of the graph is the catastrophic fracture (or Stage III) [63].

When the plastic zone size ahead of the crack tip reaches a critical size that encompasses several grains, stage I to stage II transition in fatigue is assumed to occur. Irwin's theorem, which defines the radius of the plasticity region ahead of the crack tips under plane strain conditions in Equation 2-29 and plane stress conditions in Equation 2-30, approximates the crack tip plastic zone [63].

$$r_p = \frac{1}{3\pi}\left(\frac{K_I}{\sigma_0}\right)^2 \qquad \text{Equation 2-29}$$

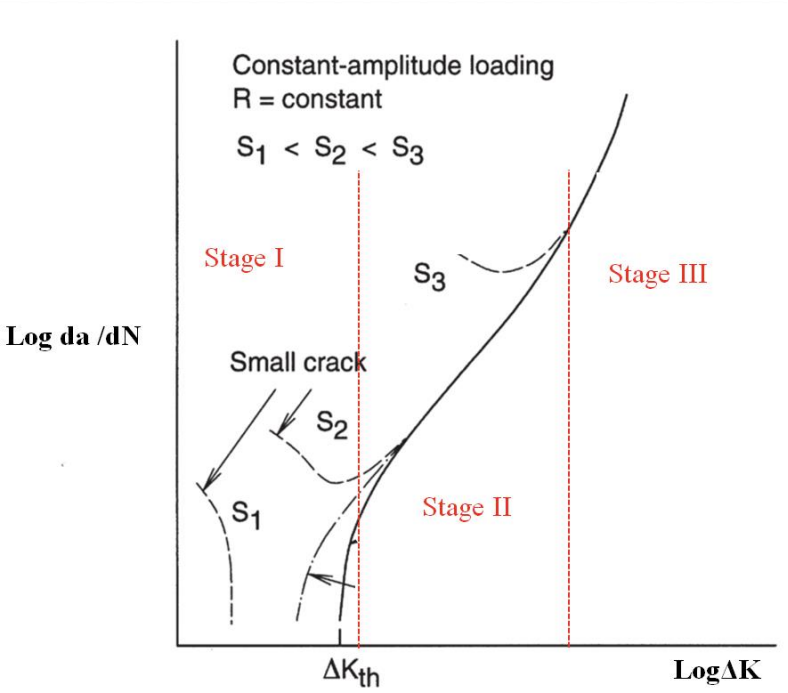

Figure 2-27: Representation of fatigue crack development for both short and long cracks [77].

$$r_p = \frac{1}{\pi}\left(\frac{K_I}{\sigma_0}\right)^2 \qquad \text{Equation 2-30}$$

Here, σ_0 is the material yield strength. Additionally, the linear log da/dN against log ΔK relationship can be defined by the Paris law:

$$\frac{da}{dN} = C(\Delta K)^m \qquad \text{Equation 2-31}$$

Where 'C' and 'm' are constants that vary for different materials, environments, and R-ratios, and are experimentally derived, although 'm' for ductile materials is usually between 2 and 4. The Paris law applies at intermediate ranges of ΔK. In the lower part of the graph (for low ΔK values), the Paris regime does not hold, and at the low ΔK value when da/dN $\simeq 10^{-1}$ nm/cycle is known as the threshold value (ΔK_{th}). Commonly described as the smallest driving force to achieve a measurable growth rate in long cracks [78]. Crack growth rate mechanisms near threshold are often termed quasi-Stage I as they often exhibit similar crack growth mechanisms to those seen in the early stages of crack growth. Usually, the ΔK_{th} value is determined by gradually load shedding from a long crack until the crack growth rate slows and stops.

2.5.4.2 Micro mechanism of fatigue crack growth

2.5.4.2.1 Stage I (early) fatigue crack growth

Crack development can occur by single shear in the primary slip mechanism's direction if the crack and the plastic deformation zone around the crack tip are limited to a few grain diameters, as seen in Figure 2-28(a) and (b). According to Forsyth [79], stage I crack growth is a single slip mechanism that leads to a zig-zag crack path. Stage I crack development can also be seen in various ferrous, aluminium, and titanium alloys even though the crack length is much greater than grain size as long as the near-tip plasticity area is lesser than grain size (i.e., for very low-level stress intensity factor, K) [63].

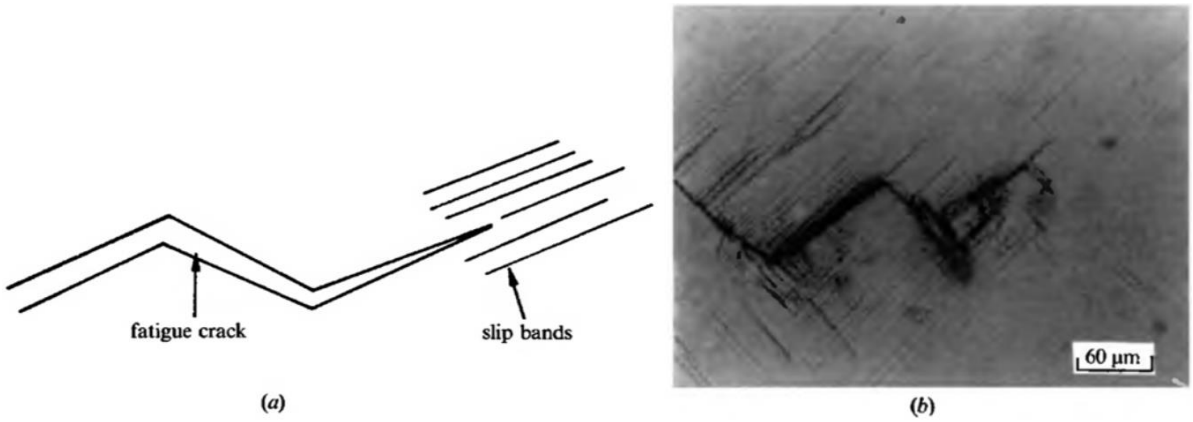

Figure 2-28: (a) Schematic of fatigue crack growth of stage I (b)Exemplary fatigue crack growth of nickel-base Mar M-200 single crystal superalloy. The vertical axis is tensile. Tensile axis is normal to {100} plane [63].

The corresponding plastic zone size has either equal or smaller dimensions than the microstructural features of the surrounding area (e.g., grain size, space between precipitates). A Stage I crack may start on the surface and then spread along a crystallographic plane along a PSB extending over a whole grain, which is oriented such that this occurs preferentially at an angle of 45 degrees to the tensile loading axis

(so the slip plane which experiences the maximum resolved shear stress). Hence coarser grains with such an optimal orientation are a preferential site for the initiation of short cracks. Stage I crack growth rate tends to fluctuate. Since Stage I crack growth is predominantly limited to shear within grains on preferential slip planes, it leads to a zig-zag crack path with temporary grain boundary arrest (at high angle grain boundaries). Such Stage I crack growth will produce a strongly faceted appearance on the surface of the specimen along the crack route. This Stage I crack growth is therefore said to be microstructurally dependent. Elastic-plastic fracture mechanics (EPFM) or statistical methods may describe the local stress state controlling short crack behaviour. Short cracks in various forms can be classified [80][81]:

- Microstructurally small cracks (MSC) have a nonuniform crack advance linked to the interactions between crack tip and microstructure and is attributed to the scale of crack size relative to the dimensions of the surrounding microstructure.
- Mechanically small cracks form when near crack tip plastic zone size begins to grow larger than the crack size and drive crack propagation, leading to multiple slip system growth.
- When cracks achieve sufficient size that their crack tip process zone experiences a more averaged effect of the surrounding microstructure, but there is insufficient crack wake to develop pronounced crack closure, then they are termed physically small cracks (PSC). This stage of transition can be considered the beginning of Stage II crack development.

D. Kwon [81] described various characteristic crack sizes which correspond to the different types of short crack. By using the stress intensity factor at transition K_T and grain size d_g, the transition crack duration from short to long crack growth regime under in-plane strain conditions can be defined as:

$$a_T = \frac{1}{A\pi Y^2}\left(\frac{\sigma_y}{\Delta\sigma}\right)^2 m d_g \qquad \text{Equation 2-32}$$

Where m is constant, A is the coefficient in the in-plane strain condition of the cyclic plastic zone size (i.e., $0.03 - 0.04$), where $\Delta\sigma$ is the stress range applied, where σ_y is the material yield strength, and where Y is the shape factor in the transition stress intensity factor such as:

$$\Delta K_T = \sqrt{\pi a_T} Y \Delta\sigma \qquad \text{Equation 2-33}$$

2.5.4.2.1.1 Short crack behaviour

The definition of initiation of a fatigue crack, or nucleation level, depends on the observation length scale. Microscopically this could start with dislocations accumulating along with persistent slip bands (PSB), accumulation of microscopic flaws at a grain boundary (GB) or inclusions causing a localised

stress concentration which leads to crack initiation. The root cause on a microscopic scale can differ but will lead to crack nucleation as discussed below:

- Surface roughness (even on the microscopic scale) causes a local concentration of stress and can lead to the nucleation of cracks. Surface roughness inherent from a manufacturing process has a clear effect on lifetimes, with higher roughness surfaces exhibiting reduced initiation lives. Even with a very smooth surface initially, cyclic loading can induce roughness by extrusion or intrusion of irreversible slip bands due to dislocation movement along shear planes. Microstructures which promote planar slip, (e.g., with low Stacking Fault Energy (SFE) or coherent precipitates) are more susceptible to initiation due to slip band crack formation [82].
- Porosities and inclusions can act as areas of stress concentration. Porosities are commonly found in LPBF processed components and can be considered as pre-cracks due to their size and shape, which corresponds to the dimension of the microstructure.
- Another factor operating in LPBF processed components can be that a mismatch in thermal expansion can cause local interface strain, create a locally weaker site or initiate slip, also resulting in crack nucleation [83].
- Grains and twin boundaries can cause the initiation of cracks. Stresses between grains due to mismatch of orientation, or the presence of inclusions, may cause weakness in the GB area. If a broad grain's orientation is at a favourable angle relative to the tensile load axis, it may lead to the formation of long PSBs, resulting in cracking where the slip band impinges on the GB [84].
- The service environment can result in localised corrosion, oxidation, wear, hydrogen embrittlement, causing initiation sites. External environmental conditions can enhance surface roughening or transportation along PSBs of chemically fragile species [80].
- Geometry changes (e.g., changes in cross-section or notches, holes etc.) can also create a concentration of localised stress within mechanical components [63].

Crack growth just after initiation is normally regarded as Stage I fatigue and refers to cracks of similar size to the microstructural dimension surrounding it. The distinction between a very early stage of crack growth and crack initiation is often linked to the resolution of measurement possible. In some engineering design and inspection regimes, a crack length below 1 mm may be defined as "initiation" as its growth cannot be easily detected in service.

2.5.4.2.2 Stage II fatigue crack growth

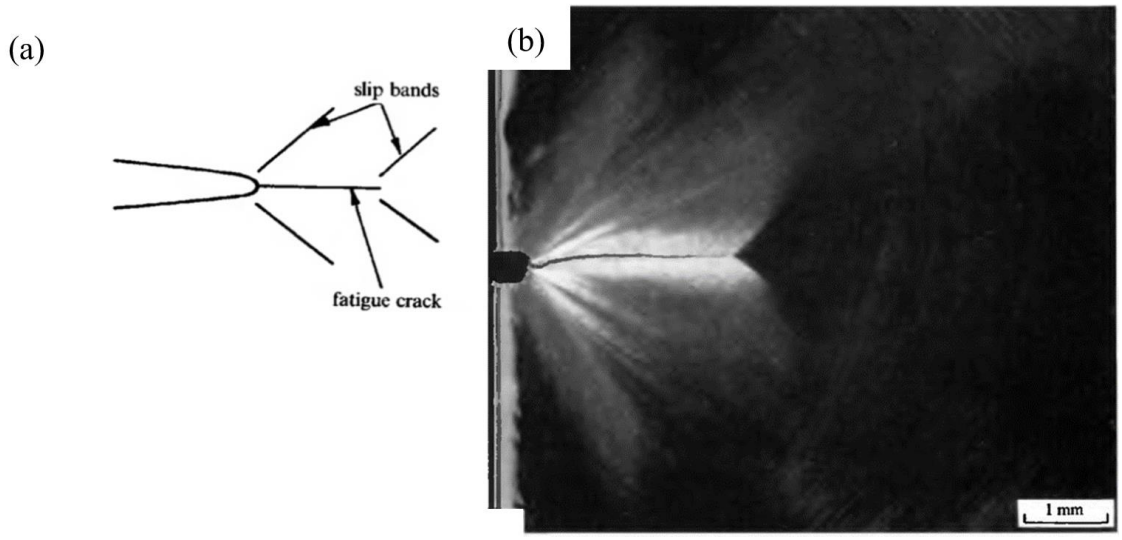

Figure 2-29: (a) An idealization of stage II fatigue crack growth. (b) An example of stage II cracks growth in a Cu single crystal. Two sets of {l JI} slip planes (white areas) are seen. The tensile axis is vertical [62]

The plastic zone at the crack tip contains several grains when microcrack evolves to larger crack lengths; for such a case, the corresponding crack growth phase would involve an alternating or simultaneous flow of two slip systems. As seen in Figure 2-29 (a), this duplex slip mechanism (stage II crack growth) results in an ordinary, planar (mode I) crack path normal to the global tensile axis [79]. Stage I fatigue fracture surfaces normally have a serrated or faced profile (due to slip band crack formation), but stage II crack growth causes fatigue striations in many engineering alloys. Zappfe and Worden [85] were the first to note such striations, which appear like ripples on the surface of the fractures. The spacing between neighbouring striations has been shown to correlate with the experimentally defined average crack growth rate per cycle while advancing in the Paris regime in cyclic fatigue crack. Forsyth [86] first showed these associations for stage II crack growth in aluminium, which led to the usage of striation spacing as an indicator of crack growth behaviour to analyse failure in both constant and variable amplitude fatigue. It is important to remember that during stage II fatigue, not all engineering materials form striations. Pure metals and several ductile alloys display striations. Most engineering polymers often show well-defined striations of fatigue on the surfaces of the fractures. These occur very infrequently in steels and are rarely noticeable in cold-worked alloys. The tendency to striation formation can be significantly affected by the stress intensity factor ΔK, stress condition, environment, and alloy content [62]

2.5.4.2.3 Fatigue striation formation mechanism

Numerous concepts were used to explain planar growth and fatigue striations of Stage II fatigue cracks. Amongst which, Laird's plastic blunting idealisation [87] is a well-known physical concept. It suggests the crack growth rate change is due to the blunting of the plastic crack tip. When tensile stress is applied to the crack tip, the crack tip blunts plastically, as seen in Figure 2-30. The crack tip re-sharpens in compression; extends and blunted again during subsequent tension [88]. Net crack during the fatigue cycle leads to the forming of striations, as seen schematically in Figure 2-30. The mechanism lies in the blunting, and subsequent extension of the crack during the tension load cannot be entirely mitigated by the crack closure during subsequent compression [62]

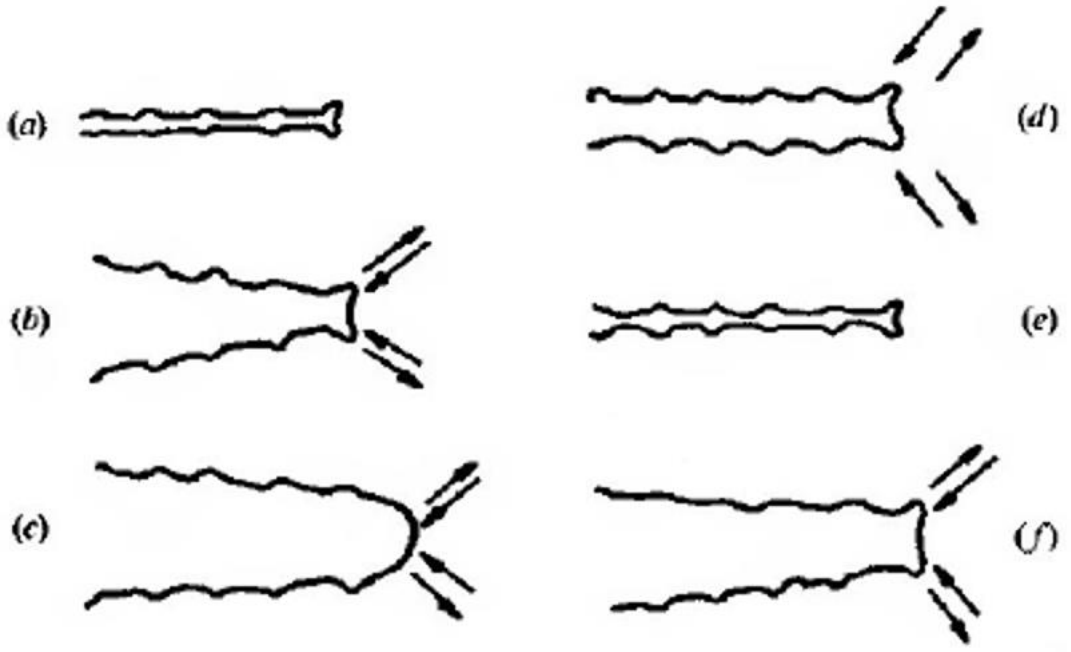

Figure 2-30: In fully reversed fatigue, an idealisation of plastic blunting and re-sharpening leads to stage II fatigue crack growth. (a) Zero loads, (b)small tensile load, (c) peak tensile load, (d) onset of load reversal, (e) peak compressive load, and (f) small tensile load in the subsequent tensile cycle. The direction of the slip is indicated by arrows [62].

2.5.4.3 Continuum mechanics description of fatigue

2.5.4.3.1 Mixed mode (mode I & II) fatigue crack

In the continuum fracture mechanics approach, mixed-mode fatigue crack propagation is a common phenomenon. One of the main problems in the analysis of mixed-mode fatigue crack development is frictional interaction between the mating crack faces. Many hypotheses have been suggested to understand the growth of mixed-mode fatigue cracks. Few of them are addressed in the following section as a theoretical basis for a more in-depth discussion of factors affecting crack paths.

2.5.4.3.1.1 Path of the mixed-mode crack

Several criteria can predict the fatigue crack path under combined mode I-mode II loading or pure mode I loading if frictional effects associated with contact between the crack faces are not significant. A single-phase angle in Equation 2-34 defines the near-tip mode mixity (φ_M) [62].

$$\varphi_M = tan^{-1}\left\{\frac{K_{II}}{K_I}\right\} \qquad \text{Equation 2-34}$$

Here, φ_M for pure mode I and pure mode II have different values, ranging from zero to π/2.

According to Griffith theory, in an elastic material, combined mode I-mode II fracture progresses along a plane (directed at an angle $\hat{\theta}$ to the pre-crack plane) that releases the maximum rate of energy. This method [89] implicitly assumes that the material's fracture strength, represented in terms of the Griffith energy release rate, is not correlated to mode-mixity φ_M. The fracture locus for mode I-mode II progression can be expressed as a function using the maximal strain energy release rate criterion: [90]

$$\left(\frac{K_I}{K_{IC}}\right) + \frac{3}{2}\left(\frac{K_{II}}{K_{IC}}\right)^2 = 1 \qquad \text{Equation 2-35}$$

where K_{IC} is the fracture initiation toughness in mode I. This theory predicts that $K_{IIC} = \sqrt{2/3}\,K_{IC}$ (where K_{IIC} is the mode II fracture initiation toughness) and $\hat{\theta}$=77.4° for pure mode II fracture.

Another theory named maximum hoop stress suggests the crack progresses in the direction where the hoop stress at the crack tip is greatest (directed at an angle $\hat{\theta}$ to the pre-crack) [91]. In brittle fracture, the crack progresses as the hoop stress exceeds a crucial value over a certain distance ahead of the crack tip. Under combined mode I-mode II loading, the hoop stress is [62].

$$\sigma_{\theta\theta} = \frac{K_I}{\sqrt{2\pi r}} f_I(\theta) + \frac{K_{II}}{\sqrt{2\pi r}} f_{II}(\theta) \qquad \text{Equation 2-36}$$

Where $f_I(\theta)$ and $f_{II}(\theta)$ are the universal dimensionless angular functions. The direction of the maximum hoop stress for a given combination of mode I and mode II is determined by the condition $(\partial\sigma_{\theta\theta}/\partial\theta)$ =0, from which $\hat{\theta}$ is calculated. When this value is substituted for in, the result is

$$\frac{K_I}{K_{IC}} f_I(\hat{\theta}) + \frac{K_{II}}{K_{IC}} f_{II}(\hat{\theta}) = 1 \qquad \text{Equation 2-37}$$

The maximum hoop stress theory predicts (K_{IIC} = 0.866K_{IC}) and $\hat{\theta}$=70.5° for pure mode II fracture. Figure 2-31 shows the values of $\hat{\theta}$ derived from the maximum hoop stress and the maximum strain energy release rate theory for various mode mixities φ_M. The trends predicted by the criterion, which assumes that the crack advances in a direction along which K_{II} = 0, [89] are also shown in this figure [62].

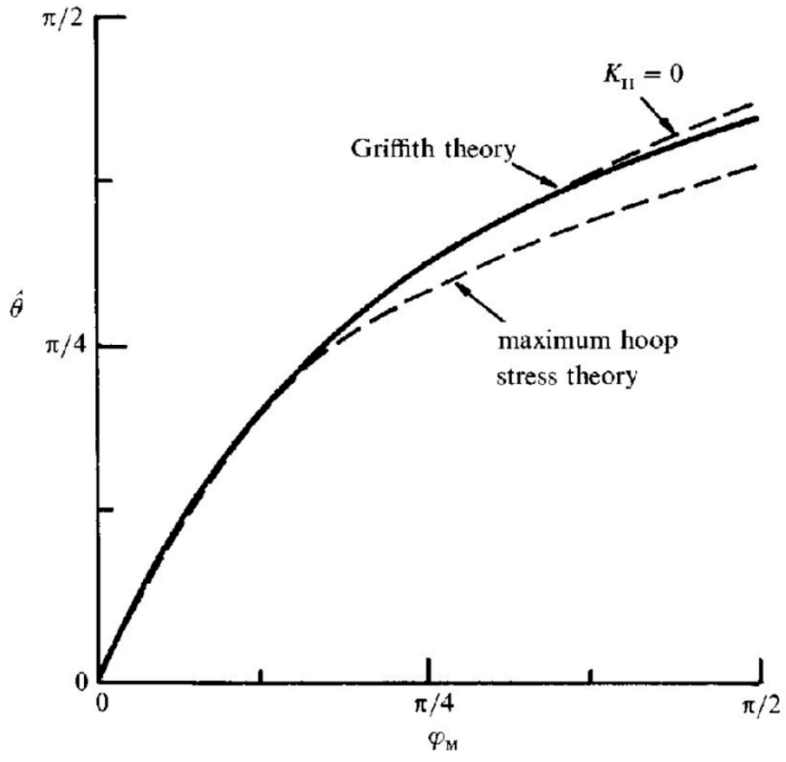

Figure 2-31: Initial crack growth angle $\hat{\theta}$ prediction in combined mode I-mode II loading, expressed by phase angle φ_M as a function of the crack-tip mixity [62].

It is worth mentioning that both Griffith energy release and maximum hoop stress theory provides similar predictions and applicable to ductile materials. Even though they were developed to explain

failure criteria of material, the principle behind the prediction of crack tip direction can potentially also be used for explaining crack propagation behaviour in fatigue loading.

2.5.4.4 Interaction between multiple cracks on the fracture surface

Multiple cracks propagating on a surface is often generalised to account for variations in the stress fields induced by their propagation. The propagation of multiple cracks is referred to as multi-cracking. The formation of multiple superficial cracks is frequently linked to the failure process. The initiation of cracks and their interaction could represent a large part of a structural material's life. Numerous experiments were performed to measure crack growth rates to analyse these interactions. The authors [92], [93], [94], [95] describe a common method for identifying crack growth behaviour on the surface by fatigue or fatigue corrosion tests. Each test was stopped at suitable intervals, and microscopic analyses were conducted to assess the size and position of surface cracks. The Ochi [96] coalescence criterion is often chosen as one of the most effective criteria; it is based on crack lengths and cracks tips distance. When the coalescence condition is satisfied, two cracks are recharacterized as a single crack. However, since in-depth crack propagation has a direct effect on material deterioration, surface inspection is insufficient. Surface crack coalescence, on the other hand, has been shown to have little impact on the critical crack's in-depth kinetics [97].

2.5.4.4.1 Criteria of crack coalescence

A colony of cracks is a group of defects that inhabit a well-defined and confined surface. Forsyth [98] first suggested a limit gap between cracks that allows 'overlapping cracks' and 'isolated cracks' to be distinguished. He stated that plastic zone size at the advancing crack tip determines this limit, and that the greatest interaction happens when the two plastic zones overlap (see Figure 2-32). Furthermore, Wang et al. [95] established a coalescence requirement based on their experimental findings, stating that the distance between two parallel cracks (h) depends on the length of surface cracks to satisfy coalescence criteria.

$$h < \frac{\sigma_{max}}{\sigma_y} \times H \times (l_1 + l_2) \qquad \text{Equation 2-38}$$

Where l_1 and l_2 are the length of approaching surface crack; σ_{max} and σ_y maximum stress and yield strength respectively. H is a constant determined from experimental curve fitting.

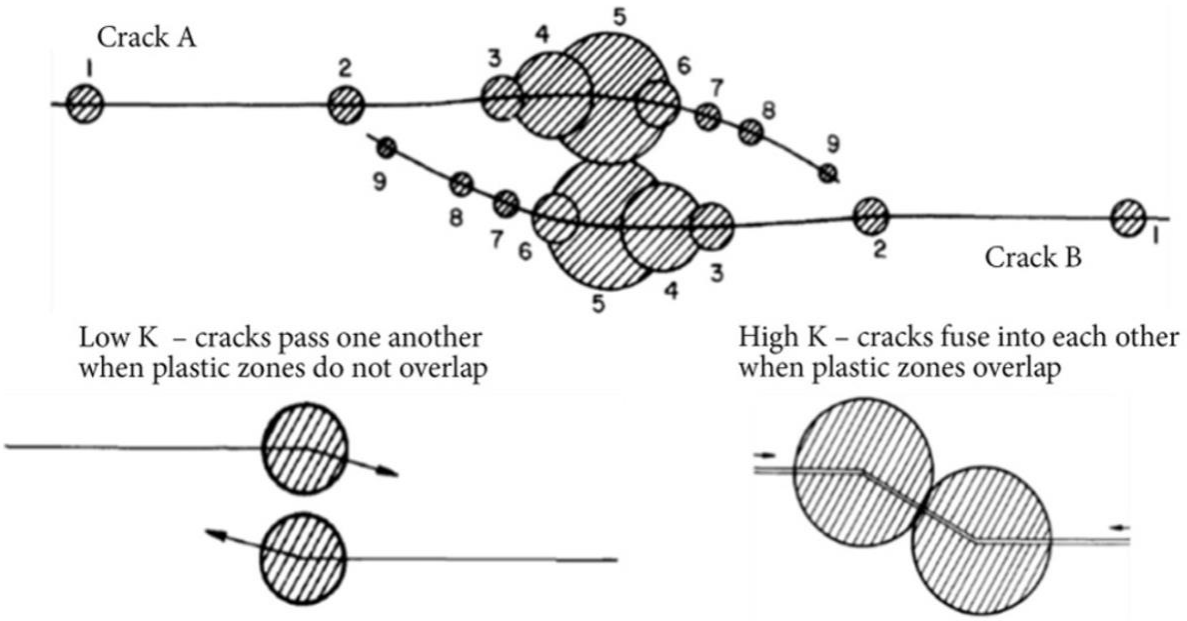

Figure 2-32: The evolution of the plastic zone size at the crack tip as bypassing cracks approach. Figures depict the crack tip's successive positions [95].

2.5.4.4.2 Mechanism of crack interaction

The formation of localized mixed-mode loading (modes I and II), accompanied by plastic ligament tearing, results in the coalescence of cracks, shown in Figure 2-33 [99].

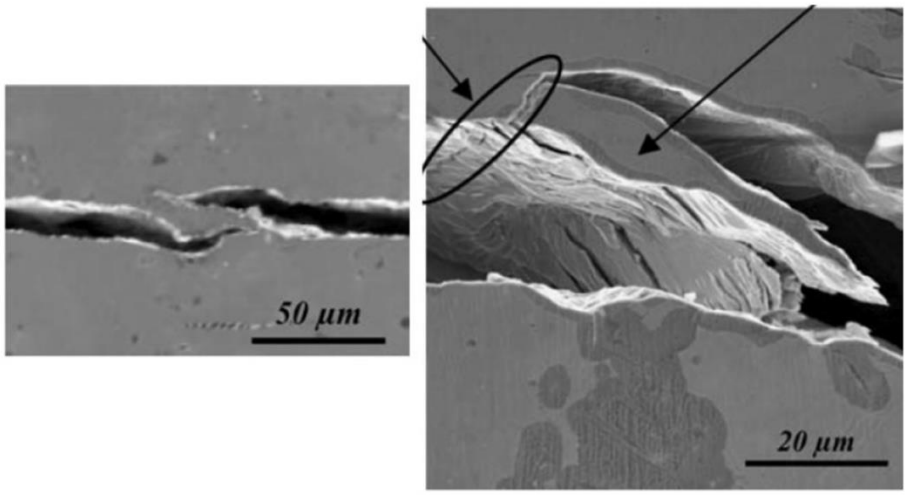

Figure 2-33: The points of two aligned cracks change directions, followed by tearing of the plastic ligament of 304L SS [99].

For structures in which plasticity governs crack growth, Mode II loading has major implications [100]. The plastic zone size in mode II is greater than in mode I for equivalent stress intensity factors, which may accelerate crack development but also allowing it to close due to plasticity. Greater plasticity at

the crack tip, according to Kamaya et al. [101], [102], will facilitate the initiation of new cracks, which lead to the propagation of the primary crack by coalescence. However, cracks may also interact without coalescence. During the propagation process, the stress intensity factor at the tips of two advancing cracks is disrupted [103]. As a consequence of the disruption, crack propagation may be increased, interrupted, or stopped. The relative location of the cracks, as well as their size, form, and initiation time, decide the degree of contact.

In separate tests, Paulin [104] used in situ video microscopy tracking multi-cracking of an AISI 304L SS throughout a slow strain rate experiment in a boiling $MgCl_2$ system. They reported, cracks occur on the entire specimen surface during tests; however, the earliest initiated cracks propagate quicker and resulted in longer cracks. In a stacked configuration, the shielding effect prevents the smallest cracks propagation, while the amplification effect accelerates the growth of the large crack in an aligned configuration. The active cracks that propagate during the test are thus taken into account when predicting the lifespan of a multi-cracked component.

In the most geometric configuration, the value of the stress intensity factor is increased in the case of two similar near cracks (of the same length), resulting in an increase in crack development [100]. The shielding effect lowers the interactions of cracks [103]. Also, the crack front shape plays important roles in interaction. For instance, at the crack tip of a semi-elliptical crack, the stress intensity factors are greater than the middle of cracks in the specimen's core. The interactions among cracks show that it is a complex process, with crack intensity factor varying dramatically based on growth stage [105].

Having reviewed the fundamentals of some fatigue theories, the next section will consider fatigue behaviours reported, particularly in 316L stainless steel.

2.6 Factors controlling fatigue lifetime of additively manufactured 316 Stainless Steel

Many studies [16][106][107][3][2] have been conducted to investigate the role of the surface finish, mechanical and materials properties affecting fatigue life in LPBF processed 316L stainless steel. These studies include average and maximum surface roughness, material properties such as yield strength, ultimate tensile strength, and defect levels such as relative density and porosity and their effects on the lifetime of 316L SS. A brief discussion is done in this section to understand the effects of materials and mechanical properties on the fatigue behaviour of the additively manufactured 316L stainless steel.

2.6.1 Influence of surface roughness

Surface roughness is usually quantified with two parameters named average surface roughness, R_a, and maximum surface roughness, R_z. R_a is the average arithmetical value of all absolute distances within the measuring range of the roughness profile from the centre line. R_z is the average cumulative peak to valley of five consecutive lengths of sampling within the period of a test [108]. Most researchers used average surface roughness, R_a, to define the surface finish condition of their specimens (See Figure 2-34).

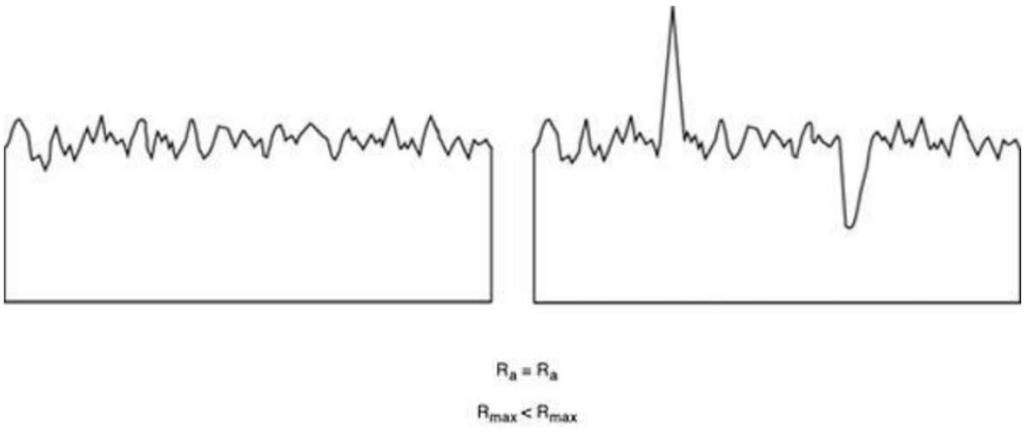

Figure 2-34: Surface roughness profile comparison between two specimens. [108]

According to Uhlmann et al. [106], surface roughness plays a significant role in fatigue failure. They used two different surface finish with a R_a value of 1.076 and 1.737 μm; the as-built surface roughness was reported as 13.28 μm. They reported that a smooth surface finish has better fatigue life compared to one with a rougher surface finish. However, even though the difference between the average roughness of these two surface finishes seems small, the difference between their lifetimes was noticeable. The reported two surface-finishes had maximum roughness (R_z) of 4.96 and 17.03μm, respectively, which could better explain such a difference in the fatigue life of the specimens. This

implies that maximum surface roughness has more relevance to fatigue life compared to average surface roughness. The maximum surface roughness can cause localised stress concentration, which could potentially initiate early-stage crack at the surface. The fatigue lifetime data from numerous research are collated, presented, and compared in Figure 2-35. In Figure 2-35 to understand the role of surface evaluate the relevance of surface roughness on fatigue failure, the same symbol is used to represent data from a single study. A colour gradient is also used to indicate the roughness of the respective specimens. Unsurprisingly, the detrimental effect of surface roughness on fatigue behaviour is very apparent in the Figure 2-35, especially within same study.

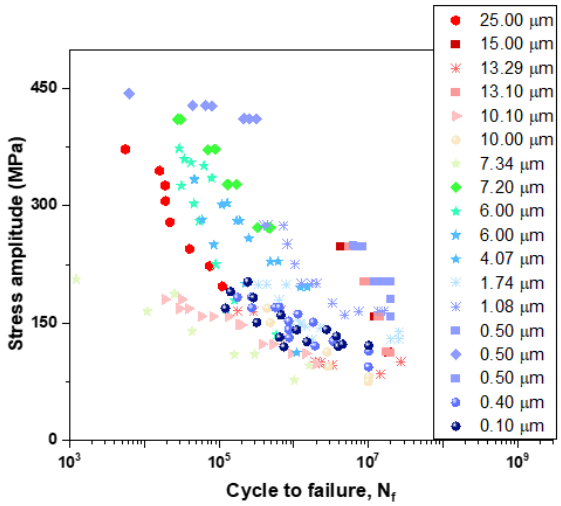

Figure 2-35: Fatigue lifetime dependency on surface roughness for additively manufactured 316L stainless steel [16][106][107][109][110].

2.6.2 Influence of material strength, elongation, and density

Some studies have investigated the relationship between fatigue lifetime and yield strength. Fatigue lifetime data from these studies are presented in Figure 2-36 (a). According to Figure 2-36 (a), no general trend between yield strength and fatigue lifetime can be found but within same study higher yield strength was associated with high fatigue life. In addition to the yield strength, the influence of elongation and tensile strength on fatigue is also presented in Figure 2-36 (b), (c). Elongation to failure and tensile strength appears to have similar trend to the yield strength. However, a lower percentage of elongation is often correlated to increased porosity level, the particular value of elongation to failure below which the fatigue lifetime decreases drastically for a specimen may indicate a critical porosity level, which may reduce lifetime due not only to ease of initiation but also potentially increased coalescence shortening lifetimes further.

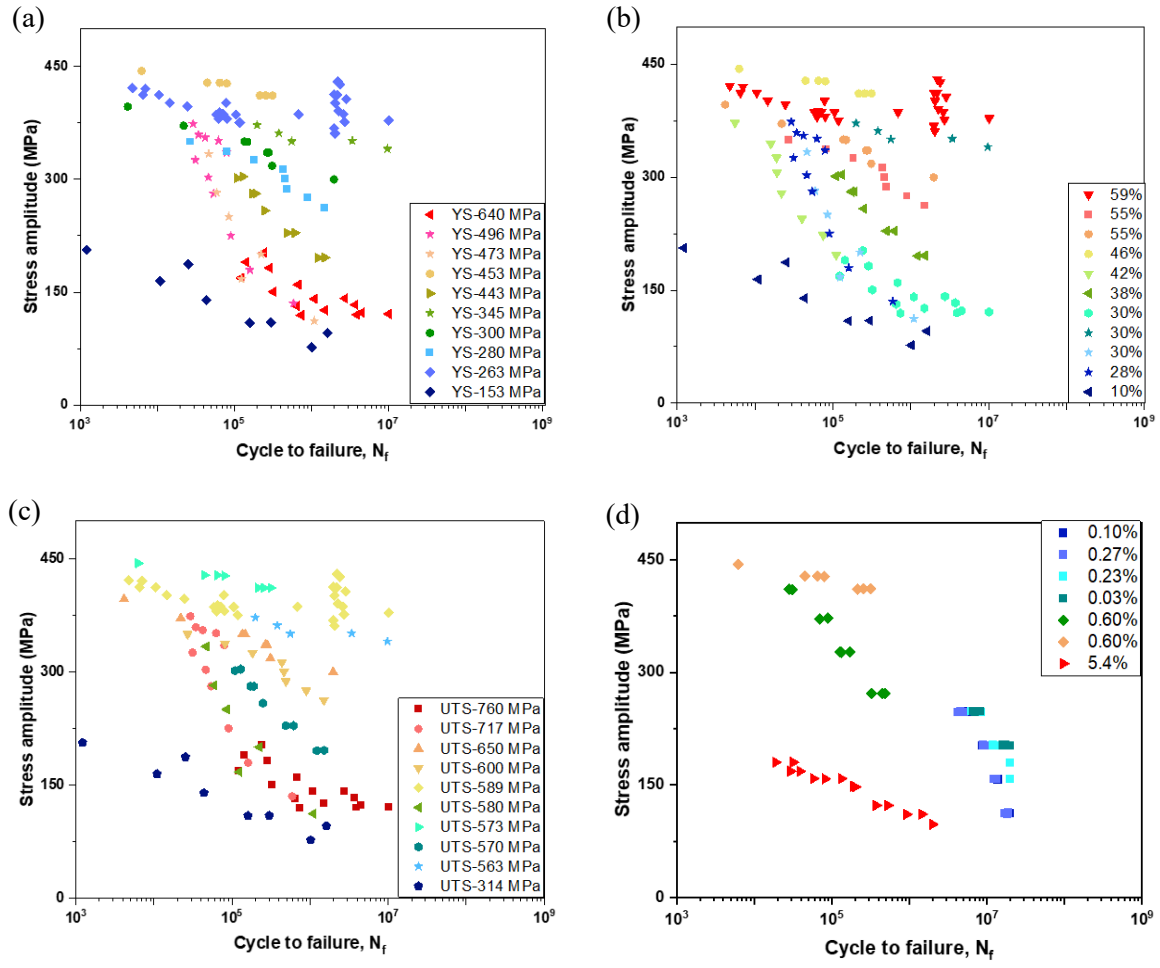

Figure 2-36: Fatigue lifetime dependency on (a) yield strength (b) elongation to failure (c) tensile strength (d) percentage porosity for LPBF processed 316L stainless steel [16][107][3][110].

Subsequently, the data on fatigue lifetime is shown in Figure 2-36 (d) based on their porosity percentage. Usually, CT-scan, Archimedes and optical microscopy methods were reported for porosity measurement for the data in the studies in Figure 2-36 (d) [2] [16][18]. Porosity is evidently strongly related to a specimen's fatigue life. It also appears that specimens of about <1% porosity have a similar lifespan of fatigue. This attribute can be called tolerable porosity, below which there is not a strong effect on fatigue behaviour.

To summarise, it is evident, the percentage of total porosity and surface roughness can play an important role in the fatigue life of a specimen. This can be considered the first step towards fatigue lifing model generation. Further information such as defect clustering and microstructure morphology needs to be taken into consideration. YS and UTS also seem to play a role in controlling fatigue behaviour and within same the study, higher YS was associated with high fatigue life.

2.7 Summary and conclusion

In summary, the Laser Powder Bed Fusion (LPBF) process presents significant advantages in terms of design flexibility and the production of near-net-shaped components. However, it is not without its challenges. Various processing parameters, including laser power, scanning speed, layer rotation, scanning strategy, and specimen size, exert influence on specimen surface roughness, percentage porosity, residual stress, and distortion. Through careful optimization of these parameters, it is possible to mitigate surface roughness, residual stress, distortion, and percentage porosity.

Considerations for effective process parameter selection include:

- Reducing laser power to avoid keyhole instability and eliminate keyhole porosity.
- Decreasing scan line spacing and layer thickness to achieve complete melting and reduce lack-of-fusion porosity.
- Reducing scan vector length through strategic scanning methods (e.g., island scanning) and using a reheated substrate/chamber to minimize residual stress and distortion.
- The choice of scanning strategy also influences porosity size and shape, with line scanning providing a denser part with small spherical pores, while island scanning results in larger irregular-shaped pores but fewer in number.
- Also, spot diameter significantly influences porosity percentage, with larger spots at very low energy density causing lack of fusion porosity and spherical pores due to trapped gas during rapid solidification.

Beyond density, surface roughness, and distortion, processing parameters significantly impact the solidification rate and thermal gradient within the part, thereby influencing the microstructure, particularly the average grain size and their preferred crystallographic orientation.

Key findings related to the LPBF process include:

- LPBF exhibits a very high cooling rate (approximately 103 K/s), resulting in a finer microstructure compared to Hot Isostatic Pressing (HIP) and casting processes.
- The finer microstructure contributes to higher strength, hardness, and elastic strain, with strength inversely proportional to average grain size and directly proportional to grain size dispersion, as suggested by an extended Hall-Petch model.
- Etched LPBF processed 316L stainless steel reveals dendritic subcellular structures, rich in Cr, Ni, and Fe.
- Energy density affects microstructure, with decreasing energy density associated with a finer average grain size. Higher energy density reduces the percentage of low and high-angle grain boundaries but has minimal impact on Geometrical Necessary Dislocation (GND) density.

- Crystallographic texture is influenced by volumetric energy density (VED), resulting in a stronger texture with higher energy density. Adjusting energy density affects texture strength, with larger and smaller melt pools yielding stronger <101> and <100> textures, respectively. Temperature gradient resulting from energy density and melt pool shape critically influences crystallographic orientations.
- Scanning strategies such as unidirectional, bidirectional (meander scanning), and chess strategy (island scanning) are employed to minimize residual stresses. The addition of a contour in the scanning strategy leads to a smaller average grain size compared to scanning without a contour, possibly due to variations in grain size within the contour.
- Variations in melt pool characteristics, including depth, were observed between specimens of different sizes, establishing a link between thermal history, microstructure, and geometry size in LPBF. Larger block specimens exhibited deeper melt pools, while smaller dog-bone specimens demonstrated shallow melt pools due to faster cooling rates resulting in more entrapped gas pores. Mechanical tests revealed substantial variations in fatigue lifespan, with smaller block specimens exhibiting shorter lifespans due to entrapped gas pores.
- Porosity plays a significant role in influencing fatigue life, with data suggesting that porosity exceeding 1% can be detrimental to fatigue life. Additionally, it has been reported that the high yield strength is associated with an extended fatigue life. This observed trend is similarly reflected in parameters such as elongation to failure and ultimate tensile strength. Notably, it is unsurprising that surface roughness can exert dominance over all the aforementioned parameters in governing fatigue life.

A comprehensive understanding of processing parameters, geometric size scales, and their interplay is essential for optimising the Laser Powder Bed Fusion (LPBF) process and achieving the desired material properties. The literature review has provided valuable insights into process optimisation and the process-property relationship.

Based on the findings reported in the literature, the selection of process parameters for specimens will aim to achieve the highest material density with reduced residual stress and distortion. However, process-induced porosity and surface roughness cannot be entirely eliminated. Given the detrimental effect of surface roughness and porosity on fatigue life, these aspects will be a significant focus of this study.

This study will investigate the effect of processing parameters on the microstructure (e.g., grain size and boundary distribution), crystallographic orientation, and recrystallisation of LPBF-processed 316L stainless steel. It will also examine the size-scale effect and the role of heat flow and thermal cycling on microstructural properties. Consequently, a thorough analysis will be conducted to understand the impact of process-induced microstructures on the tensile and fatigue properties of 316L stainless steel.

Chapter 3 Microstructure characterisation and mechanical properties

3.1 Introduction

It is apparent from the literature review that LPBF process parameters, especially energy density and scanning strategy have important effect on the microstructure. High energy density would theoretically cause coarser grain and strong crystallographic texture. In addition to that, scanning strategy such as island and bidirectional would affect thermal condition affects overall microstructure morphology (i.e., average grain size and dispersion). Also, specimen size scale would affect the heating/cooling condition, resulting microstructure inhomogeneity across the specimen. In order to investigate the effect of processing parameters and geometry size scale on the microstructure and mechanical properties, four batches containing bend bars and micro tensile specimens will be analysed. The analysis would include a thorough characterisation of microstructure with grain size and boundary distribution, inverse pole figure map and percentage of grain recrystallisation. Three different scanning strategy namely unidirectional, bidirectional and island would be considered for this study. In addition to that, effect of energy density and build location would be briefly analysed. A subsequent investigation would be carried out to understand the link between the microstructure and mechanical properties of the bend bar specimens, essentially linking process parameter, microstructure, and mechanical properties. The analysis would be continued in Chapter 4 to investigate effect of these parameters on fatigue life of the bend bars. Additionally, a key analysis would be done on the micro tensile specimen from batch two (B2) and batch three (B3), to understand the combined effect of area size scale and thermal heating cooling condition on microstructure. The mechanical properties, mainly fatigue of the micro tensile specimen would be further investigated in Chapter 5.

3.2 Specimen manufacturing details

Four batches of specimens were manufactured, each under different processing parameters. These batches were denoted as batch zero (B0), one (B1), two (B2), and three (B3). Notably, B0, B1, and B3 were produced under equivalent volumetric energy density conditions, while B2 was processed with a significantly higher energy density using a laser with larger spot size. Specimens were manufactured using gas-atomized 316L stainless steel powder particles obtained from Carpenter Additive [111]. Specimens from B0, B1, and B2 were manufactured at University of Southampton, whereas B3 specimens were exclusively manufactured at Aarhus University.

Table 3-1: The specimen variation matrix is given in the following table.

	B0	B1	B2	B3
Energy density	49 J/mm^3	49 J/mm^3	138 J/mm^3	49 J/mm^3
Scanning strategy	Unidirectional	Island	Island	Bi-directional
Build direction	Horizontal	Horizontal	Vertical	Vertical
	Vertical	Vertical		
Specimen geometry	Bend bar	Bend bar	Bend bar	Bend bar
			micro tensile	micro tensile

The Laser Powder Bed Fusion (LPBF) process was employed to produce these specimens, utilizing three distinct machines. As depicted in Figure 3-1 (a), the manufacturing of bend bar specimens for B0 and B1 involved three build directions: vertical (Z built), horizontal 0-degree (X built), and horizontal 90-degree (Y built). In contrast, B2 and B3 were made only in vertical orientation eliminating the directionality as a variable but including both bend bars and micro-tensile specimens. The motivation behind manufacturing B0 and B1 was to examine the impact of build direction and scanning strategy, whereas B2 and B3 were manufactured to explore the influence of energy density and geometric size-scale on the microstructure of additively manufactured 316L stainless steel. Detailed dimensions of these specimens can be found in Figure 3-2 and Figure 3-3.

Each of the B0 and B1 batches included five bend bar specimens for each build direction (X, Y, and Z), amounting to a total of fifteen specimens for each batch, while B2 and B3 comprised twelve bend bars for each batch. Furthermore, both B2 and B3 contained twelve micro-tensile specimens each, all built in the vertical direction.

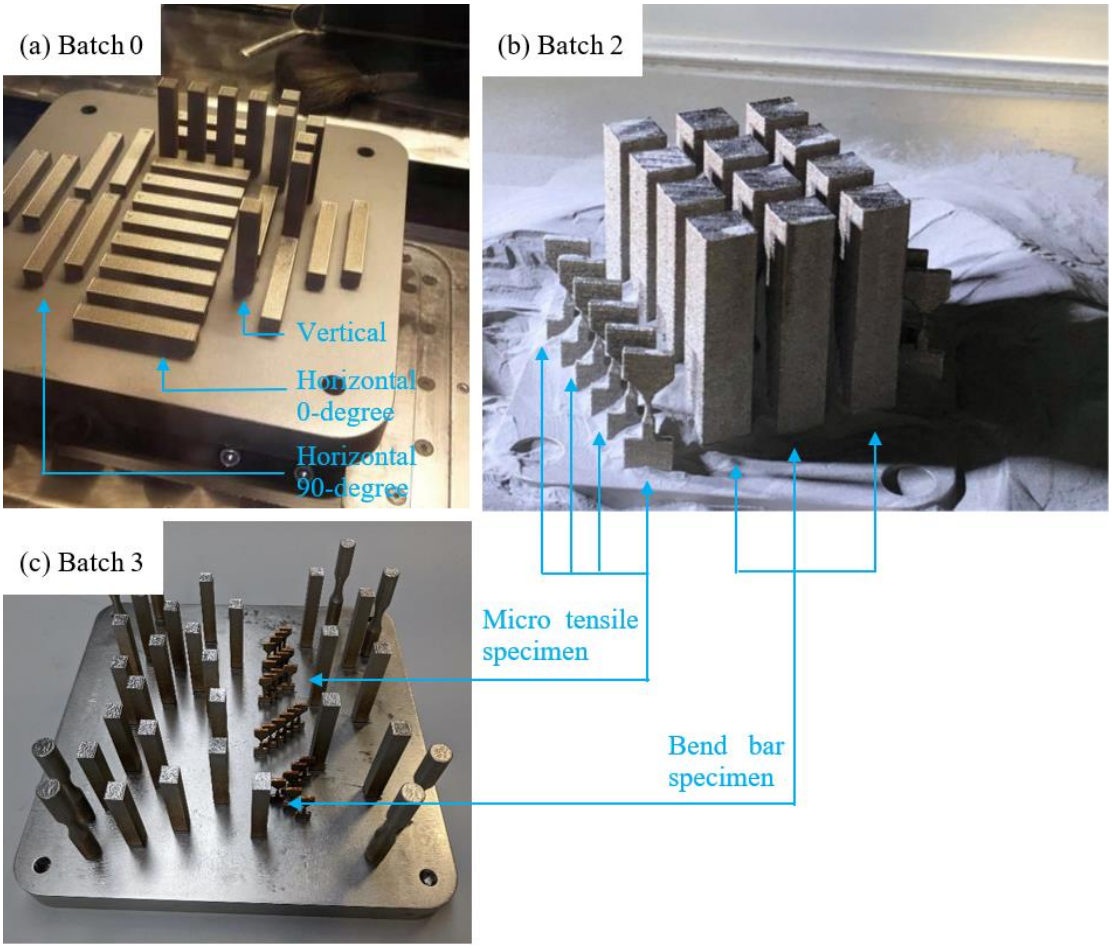

Figure 3-1: (a) Batch zero (B0) specimens built with unidirectional scanning strategy in vertical (Z built), horizontal 0-degree (X built) and horizontal 90-degree direction (Y built);and batch one (B1) specimens built with unidirectional scanning strategy simultaneously with B0 (b) batch two (B2) bend bar and micro tensile specimens in vertical build direction (c) batch three (B3) bend bar and micro tensile specimen in vertical build direction. All specimens were manufactured with 316L SS. The tensile cylindrical specimens are not within the scope of this study.

The specimens from B1, B2, and B3 were manufactured for an in-depth investigation into the impact of processing parameters and size scale on microstructural and mechanical properties. The overview of specimens and variables across different batches of specimens are summarized in Table 3-2. The study aims comprehensive examination of the four batches, each encompassing various processing parameters.

Table 3-2: Test matrix to investigate the role of processing parameters and size scale effect of additively manufactured 316L SS.

Batches	Effect of build direction	Effect of energy density	Effect of location	Area size-scale effect
B1	X	X		
B2		X	X	X
B3				X

A detailed exposition of the processing parameters, encompassing scanning strategy, input energy density, and build direction, can be found in Table 3-3. It's worth noting that B0 and B1 were manufactured utilizing the Concept Laser machine M2, while B2 and B3 were manufactured through the Wuhan Huake 3D HK PM250 printer and the SLM280 machine, respectively.

Table 3-3: LPBF processing parameters for different batches of specimens.

	B0	B1	B2	B3
Power, P	177 W	177 W	300 W	177 W
Scanning speed, v	800 mm/s	800 mm/s	900 mm/s	800 mm/s
Hatch distance, h	0.15 mm	0.15 mm	0.08 mm	0.15 mm
Layer thickness, t	30 µm	30 µm	30 µm	30 µm
Layer rotation angle, θ	45°	45°	90°	67°
Powder size	45 µm +/- 10 µm	45 µm +/- 10 µm	45 µm +/- 10 µm	-
Focus diameter	50 µm	50 µm	150 µm	50 µm
Island size	-	25 mm^2	100 mm^2	-
Scanning strategy	Unidirectional	Islands	Island	Bi-directiona

				l (Contour scanning)
Machine	Concept laser M2	Concept laser M2	Wuhan Huake 3D HK PM250	SLM 280

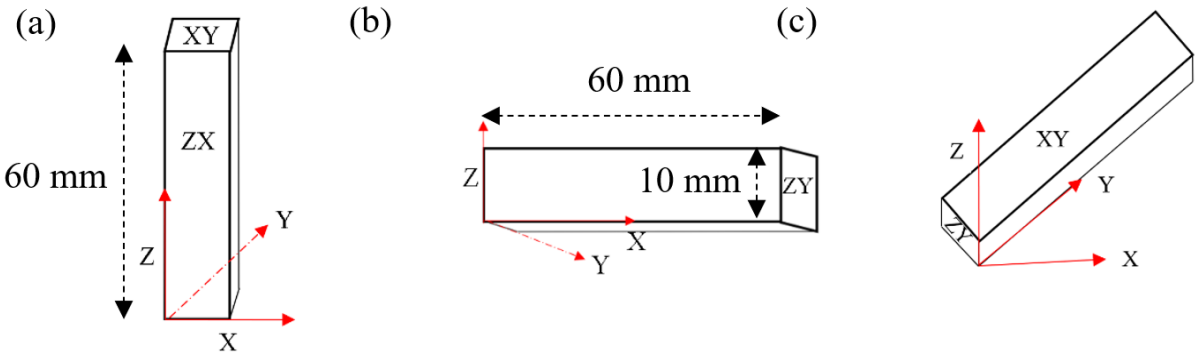

Figure 3-2: 316L SS Bend bars manufactured in (a) vertical, (b) horizontal 0-degree and (c) horizontal 90-degree direction. Bend bars have a cross section area of 10×10 mm^2 and length of 60 mm. Build direction is in z-direction.

As for the bend bars, as visualized in Figure 3-2, three distinct directions were considered: vertical, horizontal 0-degree, and horizontal 90-degree, to manufacture B0 and B1 bend bar specimens. All bend bar specimens had a uniform cross-sectional area of 10×10 mm^2. However, there was variation in their lengths, with B0 and B1 specimens being 60 mm long, and B2 and B3 specimens extending to 50 mm and 70 mm, respectively.

In contrast, micro-tensile specimens, manufactured for both B2 and B3, were consistently manufactured in the vertical direction. These micro-tensile specimens featured three distinctive sections: the grip and gauge, with respective areas of 20 mm^2 and 5 mm^2, and a central gauge section with a minimum area of 0.81 mm^2. The marked areas on the micro-tensile specimens, along with detailed dimensions, are illustrated in Figure 3-3. Kim et al. [112] used microtensile specimen of same dimension of RR1000 alloy to simulate tension-tension fatigue.

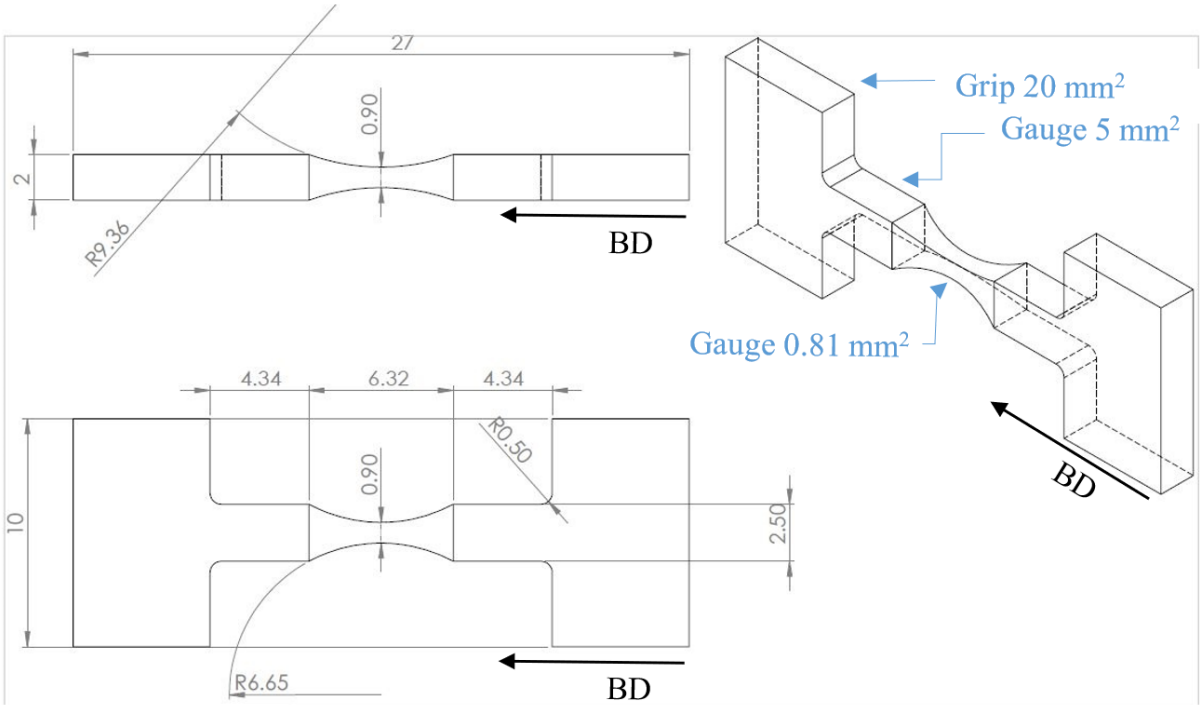

Figure 3-3: Micro tensile specimen dimensions. Specimens were built in vertical direction. It contains three different area: grip (20 mm²), gauge (5 mm²) and gauge (0.81 mm²).

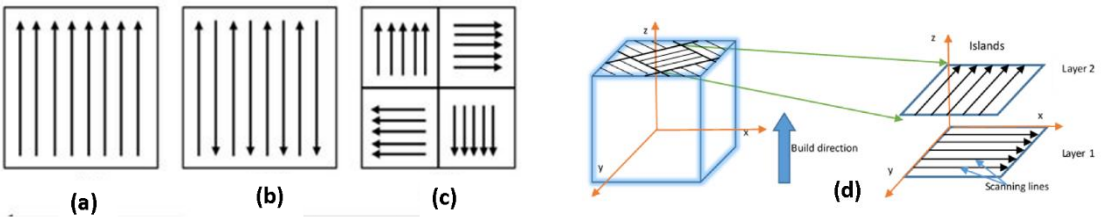

Figure 3-4: Different scanning strategies for laser powder bed fusion process (a) Unidirectional (used in B0); (b) Bi-directional (used in B3); and (c) Island (used in B1 and B2). Scan rotation of 90° shown in (d) [113][114]

The three scanning strategies used to manufacture four different baches of specimens mentioned in Table 3-3 are visually presented in Figure 3-4 (a), (b) & (c). The layer-by-layer rotation process during the laser powder process is shown for a 90° rotation in Figure 3-4 (d).

As mentioned earlier, the specimens can be categorized into four distinct groups based on differences in their processing parameters, as outlined in Table 3-1. B0, B1 and B2 were manufactured with gas atomised powder from the same supplier. The chemical composition of these specimens was analysed using the arc/spark optical emission spectrometry (OES) technique, resulting in a comprehensive breakdown detailed in Table 3-4. It is notable that all primary elemental compositions were within the manufacturer's specifications. However, trace quantities of Niobium, Copper, and Aluminium were

detected in the powder composition, plausibly due to incidental contamination within the powder chamber during the manufacturing process.

Table 3-4: Comparison of the chemical composition of specimens from different batches measured by spectrographic analysis.

Element %	**B0**	**B1**	**B2**	**B3**	**Manufacturer-specified chemical composition** [111]
Carbon	0.018	0.025	0.021	0.026	0-0.03
Silicon	0.7	0.72	0.68	0.81	0-1
Manganese	1.09	0.95	0.53	0.73	0-2
Phosphorus	<0.002	<0.002	<0.002	<0.002	0-0.045
Sulphur	<0.002	<0.002	<0.002	<0.002	0-0.03
Chromium	17.83	17.73	17.64	17.8	16.5-18.5
Nickel	12.64	12.87	12.84	12.99	10-13
Molybdenum	2.4	2.44	2.39	2.42	2-2.5
Niobium	<0.010	<0.010	<0.010	<0.010	-
Copper	0.06	0.03	0.03	0.03	-
Aluminium	<0.005	0.009	<0.005	<0.005	-

All these as-built specimens were machined, ground, and polished before microscopy and fatigue tests. These specimen preparation details are given in Section 3.3. The bend bars and micro tensile specimens were manufactured for bending and tension-tension fatigue respectively. However, a set of dogbone tensile specimens were machined from bend bar specimens to experimentally measure the tensile properties.

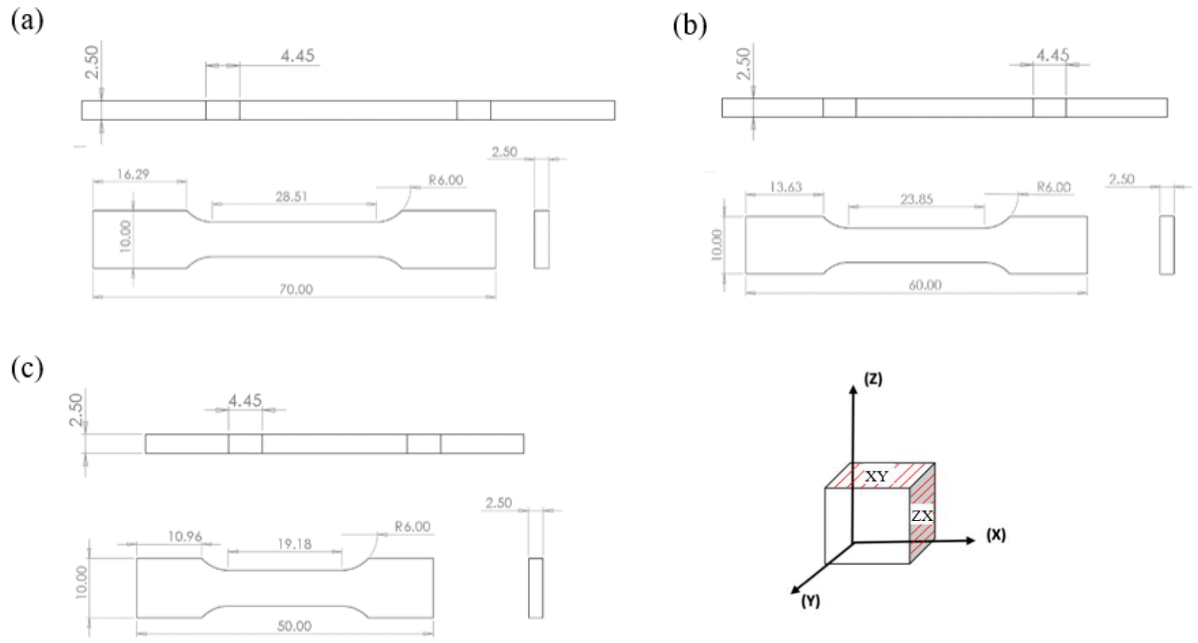

Figure 3-5: Tensile dogbone specimens machined from (a)B3 (b) B0 and B1; and B2. The designs were in accordance with BS EN ISO 6892-1:2016 standard. The tensile surface for vertically (Z) built specimens were ZX plane (i.e., B2 and B3), while for X (horizontally 0-degree) and Y (horizontally 90-degree) built specimens, it is XY plane.

The next section will discuss the effect of build direction, energy density, location and geometry size scale on average grain size, grain boundary distribution, preferred crystallographic orientation and recrystallisation of grains. Thus, it is important to implement a naming convention to identify specimen with specific planes while discussing the results. The naming convention that will be used is [batch number (BX)] _[build direction]_[build plane] in the format BX_XX_XX.

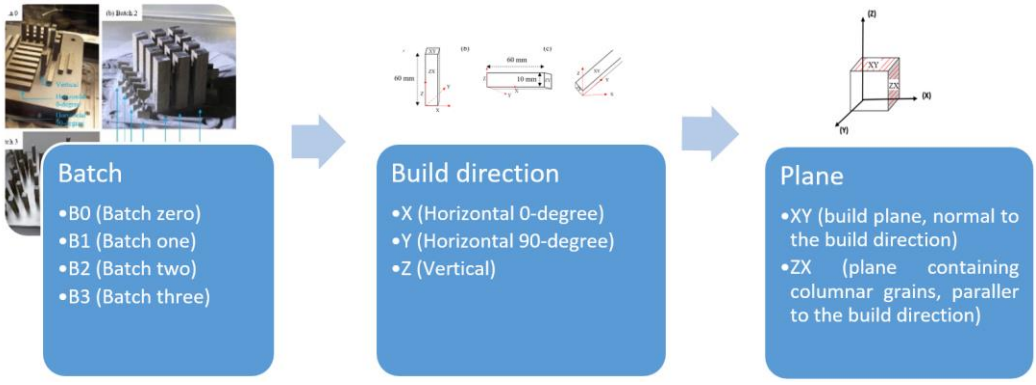

Figure 3-6: The process of naming a specific plane from specimen of different batches.

3.3 Methodology

3.3.1 Specimen preparation

The bend bar specimens were machined to remove support by the EDM centre at the University of Southampton. They were later polished on the top surface (tensile) side and around the top edge for fatigue testing. The top edges were bevelled/smoothened up to avoid corner crack initiation.

The tensile surface of the bend bars was ground and polished to achieve a one-micron smooth surface finish. They were ground with 200, 800 and 1200-grit sandpaper, respectively. Grinding was followed by 9-micron 6-micron and 1-micron diamond polishing with MD-mol and MD-nap from Struers-Ltd, respectively. The gauge section (section with the minimum area of 0.81 mm^2, see Figure 3-5) of the micro tensile specimens were ground and polished using a Dremel 3000 grinder. These specimens were ground and polished with the same steps as bend bar specimens with sanding band on mandrel and polishing wheels respectively. The specimens were then etched with Kalling's 2 Reagent for 5-20 s.

3.3.2 Optical Microscopy, SEM and EBSD

Microscopy was carried out on both mounted cubes from bend bars and sections of micro tensile specimens with various dimensions. A square block of the bend bar specimens was cut using a Mecatome T210 cutting machine with 4000 rpm speed at 0.066 mm/s feed rate. The bend bars and micro tensile specimens were both cut orthogonally with respect to the longitudinal and transverse direction to prepare them for metallographic examination.

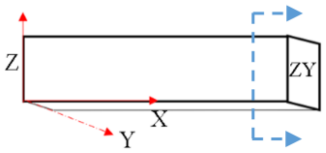

Figure 3-7: A square block cut out from the bend bar specimen.

After the cutting process, specimens were mounted in conductive Bakelite with a Hydraulic press OPAL 410 machine. The machine was configured to heat the Bakelite at 180° C for 6 minutes, followed by 5 minutes of cooling time, totalling 11 minutes cycle.

To reveal the microstructure of the austenitic 316L SS, Kalling's Reagent No. 2 was used as an etchant, which consists of 20 mL HCL, 20 mL ethanol, and 1 g Cupric Chloride. Porosity and microstructural features such as melt pool were observed using an Olympus BX-51 optical microscope (OM).

Electron backscattered diffraction (EBSD) technique was used to obtain detailed grain boundary and crystallographic orientation information using the Oxford Instruments® C-NANO software-based JEOL JSM-7200F Field Emission Scanning Electron Microscope machine. An acceleration voltage of

15-20 kV was used at a working distance of around 10 mm. The distribution of grain boundaries, misorientation angles, and crystallographic orientation maps were analysed with the Aztecrytal software. Most of the EBSD maps were scanned at 200x magnification with 1-micron step size. The low and angle high angle grain boundary was determined with 2 and 15 degrees respectively. The elemental composition was analysed using energy dispersive X-ray spectrometer technique with acceleration voltage of 10-15 kV.

3.3.3 Hardness and tensile testing

Microhardness testing was performed using FM-300 Vickers microhardness tester at 200 g load with 10 s dwell time at room temperature on the polished specimens. All indentation was done following BS EN ISO 6507-1:2018 standard. A minimum of 5 indents were made in linear pattern to find the average hardness and its standard deviation.

Tensile tests were conducted at room temperature using Instron 5569 electromechanical test instrument on the dogbone specimens shown in Figure 3-5 (machined from bend bar specimens) in accordance with BS EN ISO 6892-1:2016 standard. An extensometer was used to measure the strain at 2 mm/min crosshead speed.

3.4 Results and discussion

3.4.1 Introduction

In Figure 3-8, the etched microstructure of a 316L SS bend bar has been shown with different magnifications. In Figure 3-8, optical images of the microstructure on the ZX plane (parallel to the build direction) from a vertically built B0 specimen are shown with different magnifications. The visible scaly pattern melt pool is a characteristic feature of additively manufactured specimens identified in the Figure 3-8 (a). These features were observed in bend bars from all batches (including B1, which has the same processing parameters but was manufactured with island scanning strategy), orientations, and locations of the specimens. However, only B0 is shown in Figure 3-8 as these are representative images. The etched melt pools contain honeycomb shaped subcellular microstructure ranging from 0.5-2 micron depending on processing parameters of the specimens, shown in Figure 3-8 (b). The elongated cells visible in the image are columnar dendrites, which are shown at higher magnification in Figure 3-8 (c) and contains voids, shown in Figure 3-8 (c) in the cell boundary along with randomly distributed nanoparticles.

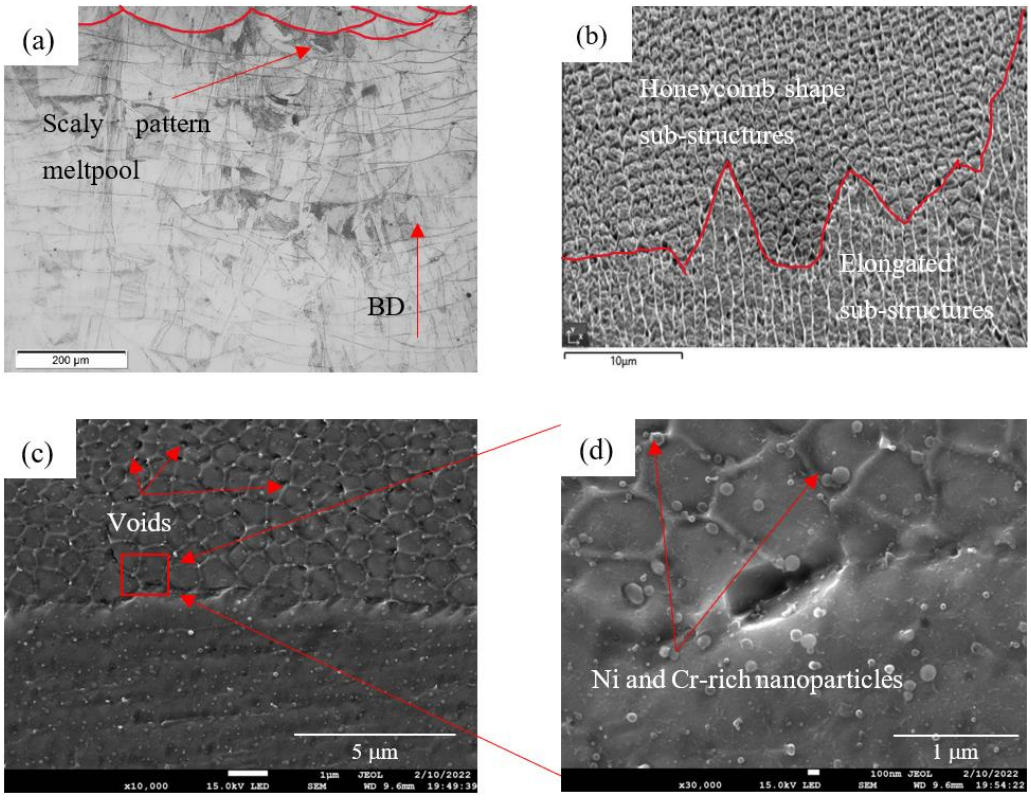

Figure 3-8: Etched microstructure of 316L SS (a) melt pool (b) honeycomb shape and elongated sub-cellular structure (c) high magnification view of sub-cellular structure network (d) further magnified sub cells with randomly distributed nano particles. Build direction (BD) is indicated and consistent for all micrographs.

An EDX analysis was conducted to characterise the elemental composition of the nanoparticles shown in Figure 3-8 (d). The elemental compositions of four nanoparticles are presented in Table 3-5. These particles are all Fe, Ni and Cr rich while two particles contain relatively high percentage of Molybdenum compared to the manufactured provided composition list. The Cr and Ni rich particles indicate elemental segregation due to fast solidification rates. Similar findings were reported by Qu et al. [30], who used gas atomised powder with similar composition (especially the Cr, Ni and Mo percentage) for LPBF with an island scanning strategy.

Table 3-5: Elemental composition of nanoparticles at 10 Kev with EDX technique

Element %	**Site 1**	**Site 2**	**Site 3**	**Site 4**
Ferrous	55.1	64.5	58.6	65.9
Chromium	20.1	18.5	19.4	17.3
Nickel	17.8	13.4	16.4	15.2
Molybdenum	5.3	3.5	-	-
Silicon	1.4	-	-	0.8
Phosphorus	0.3	-	-	-
Manganese	-	-	1.4	
Sulphur	-	-	1.4	0.8
Tantalum	-	-	2.8	-

Even though similar microstructural features were observed across different batches of specimens with multiple orientations, significant variation between average grain size, grain boundary distribution and recrystallization have been recorded. A comparison of microstructure between different build directions will be discussed in the sections 3.4.2. Then the anisotropy within a bend bar would be discussed by comparing the microstructures on two different locations (top and bottom) in section 3.4.3. Afterwards, geometry size scale effect would be investigated in depth by comparing microstructures from XY and ZX planes within and across the batches for different area size in section 3.4.4. The discussion will be carried on by a consistent comparison of the microstructural properties such as average grain size, inverse pole figure (IPF), high angle grain boundary distribution, percentage of recrystallisation and preferred crystallographic orientation. The IPF map will be presented with respect to longitudinal

direction (LD) and transverse direction (TD). For the maps in XY plane, the build direction (BD) lies in the normal direction (ND); while for the maps in ZX plane, the build direction (BD) lies in the transverse direction (TD). The IPF map intensity is measured with multiples of the random distribution (MRD) value. The MRD value is indicative of crystallographic texture within a polycrystalline material. A crystallographic texture is the distribution of the crystallographic orientation of grains relative to the specimen orientation in a polycrystalline material. Next to the IPF maps, grain orientation spread maps (GOS) with threshold <1°, interpolated on the high angle grain boundaries (HAGB) will be displayed to show recrystallized grain distribution. Numerous studies have reported the technique of utilizing the grain orientation spread value as a mean to identify recrystallized grains. [115][116][117].

3.4.2 Microstructural comparison between build direction

This section would discuss the comparison between microstructure of two horizontally built specimen along with a vertically built specimen from B1, shown in Figure 3-2. The processing parameters of B1 specimens were already given in Table 3-3 and the microstructures on both the XY and ZX planes are compared in this section. As mentioned earlier, XY and ZX are planes normal and parallel to the build direction (BD) respectively.

The initial observation on IPF map regardless of the build direction reveals checkboard pattern on the XY plane (See Figure 3-9 (a), (b) & (c)), which is characteristic to island scanning strategy. While comparing the crystallographic texture on the XY and ZX plane between X, Y built specimen in the Figure 3-9 (a)(b), a weak MRD value for X built (Figure 3-9 (a)) and Y built specimen (Figure 3-9 (b) was observed in <001> and <101> directions with respect to the BD. However, Z built specimen showed relatively stronger intensity in <101> direction for both ZX and XY plane (see Figure 3-9 (c)). This is due to longer heat path for Z built specimen which causes localized heat concentration causing slow cooling and deeper melt pool. The high energy input was reported by Qu et al. [30] to cause strong crystallographic texture.

Further microstructure characterization can be done using GOS maps to show recrystallized grains. Initially, a random distribution of recrystallized grains can be seen on the GOS map for all the specimens in the Figure 3-9 but upon careful observation it is apparent that the most significant portion of nuclei for recrystallization on the build plane can be observed along the melt tracks. One of the necessary criteria for the recrystallisation process reportedly is high stored energy during the manufacturing process along the melt track, which agrees with Pinto et al. [117]. In addition to that, finer grains surrounded by larger grains are potential spot for nucleation as they have higher deformation nearing the boundary, which is another contributing factor to nucleation for recrystallisation and it is consistent across all specimens.

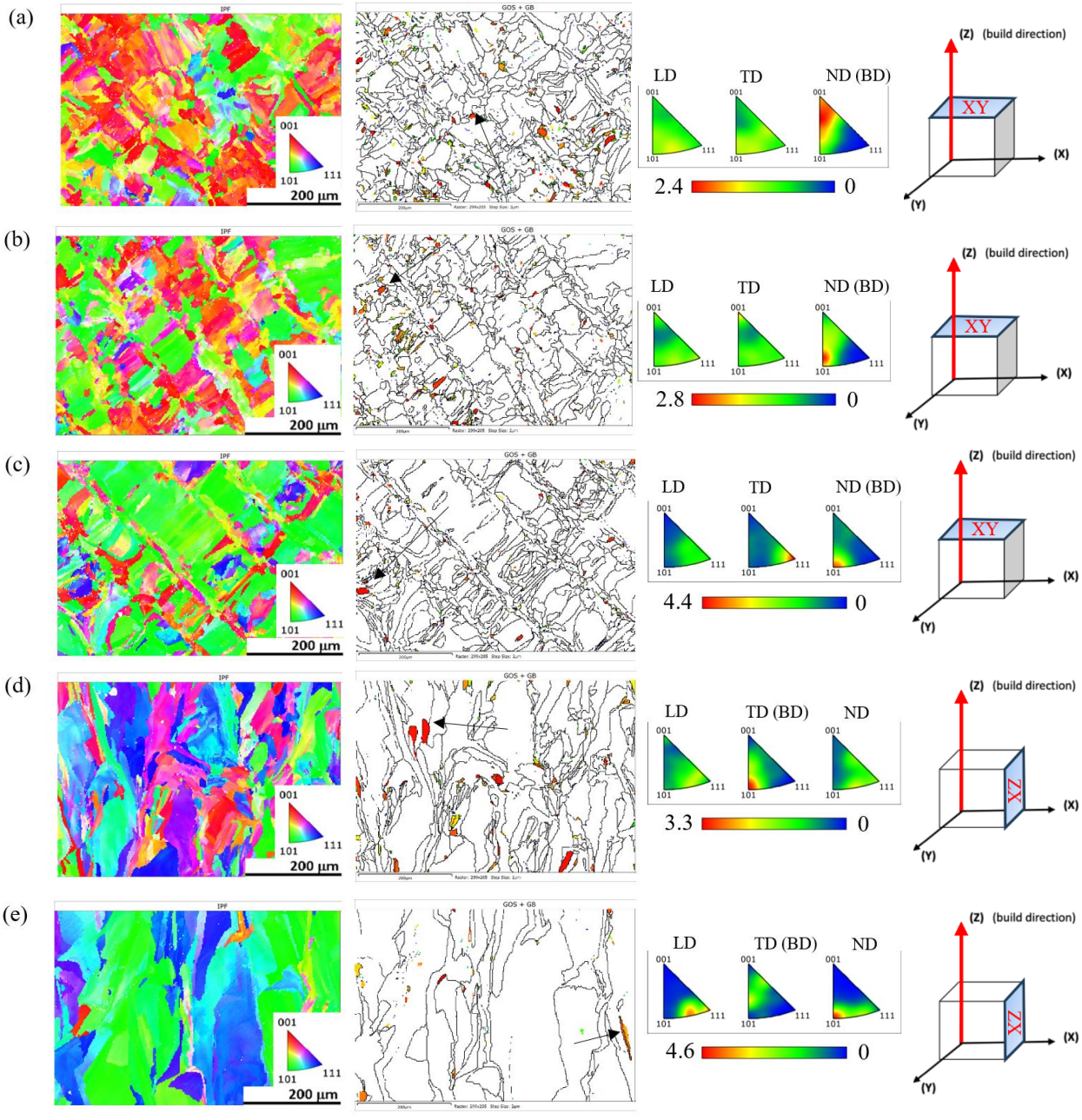

Figure 3-9: B1 bend bar specimen IPF map (left), HAGB distribution with recrystallised grains GOS<1° (middle) and IPF with MRD values (right). Results shown on the XY plane for (a) X built [3.19% recrystallisation] (b) Y built [2.39% recrystallisation] (c) Z built [0.74% recrystallisation] specimen and on the ZX plane for (d) Y built [5.53% recrystallisation] (e) Z built [3.74% recrystallisation] specimen. The recrystallised grains are indicated with black arrows.

A comparison between the average grain size for the specimens mentioned in

Figure 3-9 is present using a bar chart in Figure 3-10. The average grain size was measured using Aztec Crystal by considering each grain's area to match a circle that can closely resemble to the area of the grain. The diameter of each of these circles is then calculated and then averaging all the diameters give the average grain size. All the specimens in Figure 3-10 appeared to have similar values of area weighted average grain size distribution on the XY plane, especially between horizontal specimens (X and Y built), as shown in Figure 3-10. Since difference in solidification conditions for both X and Y built specimen is expected to be similar only Y and Z built specimens were considered while the microstructure on the ZX plane is compared. The columnar grain size on the ZX plane appeared to be significantly different between Y and Z built direction. The Z built specimen on ZX plane has nearly fifty percent larger average grains compared to Y built specimen.

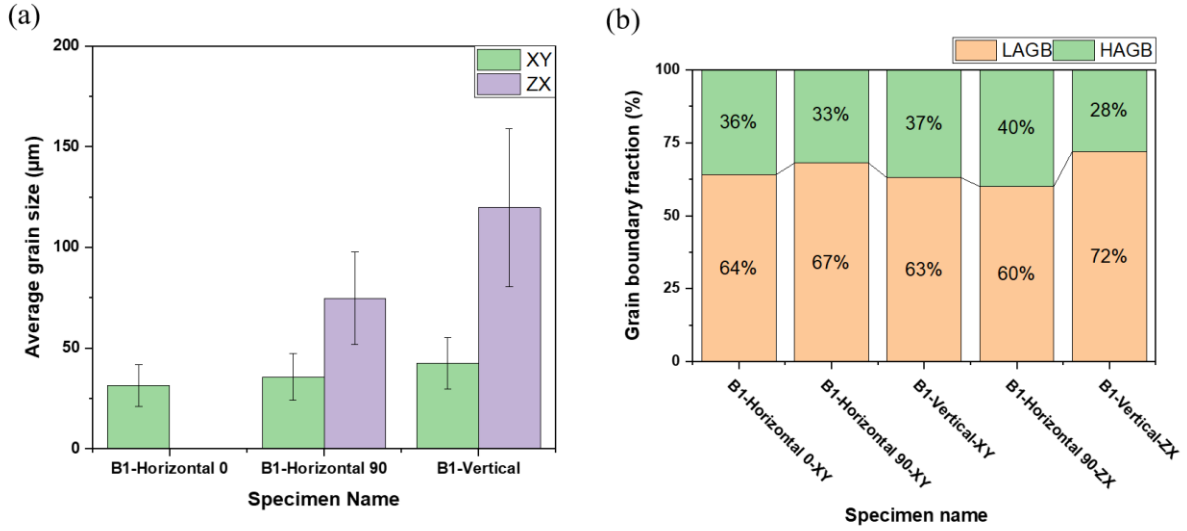

Figure 3-10: Quantitative representation of data from

Figure 3-9 to compare between (a) average grain size and; (b) low angle and high angle grain boundary distribution on XY plane (normal to BD) and ZX (parallel to BD) plane for X, Y and Z built specimen from B1. Error bars bound one standard deviation.

A quantitative representation of the comparison of the average grain size and grain boundary distribution from Figure 5-9 is shown in Figure 3-10. The XY and ZX plane in Figure 5-9 gives an idea of the columnar grain shape in the bend bar specimens. The elongated columnar grains are visible on the ZX plane while the equiaxed shaped top of the grain is visible in the XY plane. According to Figure 3-10 (a), the z-built specimen has significantly longer columnar grains compared to the Y built specimen and higher proportion of high angle grain boundary (HAGB). It is apparent that the value of average grain size is proportional to the standard deviation implying the fact that, grain distribution tends to get inhomogeneous as the average grain size increases, which agrees to the Salman et al [40].

The average grain size variation of these specimens is due to the thermal history during the LPBF process. Even though the average grain size on the XY plane remains independent of area size effect and subsequent thermal history, the columnar grain size on the ZX plane appears to be dependent on localized thermal heating/cooling condition. Each layer normal to the build direction is 100 mm^2 and 600 mm^2 for Z and Y built specimen respectively. As both the specimen experiences same energy density during their manufacturing process, the Y built specimen has larger area heat flow rate is higher leading to finer grains compared to Z built specimen.

$$\frac{Q}{t} = \frac{kA(T_2 - T_1)}{d} \qquad \text{Equation 3-1}$$

The heat Equation 3-1 indicates a proportional relationship between heat flow rate and surface area. In the equation Q/t is the heat flow rate, (T_2-T_1) is the temperature difference, d is the thickness and k is the conductivity. In addition to build direction, the effect of scanning strategy and layer rotation on microstructure and mechanical property is also investigated. The Figure 3-11 compares grain boundary distribution interpolated on the IPF map for ZX plane of Z built specimens from B0, B1, B2 and B3 respectively. The columnar grains corresponding to island scanning strategy for B1 and B2 specimen in Figure 3-11 (b), (c) are elongated and show preferred crystallographic orientation in the <101> direction. In the meanwhile, B0 and B3 specimen have randomly oriented relatively finer grains. B3 specimen columnar grain morphology is similar to finding of Zhao et al and Marattukalam et al. [118] [53], which used different processing parameter but bidirectional scanning strategy with 67°-layer rotation angle. The grain morphology for B3 specimen is likely characteristic to the specific scanning strategy. These studies further reported the morphology of unidirectional scanned specimen with no layer rotation, which is similar to the Figure 3-11 (a). This implies that, layer rotation is not a dominant factor determining microstructure for unidirectional scanned specimen. On the other hand, B1-Z built and B2 specimens in Figure 3-11 (b), (c) have both been printed with island scanning strategy with 45° and 90° layer rotation but have similar elongated columnar grains with <101> preferred crystallographic orientation. However, the grains are finer for B1-Z built specimen corresponding to 45° layer rotation angle compared to B2 with 90° layer rotation. Leicht et al. [46] reported similar finding for which agrees with the observation. They reported finer grains for 45° respect to 90° layer rotation, and these were elongated columnar grains with preferred crystallographic orientation in the <101> direction.

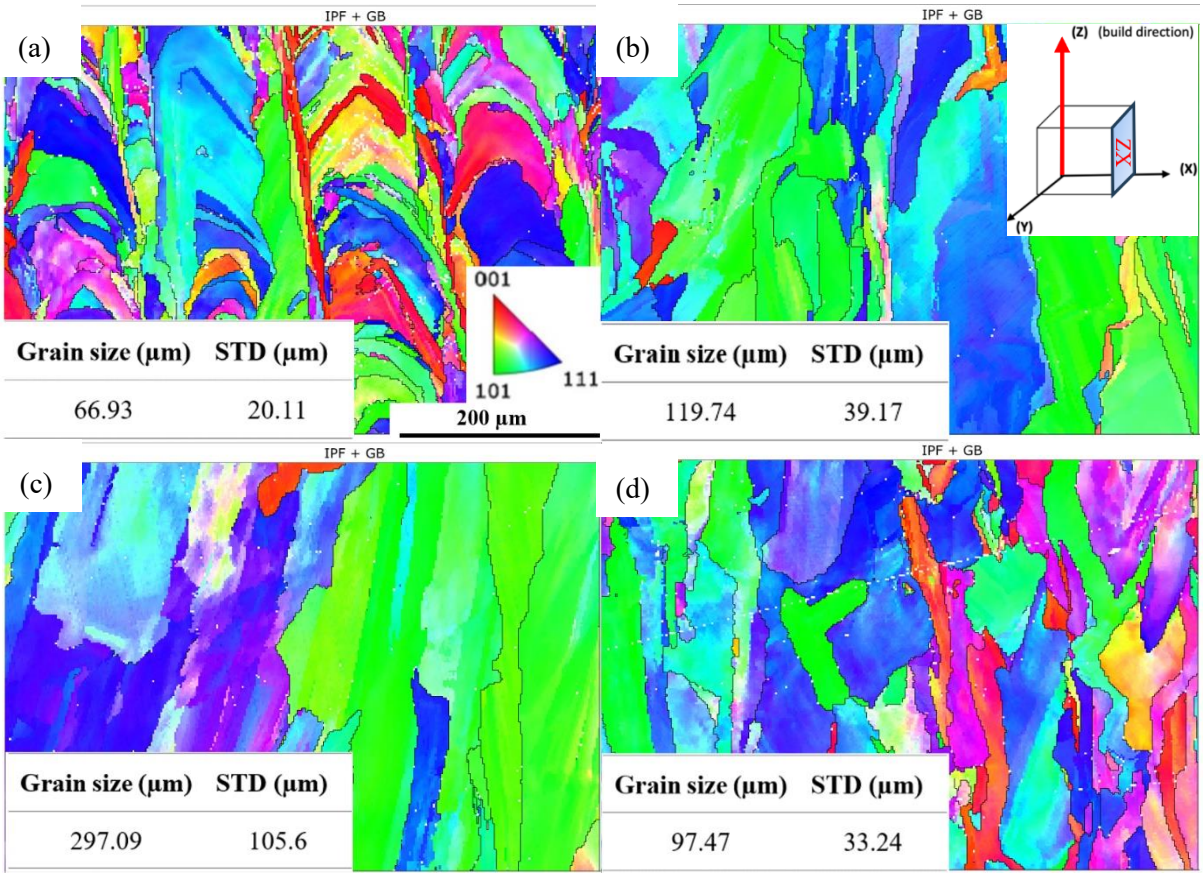

Figure 3-11: IPF map and grain distribution of Z built ZX plane of (a) B0 (b) B1 (c) B2 and (d) B3 bend bar specimen; B0 and B2 have lowest and highest average grain size respectively.

In addition to the layer rotation, energy density plays an important role on the average grain size and their distribution. The average grain size and the dispersions is reported to be proportional to the energy density [43][44]. The combined effect of 90 ° layer rotation and high energy density is responsible for large grains oriented in <101> direction.

To further our understanding of the role of microstructure on mechanical property, tensile tests were conducted on all batches bend bar specimens. The bend bar specimens were machined with the dimensions mentioned in Figure 3-5 following BS EN ISO 6892-1:2016 standard. A comparison of engineering stress-strain behaviour between Y and Z built specimen from all batches has been shown in Figure 3-12. The Z built specimens for both B0 and B1 appears to be less ductile and have lower yield strength compared to their Y built counterparts. This confirms high level of anisotropy in mechanical properties for B0 and B1 bend bar specimens. The low mechanical properties for Z built specimen are consistent for B2 specimen, where it has the lowest yield strength (YS) amongst all specimens and very low ultimate tensile strength (UTS) value. On the contrary, Z built specimen for B3 displayed very high ductility, UTS and good yield strength. B3 specimens are manufactured with bidirectional scanning strategy with a contour. High ductility and UTS for B3 specimen are due to this

contour scanning on the outer area of the specimen, mentioned earlier in the list of processing parameters in Table 3-3.

(a)

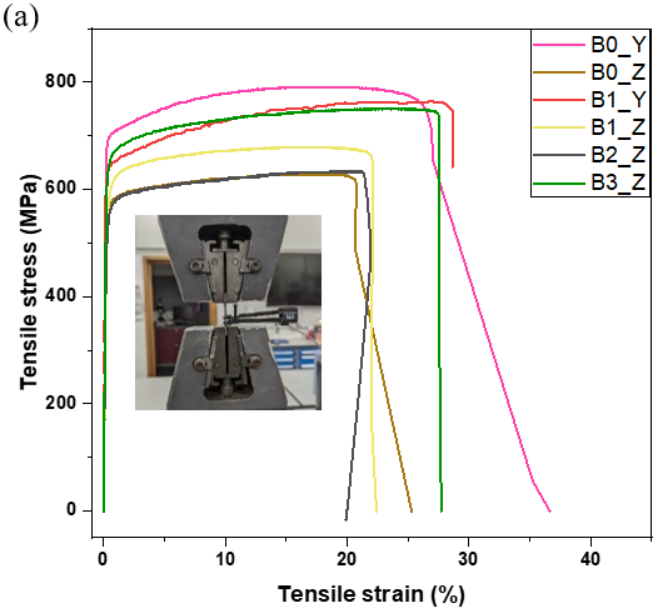

(b)

Specimen Name	Elongation (%)	UTS (MPa)	YS (MPa)
B0_Y	27	791	645
B0_Z	21	629	496
B1_Y	29	765	604
B1_Z	22	679	462
B2_Z	22	635	452
B3_Z	28	752	565

Figure 3-12: A comparison of (a) tensile stress-strain behaviour and (b) mechanical properties of specimens with different build direction and processing parameters.

The broader range of mechanical properties across batches with different build direction necessitates a comprehensive examination to understand the underlying factors affecting it. The exceptional mechanical properties of B3 were addressed in a study conducted by Salman et al [40], which reported an increase of 13.4% YS and 3.6% UTS due to the addition of contour with the Z built bidirectional scanning strategy [40]. The study further compared the mechanical properties and microstructures of unidirectional, bidirectional and island scanned specimen and reported them as following in Figure 3-13 (a). The relationship between grain size and YS manifests an inverse correlation, while concurrently demonstrating a direct proportionality to the dispersion of grain size. In accordance with the findings of the study, Figure 3-13 (b) illustrates the correlation between the average grain size and the UTS as well as the YS across specimens from all batches. It is worth noting that the LAGB and the average grain size of these specimens were assessed on the tensile side to specifically address the microstructures influencing mechanical properties. For Y and Z built specimens, the dominant microstructures are on the XY and ZX planes, respectively. In addition to the grain size, the relationship between LAGB fraction, grain size and tensile stress has been investigated in Figure 3-13 (b), where a general trend suggesting weak link between LAGB, and tensile stress is observed.

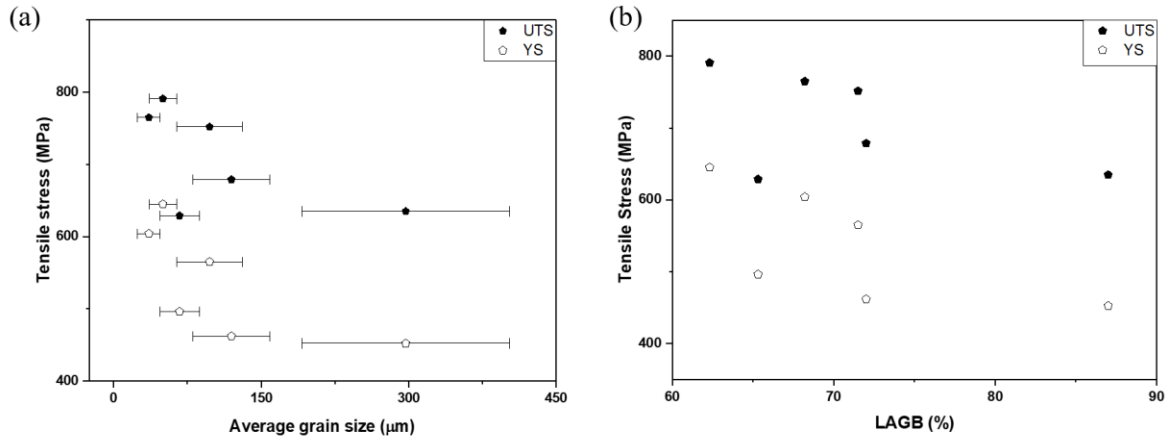

Figure 3-13: Relationship between tensile stress and (a) grain size; (b) LAGB fraction for B0, B1, B2 and B3 bend bar specimen.

Subsequently, the tensile properties of all batches of specimens appeared to be almost independent of the preferred crystallographic orientation. According to Figure 3-11, B2 specimens have the strongest texture, whereas B0 specimens have the weakest texture. However, as indicated in Figure 3-12 (b), they exhibit similar tensile properties, suggesting that the influence of texture on mechanical properties is insignificant.

3.4.3 Microstructural inhomogeneity along the build direction

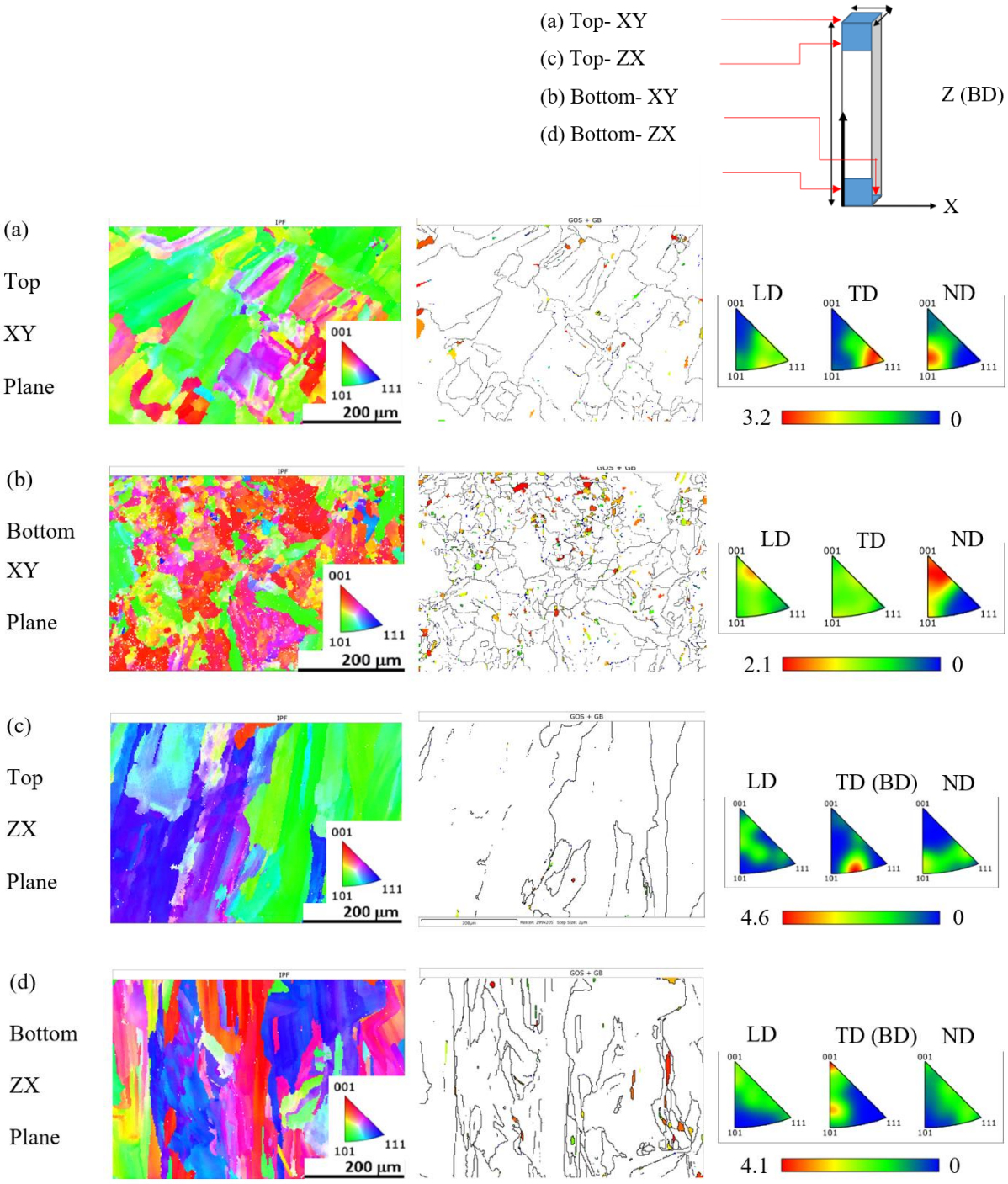

Figure 3-14: B2 bend bar specimen IPF map (left), HAGB distribution with recrystallised grains GOS <1° (middle) and IPF with MRD values (right). Results shown on the XY plane for (a) top [3.41% recrystallisation] (b) bottom [5.53% recrystallisation] and ZX plane (c) top [0.47% recrystallisation] (d) bottom [5.04% recrystallisation] of the specimen. The recrystallised grains are indicated with black arrows.

This section would discuss the inhomogeneity in the microstructure along the build direction for Z built specimen from B2. The specimens from B2 were manufactured with island scanning strategy but with nearly three times higher energy density. Thus, the effect of heat transfer would be more apparent for B2 bend bar specimens. In Figure 3-14, a comparison of microstructure between the top and bottom location of a B2 bend bar is shown. Regardless of the location, the columnar grains in the BD appear to have a stronger MRD value compared to the equiaxed structured grains on the build plane. The thermal gradient parallel to the build direction could explain the inhomogeneity in microstructure within the bend bar specimen. A simple explanation could be longer heating path at the top of bend bar leading to slow heat transfer and larger columnar grains. Additionally, as new layer scan proceeds, residual heat from previous scan contributes to the cooling rate. The residual build-up of heat increases as the number of layer increases. This essentially effects the size and distribution of columnar grains. An additional factor contributing to grain morphology is the epitaxial grain growth, which generally promotes directionality, shown in Figure 3-14 (a). In the meanwhile, significantly higher recrystallisation has been observed at the bottom of the bend bar compared to the top on the ZX plane, shown in Figure 3-14 (a)(b), which is consistent with the continuous flow of heat during the LPBF process providing time and heat input for nucleation and grain growth processes. As the bend bar was being built layer by layer, the energy dissipation path to the base plate was getting longer, and the heat flux was decreasing. As lower heat flow rate results in larger grains, the columnar grain is larger compared to the bottom of the specimen, shown in Figure 3-15(a). In Figure 3-14 (c)(d) due to higher heat flux resulting in finer grains and subsequent grain growth shown in, which is consistent with the finding in the previous section and agrees with the finding reported by Wei et al [119]. They reported that, for Co-Cr-Mo alloy fabricated with EBM, the top location is significantly coarser grains compared to the bottom location, which agrees with the observation.

Subsequently, the highest percentage of recrystallisation can be observed at the bottom of the bend bar shown Also, according to Figure 3-15 (b), the specimen with higher recrystallisation (XY plane at the bottom) appears to have a higher percentage of HAGB, suggesting a link between HAGB and percentage of recrystallisation.

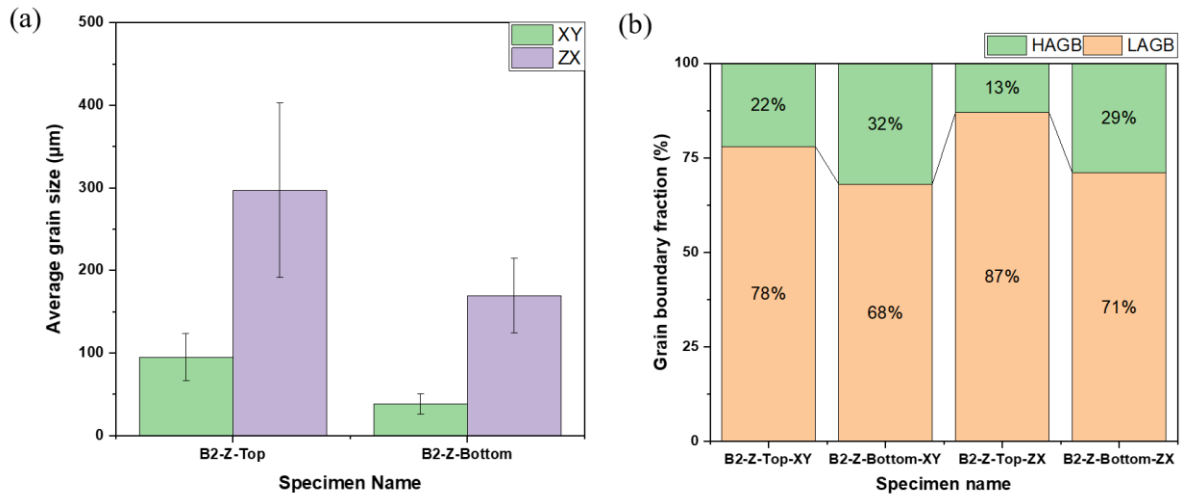

Figure 3-15: Quantitative representation of data from Figure 3-14 to compare between (a) average grain size and; (b) low angle and high angle grain boundary distribution on XY and ZX plane (normal to BD) and ZX (parallel to BD) plane for top and bottom location in B2 bend bar. Error bars bound one standard deviation.

3.4.4 Size scale effect on microstructure for micro tensile specimen

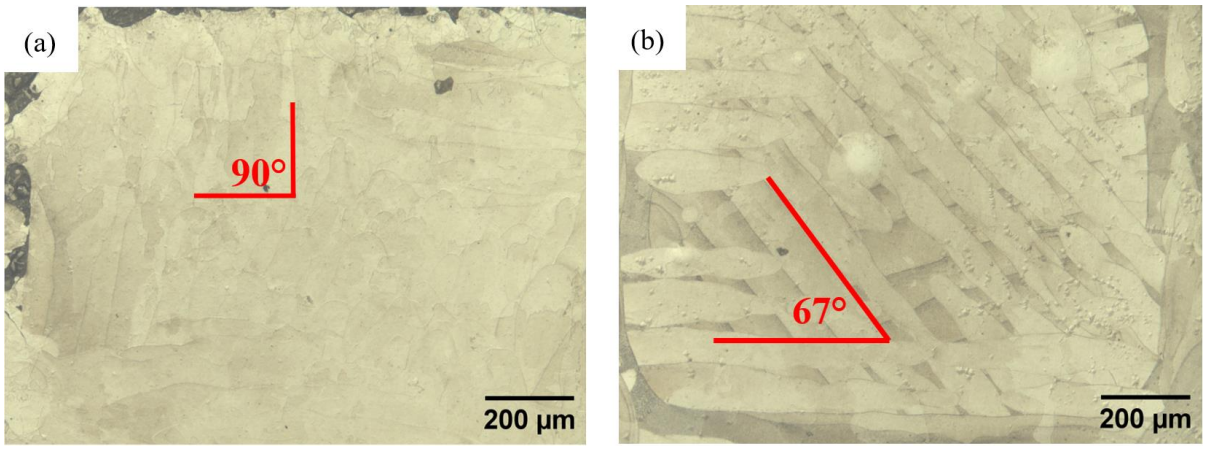

Figure 3-16: Comparison between the cross-section area of the micro tensile specimen on XY plane at same magnification; (a) B2 as the smallest gauge section area of 0.68 mm^2 (b) B3 has the smallest gauge section area of 0.68 mm^2. The layer rotation angle is visible for both B2 and B3 specimens, which is 90° and 67° respectively.

This section will discuss the geometry size scale effect on LPBF processed 316L SS microstructure. In Figure 3-16, comparison between two micro tensile specimens (See Figure 3-3 for dimension) from B2 and B3 are shown. Figure 3-16 (a) & (b) are the cross section smallest gauge area at low magnification. The initial comparison of these cross sections shows relatively rougher surface for B2 compared to B3 micro tensile specimen, which is likely due to the absence of the contour scanning during the manufacturing process in addition to the higher energy density. The etched surface of B2 and B3 specimen in Figure 3-16 shows the melt tracks with layer rotation angle, which are 90° and 67° respectively. The smallest cross section for B2 and B3 was measured from the microscopy images of XY and ZX plane and is found to be 0.68 mm^2 and 0.28 mm^2 respectively.

To further understand the effect of size of area on microstructure, a comparison within and across two micro tensile specimens from B2 and B3 in three different locations with corresponding cross section is represented. In Figure 3-17, the microstructure of B2 at different size areas within the micro tensile specimen is shown. As the cross-sectional area of the micro tensile specimen increases together with distance along the BD, the crystallographic orientation becomes stronger. In fact, the top grip section (farthest along BD) with an area of 20 mm^2 appears to have the strongest crystallographic orientation and all the specimens have <001> preferred crystallographic growth direction indicating epitaxial growth. Also, the equiaxed structured grains on the build plane get finer as the cross-section area increases from 0.68 to 20 mm^2. The grip area appears to have insignificant recrystallisation (less than 3%), while the 5 mm^2 gauge has the highest percentage of recrystallisation (See Figure 3-17).

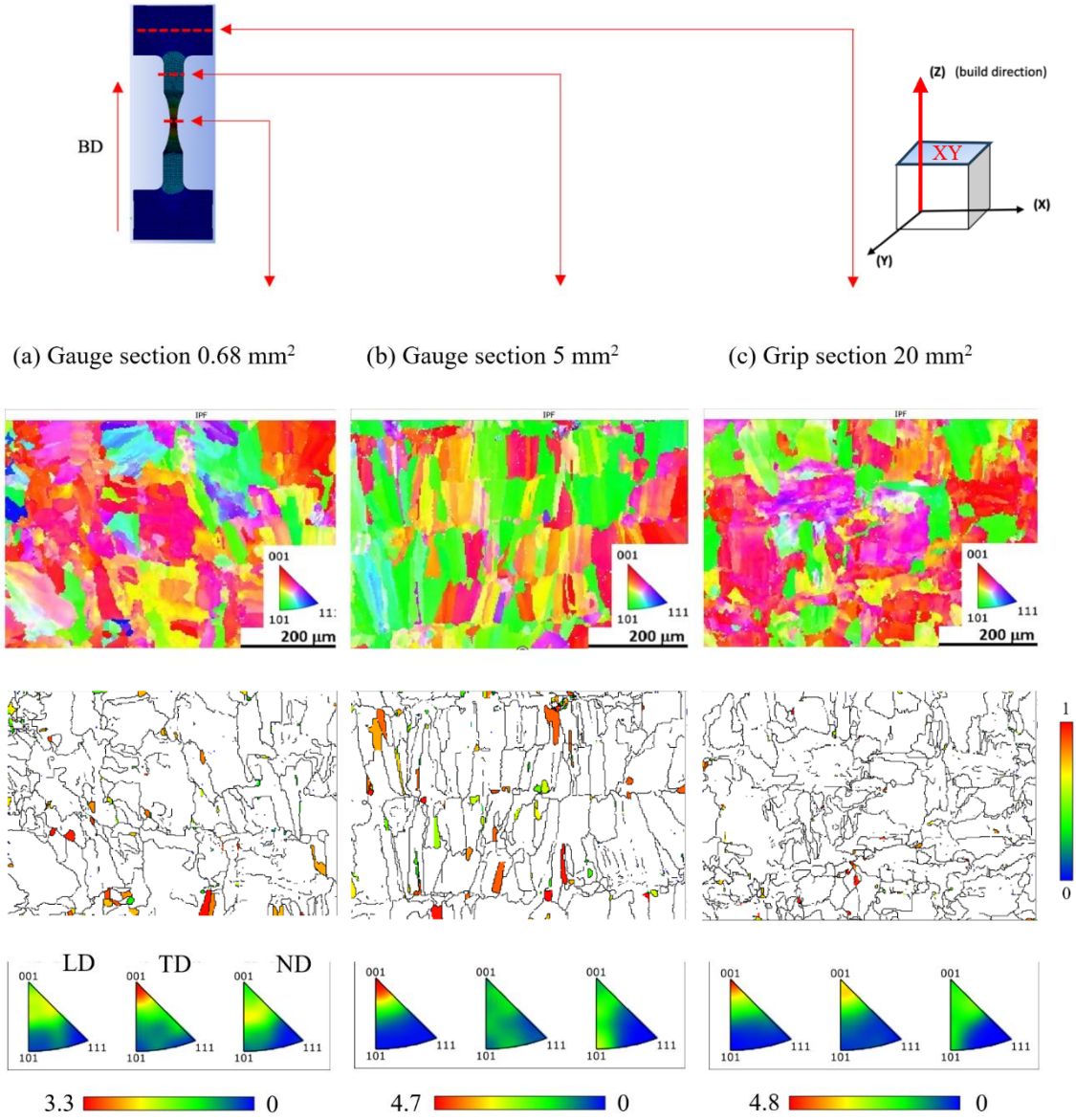

Figure 3-17: B2 micro tensile specimen IPF map (first row), HAGB distribution with recrystallised grains GOS <1° (second row) and IPF with MRD values (third row). Results shown on the XY plane for (a) 0.68 mm² gauge area [2.1% recrystallisation] (b) 5 mm² gauge area [4.09% recrystallisation] (c) 20 mm² grip area [0.33% recrystallisation] of the specimen.

A similar trend in terms of the preferred crystallographic orientation on ZX plane (columnar plane, parallel to the build direction) can be seen in Figure 3-18. As the area increases from 0.68 mm² to 20 mm², the MRD value gets larger. The weakest MRD value in the 0.68 mm² gauge section is associated with the highest percentage of recrystallisation, which is nearly 12.60 %. This suggests the necessity of further investigation to understand the recrystallisation mechanism within the micro tensile specimen.

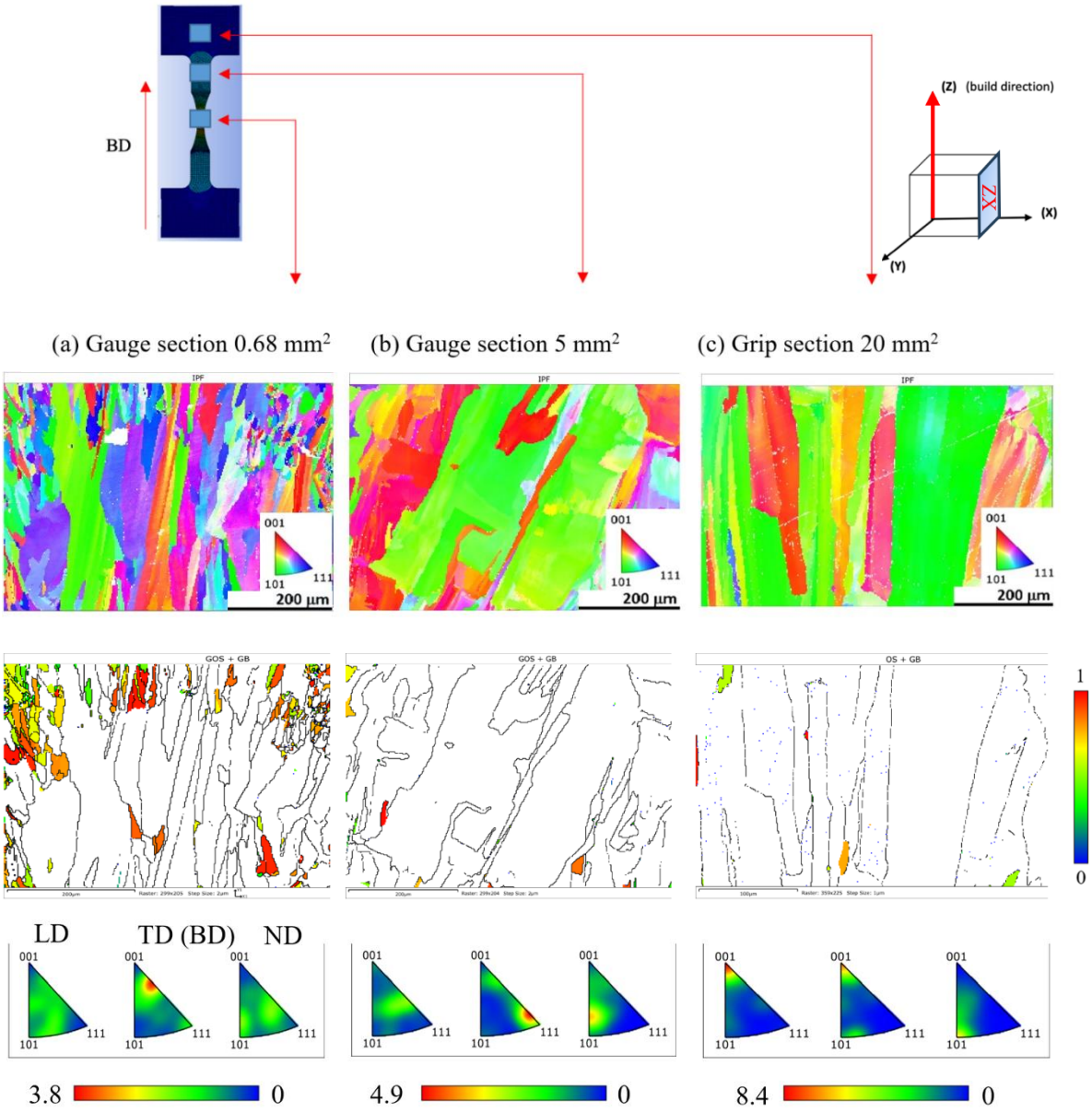

Figure 3-18: B2 micro tensile specimen IPF map (first row), HAGB distribution with recrystallised grains GOS <1° (second row) and IPF with MRD values (third row). Results shown on the ZX plane for (a) 0.68 mm² gauge area [12.60% recrystallisation] (b) 5 mm² gauge area [0.93% recrystallisation] (c) 20 mm² grip area [1.01% recrystallisation] of B2 of a micro tensile specimen.

Subsequent analysis on the average grain size and boundary distribution between different cross section and planes in Figure 3-19 reveals that the average grain size on the XY (build plane) decreases as the cross section area increases, while it does not follow same trend on the ZX plane, the smallest average grain size is on ZX plane is observed on the 0.68 mm² area and the 5 mm² has the highest average grain size. In the meanwhile, an increase in the HAGB fraction is observed as the area increases on ZX plane

but for XY plane, 5 mm^2 area has the lowest HAGB percentage. This is suggestive of a correlation between recrystallisation and grain boundary fraction.

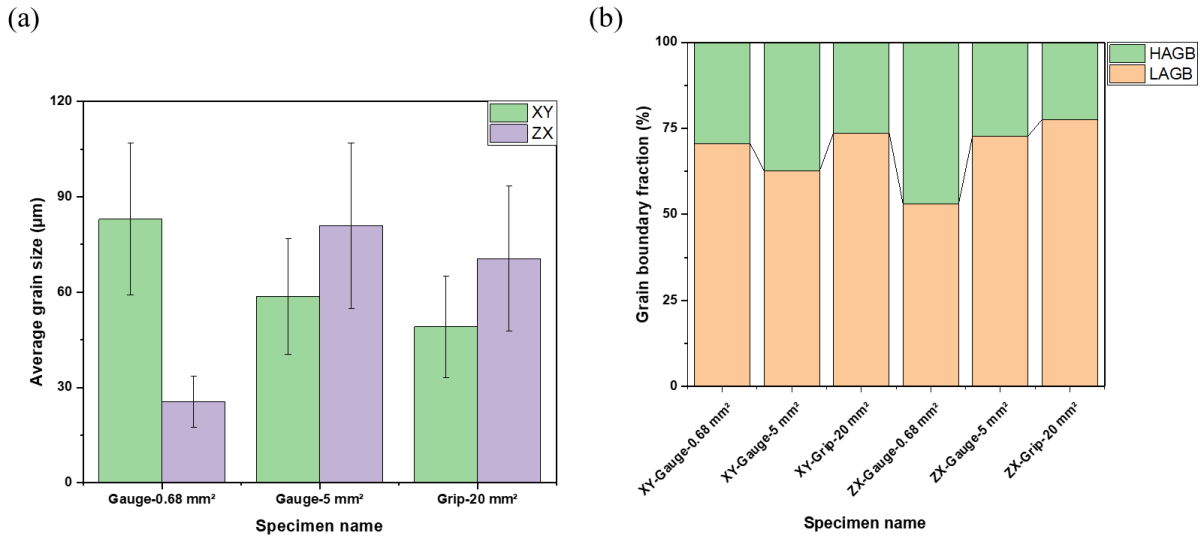

Figure 3-19: Quantitative representation of data from Figure 3-17 and Figure 3-18 to compare between (a) average grain size and; (b) low angle and high angle grain boundary distribution on XY and ZX plane (normal to BD) and ZX (parallel to BD) plane for different areas of B2 micro tensile specimen. Error bars bound one standard deviation.

A comparison between B2 and B3 microstructure will be done to investigate whether area size scale effect is independent of process parameters. For the comparison, microstructure from the cross section with similar area on the same locations (the area increases along with the distance from the build plate). The equiaxed structure on the XY build plane for B3 appears to have finer microstructure as the cross-section area increases which agrees with the finding for B2 micro tensile specimens. Regardless of the different scanning strategies, energy density and layer rotation, the average grain size follows a consistent trend due to a similar thermal cycle history. In contrast to B2 specimens, the percentage of recrystallisation for the intermediate 5 mm^2 cross-section on the XY build plane appears to be the lowest in Figure 3-20. However, the percentage of recrystallisation for the cross sections in all cases are relatively low at less than three percent and comparable to the recrystallisation observed in larger bend bars (up to 4%).

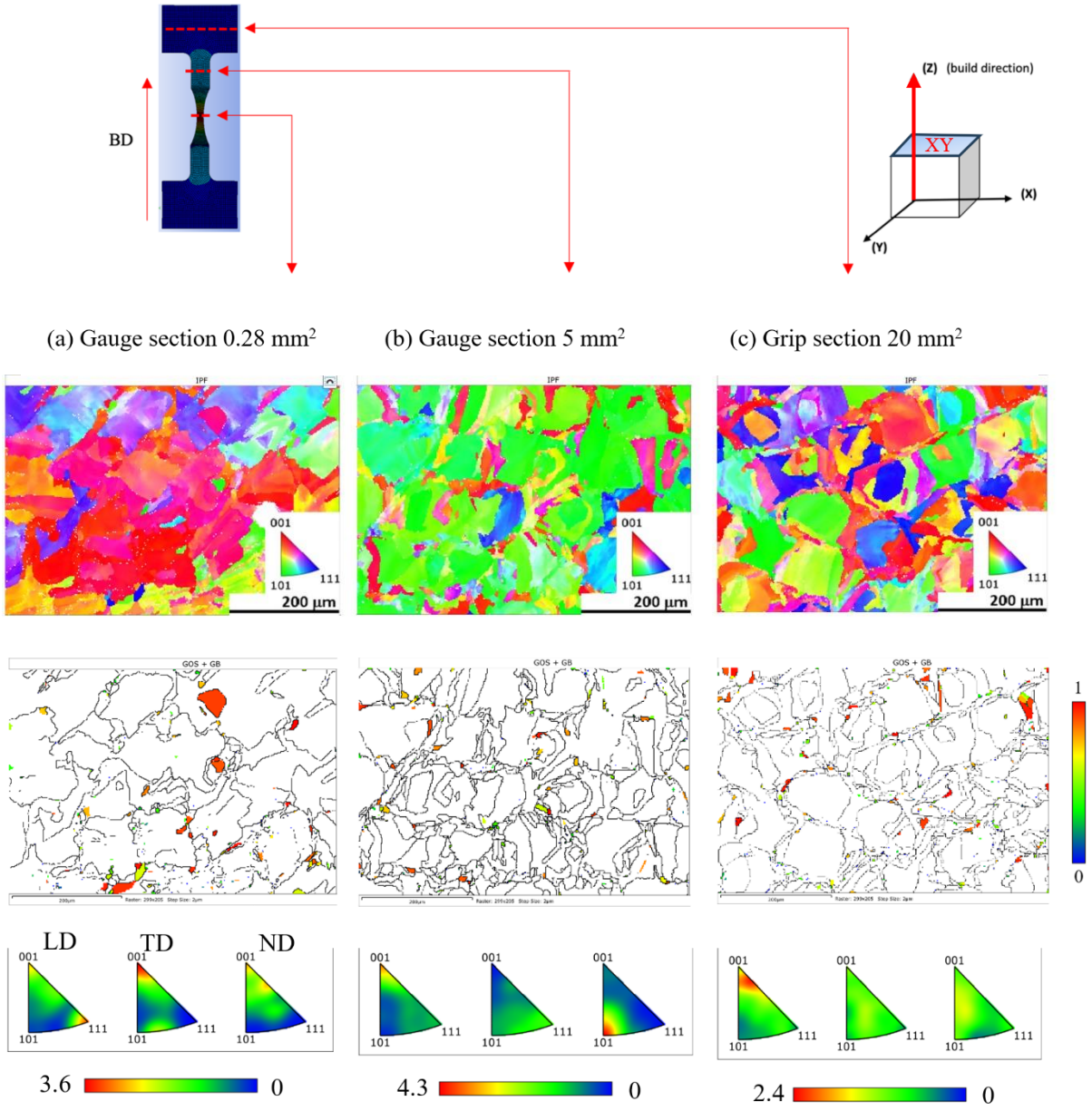

Figure 3-20: B3 micro tensile specimen IPF map (first row), HAGB distribution with recrystallised grains GOS <1° (second row) and IPF with MRD values (third row). Results shown on the ZX plane for (a) 0.28 mm² gauge area [2.75% recrystallisation] (b) 5 mm² gauge area [1.13% recrystallisation] (c) 20 mm² grip area [1.46% recrystallisation] of the specimen.

The columnar grains on the ZX plane in Figure 3-21 has relatively weaker crystallographic orientation compared to B2 specimen. A small decrease in grain size can be observed on the XY plane as the area decreases for B3, which is consistent with the finding for B2. However, significantly higher percentage of recrystallized grains can be observed in B3 specimen in the ZX plane for the smallest 0.28 mm² gauge section. The highest average size columnar grains are present in the intermediate 5 mm² gauge section and very low recrystallisation can be observed on the cross-section area other than the smallest

0.28 mm^2 gauge section. The average percentage of LAGB is higher for B3 compared to B2 micro tensile specimens according to Figure 3-22.

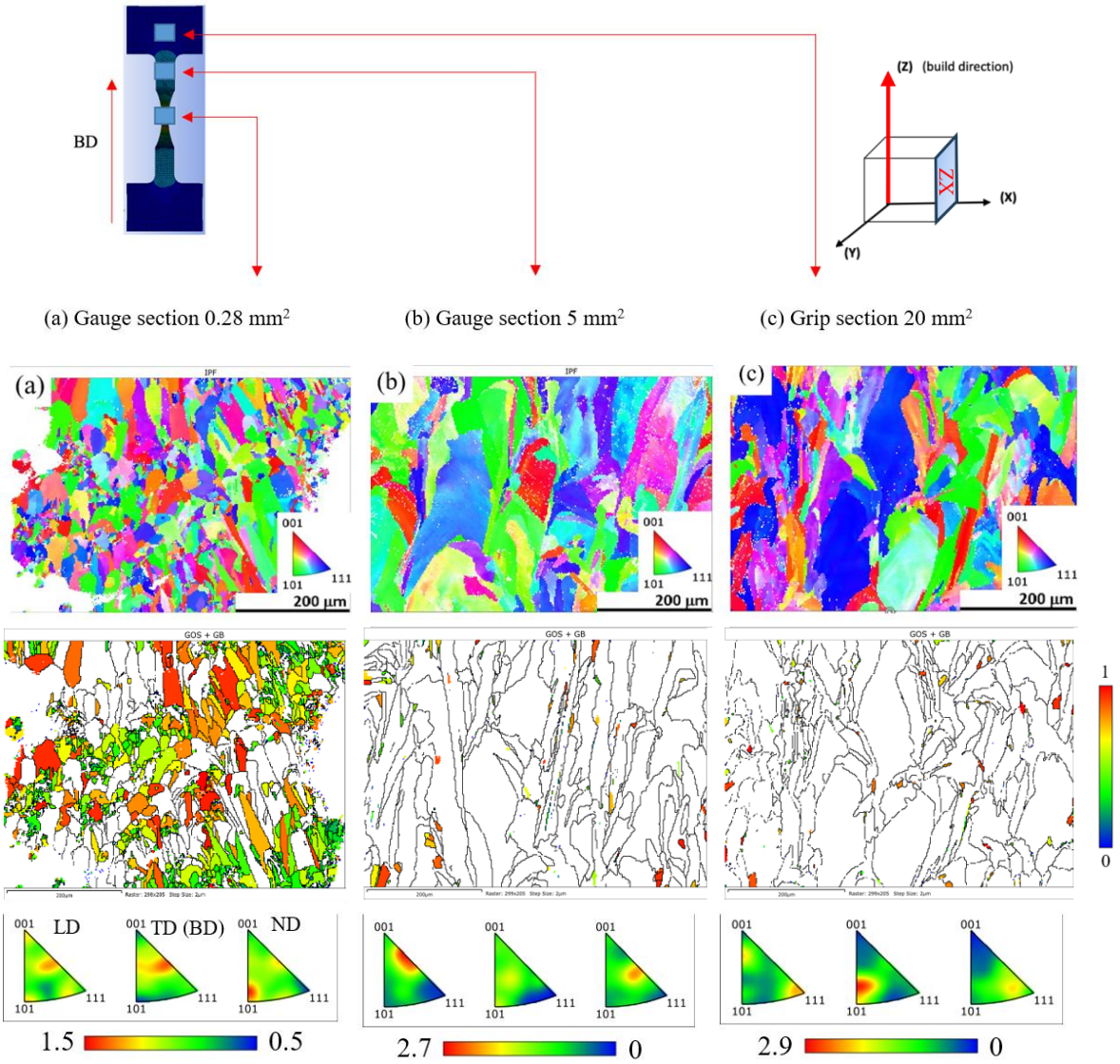

Figure 3-21: B3 micro tensile specimen IPF map (first row), HAGB distribution with recrystallised grains GOS <1° (second row) and IPF with MRD values (third row). Results shown on the ZX plane for (a) 0.28 mm^2 gauge area [47.5% recrystallisation] (b) 5 mm^2 gauge area [0.71% recrystallisation] (c) 20 mm^2 grip area [1.03% recrystallisation] of the specimen.

A consistent pattern is noticed in terms of average grain size for both B2 and B3 in Figure 3-23, which is due to similar heating/colling cycle. A link is suggestive at this point between grain boundary distribution, recrystallisation, and average grain size. The significant stronger texture in B2 can be due to high energy density as it is reported to have strong link to materials anisotropy for additive manufacturing process. [120]

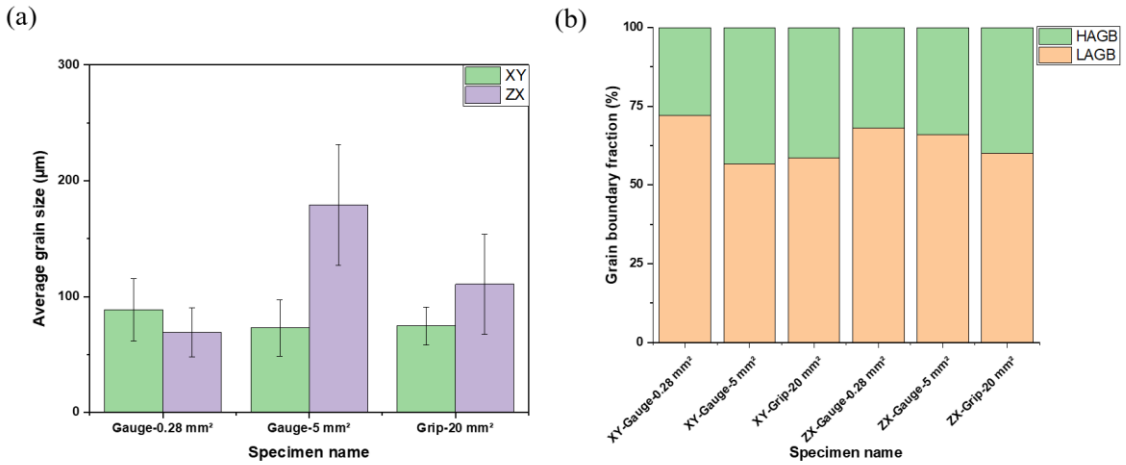

Figure 3-22: Quantitative representation of data from Figure 3-20 and Figure 3-21 to compare between (a) average grain size and; (b) LAGB and HAGB on XY plane (normal to BD) and ZX (parallel to BD) plane for different areas of B3 micro tensile specimen. Error bars bound one standard deviation.

For B2 micro tensile specimen, as the area decreases, heat flow path proportionally become restricted. This results an inversely proportional relationship between the area and average subcellular structure diameter, shown in Figure 3-23. As the area decreases, the heat accumulation increases leading to higher temperature resulting an increase in subcellular size, which agrees to the recent research [121], [122].

Theoretically, B3 specimen would follow similar trend. However, the minimum gauge section area for B3 is 0.28 mm^2, which is approximately one-third compared to B2 specimen, this creates a severely restricted heat transfer pathway, resulting a hotspot in 5 mm^2 gauge area. Due to the extreme temperature in 5 mm^2 gauge area, subcellular boundary starts to dissolve, shown in Figure 3-23 (e), and relatively larger grains are formed compared to the grip area (nearly fifty percent larger average grain size) shown in Figure 3-19(a) & Figure 3-22(a), the large grain formation mechanism was reported by Kong et al. [121].

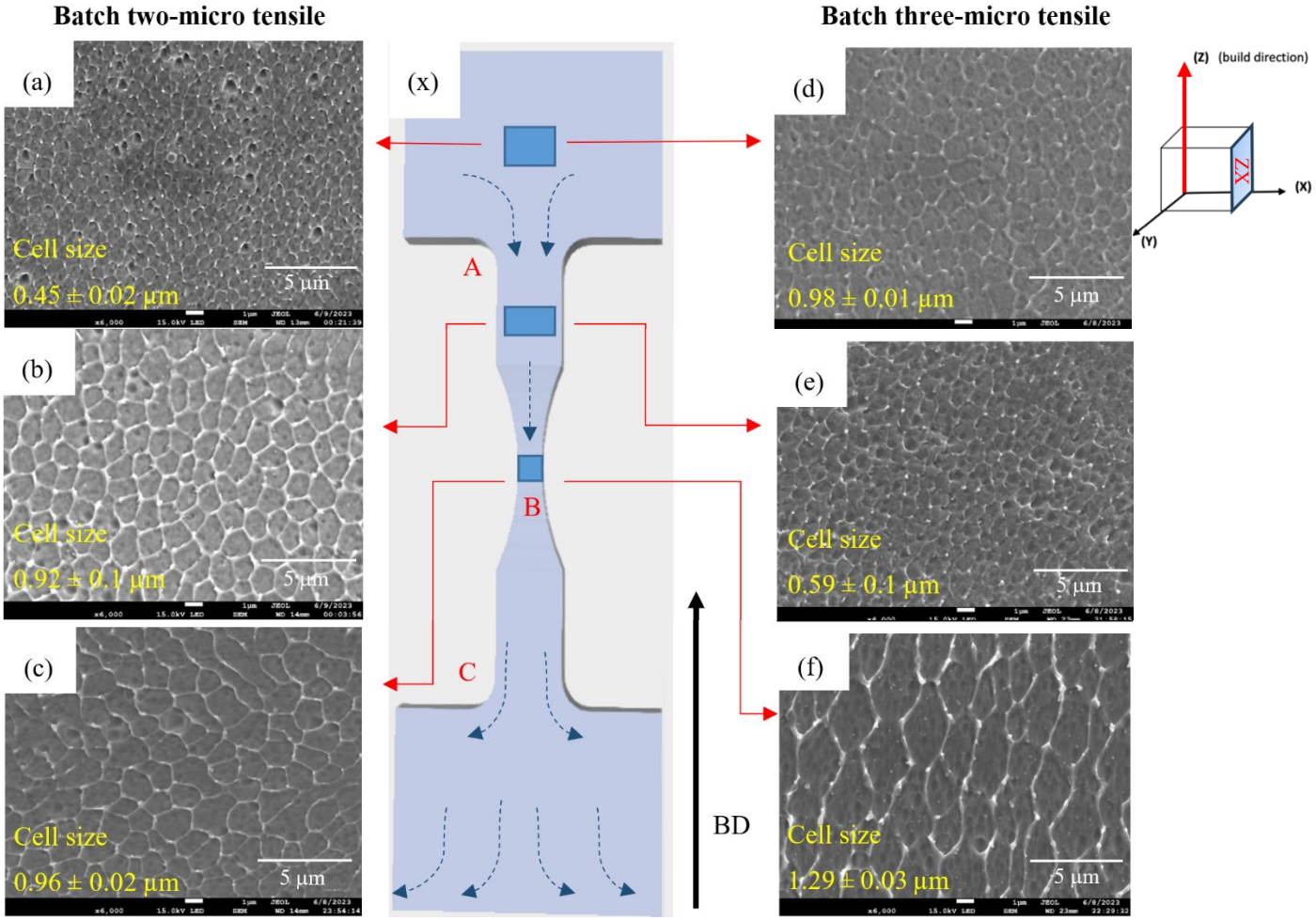

Figure 3-23: (x) Qualitative representation of heat flow path of the micro-tensile specimen during the LPBF process. Comparison between ZX plane of B2 (a) 0.68 mm^2 gauge (b) 5mm^2 gauge (c) 20mm^2 grip and B3 (d) 0.28 mm^2 gauge (e) 5mm^2 gauge (f) 20mm^2 grip.

Strong relation between percentage of total recrystallisation and average recrystallised grain can be seen in Figure 3-24 for the B2 and B3 micro tensile specimen, indicating grain growth stage. The average grain size is driven by growth of recrystallised grains. High recrystallisation compared to the bend, for intermediate 0.28 mm^2 gauge section in B3 micro tensile specimen is due to restricted heat flow leading to grain growth during the LPBF process.

Maximum intensity of preferred crystallographic orientation from pole figure increases as average grain size increases suggesting a strong link between them.

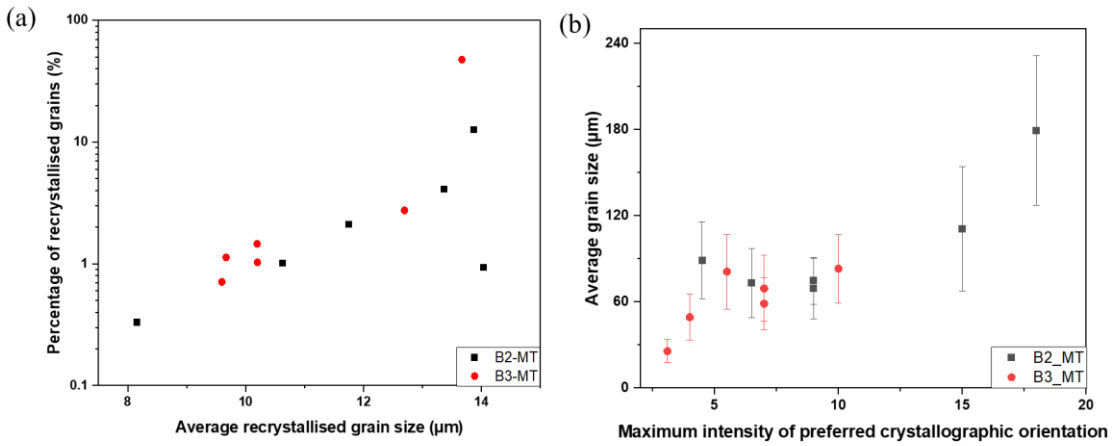

Figure 3-24: Average grain size on ZX plane as a function of (a) percentage fraction of recrystallised grain and (b) highest MUD value indicating preferred crystallographic orientation.

In Figure 3-25, the relationship between hardness; LAGB, average grain size and recrystallisation has been investigated. The data points are independent to the build direction. In Figure 3-25, the BB and MT stands for data extracted from bend bar and micro tensile specimen respectively. A strong link between the hardness; LAGB and average grain size (on ZX plane) can be observed. A consistent increase in hardness is apparent as average grain size reduces. In the next chapter, the stress-strain behaviour under three-point bending would be investigated and the effect of materials and mechanical properties on high cycle fatigue would be discussed at length. Due to the consistency of the analysis, a fixed cross-sectional area was considered to compare microstructure between batches. However, the average grain size variation between batches and even within same specimen (micro tensile) affects the number of grains averaged for the measurement. For instance, B2 bend bar top section has nearly 300-micron average grain size, which is nearly five times of the average grain size of B1 bend bar specimen. While average grain size comparison can be insightful, but the technique certainly has its limitation.

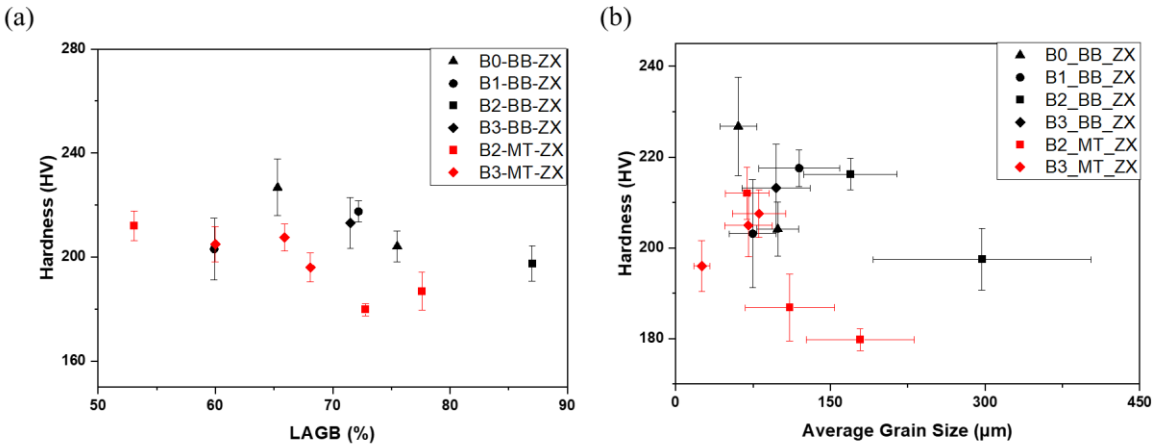

Figure 3-25: The comparison between Z built bend bar and micro tensile specimen is shown BB and MT are bend bard and micro tensile respectively. Only the ZX plane has been considered. The relationships between LAGB vs (a) yield strength & ultimate tensile strength (b) Vickers hardness; and (c) average grain size vs Vickers hardness. The Vickers hardness was averaged from five data points and measured from a straight single line on the plane parallel to the build direction.

3.5 Summary and conclusion

Stainless steel specimens were processed using LBPF with different geometries (bend bars or microtensile), orientations (X, Z, Y), energy densities, and scan strategies, and the resulting microstructures were assessed. The average grain size on the XY plane remains consistent across all specimens, while the columnar grain in the ZX plane for the Z built exhibits a significantly larger size. This phenomenon is attributed to the concentrated laser heat input into smaller areas of each layer and slower conductive cooling into the layers below due to the extended heat path. Furthermore, the Z built specimen manifests a robust crystallographic texture in the <101> direction, attributed to prolonged heat exposure. Both these properties, the larger columnar grains, and the crystallographic texture, resulted from heat accumulation due to the extended heat path. Subsequently, the average grain size has also been found to be inversely proportional to material strength and directly proportional to grain size dispersion.

A general observation suggests that Z built specimens exhibit significantly stronger crystallographic texture and lower percentage of recrystallization, regardless of XY and ZX planes, when compared with X and Y built specimens. These microstructural differences, correlated with lower strength and ductility of Z built specimens loaded in tension along the build direction (compared with XY specimens loaded in tension perpendicular to the build direction), which may be attributed to anisotropy parallel to the build direction. Hardness testing on XY and ZX planes for X and Z built specimens for both B0 and B1 further confirmed this anisotropy. Subsequently, the Z built specimen from B3 demonstrates high strength and ductility, properties likely attributable to the additional contour scanning, which distinguishes it from the remaining Z built specimens. Another factor affecting mechanical properties could be different porosities in the XY and Z built specimens. Porosity is known to reduce ductility and may explain why Z built specimens exhibit lower strength and ductility, contrary to the expected correlation between these two properties (i.e., higher strength usually decreases ductility). Looking ahead to results from the next chapter, the average porosity of B1-Z built specimens is nearly 1%, and pores are significantly higher in number when compared to X and Y built specimens with porosity of 0.23% and 0.43%, respectively.

Micro tensile specimens consistently exhibit a decrease in average grain size on the XY plane as the cross-sectional area increases. For the ZX plane, the average grain size is highest for the intermediate

gauge section (5 mm^2). This consistent trend is observed in both B2 and B3 micro tensile specimens, with the trend being most prominent in the B2 specimen due to high heat input. The restricted heat flow in the intermediate gauge section (5 mm^2) creates a hotspot, evident from the subcellular boundary dissolution. This restricted heat flow in the hotspot caused large grain formation during the LPBF process in the intermediate gauge section. Subsequently, the complex thermal conditions within the specimen affected microstructure characteristics, initiating recrystallization-driven grain growth processes.

These results contribute to the understanding of how decisions about LPBF laser parameters, orientation, and specimen geometry interact to produce varied microstructures and properties. Generally, higher strength and ductility result from orientations with larger layer areas and low energy density, while restricted heat flow can affect the recrystallization process and thus weaken material strength.

The stress-strain behaviour under three-point bending and the effect of microstructure and mechanical properties on high cycle fatigue will be discussed in the Chapter 4.

Chapter 4 Short crack testing of bend bar specimens

4.1 Methodology

4.1.1 Machine and materials

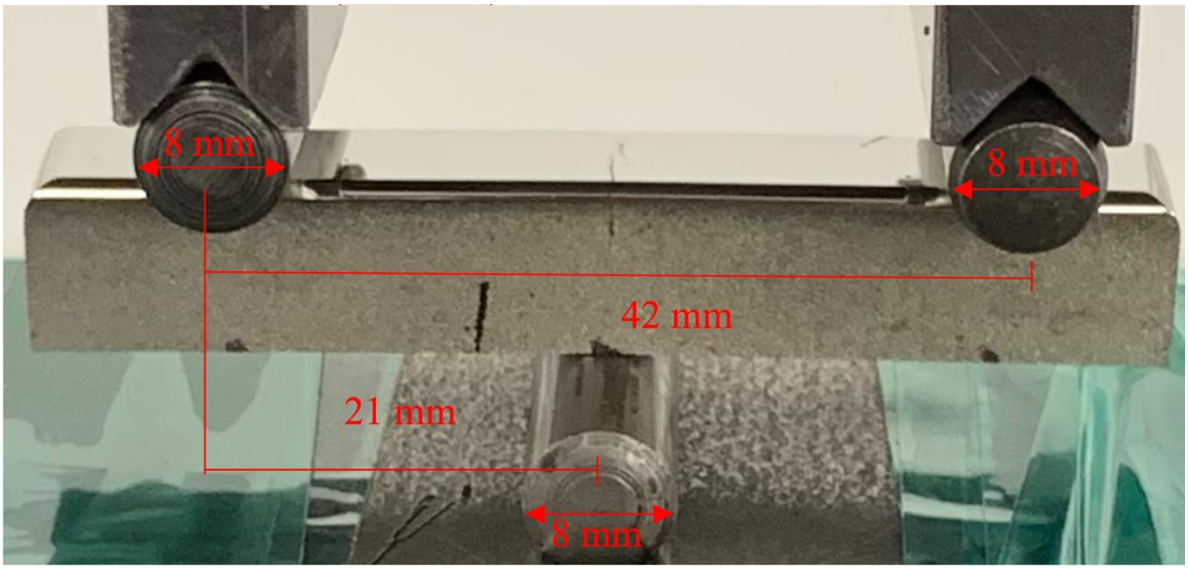

Figure 4-1: Three-point bending test setup in a servo-hydraulic Instron 2 machine tested at 10 Hz frequency with R = 0.1.

A high cycle fatigue test (HCF) was conducted with a three-point bending test set up on an Instron servo-hydraulic machine on plain bend bars (see Figure 4-1). These bend bars were polished on the top surface, and their average roughness value was measured using a profilometer. This was to ensure the underlying microstructure response to fatigue loading was established without considering surface roughness effects initially. Three contact rollers were used to apply three-point bend loading with the distance between the two edge rollers set as 42 mm. All three rollers were 8 mm in diameter. The detail of the experimental setup can be seen in Figure 4-1. The experiment was conducted at 10 Hz frequency with a stress ratio of R = 0.1. In total, thirteen tests were conducted for batch one, five of which were uninterrupted tests. The test matrix is given in Table 4-1. The stress at the middle of the beam was determined using Bernoulli's beam theory. The relationship between force and stress is as follows.

$$F = \frac{2\sigma_x bd^2}{3L} \qquad \text{Equation 4-1}$$

In this equation, σ_x is the maximum stress in the middle of the beam; F is the applied force at the middle; b and d are the beam's width and depth. L is the distance between the outer rollers.

For the rest of the experiments, the crack initiation and propagation were monitored at regular intervals using a non-destructive surface replication technique with silicone RepliSet-F5 from Struers-Ltd. Surface cracks were observed with Olympus BX-51 optical microscopy, and the projected length normal to the applied tensile axis was measured with ImageJ in the Fiji package. The crack growth rate and stress intensity factor ΔK was measured from half surface crack length under the assumption of linear elastic loading conditions. Scott and Thorpe's model [123] was used for ΔK calculations for a semi-elliptical crack. The half surface length to crack depth ratio (a/c) was assumed to be 1 in this case. In the case of edge/corner crack, the model from Newman and Raju [37] was used.

4.1.2 Porosity measurement

4.1.2.1 Total area fraction with an Imaging technique

ImageJ in the Fiji software package was used for surface porosity analysis. Firstly, the image was converted to 8-bit. Then, a scale was set from the reference micron bar, which was obtained from a microscope calibration with a stage micrometre. The "Adaptive Threshold" plugin was used to locate pores and their boundaries. Generally, every image requires manual adjustment of the threshold value. However, the "Adaptive Threshold" plugin can automatically conduct image segmentation with a single step. A comparison between thresholding technique is shown in Figure 4-2. Area fraction of the pores obtained from analysing particle function in ImageJ was used to calculate the percentage of porosity on the surface. An area of 3.5x8.4 mm^2 was used for the measurement of the percentage of porosity during most of the image analysis.

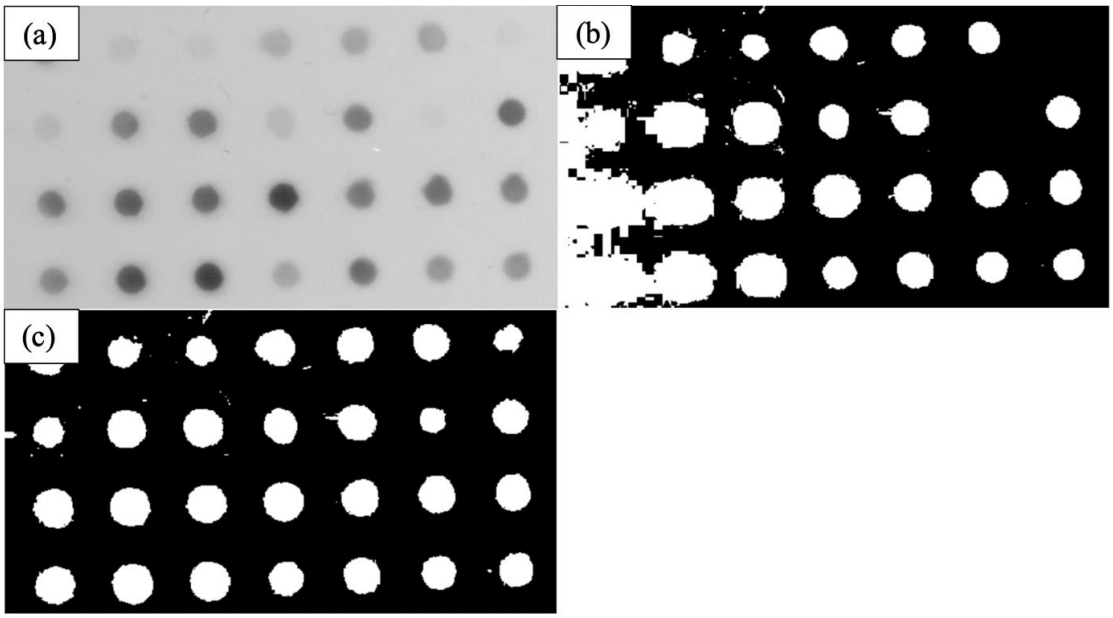

Figure 4-2:(a) 8-bit image before processing (b) image segmentation with a default threshold value (c) single-step image segmentation with "Adaptive Threshold" plugin [124]

4.1.2.2 Total percentage with Archimedes principles

The specimen density was measured using the Archimedes principle, following the ASTM B962-2017 standard. The following equation was used to calculate the density of the specimen [125].

$$\rho_p = (\rho_{fl} - \rho_{air}).\frac{m_a}{m_a - m_{fl}} + \rho_{air} \qquad \text{Equation 4-2}$$

In this equation, ρ_p, ρ_{air} and ρ_{fl} are the specimen density, density of fluid and density of air respectively at room temperature; $m_a$and m_{fl} are specimen mass in air and fluid, respectively. The specimen mass in the fluid was measured by completely submerging a specimen within the fluid with a bracket, as shown in Figure 4-3. The specimen was submerged in the fluid without touching the beaker, and the added mass to the liquid was measured with an analytical mass balance, which can measure accurately up to 0.001g. Initially, water was used as the fluid for the experiment, but there was significant bubble formation which caused an error in the measurements. This was solved by using acetone instead of water.

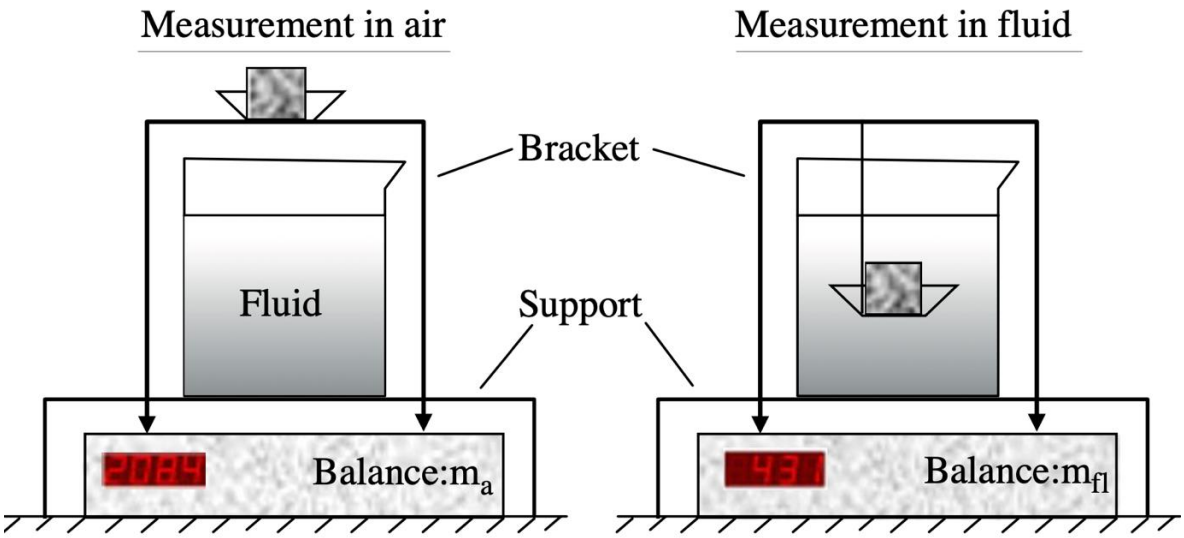

Figure 4-3: Experimental setup to measure the density of specimen using Archimedes principle [125].

4.1.2.3 Nearest neighbour proximity

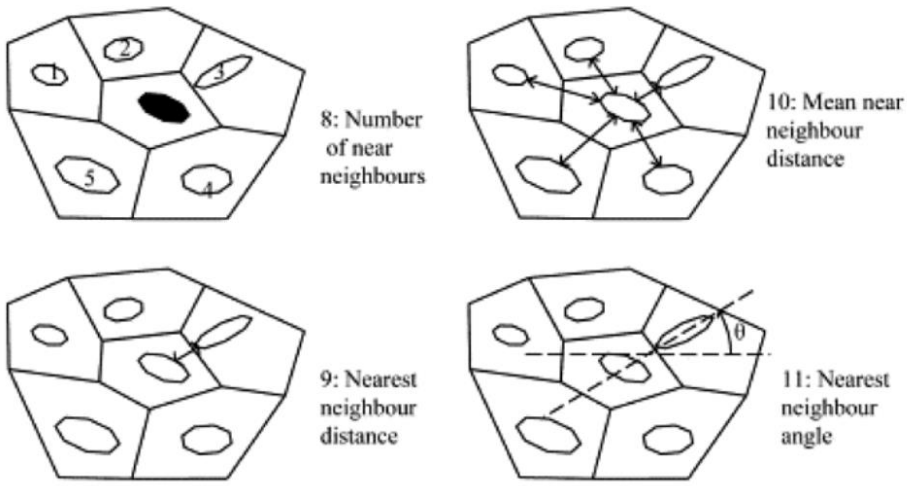

Figure 4-4: Tessellation measurement definition for nearest neighbour proximity [126].

The statistical distribution of porosity on specimen surface can be quantified with the finite body tessellation technique. The nearest neighbour distance in this study was measured with the aid of the NND (nearest neighbour distance calculation) plugin of ImageJ software. This plugin can measure the distance between the centroids of two neighbouring particles. Further study has been conducted in the later section to also measure the number of nearest neighbours, mean neighbour distance and nearest neighbour angle.

4.1.2.3.1 Equivalent stress intensity factor for pores

From the point of view of fatigue, Murakami [127] has shown that defects like pores are comparable to cracks with a similar stress intensity factor. The maximum stress intensity factor (K_{max}) produced by a porosity is calculated by the following equations.

$$K_{max} = 0.5\sigma_{\infty}\sqrt{\pi\sqrt{A_n}} \qquad \text{Equation 4-3}$$

$$K_{max} = 0.65\sigma_{\infty}\sqrt{\pi\sqrt{A_n}} \qquad \text{Equation 4-4}$$

Equation 4-3 and Equation 4-4 can be used to calculate the equivalent stress intensity factor for subsurface and surface pores, respectively. Where σ_{∞} and A_n are the global stress applied and the pore area normal to the stress applied, respectively. According to Murakami's study, when a defect is at a surface, the constant '0.5' in Equation 4-3 increases to '0.65' to represent the higher stress resulting from surface cracks.

4.2 Results and discussion

4.2.1 Introduction

The fatigue behaviour of metallic materials can be analysed mainly with two approaches, namely total lifing and damage tolerant approaches as mentioned in the earlier section. Much research has been conducted to understand crack initiation and propagation mechanisms for conventionally manufactured metallic materials using these approaches [128]. Recent advancement in additive LPBF process has brought its own sets of challenges affecting fatigue behaviour. For instance, previous research has established the effect of process induced surface roughness on fatigue life, which is a major drawback of LPBF processed parts. In addition to that, surface and subsurface defects and porosities are also likely to play a role in fatigue crack initiation and propagation behaviour. Understanding the link between total percentage of porosity, the pore distribution and clustering on fatigue behaviour will be beneficial. Moreover, microstructure inhomogeneity due to complex thermal heating/cooling cycle and size scale effects adds further to the uncertainty in what will affect the fatigue crack initiation and propagation mechanism. Previous research has been conducted to understand the effect of LPBF processing parameters on microstructure and mechanical properties, however limited research has been found till date to encompass all the interwoven aspects including processing parameters, microstructure, mechanical properties, and statistical distribution of porosity on fatigue behaviour of LPBF processed 316L stainless steel. To investigate the fatigue behaviour under different stress levels and to assess the influence of crack initiation, propagation and coalescence events on the overall fatigue lifetime, the test matrix in Table 4-1 has been devised.

Table 4-1: The three-point bending fatigue test matrix.

Batch	Type of test	Build direction	Number of samples	Nominal stress, MPa
One	Uninterrupted test	X built	1	576 MPa
		Y built	1	576 MPa
		Z built	1	576 MPa
	Interrupted replica test	X built	1	576 MPa
		X built	1	648 MPa
		Y built	1	576 MPa

		Y built	1	648 MPa
		Z built	2	648 MPa
Two	Interrupted replica test	Z built	1	576 MPa
		Z built	1	648 MPa
	Uninterrupted test	Z built	1	760 MPa
		Z built	1	840 MPa

The batch one specimens were tested to understand the influence of build direction on crack initiation and propagation behaviour under same stress states. Since Z built specimens contain a significantly higher percentage of total number of pores, they were tested to understand the effect of the distribution of porosity on the fatigue behaviour. On the other hand, batch two specimens with inferior mechanical properties compared to their batch one counterpart were also tested to investigate the influence of yield strength on fatigue crack initiation behaviour. All bend bar specimens underwent polishing until no cracks were visible under a microscope at 100x magnification, focusing solely on the top surface, following the method outlined in the section 3.3.1. Subsequently, the 2D surface roughness profile was measured using the Taylor-Hobson Talysurf 120L contact profilometer, revealing R_a values of less than 0.06 microns for all specimens. This level of surface finish can be deemed sufficiently polished for fatigue crack testing.

4.2.1.1 Fatigue lifetime data analysis

The fatigue tests in Table 4-1 were conducted on a three-point bending setup under force control. Two nominal stress levels were considered for the fatigue test experiments, which are 576 and 648 MPa. These nominal stresses were calculated using Euler-Bernoulli's beam theory. Initially, the stress strain behaviour due to the bending for batch one and two specimens had been measured by putting a strain gauge on the tensile surface, shown in Figure 4-5. Afterwards, five uninterrupted fatigue tests were conducted on batch one and two specimens to record their estimated fatigue life under cyclic loading for two stress levels. The remaining eight specimens were cyclically loaded with interrupted tests. The first replica record was collected around fifteen percent of the total life of the specimen. The replica records were collected with every five percent increment of total life until nearly eighty percent of the total life. Afterwards, replica records were taken more frequently to monitor crack growth and coalescence behaviour in as much detail as possible.

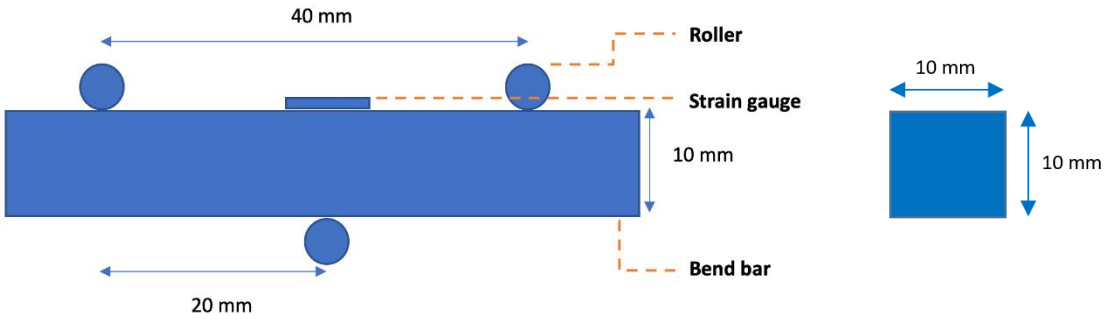

Figure 4-5: Three-point bending fatigue test setup at load ratio R=0.1. Contact rollers have been used to apply the force. The strain gauge at the top of the tensile side to measure the deformation due to applied force.

The stress-strain behaviour from the tests on both batch one and two specimens is represented in Figure 4-6 (a). All specimens showed cyclic hardening behaviour with X built batch one specimen having the highest yield strength (YS) and Z built batch two with the lowest YS. In addition to that, batch two specimens were observed to have experienced higher plastic deformation compared to its counterparts in batch one under similar stress state. The initial stress-strain behaviour of Z built specimens for both batches appear to be comparable, which agrees with the mechanical property information obtained from the tensile test data shown in Figure 3-12(b). However, a major difference between the hardening behaviour of batch one and two specimens is apparent in Figure 4-6 (a). Batch one Z built specimen experiences a more pronounced increase in YS over repeated loading cycles compared to Z built batch two, which implies batch one exhibits a higher degree of cyclic hardening than batch two. This suggests that the batch one bend bars with higher cyclic hardening are likely to exhibit improved resistance to plastic deformation and fatigue, making it potentially more suitable for applications involving cyclic loading or stress. The fatigue behaviour of all specimens regardless of their processing parameters can be explained in terms of maximum strain experienced on the tensile surface. Bending, when compared to uniaxial tension, proves more detrimental to fatigue lifetime due to the higher stress concentration at the middle of the bend bar, in contrast to the uniformly distributed stress in the uniaxial case. To further confirm the hypothesis, the bend bars were cyclically loaded and the total cycle to failure is then plotted against the maximum strain in Figure 4-6 (b). The fatigue tests were load controlled and conducted at 10 Hz frequency with R=0.1. Even though a strong link between maximum strain and fatigue life could be seen in Figure 4-6 (b), three specimen's life data indicated by the red arrows outperformed the estimated lifetime predicted by the strain life (ε-N) curve. These specimens are all Z built and detailed investigation is reported in section 4.2.4 and 4.2.5 to qualitatively analyse the fatigue crack growth behaviour of these specimens. The complex nature of crack initiation, their interactions and resulting effect on overall fatigue response need to be investigated further to fully understand the fatigue behaviour.

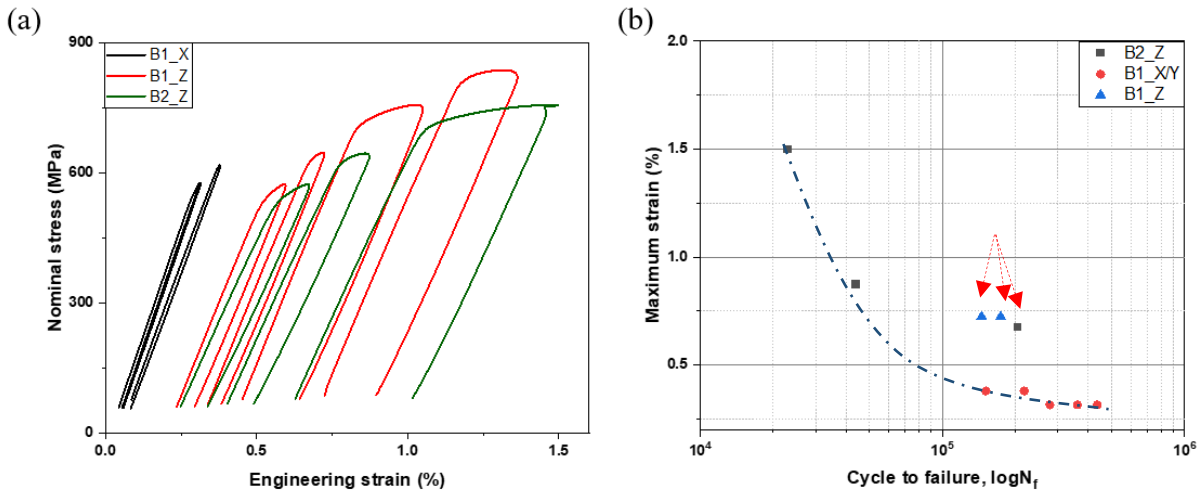

Figure 4-6: (a) A comparison of bending stress-strain behaviour between specimens under different stress conditions (b) Maximum strain against total cycle to failure, red arrows the fatigue lifetime of specimens which do not follow the trendline.

4.2.1.2 Comparison of porosity distribution within batch one bend bar specimens

The statistical comparison of porosity in Figure 4-7(c) reveals, X3 and Z2 specimens exhibits the lowest and highest percentage of porosity. This porosity area fraction was measured using a surface porosity imaging technique, as fatigue is predominantly a surface-initiating phenomenon. The use of a contact profilometer revealed that average specimen roughness values are consistently less than 0.1 microns after polishing and no cracks were observed to initiate from scratches from the fatigue initiation stage on these polished samples. This indicates that surface roughness is not a variable requiring consideration in this particular fatigue lifetime study.

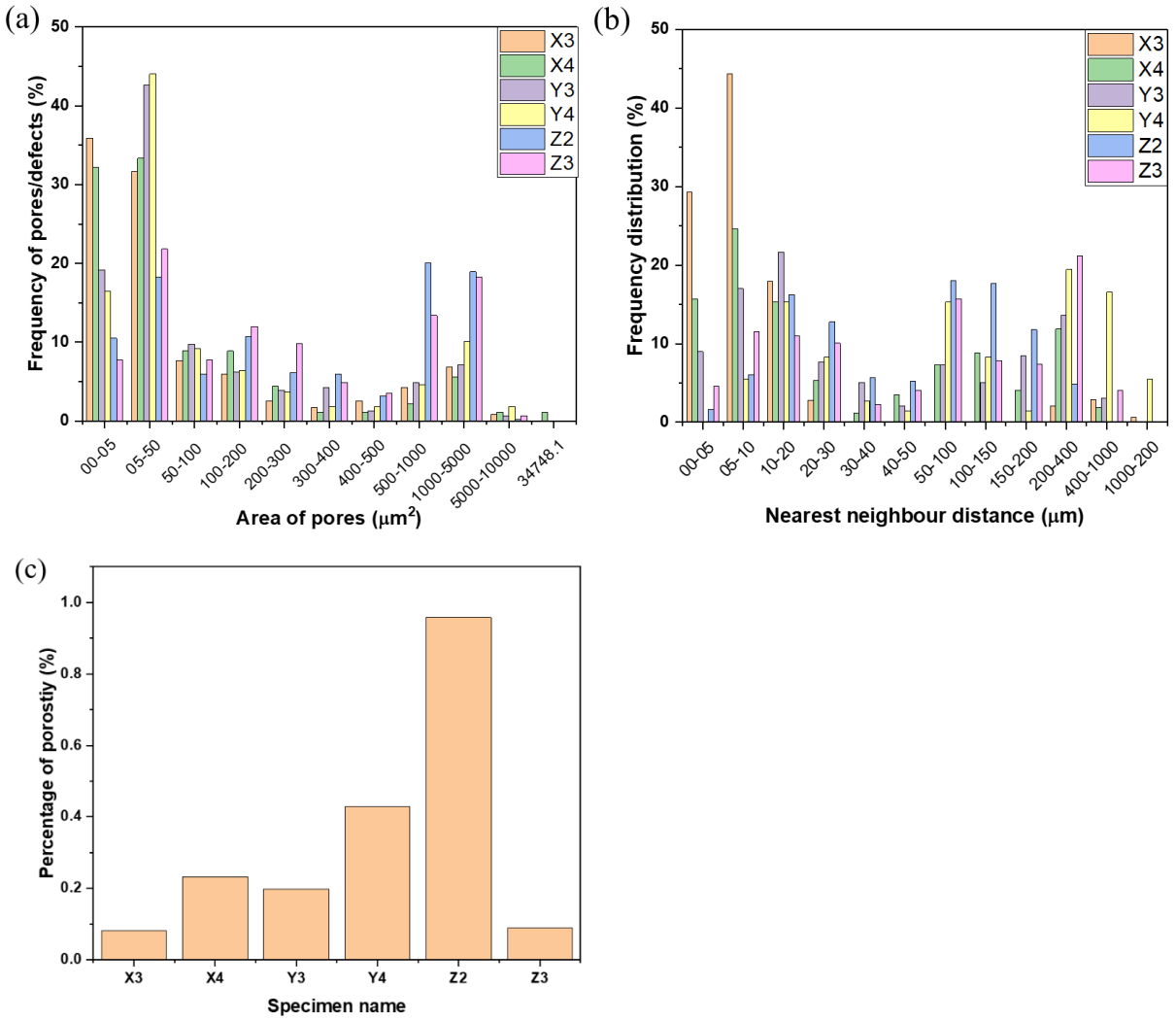

Figure 4-7: (a) Porosity/defects distribution (b) Neighbour distance proximity of pores on the top (tensile) surface of bend bar specimens (c) total percentage of porosity on tensile surface for batch one specimens.

Figure 4-7 (a) showcases a histogram detailing the distribution of pores/defects in terms of their observed area on the top (tensile) surface of the bend bar specimens. Most pores/defects are below 100

μm^2 in size, except for those observed in the Z2 specimen, which has a noticeably larger size distribution. Z2 specimens exhibit a significantly higher number of larger pores/defects in the range of 500-1000 μm^2 and 1000-5000 μm^2 and above (comprising nearly 30% of the total). Additionally, Z2 specimens contains the highest total number of defects compared to all other specimens. Interestingly, despite the X4 specimen having the lowest number of defects, it exhibits a similar fatigue lifetime under the stress levels as the Z2 specimen. Figure 4-7 (a) highlights the presence of the largest single defect on the X4 specimen, with an area of 34,748 μm^2. The proximity of pores to their nearest neighbours is illustrated in Figure 4-7 (b), providing insights into the clustering of surface pores. While X3 exhibits the highest percentage of pores with neighbouring distances ranging from 5-10 μm, it possesses the lowest area percentage of pores (see Figure 4-7 (c)) compared to all other specimens. In contrast, Z2 specimens feature the highest number of pores, with nearly half having neighbouring distances smaller than 50 μm.

It's worth noting that the polished surface of the bend bar specimens reveals an uneven distribution of porosity on the sides, suggesting a clear link between the percentage of porosity and the specimen's build direction. Further investigation is imperative for a comprehensive assessment of the factors governing the fatigue lifetime of these bend bar specimens.

4.2.2 Comparison between horizontally built specimen tested at lower maximum stress state (576 MPa)

This section evaluates the crack initiation, propagation, and coalescence behaviour in two horizontally built specimens from batch one, tested under the same stress levels. A detailed analysis is conducted to understand the factors dominating the fatigue lives of X3 and Y3 bend bar specimens.

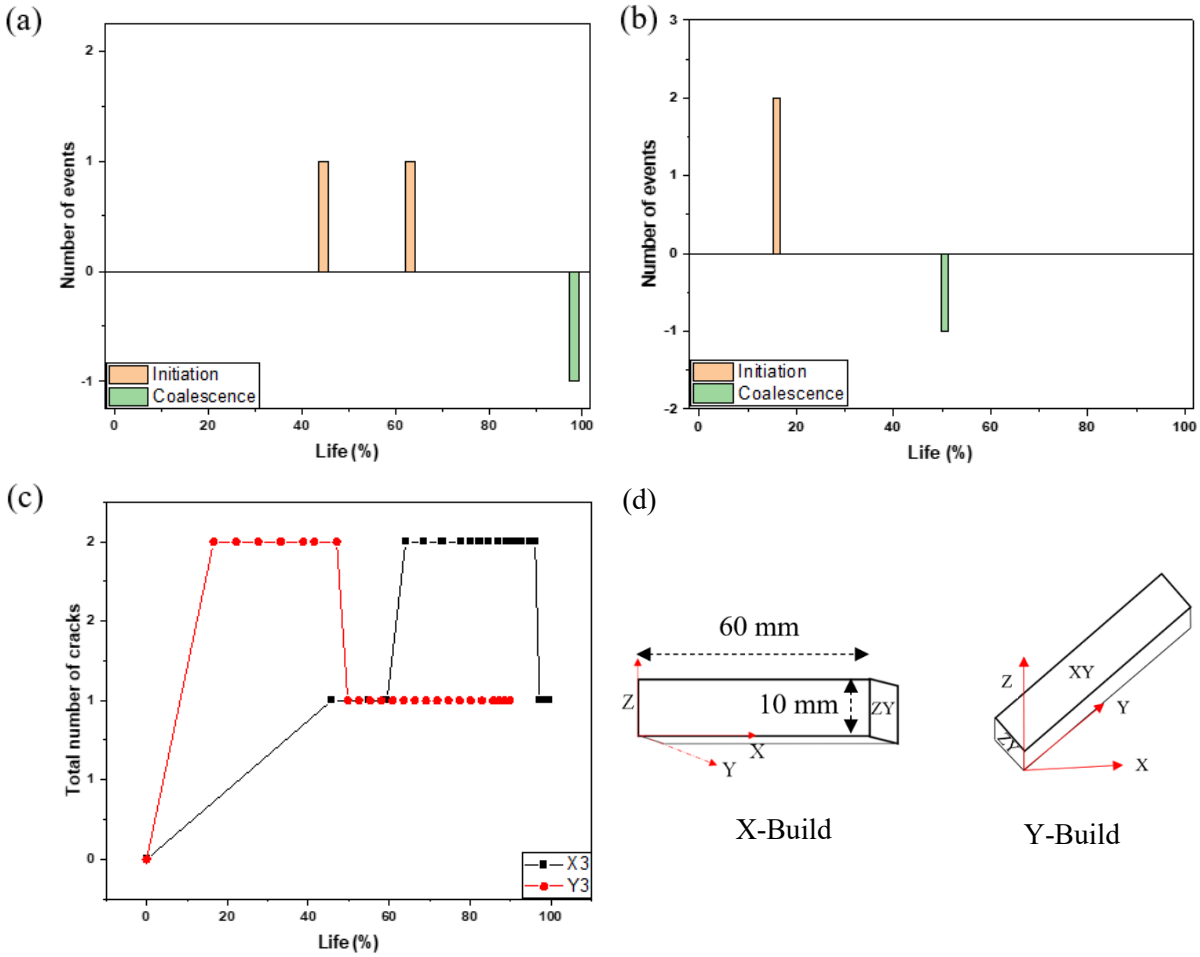

Figure 4-8: Crack initiation and coalescence events over the lifetime of batch one horizontally built specimens tested at 576 MPa maximum stress, R=0.1 for (a) X3 (b) Y3 specimen (c) comparison between total number of cracks throughout the lifetime of X3 and Y3 specimen.(d) X (left) and Y (right) build specimen, where the tensile axis is XY for both of them.

In Figure 4-8, a comparison between crack initiation and coalescence events is presented for the X3 and Y3 specimen which are horizontal 0-degree (X) and horizontal 90-degree (Y) built samples respectively (as shown in Figure 4-8 (d)). The key observations from the test results and replica record can be summarised as following.

1. The X3 and Y3 specimens failed at 436k and 361k cycle respectively.

2. Although tested under the same stress levels, two simultaneous cracks initiated in Y3 at around 17% life, whereas no initiation was observed in X3 specimen until nearly half of its lifetime.
3. Cracks in the X3 specimen did not coalesce until the final failure stage, whereas the Y3 specimen exhibited crack coalescence at around half its lifetime.
4. Fatigue life was dominated by early initiation and coalescence events resulting in a shorter fatigue life for the Y3 specimen.

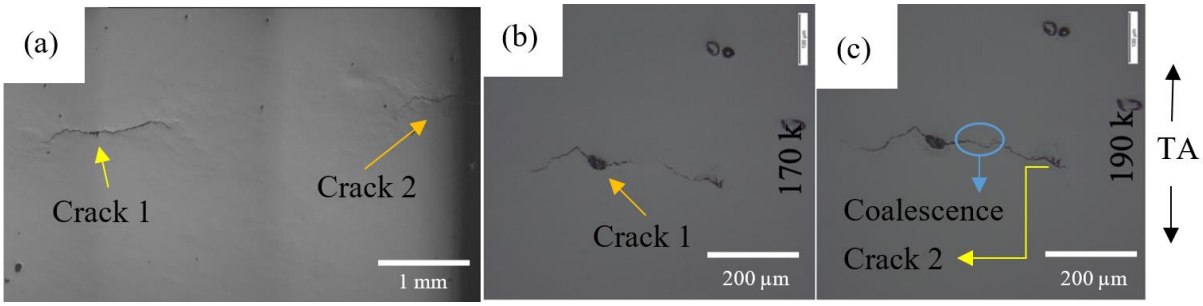

Figure 4-9: Early stages of crack initiation in (a) X3 at 390k cycles, (b) Y3 at 170k cycles and (c)crack coalescence at 190k cycles. Yellow and darker yellow arrows indicate a crack initiated due to pore/defect and slip band respectively. Blue and black arrows indicate coalescence and tensile axis (TA) respectively.

5. Crack initiation sites are shown in Figure 4-9 for both the X3 and Y3 specimens. Early coalescence of cracks at 190k cycles is also shown Figure 4-9 (c).

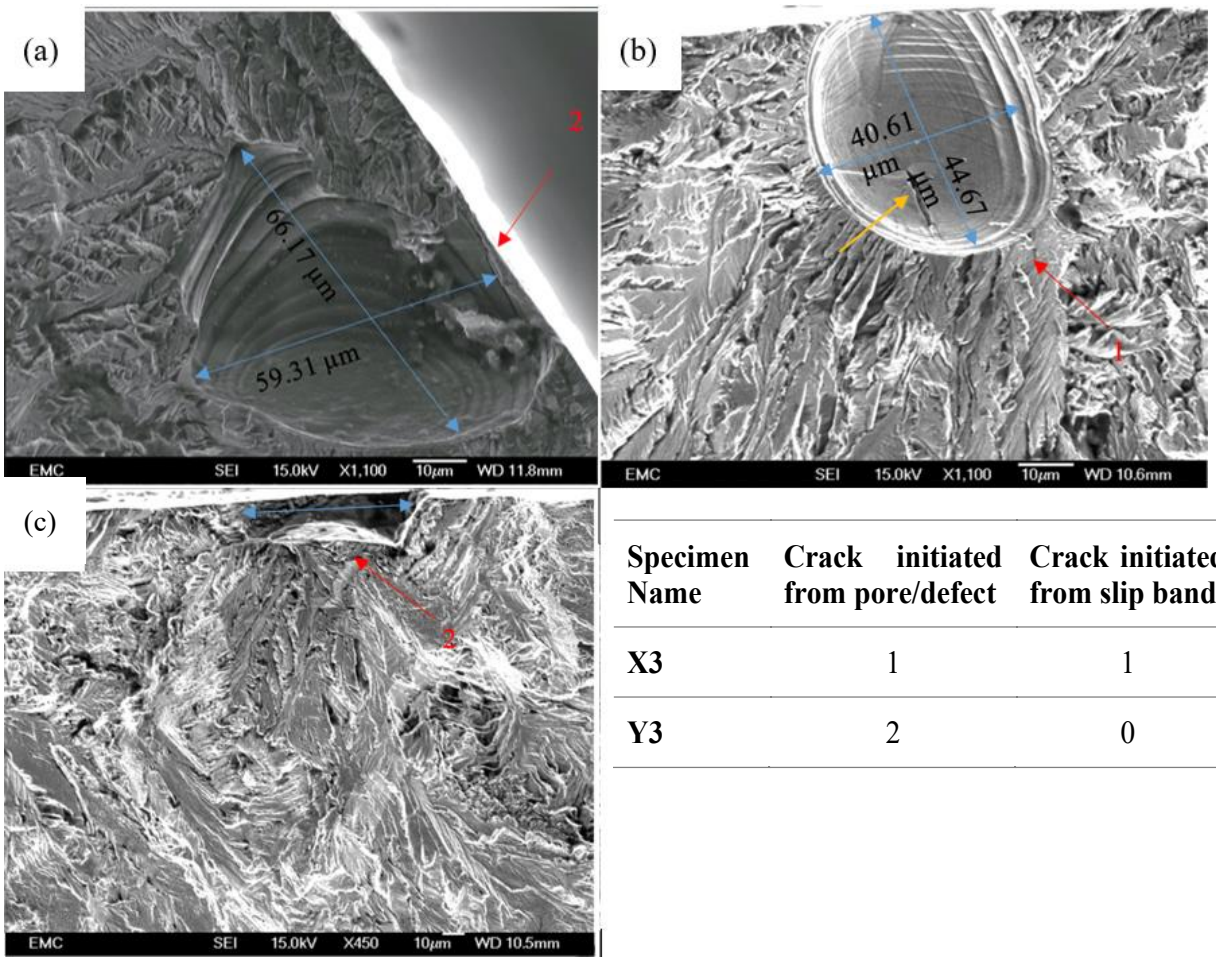

Specimen Name	Crack initiated from pore/defect	Crack initiated from slip band
X3	1	1
Y3	2	0

Figure 4-10: Crack initiation sites in: (a) X3 specimen for crack 2 and in Y3 specimen for (b) crack 1 (c) crack 2. The dimension of the pores/defects are indicated with blue arrows, while red arrows identify the pores/defect responsible for crack initiation.

6. In both X3 and Y3 specimen's cracks initiated from spherical open surface pores, shown in Figure 4-10. However, the Y3 specimen also had an underlying lack of fusion pore (see Figure 4-10 (c)) , which is linked to processability of the materials and can be considered a more severe manufacturing defect.
7. In the X3 specimen crack 1 had initiated in the middle of the tensile top surface at a slip band.

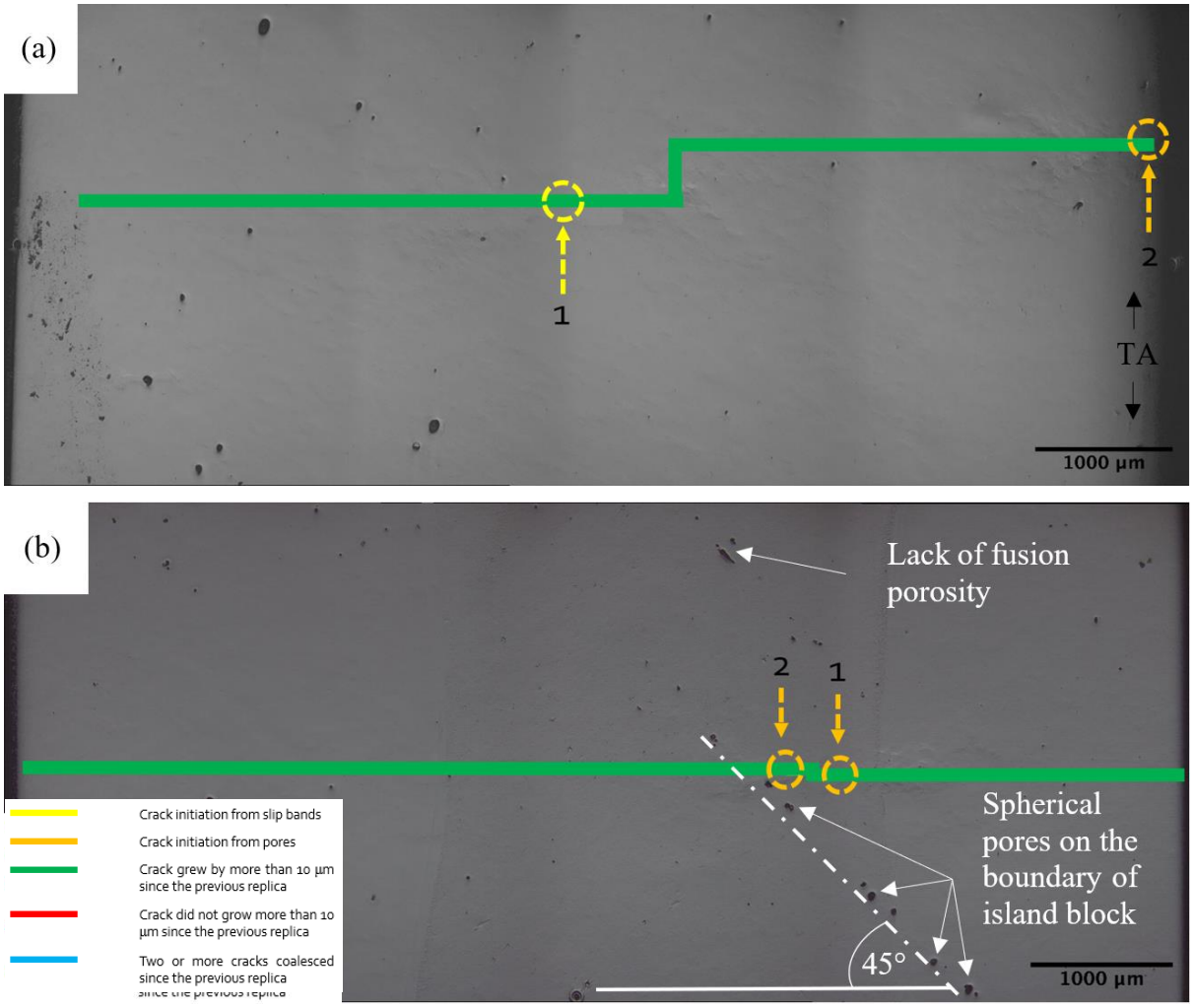

Figure 4-11: Initiated cracks and their propagation pathway (a) X3 specimen; black arrow indicating tensile axis (b) Y3 specimen, white arrow indicating spherical pores on the boundary of a scan island, aligned 45° with tensile axis. The green bar indicates the crack propagation behaviour until final failure.

8. No secondary cracks can be seen in Figure 4-11 for both the X3 and Y3 specimens, which gives an overview of the interaction between cracks on the tensile surface. A line of pores in Figure 4-11 (b) is indicative of high energy concentration on the boundary of island block causing spherical pores.
9. After 50% of life, steady growth of the crack was observed similar to long crack growth behaviour in the Y3 specimen, when da/dN versus ΔK plots are examined. No shielding/anti-shielding crack growth behaviour was observed. However, anti-shielding crack growth behaviour was observed for the X3 specimen nearing the end of its life, as shown in Figure 4-12 (a).

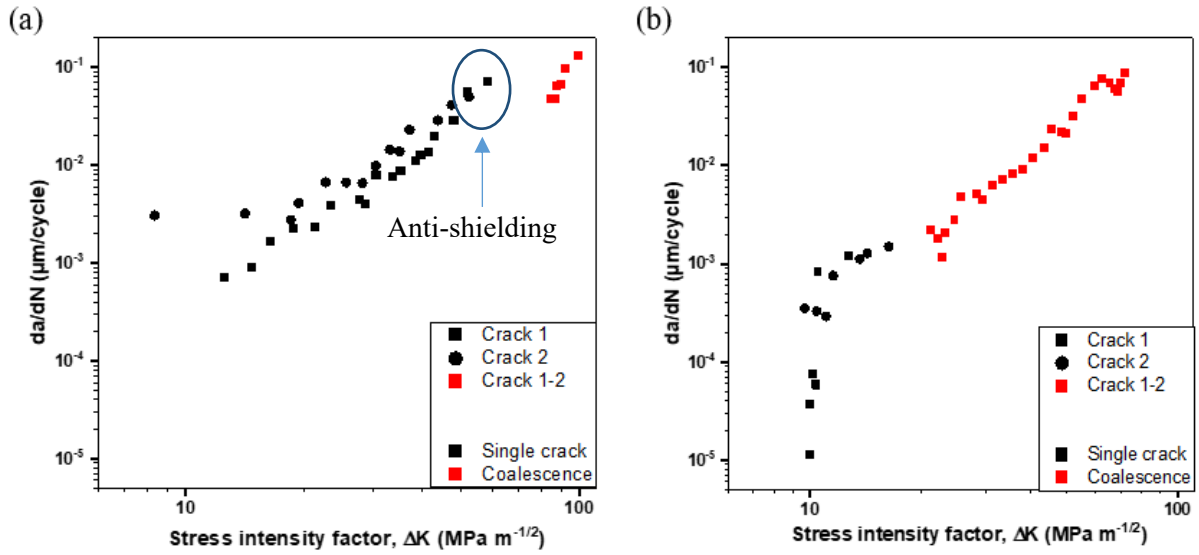

Figure 4-12: Crack growth rate vs stress intensity factor under cyclic loading at σ_{max}= 576 MPa of (a) X3 specimen (b) Y3 specimen.

10. The X3 specimen initially formed a corner crack (Crack 1) as shown in Figure 4.12. The corner crack was propagating from the left-hand side of the figure with an angle of 82.7° to the loading direction, and the crack tip is oriented at an angle of 8.3° from the expected crack propagation direction (normal to the applied tensile axis, TA) at 420k cycles, which indicates crack growth under an element of mixed-mode loading [63]. At around seventy percent of the lifetime, the centre crack (Crack 1) initiated and grew exhibiting a high growth rate. However, due to the shielding effect of the encroaching corner crack, the propagation rate then became steady and then decreased. The growth rate of the centre crack therefore had a fluctuating behaviour throughout its lifetime, which can be explained in terms of the significant interaction between the corner and centre cracks. At around 96% of the total lifetime, an overlap of the plastic zone of two crack tips is apparent in Figure 4-13, indicating maximum interaction, according to Forsyth [98]. Even though a fluctuation in crack growth rate was observed for centre crack, the average growth rate of both cracks was very similar.

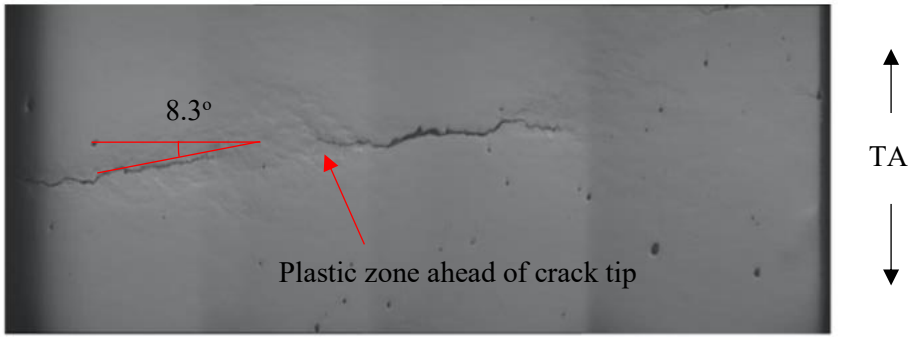

Figure 4-13: Top surface of X3 specimen at 420k cycles, showing corner crack (Crack 2) propagating at a slight angle and interaction zone between the 2 cracks that formed.

4.2.3 Comparison between specimens with different build direction under high maximum stress (648 MPa)

A comparison between three specimens from batch one: X4, Y4 and Z3 with horizontal 0-degree, horizontal 90-degree and vertical build directions respectively (as shown in Figure 4-14 (e)) is now shown to investigate the role of build direction on crack initiation and propagation behaviour at the higher maximum test stress level.

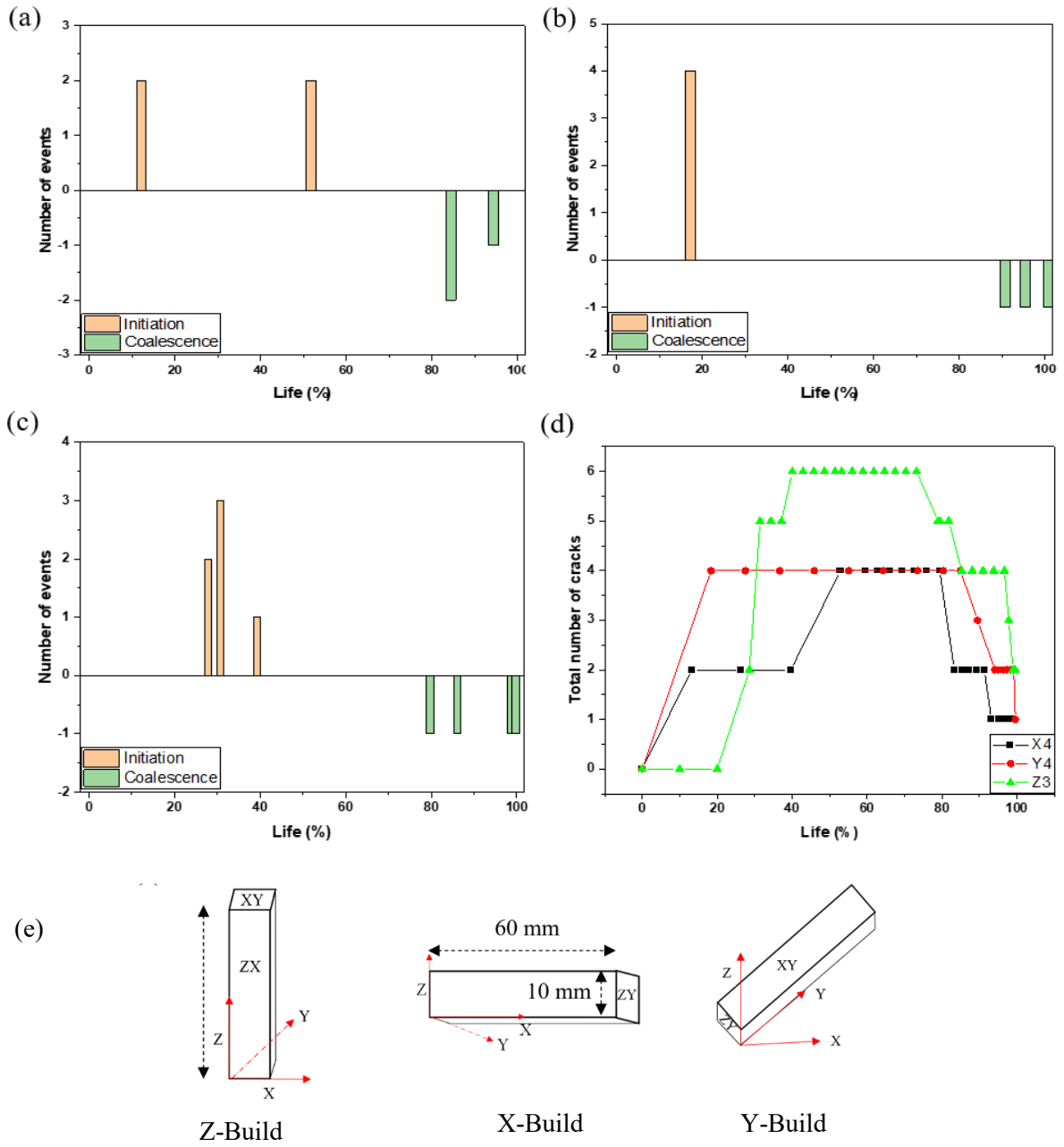

Figure 4-14: Crack initiation and coalescence events over the lifetime of batch one (a)X4 (b) Y4 (c) Z3 specimens (d) comparison between total number of cracks throughout the lifetime of the X4, Y4 and Z3

specimens. (e) X (left), Y (middle) and Z (right) built specimen. All have build direction in parallel to Z axis. The horizontal X, Y built specimen tensile surface is XY plane and vertically built Z specimen tensile axis is on ZX plane.

The key observations from the replica record and test results can be summarised into the following points.

1. Regardless of the build direction, at this high stress state, cracks initiated at between 15-25% of the total life of the specimens.
2. X4, Y4 and Z3 specimens failed at around 151k, 217k and 174k cycles respectively. The total number of initiated cracks for these tests are four, four and six respectively. Horizontally built specimens had 75% of cracks which initiated from a pore/defect, while the vertically built specimen had two-thirds of the cracks initiating from a slip band.
3. Coalescence appears to be more dominant compared to initiation on overall fatigue life at these higher stress levels; early coalescence can considerably shorten fatigue life. The Y4 specimen (longest lifetime) had three coalescence events near the end of its life which was reflected in its longer overall fatigue life.

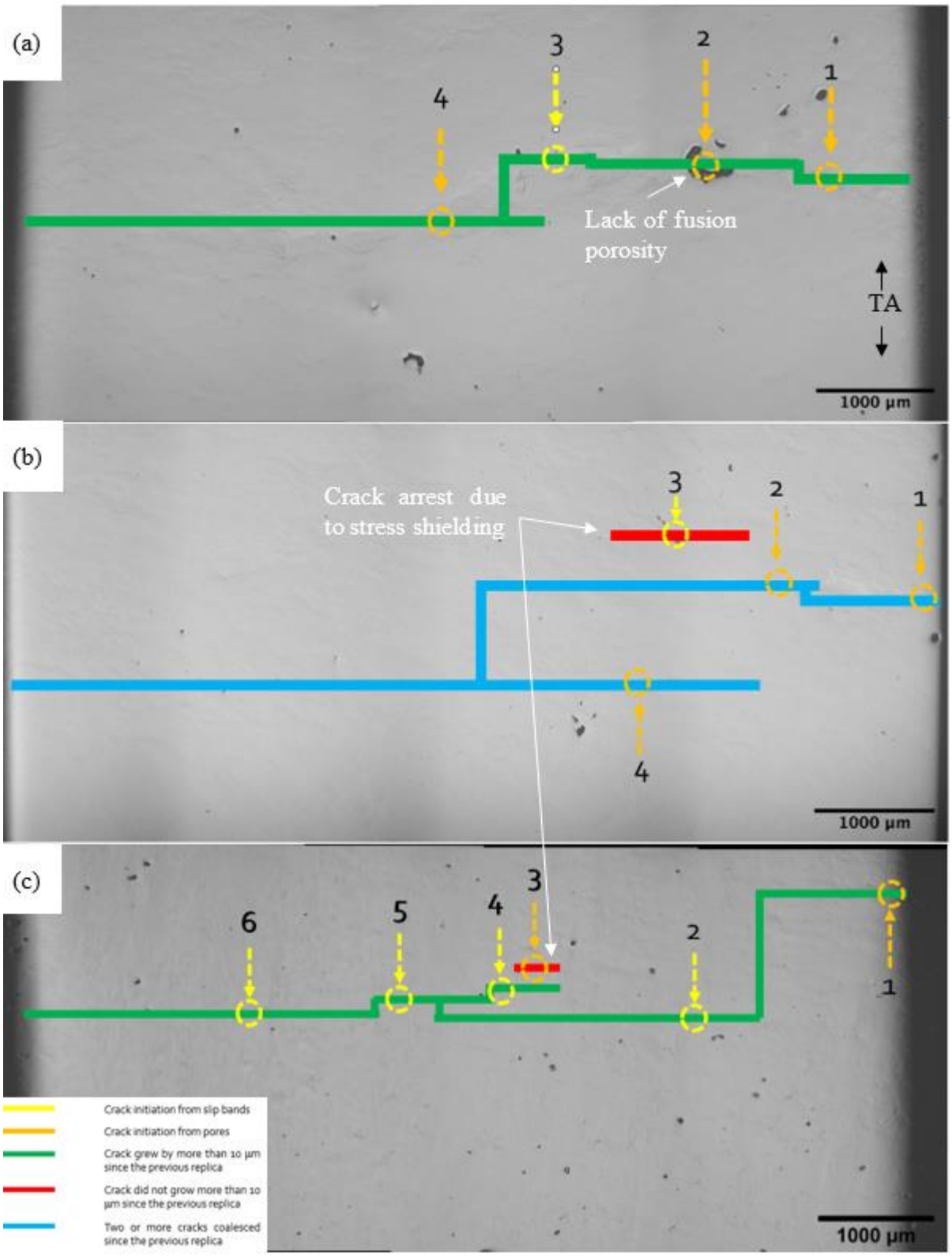

Figure 4-15: Comparison between initiated cracks and their propagation behaviour in bend bars from batch 1 tested at 648MPa maximum stress, R =0.1 (a) X4 specimen (b) Y4 specimen and (c) Z3

specimen. The red, green, and blue colours represent respectively: arrested cracks, cracks growing at a steady speed and coalescence events before final failure.

4. Secondary crack arrest has been observed in the Y4 and Z3 specimens due to stress shielding by the primary crack.
5. Crack stress shielding behaviour between parallel cracks in the Y4 specimen significantly slowed down the propagation of the primary crack resulting in a longer fatigue life.

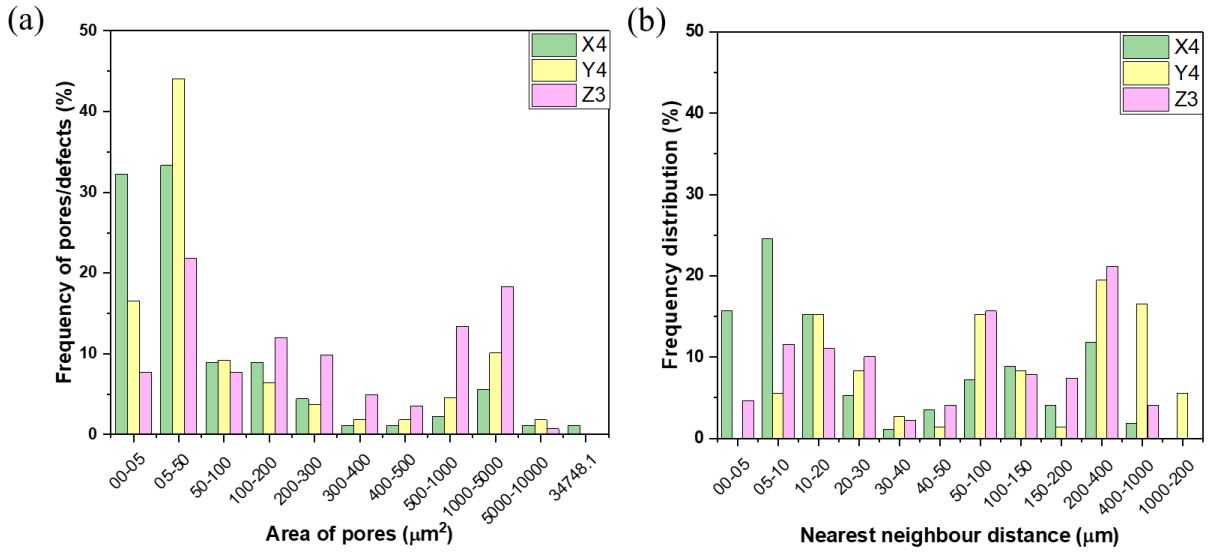

Figure 4-16: (a) Porosity/defects distribution (b) Neighbour distance proximity of pores on the top (tensile) surface of bend bar specimens.

6. It is apparent from a qualitative comparison of the bend bar surfaces from Figure 4-16 that the Z3 specimen has the highest number of small pores, whereas the X4 and Y4 specimens have larger but fewer pores/defect. In addition, pores/defects in the X4 specimen have more neighbours compared to the Z3 specimen indicating more clustered pores. However, no clear evidence was found to support any role of surface porosity clusters in crack initiation or propagation in these tests.
7. Only the horizontal 0-degree built specimen (X built) contains lack of fusion porosity as shown in Figure 4-15 (b) amongst all three specimens.
8. The largest lack of fusion porosity of X4 specimen has an area of 0.035 mm^2, which is equivalent to nearly a 100-micron long crack.

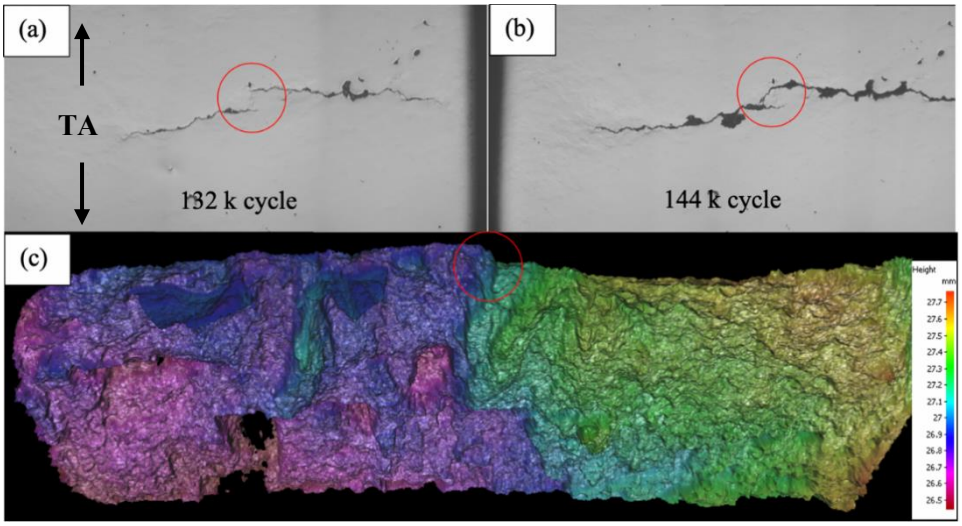

Figure 4-17: Crack coalescence mechanism in X4 specimen under cyclic loading at σ_{max}= 648 MPa. Coalescence is identified on the fracture surface in (c).

9. Coalescence between crack 1-2 and crack 3-4 for the X4 specimen is shown in Figure 4-17 (a) & (b). The coalescence mechanism was driven by anti-shielding behaviour leading to an increase in both crack growth rates evident in Figure 4-18 (a). Similar anti-shielding behaviour due to overlap of plastic zone was reported by Poulain et al. and shown in Figure 2-33 [99]. This crack anti-shielding behaviour is also evident in the Y4 specimen, accelerating the growth of crack 1-2 and crack 3-4 nearing the end of total life. Anti-shielding behaviour was also noticed in two instances for the Z3 specimen.

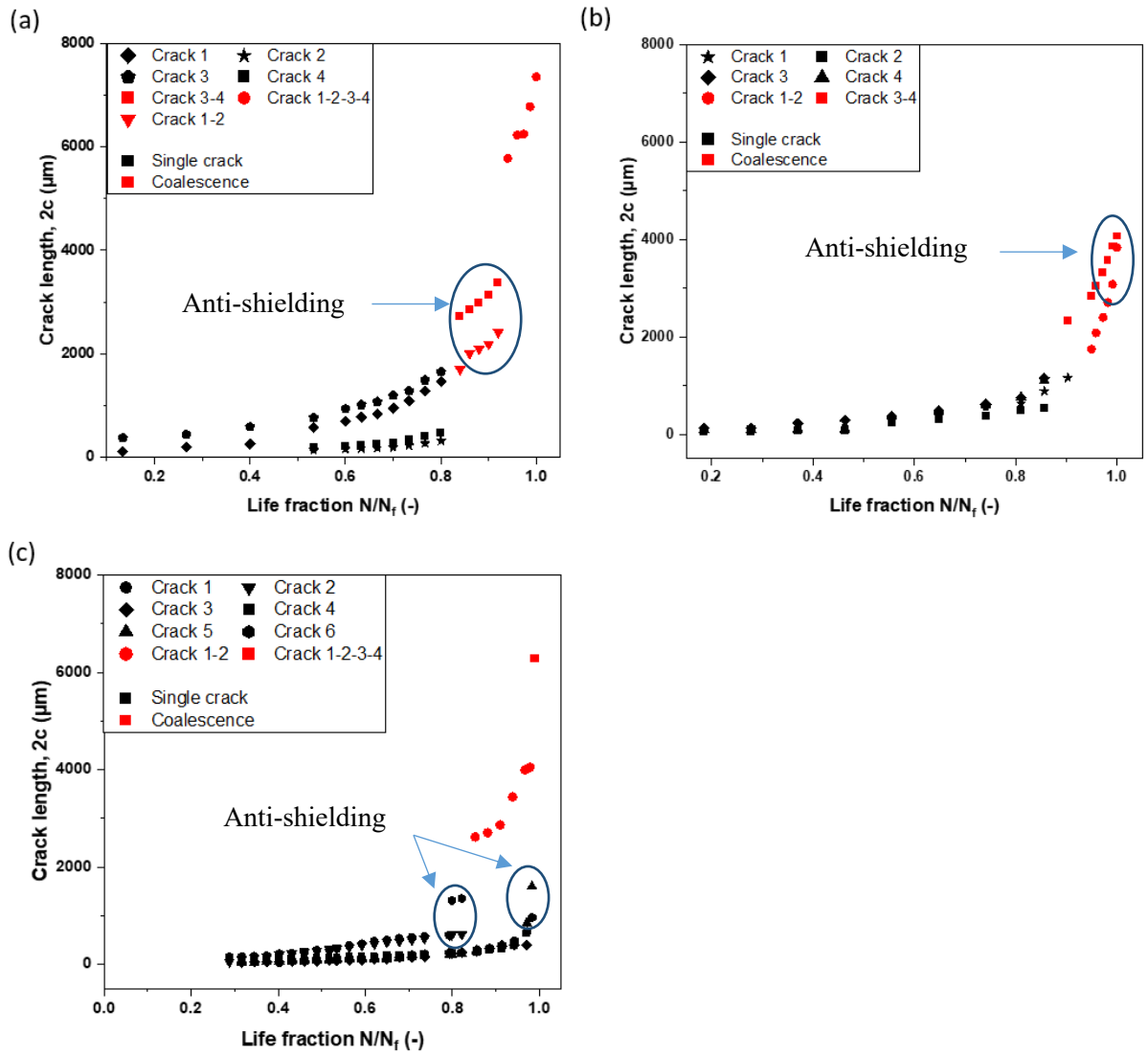

Figure 4-18: Crack initiation and propagation behaviour under cyclic loading at σ_{max}= 648 MPa, R=0.1 on (a) X4 specimen, N_f= 151k cycle and (b) Y4 specimen, N_f= 217k cycle, (c) Z3 specimen, N_f= 174k cycle.

10. For the X4 specimen, later initiated small cracks appeared to be stress shielded by larger cracks for approximately half of their life (crack 1 & crack 3), and crack 1, crack 2 & crack 3 simultaneously merged into a single crack (crack 1-2-3) at around 80% of total life. Meanwhile, a dramatic increase in the growth rate of crack 4 was recorded, which could be due to the influence of crack 1-2-3; this agrees with Poulin's [104] observation.

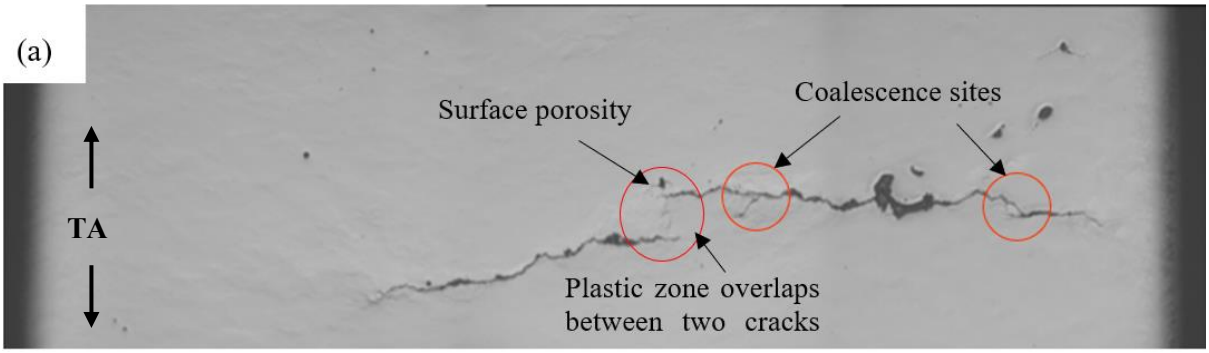

Figure 4-19: (a) Crack initiation sites at 63% life (b) Coalescence sites at 87% life for X4 specimen.

11. In addition, an overlap between the plastic zone of the two crack tips is apparent in Figure 4-19 for the X4 specimen, which could explain the dramatic increase of the growth rate of crack 4.

Table 4-2: Ochi's coalescence criteria evaluation for crack 4 & crack 2 for X4 specimen.

Number of cycles in thousand	**Length of crack 4, l_1**	**Length of crack 1-2-3, l_2**	**Distance between cracks, h**	**Coalescence**	**The multiplying factor, H**
129	1236.24	1422.12	151.57	No	0.031
132	1280.20	1489.16	147.16	No	0.029
135	1326.99	1571.14	146.51	No	0.028
138	1442.69	1687.60	150.59	Yes	0.026

12. The coalescence sites and overlap between the plastic zone are shown in Figure 4-19. Ochi's criteria from Equation 2-38 was used to evaluate coalescence mechanism in Table 4-2. In addition, it is worth mentioning that crack 1-2-3 avoided a surface porosity in its path to merge with crack 4.

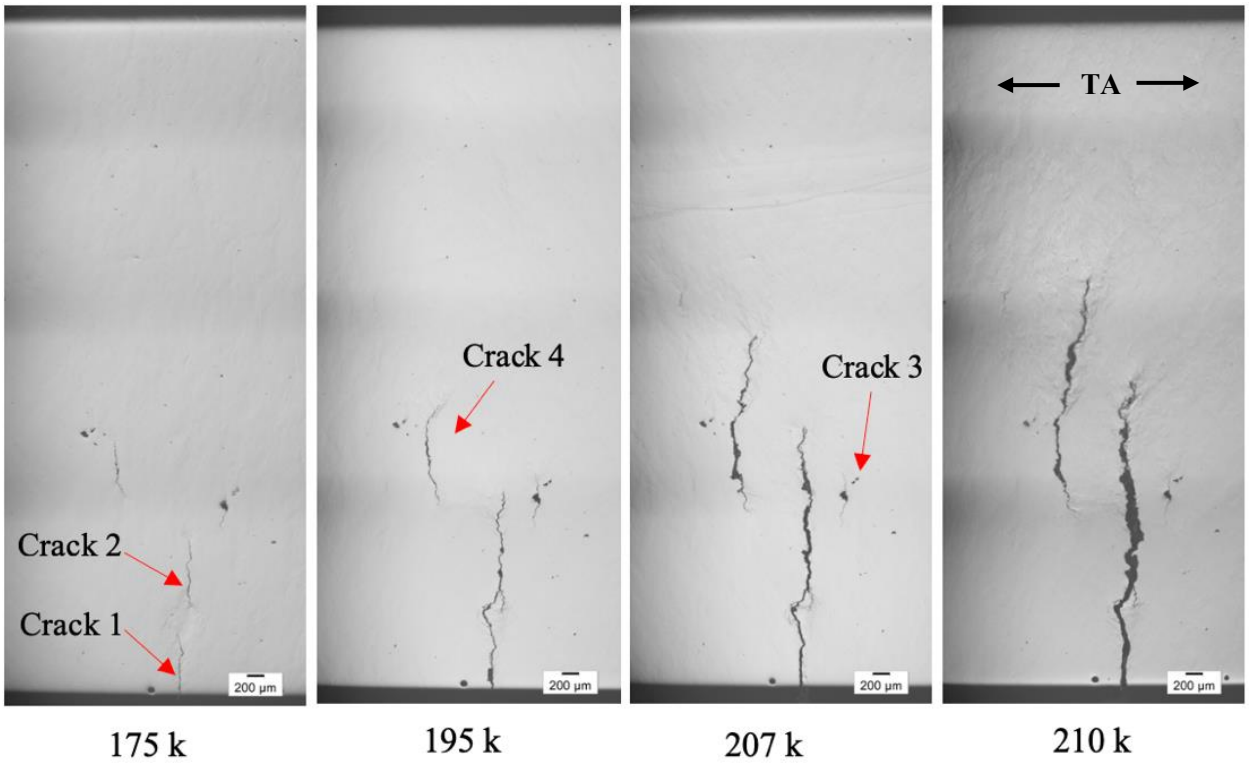

Figure 4-20: Crack initiation sites at the top surface of Y4 specimen under cyclic loading.

13. As mentioned earlier, at 90% of the total life of Y4, a coalescence between crack 1 & crack 2 and subsequently a sharp increase in the growth rate of crack 4 was observed in Figure 4-20. Then both cracks grew at a very high rate parallel to each other. Meanwhile, crack 3 was heavily stress shielded by crack 1-2 and completely stopped growing as a result. Eventually, these cracks merged, leading to catastrophic failure. The coalescence criteria for crack 1 and crack 4 was evaluated in Table 4-3. The multiplying factor according to Ochi's criteria is 0.025 for this specific case.

Table 4-3: Ochi's coalescence criteria evaluation for crack 1 & crack 4 for Y4 specimen.

Number of cycles in thousand	**Length of crack 1-2, l_1**	**Length of crack 4, l_2**	**Distance between crack, h**	**Coalescence**	**The multiplying factor, H**
195	1157.04	2321.05	362.11	No	0.057
205	1747.14	2825.98	390.34	No	0.047
207	2083.69	3051.88	382.47	No	0.041

210	2402.26	3313.90	329.56	No	0.032
212	2706.76	3569.03	374.00	No	0.033
214	3079.62	3858.21	386.54	No	0.031
216	3833.45	4064.34	362.13	Yes	0.025

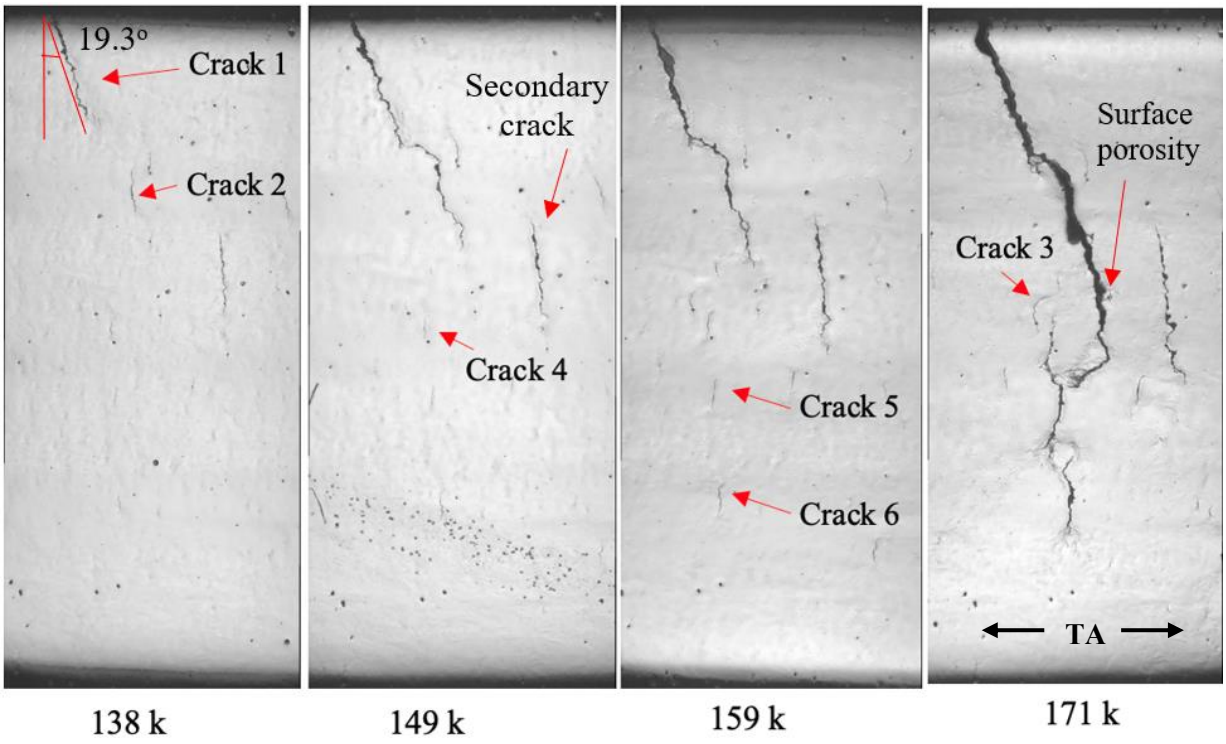

Figure 4-21: Crack initiation site on the top surface of Z3 specimen under cyclic loading.

14. The Z3 specimen has six initiation sites with the primary crack starting from the corner with an angle of 19.3°, indicating some possible mode I-mode II mixed loading. Several coalescences took place throughout the lifetime of this specimen. At around 97% of the total life, a secondary crack shown in Figure 4-21 stopped due to the stress shielding effect. It is apparent, initially, the crack 1 growth direction was influenced by crack 2 and secondary crack. However, after coalescence, crack 1-2 started growing in nearly pure mode I loading. It avoided a large surface pore on its path and merged with its smaller neighbour pore. Then rapid propagation was noticed in crack 5 & crack 6 due to the stress anti-shielding effect.

Table 4-4: Ochi's coalescence criteria evaluation for crack 1-2 and secondary crack for Z3 specimen.

Length of crack 1-2, l_1	Length of secondary crack, l_2	Distance between crack, h	Coalescence	The multiplying factor, H
2617.48	1128.43	784.82	No	0.115
2700.36	1202.84	801.86	No	0.113
2862.62	1529.50	711.86	No	0.089
3437.22	1677.59	654.60	No	0.070

15. The selective coalescence of crack 1-2 with crack 4-5, instead of the secondary crack for the Z3 specimen is worth discussing. Ochi's criteria for coalescence mechanism is given in Table 4-4. Throughout the entire propagation, the lowest value of multiplying factor was calculated 0.07, which is much higher than that found for X4 and Y4 specimens. Ochi's [96] coalescence criterion was not met between crack 1-2 and secondary crack as the ratio between the distance of the two parallel tips and their cumulative length was not sufficiently small. If this coalescence criterion had been met, the Z3 specimen could potentially have failed earlier.

4.2.4 Role of porosity in fatigue crack propagation

This section analyses in more detail the role of porosity in fatigue crack initiation and propagation behaviour, ultimately affecting overall lifetime. The Z2 and Z3 specimens from batch one tested at 648 MPa maximum stress are considered in detail for this analysis.

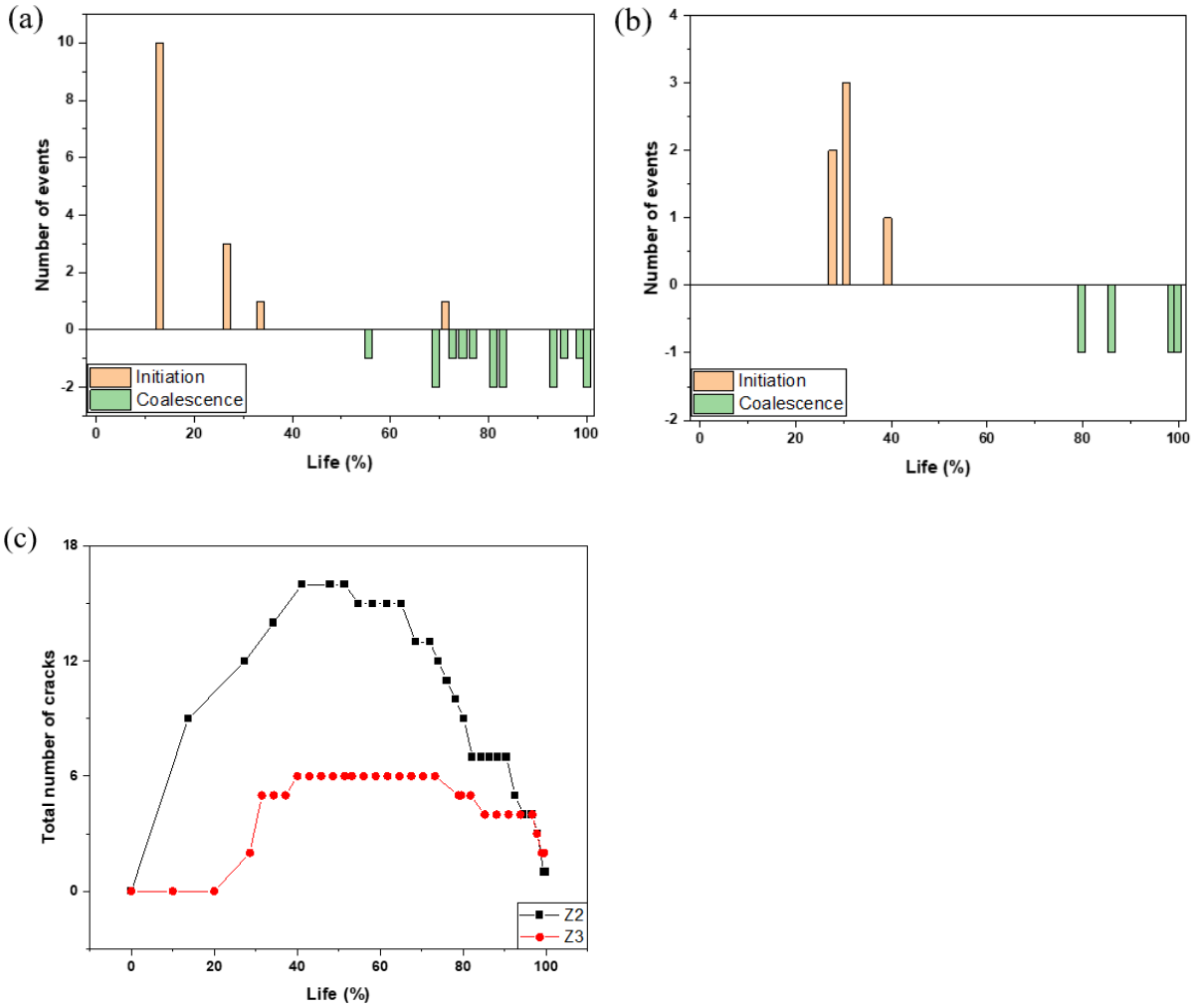

Figure 4-22: Crack initiation and coalescence events over the lifetime of batch one for (a)Z2, (b) Z3 specimen (c) comparison between total number of cracks throughout the lifetime of Z2 and Z3 specimen.

After carefully analysing the replica records, the following can be summarised.

1. The Z2 and Z3 specimen failed at 145k and 174k cycle respectively.
2. In Figure 4-22, the Z2 specimen had simultaneous initiation of nine cracks at around 17% of its total life followed by eight more cracks throughout its life. Two-thirds (eleven) of these cracks have been identified (from subsequent fractography) to be initiated from pores, although no defects were observed on the specimen surface. Unlike any other specimens discussed, Z2 had a crack which initiated at around 70% of its total life. On the other hand, the Z3 specimen

had all the cracks initiated between 25-40% of its total life. No further crack initiation events were observed after this on Z3 specimen. Two-thirds (four) of these cracks were initiated from slip bands and similar to Z2 only spherical/semi-spherical pores were observed on the surface.

3. Crack coalescence events were first recorded at around 55% of the total life for the Z2 specimen, followed by fifteen more coalescences throughout its lifetime. On the other hand, the first coalescence event recorded for the Z3 specimen was at around 80% of its total life followed by three more coalescences with two of them being simultaneous, leading to the final failure of the specimen.

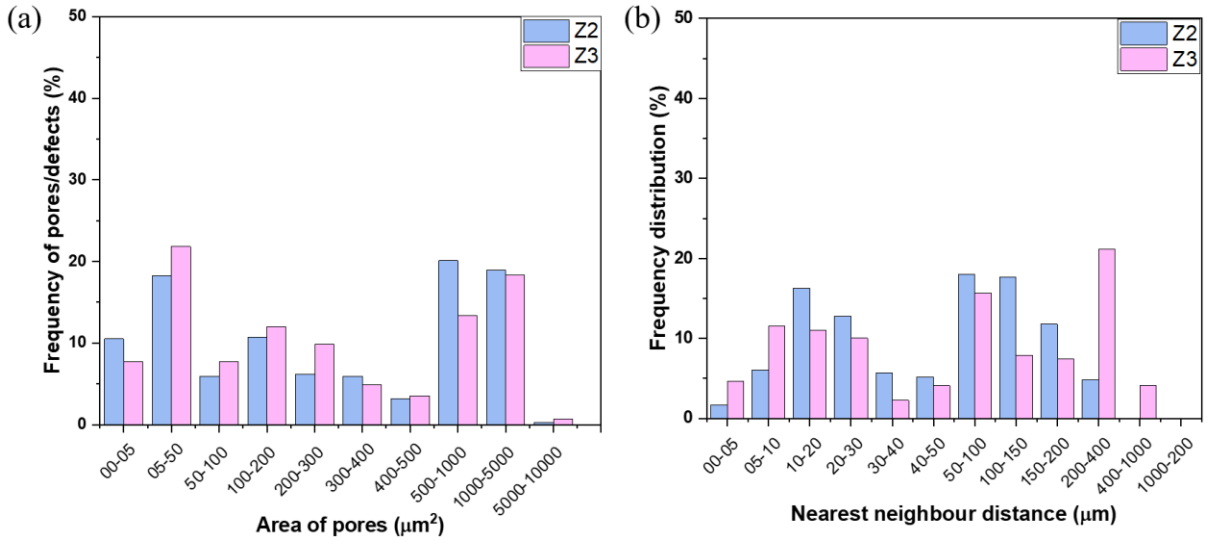

Figure 4-23: (a) Porosity/defects distribution (b) Neighbour distance proximity of pores on the top (tensile) surface of bend bar specimens.

4. According to the statistical distribution of porosity in Figure 4-23 (a), the difference between the frequency percentage of pore area for Z2 and Z3 appears to be insignificant. However, a significantly higher statistical number of close neighbours can be observed in Figure 4-23 (b) for Z2 specimen compared to Z3, suggesting clustering of the pores for Z2 specimen.

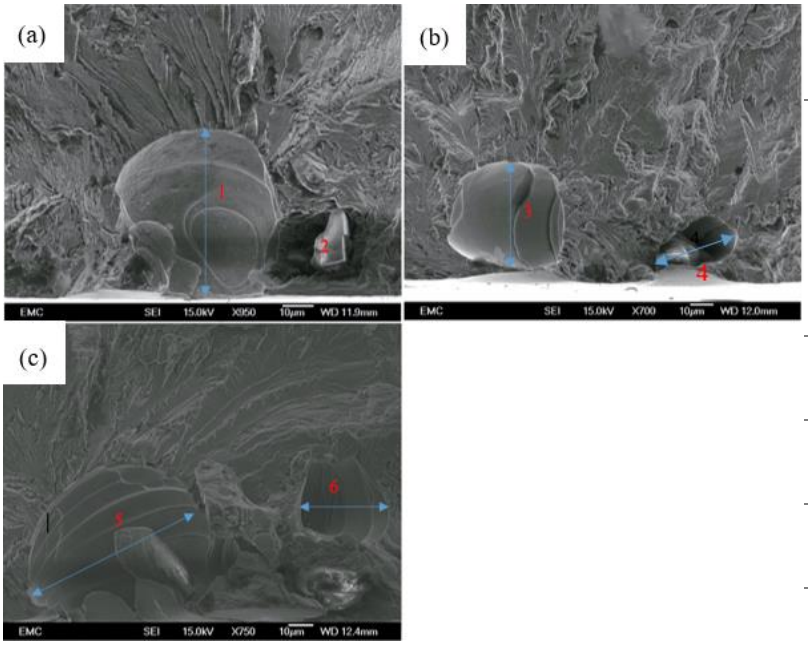

Specimen name	Stress intensity factor for pore		
Z2	Stress, MPa	Area, μm^2	Stress intensity factor ΔK, MPa m$^{-1/2}$
1	648	2415	5.23
2	648	780	3.95
3	648	1935	4.95
4	648	591	3.68
5	648	3836	5.88
6	648	1036	4.24

Figure 4-24: SEM images (a), (b) and (c) of the pores on the fracture surface of Z2 specimen responsible for crack initiation. The table on the right shows equivalent stress intensity factor for these subsurface pores.

5. Numerous crack initiation from twinned pores have been observed on the fracture surface of the Z2 specimen, shown in Figure 4-24.
6. The area and equivalent stress intensity factor of these pores is given in the Figure 4-25.

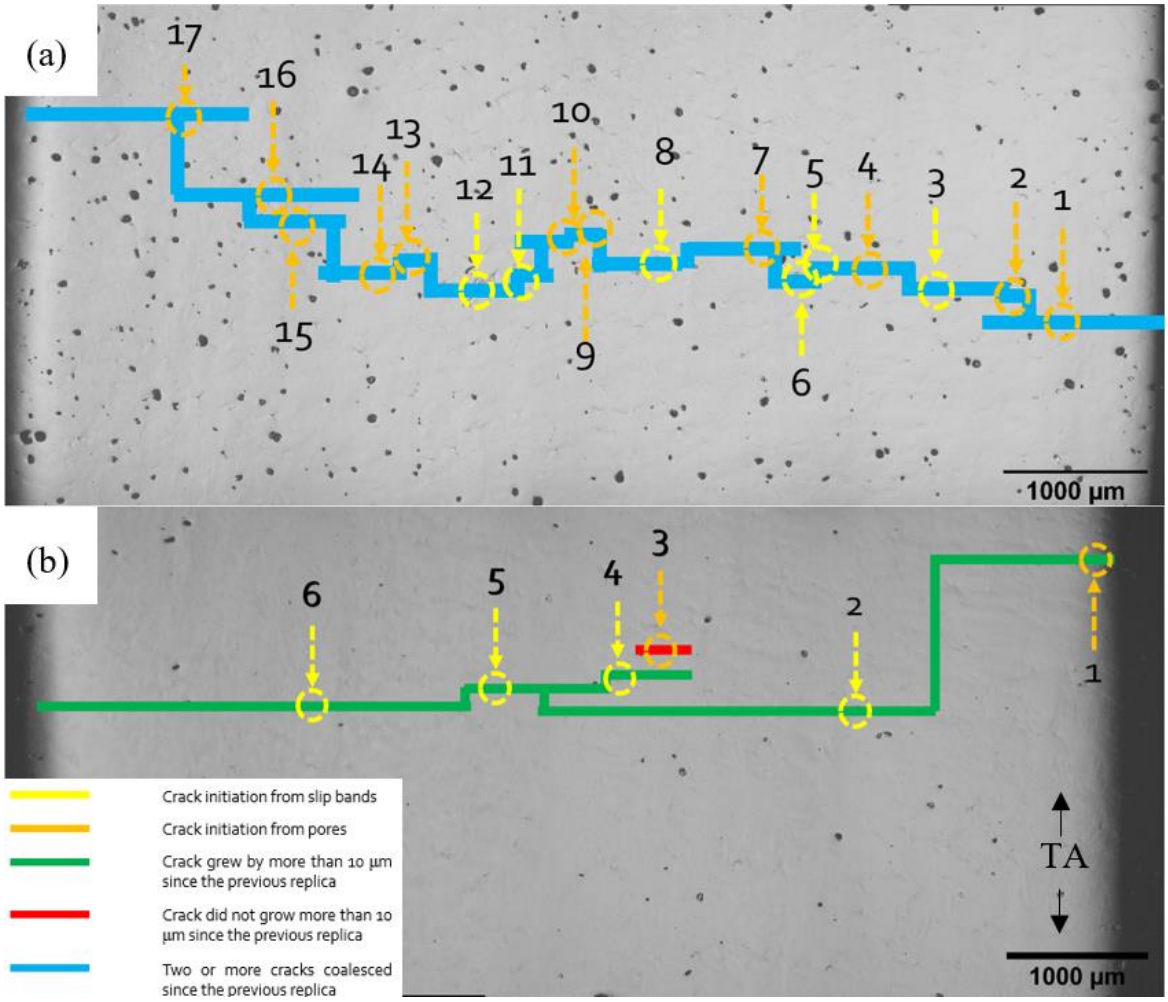

Figure 4-25: Comparison between initiated cracks and their propagated paths (a) Z2 specimen indicating coalescence before final failure (b) Z3 indicating steady crack growth until final failure.

7. A comparison between crack paths shows numerous interactions between cracks leading to final failure for Z2, while the Z3 specimen had steady crack growth with limited interactions between cracks.
8. Due to the complex nature of crack initiation, propagation, and interaction behaviour, the Z2 specimen displayed short crack behaviour throughout its entire life. As shown in Figure 4-27, significant scatter in crack growth behaviour is observed due to the interaction between these cracks. The Z3 specimen exhibits more stable stage II type long crack propagation behaviour towards the end of life.
9. Numerous stress-shielding and anti-shielding behaviours can be observed for the Z2 specimen in Figure 4-26. Between 50-80% of total life, stress shielding behaviour appears to be the dominating mechanism in controlling fatigue life. Afterwards, several anti-shielding behaviours can be observed leading to accelerated crack growth.

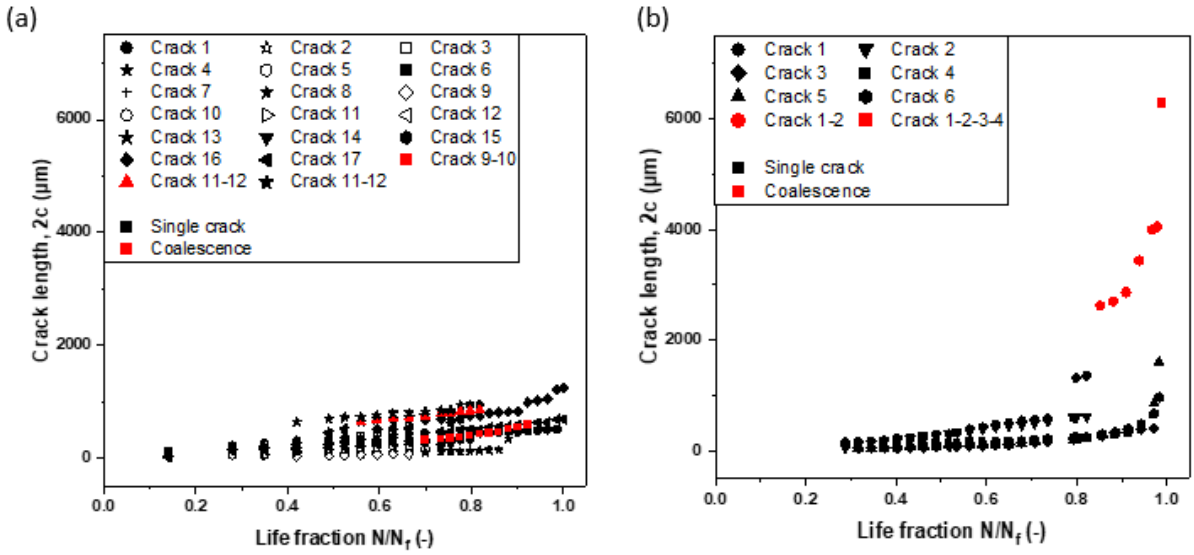

Figure 4-26: Crack initiation and propagation under cyclic loading at σ_{max}= 648MPa for batch one (a) Z2 specimen, N_f=145k cycle (b) Z3 specimen, N_f=174 K cycle.

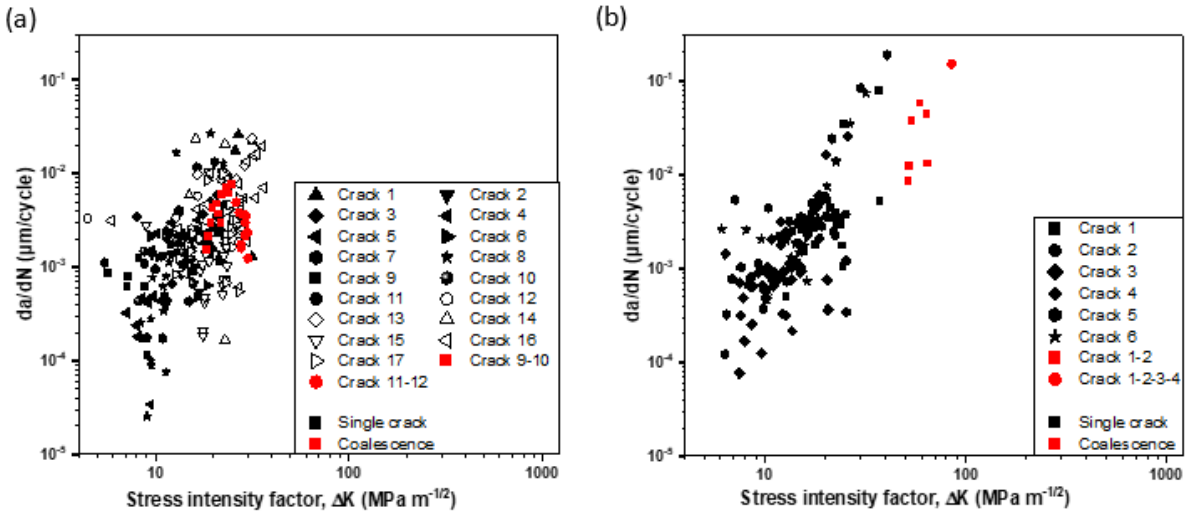

Figure 4-27: Crack growth rate vs stress intensity factor of Z3 under cyclic loading at σ_{max}= 648 MPa for batch one (a) Z2 specimen, N_f=145k cycle (b) Z3 specimen, N_f=174 K cycle.

For all specimens from batch one, a series of animations of the top surfaces (based on the replica record) have been constructed to allow the evolving initiation, growth, and coalescence behaviours to be visualised as a function of lifetime fraction. Links to these animations can be found here:

Short crack behaviour of 316L SS bend bar at R=0.1 cyclic loading.

4.2.5 Crack initiation and propagation behaviour of specimen build with high energy density.

This section discusses crack initiation and propagation behaviour of the batch two specimens manufactured with relatively high energy density (E_D= 138 J/mm^3). Batch two specimens have lower yield strength compared to batch one (as shown in Figure 3-12 (b)) and thus are more prone to fatigue failure due to the formation of more persistent slip bands (PSBs) at equivalent stress levels. However, fatigue failure is a complex mechanism affected by numerous factors such as initiation features, crack coalescence and interaction between cracks.

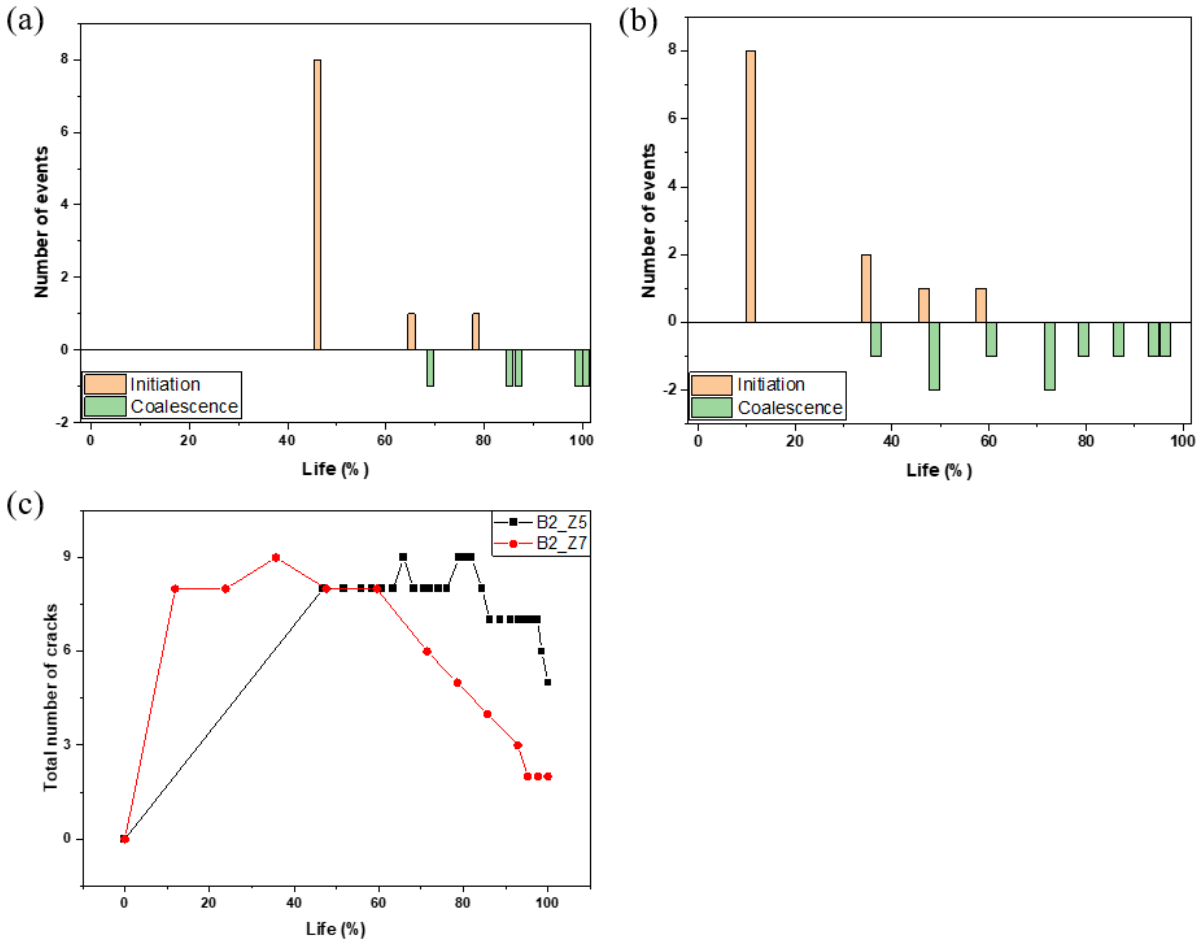

Figure 4-28 Crack initiation and coalescence events over the lifetime of batch two (a)Z5 at 576 MPa (b) Z7 specimen at 648 MPa (c) comparison between total number of cracks throughout the lifetime of Z5 and Z7 specimen.

The key observations from replica record for both Z5 and Z7 can be summarised as following.

1. Z5 and Z7 specimens failed at 205k and 42k cycle at the maximum stress of 576 MPa and 648 MPa respectively (note their differing applied stress levels).

2. The maximum number of total cracks for Z5 and Z7 are the similar. Both specimens had nearly all their cracks initiating from PSBs regardless of their differing test stress levels and varied porosity distribution.
3. The Z7 (648MPa) specimen has crack initiation from around 15% of its total life and the initiation events continued up to 60% of the total life. On the other hand, crack initiation in the Z5 specimen (576MPa) occurred on nearing half its total life and the initiation activities continued up to 80% of its life.
4. Coalescence events for Z7 began at around 35% of life and continued up to 60% life, coalescence was also accompanied by further initiation events. In total, eleven coalescence events took place for the Z7 specimen, twice that of the Z5 specimen. Coalescence events begin for the Z5 specimen only at 70% of its life and continued up until final failure.

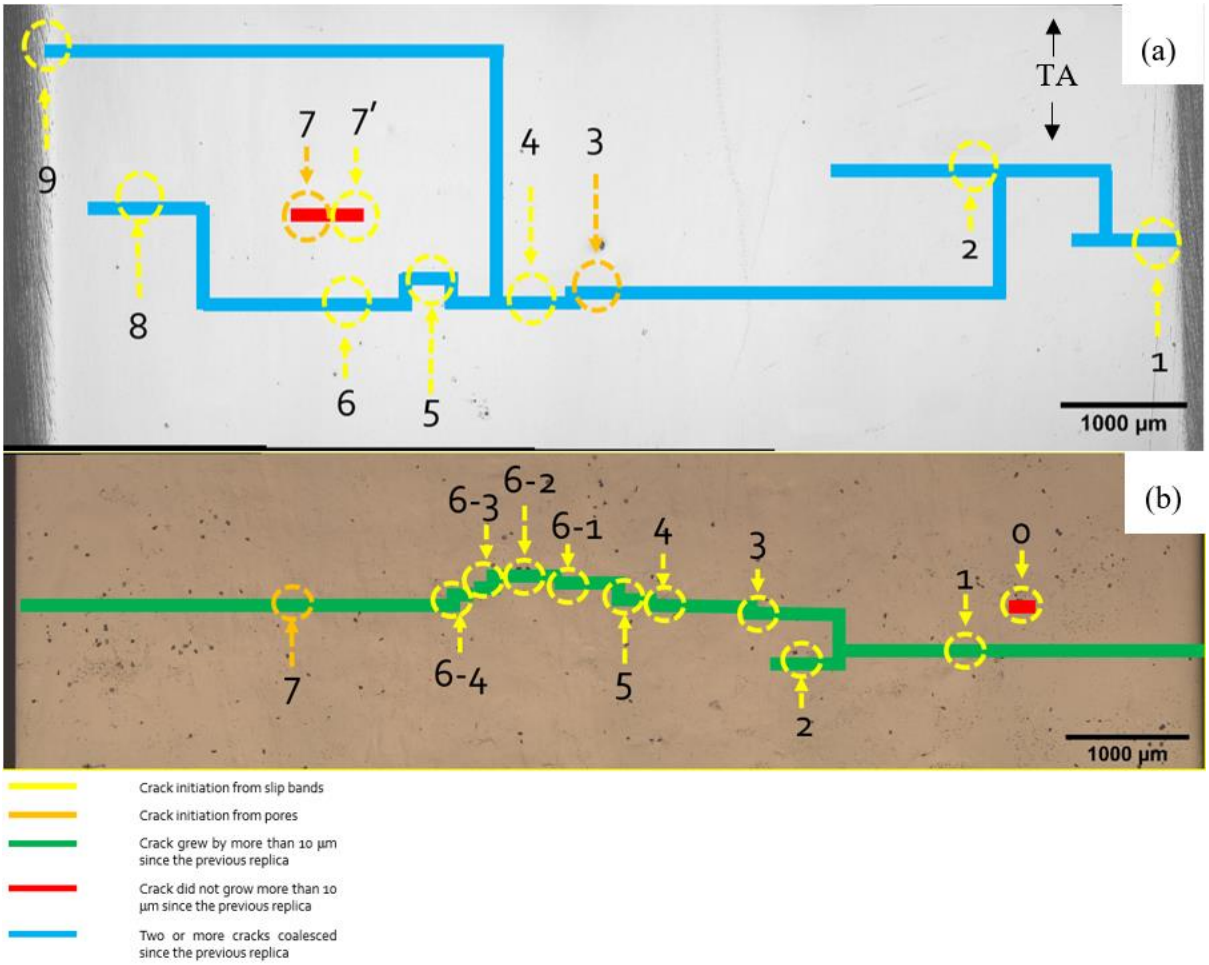

Figure 4-29: Initiated cracks and their propagation pathway for batch two (a) Z5 at 576 MPa, multiple coalescence events before final failure (b) Z7 at 648 MPa, steady growth of crack before final failure.

5. The final replica record from Figure 4-29 reveals numerous interactions between cracks. At the end of total life, a coalescence event led to the failure of Z5 specimen. Whereas the primary

crack grew steadily up until final failure, with little effect of coalescence events for the Z7 specimen.

6. Secondary crack arrest due to stress shielding can be observed for both the Z5 and Z7 specimen.
7. At around 80% life of Z5 specimen, numerous shielding and anti-shielding behaviour can be observed in Figure 4-30 for crack 3-4-6, crack 2 and crack 9. In the meanwhile, crack 7-7' and crack 8 become static. On the other hand, crack shielding behaviour can be observed in case of crack 0 at around 85% life in the Z7 specimen.
8. Considering crack growth rate da/dN as a function of ΔK, shown in Figure 4-31, Z5 specimen life was dominated by scattered short crack growth behaviour while Z7 specimen fatigue life has been mostly dominated by steadier long crack growth behaviour.

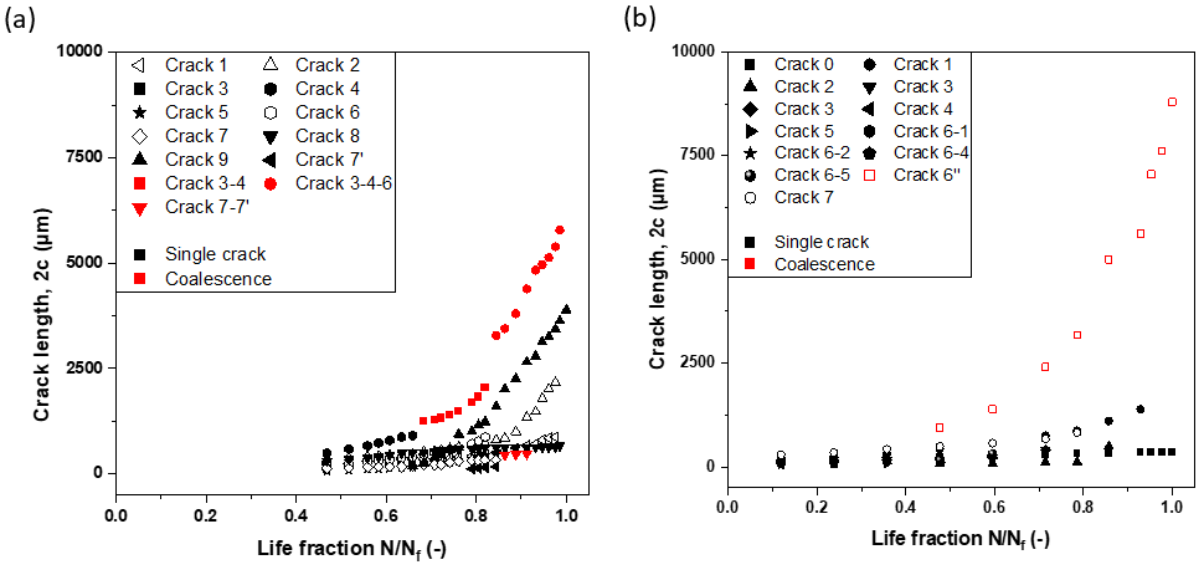

Figure 4-30: Crack initiation and propagation under cyclic loading for batch two (a) Z5 specimen, N_f=205k cycle (b) Z7 specimen, N_f=42k cycle.

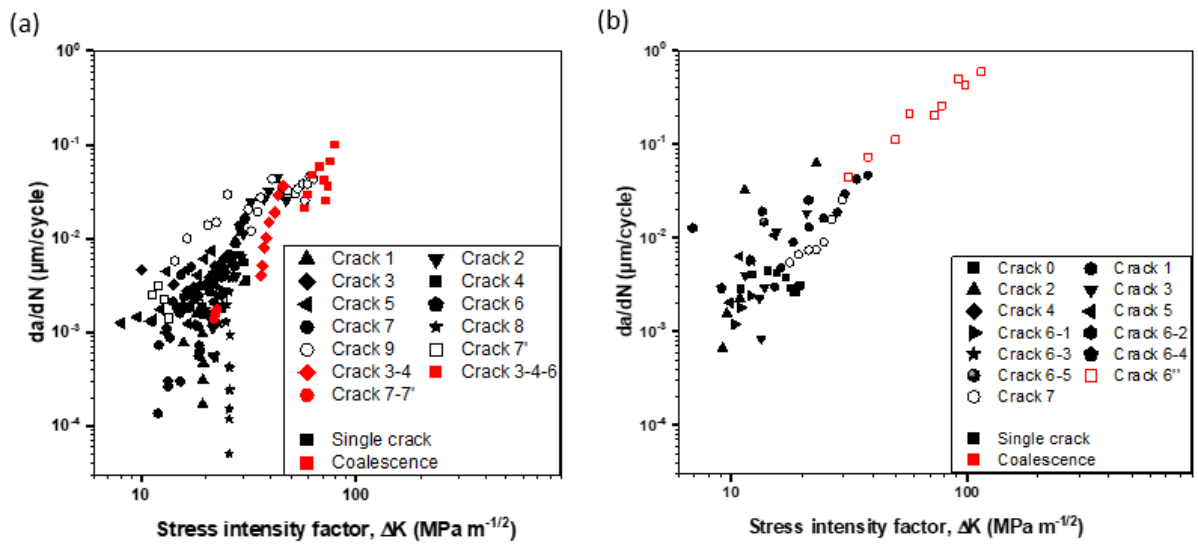

Figure 4-31: Crack growth rate vs stress intensity factor under cyclic loading for batch two (a) Z5 specimen, Nf=205k cycle (b) Z7 specimen, Nf=42k cycle.

4.3 Summary and conclusion

The study was conducted on bend bar specimens using a three-point bending setup with force control, focusing on mainly two nominal stress levels (576 and 648 MPa). The stress-strain behaviour was measured initially, and cyclic hardening was observed, with batch one exhibiting higher cyclic hardening than batch two and subsequent fatigue tests were conducted on two batches of specimens to monitor their fatigue life under cyclic loading. The fatigue tests included uninterrupted and interrupted loading with replica records collected at various points during the specimen's life. The study correlated fatigue life with maximum total strain, finding a strong relationship, although some specimens outperformed strain-life trend. This necessitates the need for a detailed investigation into crack growth behaviour for a comprehensive understanding of fatigue lifing. A comparison of porosity distribution in batch one specimen's revealed variations, with X3 and Z2 specimens exhibiting the lowest and highest porosity percentages, respectively. Surface roughness was considered negligible in the fatigue lifetime study.

The study explored the influence of various factors, such as build direction, energy density, porosity, and the relative balance of crack initiation, coalescence, and propagation, on the fatigue life of these specimens. The findings suggest that factors like build direction energy density, porosity, crack initiation, and coalescence events have a substantial impact on the fatigue life of the bend bar specimens and the crack initiation and propagation mechanisms of LPBF processed 316L SS are clearly complex. Understanding these factors is essential for predicting material behaviour and improving the durability and reliability of components made from LPBF processed 316L SS material. As mentioned earlier, the

fatigue life was evidently dominated by early-stage crack initiation and coalescence mechanisms. The early-stage cracks, on many occasions, were observed to initiate from open surface pores and lack of fusion defects. Thus, understanding the mechanism of early-stage crack initiation and investigating the correlation of porosity distribution and total fatigue life was a further focus for this study.

The overall findings looking across the range of controlling parameters extends to the following:

- The detailed analysis of fatigue behaviour in batch one horizontally built specimens (X3 and Y3) and a comparison between three specimens (X4, Y4, and Z3) with different build directions reveals crucial insights into crack initiation, propagation, and coalescence mechanisms. The results highlight the significant impact of build direction on fatigue life, with horizontal specimens generally exhibiting longer fatigue lives compared to the vertical one.
- In the case of batch one X3 and Y3 specimens, differences in crack initiation times, coalescence behaviour, and the presence of manufacturing defects contribute to variations in fatigue life. The study identifies specific initiation sites, crack growth patterns, and the influence of manufacturing defects, such as lack of fusion pores.
- The analysis of three specimens from batch one (X4, Y4, and Z3) emphasizes the role of build direction in crack initiation and propagation at higher stress levels. The study indicates that coalescence events, stress shielding, and the presence of surface porosity clusters significantly affect fatigue life. Anti-shielding behaviour is observed in some specimens, impacting crack growth rates.
- Further investigation into the role of porosity in fatigue crack initiation and propagation was conducted on Z2 and Z3 specimens. The results demonstrate the influence of porosity distribution, clustering, and interaction between cracks on fatigue behaviour. The Z2 specimen displays short crack behaviour, while the Z3 specimen exhibits more stable long crack propagation towards the end of its life.
- Batch two specimens (Z5 and Z7) with lower yield strength were analysed, revealing the complex interplay of factors affecting fatigue failure. Persistent slip bands, crack initiation from different stages of the specimen's life, coalescence events, and interactions between cracks contributed to the observed fatigue behaviour. The study highlights the importance of considering multiple factors, including stress levels, initiation features, and crack interactions, in understanding fatigue failure mechanisms. Z7 (tested at 648MPa) unsurprisingly had a significantly shorter fatigue life than Z5 (tested at 576 MPa), both had similar numbers of initiated cracks. Coalescence events and crack interactions were prominent in both cases, with Z7 demonstrating more coalescence events. However, Z5's fatigue life was more dominated by short crack behaviour and the many shielding events from multiple crack interactions, while Z7 largely exhibited long crack behaviour, with the major crack growing fast and dominating the

lifetime (despite multiple crack initiations and coalescences) thus showing the importance of overall strain levels in determining which factors control lifetime.

- Mixed mode (mode I-mode II) crack propagation was observed on several occasions in nearly all specimens and on several occasions, the crack path avoided open surface pores even though they are evidently responsible for crack initiation. This reconfirms the importance of investigating the relation of pore distribution and fatigue lifetime (and also in understanding the role of sub-surface defect distributions).
- The coalescence mechanism was found to be in good agreement with Ochi's criteria mentioned in section 4.2.3. The multiplying factor was found to be in range of 0.025-0.026.
- Coalescence between cracks on several occasion induced rapid growth in other cracks, often leading to multiple simultaneous coalescences.
- In summary, the comprehensive analysis provides valuable insights into the intricate dynamics of fatigue crack initiation and propagation in additive manufactured specimens. The findings underscore the importance of considering various factors, including build direction, manufacturing defects, and porosity, in predicting and mitigating fatigue failure in components produced through additive manufacturing processes.

Chapter 5 Fatigue behaviour of micro tensile specimen

5.1 Methodology

5.1.1 Finite element model development

This study adopts a similar approach to that of Shrestha et al. [49], who utilised the Coffin-Manson and Ramberg-Osgood curve-fitting functions to derive a constitutive model from strain-life data (see Figure 5-1) and cyclic stress-strain behaviour (see Figure 5-2). The Coffin-Manson and Ramberg-Osgood functions, discussed in the earlier sections, are described by Equation 2-23 and Equation 2-20, respectively. The Ramberg-Osgood function has been frequently used in recent studies to evaluate the stress state of various specimen types and loads, including buckling behaviour [129], [130].

The parameters K' and n' were derived from the plastic portion of the tensile data (see Figure 5-1 (a)) using the assumption of the Ramberg-Osgood relation. These parameters are presented in Figure 5-1 (b). A similar technique for parameter identification was employed by Yanchukovich et al. [131] in their study, where they simulated notch strain using finite element modelling.

(a)

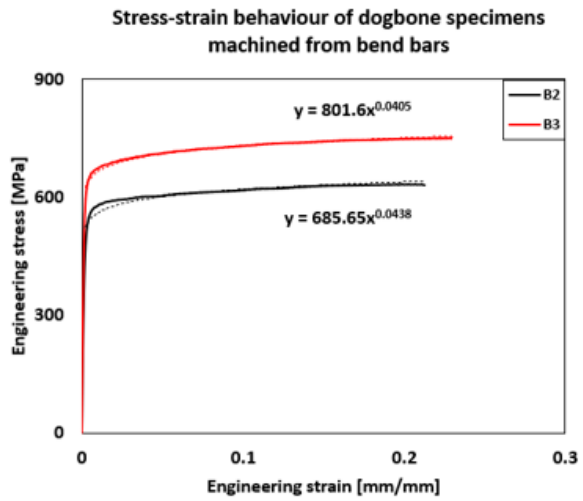

(b)

Tensile properties	Batch two	Batch three
Yield Strength (0.2%offset), σ_y [MPa]	452	565
Ultimate Tensile Strength, σ_u [MPa]	634	752
Elongation to Failure [%]	22	28
Strength Coefficient, K' [MPa]	685.65	801.60
Strain hardening exponent, n'	0.0458	0.0405

Figure 5-1: Constitutive material model of B2 and B3 specimen (a) stress vs strain relationship (b) mechanical properties.

The parameters σ_f', b, ε_f' and c were derived from the Coffin-Manson curve fitting, which characterises the fatigue behaviour of a material. Both strain-life and stress-life representations of the fatigue data are presented in Figure 5-2. For this specific finite element model, strain-life has been selected to predict the total fatigue life, as strain has been demonstrated in Section 4.2.1 to have a strong correlation with total life. The Coffin-Manson theory has been utilised in numerous recent studies for both low and high-cycle fatigue, often in combination with various isotropic and kinematic hardening techniques, notably those by Chaboche, Voce, and Ramberg-Osgood [132], [133], [134], [135].

(a)

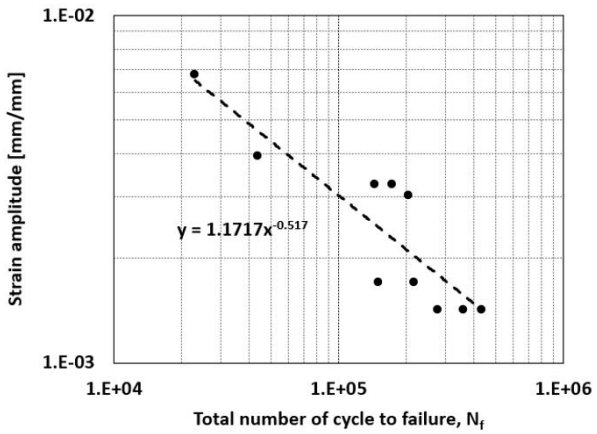

(b)

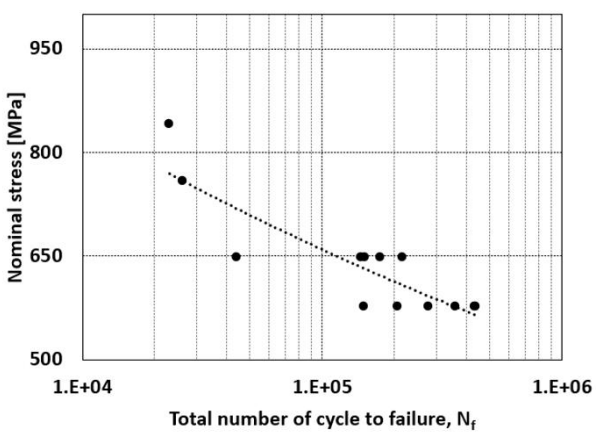

(c)

Cyclic properties		
Batch	**Two**	**Three**
Modulus of Elasticity, E' [GPa]	226.5	310.5
Cyclic Strength Coefficient, K' [MPa]	561.53	665
Cyclic Strain hardening exponent, n'	0.0432	0.0405
Fatigue strength coefficient, σ_f' [MPa]	2644	3802.5
Fatigue Strength Exponent, b	-0.517	
Fatigue Ductility Coefficient, ε_f'	1.1717	
Fatigue Ductility Exponent, c	-0.517	

Figure 5-2: Representation of fatigue life of B1 and B2 bend bar specimens (a) strain-life (b) stress life (c) cyclic properties obtained from the tensile test and the remaining parameters from the three-point bending fatigue test.

Ansys 2022 R1 was used for finite element modelling of the tension-tension setup of the micro-tensile specimen. Ansys is a widely utilised software among researchers [136], [137], [138] due to its robust

nature and the flexibility to customise material models. It also supports non-linear material behaviour and offers efficient meshing techniques. The three-dimensional micro-tensile model was initially created in SolidWorks, based on the design in Figure 5-3 (d), and exported as an IGES (Initial Graphics Exchange Specification) file for compatibility with Ansys. The non-linear material model mentioned earlier was then imported into Ansys. The entire part was meshed using the 'Quad/Tri' mesh type with the 'Hex Dominant' method, as shown in Figure 5-3 (a). A fixed support boundary condition was applied to one grip to restrict movement, while a force was applied to generate tensile stress, as depicted in Figure 5-3 (b).

Subsequently, a mesh sensitivity analysis, similar to that conducted by Cunningham [139], was performed to optimise the mesh for force convergence and to minimise stress concentration, as shown in Figure 5.3 (c). Mesh sensitivity analysis is a fundamental aspect of stress analysis using the finite element method and is commonly employed in various studies [140], [141], [142]. The critical element size for the gauge area was set at 0.2 mm, while the global element size was chosen as 0.4 mm. Similar techniques were used to simulate low-cycle fatigue in a three-point bending setup by You and Cunningham [139], [143]. After mesh generation, the total number of nodes and elements was recorded as 33,927 and 7,662, respectively. The analysis settings were configured to account for large deflections, and the force was applied in twenty-one steps to capture the non-linear behaviour of the micro-tensile specimen.

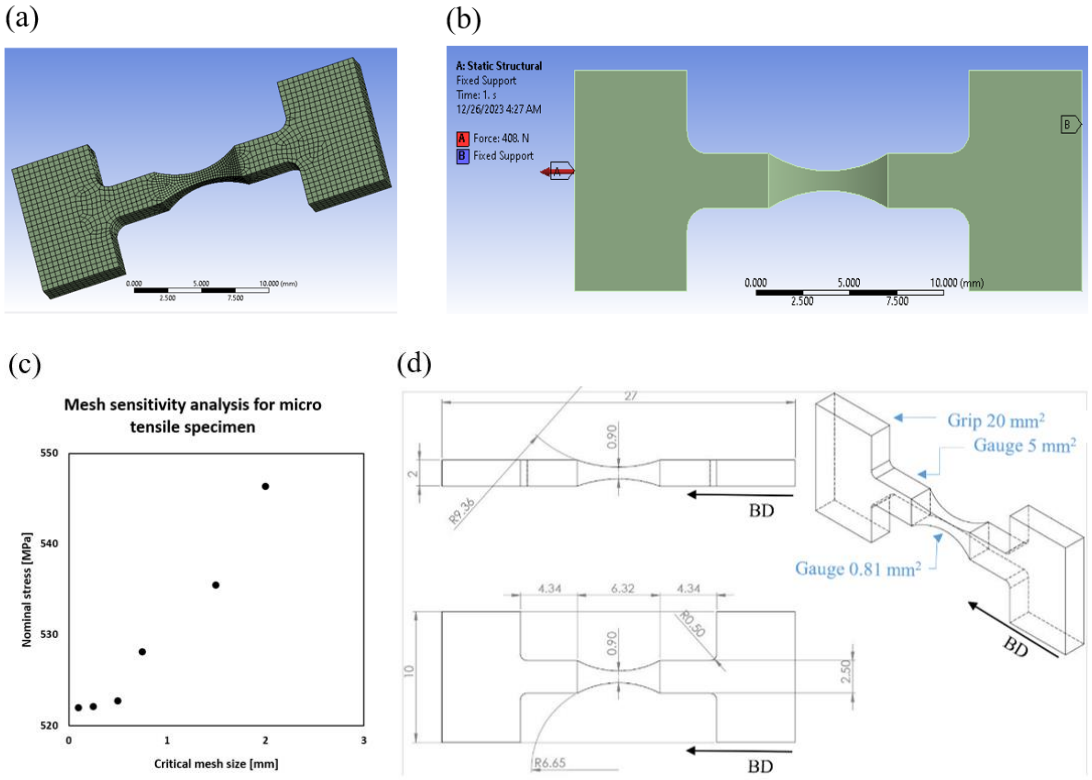

Figure 5-3: FE model of micro tensile specimen in Ansys mechanical workbench (a) meshed part with global and critical mesh size are 0.4 and 0.2 mm respectively (b) fixed support and force was applied on two end of the micro tensile specimen (c) the mesh sensitivity analysis was done to estimate optimised critical mesh size (d) dimension of micro tensile specimen used for the FE analysis and experiments.

5.1.2 Short crack test setup, specimen preparation and characterisation

The grip section of the micro-tensile specimen was sequentially ground using 120-grit and 800-grit sandpaper. The grinding and polishing of the gauge section were carried out with a Dremel 8240. The gauge section was initially ground with a 120-grit sanding band on a 13 mm mandrel, followed by additional grinding with a silicon carbide stone. The specimens were then polished sequentially with 6-micron and 1-micron diamond paste using a 10 mm polishing point.

An Alicona G4 infinite focus microscope was employed to measure the dimensions of the gauge section and later to map the three-dimensional roughness profile of the fracture surface. The smallest edge-to-edge distance from all four sides of the gauge section was measured using the Alicona, in order to determine the smallest gauge section area, which would be subjected to the highest stress. The applied force was then calculated using the following equation:

$$\text{Force} = \text{smallest area of the gauge section} \times \text{nominal stress} \qquad \text{Equation 5-1}$$

After calculating the maximum force for all the micro-tensile specimens, the mean force and amplitude were determined using Equation 2-6.

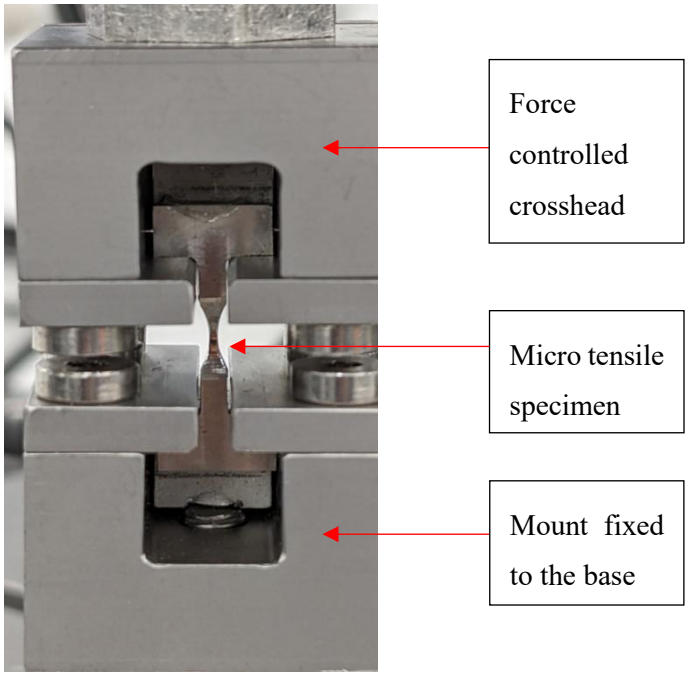

Figure 5-4: Tension-tension fatigue test of polished micro tensile specimen with E1000 electric pulse machine at R= 0.1 load ratio. Similar test setup was used by Kim et al. [112] for simulate tension-tension short crack fatigue behaviour for the micro tensile specimen.

With the exception of the rough micro-tensile specimen from batch B2, the narrowest area of the gauge section for all three specimens was measured based on the edge-to-edge distance. Detailed force calculations for these specimens are provided in section 5.2.

Additionally, a micro-tensile specimen from each batch was scanned using a Diondo D5 X-ray machine at the μ-VIS centre, operating at 10 W.

5.2 Result and discussion

5.2.1 Stress-strain response and fatigue life estimation using constitutive material model

As previously mentioned, the finite element analysis was conducted using Ansys Mechanical 2022 R1. The calculated force, based on the required nominal stress, was applied to both B2 and B3 micro-tensile specimens to simulate their stress-strain behaviour, as illustrated in Figure 5-5. A similar representation of the constitutive behaviour of micro-tensile specimens was also reported by Zhao et al. [144].

As noted in Figure 5-1 and Figure 5-2, the B3 bend bar specimen exhibits significantly higher yield strength and modulus of elasticity. Consequently, under the same applied stress, B3 specimens experienced only elastic deformation, whereas the B2 specimen underwent considerable plastic deformation. Therefore, it is anticipated that the B2 micro-tensile specimen will exhibit a significantly shorter fatigue life compared to the B3 specimen under the same nominal applied stress.

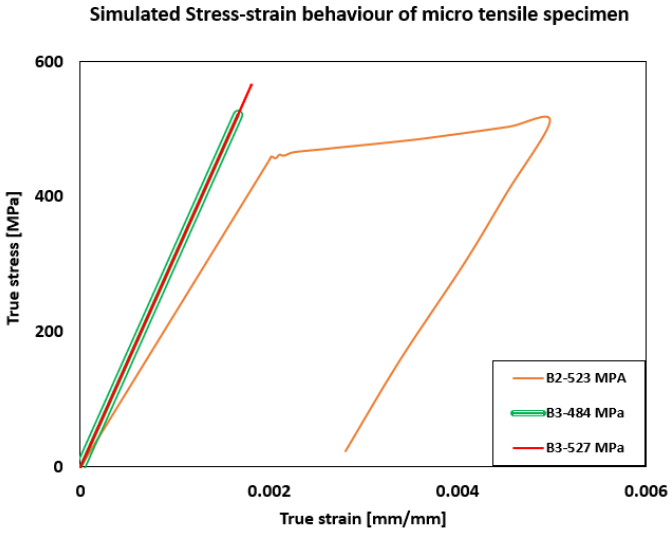

Figure 5-5: Comparison of simulated stress-strain behaviour of micro tensile specimen for B2 and B3 specimen using FE analysis.

Following the stress-strain simulation, the tension-tension fatigue life was estimated for R = 0.1 using the strain-life approach with the built-in tool in the Ansys Mechanical software package. The simulated strain deformation and stress distribution profiles are presented in Figure 5-6 and Figure 5-7, respectively. For the B2 specimen, at a nominal stress of $\sigma_{\max} = 523\,MPa$, the maximum strain recorded was 0.0051 (Figure 5-6 (c)), indicating severe plastic deformation. In contrast, for the B3

micro-tensile specimen, at nominal stresses of $\sigma_{\max} = 527\ MPa$ and $\sigma_{\max} = 484\ MPa$, the maximum strains were recorded as 0.0018 and 0.0017, respectively.

Consequently, the true stress was lower for the B2 specimen and higher for the B3 micro-tensile specimen compared to the calculated nominal stress, as shown in Figure 5-7. This is likely due to the plastic deformation of the B2 specimen, attributed to its lower elasticity limit. The strain deformation gradient pattern observed in Figure 5-6 for the micro-tensile specimens aligns with the findings reported by Zhao et al. [144]. The maximum strain deformation directly influenced the fatigue life of all specimens. Under nearly identical stress conditions, the B3 micro-tensile specimen was predicted to have a 50% longer fatigue life compared to B2 specimen, as illustrated in Figure 5-8.

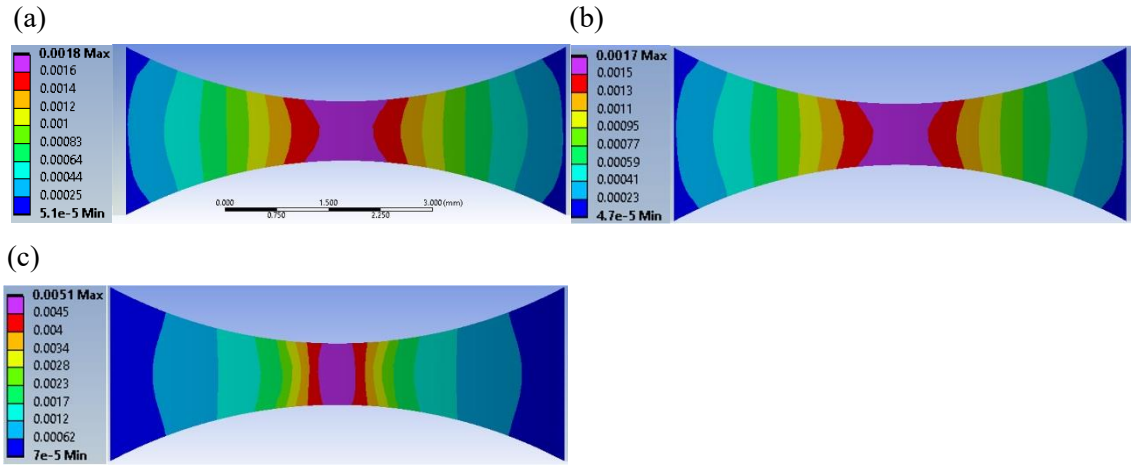

Figure 5-6: Strain deformation profile of the gauge section of the micro tensile specimens at maximum nominal stress (a) B3 at $\sigma_{nom} = 527\ MPa$, $\varepsilon_{max} = 0.0018$ *(b) B3 at* $\sigma_{nom} = 484\ MPa$ $\varepsilon_{max} = 0.0017$ *and (c) B2 at* $\sigma_{nom} = 523\ MPa$ $\varepsilon_{max} = 0.0051$. *The maximum deformed region is marked with purple colour.*

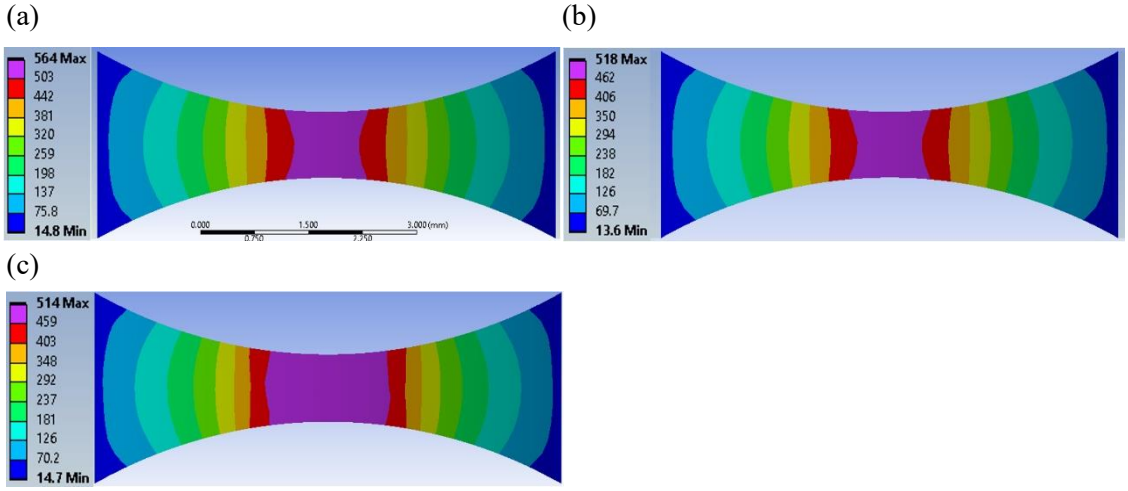

Figure 5-7: True stress distribution profile the gauge section of the micro tensile specimen (a) B3 at $\sigma_{nom} = 527\ MPa$, $\sigma_{true} = 564\ MPa$ *(b) B3 at* $\sigma_{nom} = 484\ MPa, \sigma_{true} = 518\ MPa$ *and (c) B2 at* $\sigma_{nom} = 523\ MPa$, $\sigma_{true} = 514\ MPa$. *The maximum stressed region is marked with purple colour.*

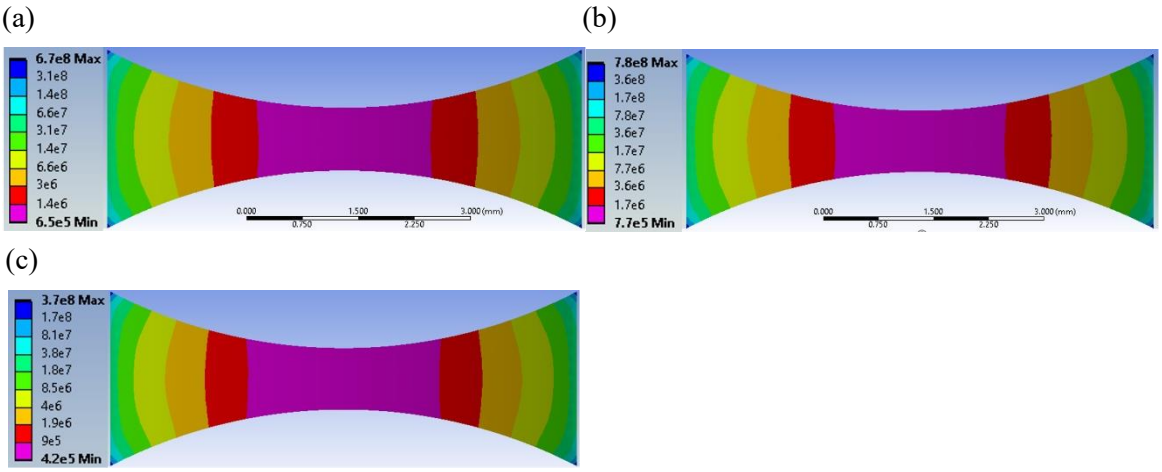

Figure 5-8: Fatigue life profile of the gauge section of the micro tensile specimen estimated with strain life approach for (a) B3 at $\sigma_{nom} = 527\ MPa$, N_f= *650k cycle (b) B3 at* $\sigma_{nom} = 484\ MPa$, N_f=*770k cycle and (c) B2 at* $\sigma_{nom} = 523\ MPa$, N_f=*420k cycle. The shortest life was marked with purple region.*

5.3 Short crack testing

Four specimens from batches B2 and B3 were cyclically loaded until failure to evaluate the fatigue behaviour of micro-tensile specimens. The objectives of the experiment were as follows:

- To assess the influence of surface roughness on the fatigue behaviour of B2 micro-tensile specimens.
- To investigate the fatigue failure of B3 specimens under two different stress levels (527 MPa and 484 MPa).
- To analyse the role of subsurface pores/defects in crack initiation and propagation behaviour.

Before conducting the short crack test, a micro-tensile specimen from each batch was scanned to map the distribution of porosities. As a baseline reference, Archimedes' principle was employed to measure the density of the B2 and B3 specimens, which were found to be 1.45 ± 0.12% and 3.31 ± 0.79%, respectively (averaged from seven specimens). However, the grip sections of the B3 specimens were not ground or polished, which may introduce error in the porosity measurement. A qualitative representation of the porosity distribution in the B2 and B3 micro-tensile specimens is presented in Figure 5-9. The B3 micro-tensile specimens displayed a significantly higher number of spherical pores and defects, whereas the B2 micro-tensile specimens exhibited a greater number of irregularly shaped defects compared to the more circular pores.

As established in Chapter 4, porosity size and distribution play a critical role in fatigue crack initiation and propagation behaviour. Therefore, the 3D porosity distribution data for the micro-tensile specimens offers potentially valuable insights. A study conducted by Liu et al. [145] reported findings that contrast with the X-ray CT data visuals Figure 5-9. According to their study, small and regular spherical pores were observed in specimens with high VED (132.4 J/mm³), in comparison to the large irregular pores formed at low VED (32.7 J/mm³) for AM Ti6Al4V specimens. The VEDs of the specimens in the study are comparable to the B3 (VED = 49 J/mm³) and B2 (VED = 138 J/mm³) specimens, respectively. Liu et al. further claimed that percentage porosity is inversely proportional to the VED, which contradicts the findings of Meier et al. [146]. However, Meier et al.'s study mainly focused on theoretical models simulating melt pools and the dynamics of heat flow rate but did not report on the shape of the melt pool as a result of varying VED.

The pore formation due to different VED values reported by both Liu et al. [145] and Meier et al. was based on blocks with a continuous cross-section unaffected by restricted heat flow. However, the micro-tensile specimens have variable cross-sectional areas across the build direction, making the heat transfer process more complex. Therefore, instead of VED, the cross-sectional area, which directly influences the heat flow rate, is more relevant for the B2 and B3 specimens. The smallest cross-sectional areas at

the gauge for the B2 and B3 specimens in Figure 5-9 are 0.44 mm² and 0.60 mm², respectively. As shown in Figure 3-23, the minimum cross-sectional area can restrict heat flow, potentially creating a thermal hotspot. It is likely that the large irregularly shaped pores in the B2 specimens result from a combination of factors, including heat flow rate and energy density.

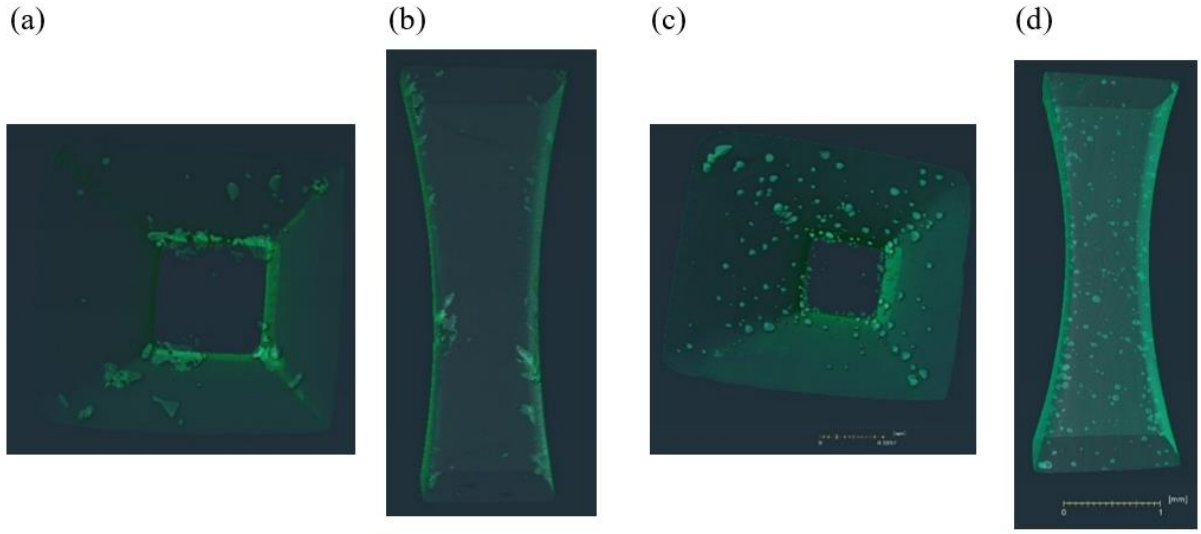

Figure 5-9: CT-scan data of micro tensile specimen after thresholding. A qualitative representation of B2 micro tensile specimen (a) cross section view (b) isometric view; B3 micro tensile specimen (c) cross section view (d) isometric view.

Before conducting the micro-tensile fatigue tests, it was crucial to accurately measure the cross-sectional area of each micro-tensile specimen to ensure appropriate load calculations and control the applied stresses. The specifications for all micro-tensile specimens are provided in Table 5-1. The smallest cross-sectional area of the gauge section was determined from the edge-to-edge length, and Equation 5-1 was then used to calculate the force corresponding to the maximum required nominal stress.

All specimens were polished, with the exception of the B2-MT1 specimen. For this specimen, the approximate cross-sectional area of the gauge was determined by subtracting the surface roughness from the measured edge-to-edge length. The surface roughness was measured using an Alicona system, expressed as the average height of the selected area, Sa. A similar technique and data representation were used by William et al. [147].

Table 5-1: Specification of the micro tensile specimens selected for fatigue testing.

	B2-MT1	B2-MT2	B3-MT1	B3-MT2
Gauge, side 1 [µm]	932 ± 46	661	785	724
Gauge, side 2 [µm]	888 ± 33	674	834	708
Gauge, side 3 [µm]	952 ± 46	637	825	766
Gauge, side 4 [µm]	922 ± 39	677	805	773
Gauge area [mm^2]	0.78	0.44	0.66	0.55
Nominal stress [MPa]	523	523	484	527
Calculated force [N]	408	229	319	218

As mentioned in the earlier section and shown in Table 5-1, a total of four micro-tensile fatigue tests were conducted to investigate the effects of process-induced surface roughness and the different stress states (uniaxial compared to the bending stress state tested in the larger samples in Chapter 4). A comparison between the stress-life data obtained from the large bend bars, the finite element (FE) simulation, and the micro-tensile fatigue tests is presented in Figure 5-10. The experimental strain-life data for the micro-tensile specimens were plotted against the strain obtained from the simulation.

The experimental data for the micro-tensile tension-tension fatigue life is slightly lower than that observed in the bending fatigue tests, while the simulated strain-life data overestimates the fatigue life of the micro-tensile specimens. The experimental results suggest that the micro-tensile specimens underperform compared to the bend bar specimens under a similar stress state. This observation contrasts with the findings of Tridello et al. [148], who asserted that smaller specimens generally exhibit a longer fatigue life due to a lower likelihood of containing critical defects that could result premature fatigue failure. They further argued that smaller specimens typically demonstrate longer fatigue life compared to larger ones, primarily due to the size effect observed in very high cycle fatigue (VHCF). This phenomenon occurs because larger specimens or components are more likely to contain significant defects within their increased volume, thereby reducing their fatigue life. As the volume of material increases, so does the probability of encountering a critical defect capable of initiating a fatigue crack, leading to failure after fewer cycles.

Numerous studies have investigated the impact of specimen size on fatigue life in metallic materials. Some of these studies [149], [150], [151], [152], [153] highlight that the size effect significantly reduces fatigue life in the very high cycle regime, with larger specimens exhibiting shorter fatigue lives. This observation is consistent with the weakest-link theory, which suggests that the fatigue life of a large specimen is governed by the shortest fatigue life among its smaller constituent volumes. However, others [151], [152], [153] suggested that the finer microstructure associated with large specimen leads to better fatigue life.

However, as briefly discussed in Chapter 4, the fatigue failure mechanism of additively manufactured specimens can be complex, and thus specimen size alone is insufficient to determine the fatigue life of microtensile specimens.

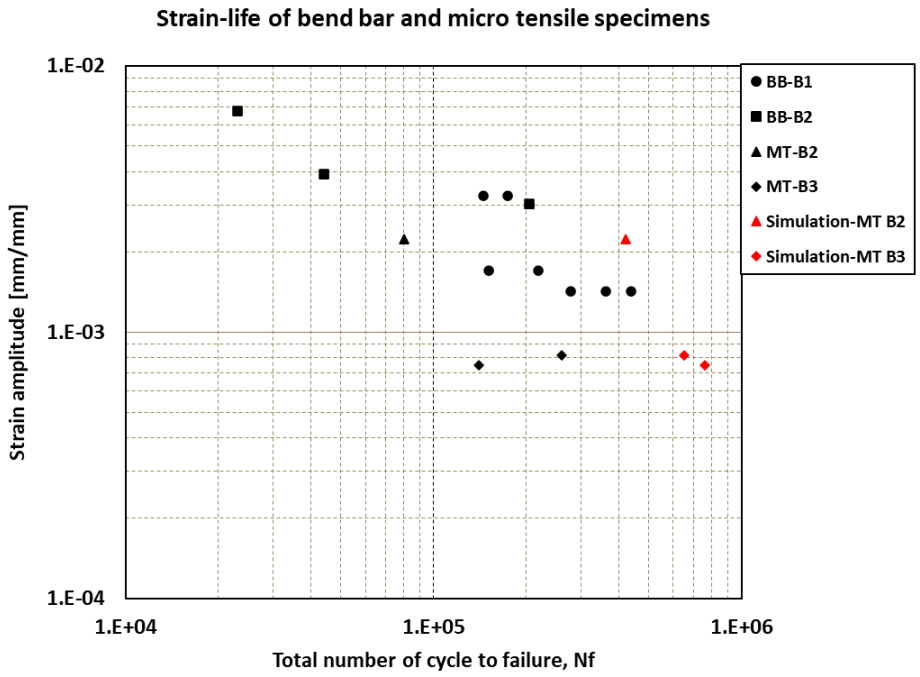

Figure 5-10: Comparison of strain-life between bending (bend bars), tension (micro tensile) and the FE simulation in Ansys. The black and red markers indicate experimental and simulation data respectively. BB and MT are data from bend bar and micro tensile specimens respectively.

5.3.1 Effect of surface roughness on fatigue behaviour

After calculating the maximum force required to achieve the desired nominal stress, a force-controlled fatigue test was conducted on the micro-tensile specimen, and force-displacement data was recorded. A comparison of the stress-displacement data obtained experimentally and through simulation is presented in Figure 5-11 for the B2 specimen. This comparison is made between the experimentally obtained nominal stress and the simulated true stress. The polished B2 specimen demonstrated good agreement with the simulated stress-displacement data. However, the rough, as-built specimen experienced severe plastic deformation during the first cycle. Subsequently, the specimen underwent constant, steady cyclic deformation for the next three cycles. Afterward, a steady increase in cyclic deformation was observed for the as-built micro-tensile specimen until it ultimately failed.

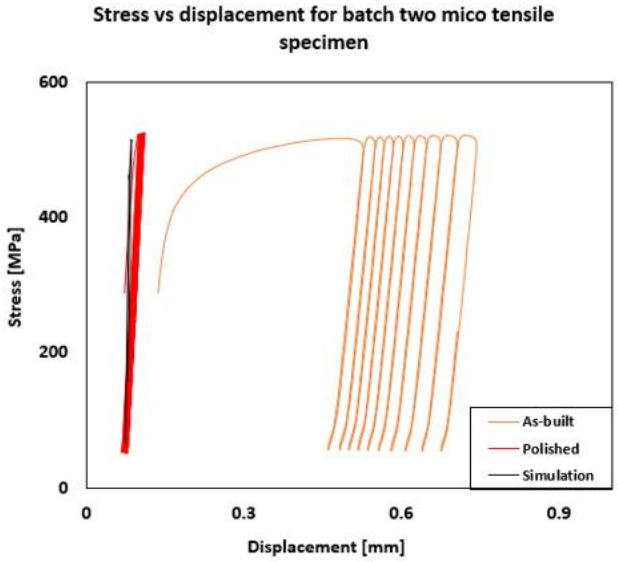

Figure 5-11: The comparison of stress-displacement data between experiment and simulation for B2 at 523 MPa maximum nominal stress.

The LPBF process introduces specific microstructural defects that play a critical role in fracture behaviour. These include residual stresses, porosity, and incomplete fusion between layers. It was evident in Chapter 4 and several studies including Tang et al. [154] that porosity in LPBF-processed 316L SS is a major contributor to crack initiation under stress. Spiering et al. [155] observed that internal defects, especially subsurface pores, reduce fatigue life by serving as nucleation sites for cracks during cyclic loading. This observation supports the understanding that subsurface defects are critical factors in fatigue failure.

The formation of pores as a function of VED is another vital aspect affecting fatigue performance. High energy density can result in larger, irregular pores due to incomplete melting or keyhole formation in

the material, leading to high porosity in AM parts, discussed in section 2.4.2.1. Ponticelli et al. [156] demonstrated that increased VED leads to a greater porosity in AM materials, which in turn affects the initiation and propagation of fatigue cracks. This suggests a direct correlation between VED and the formation of larger defects, which is a crucial factor in fatigue failure.

In addition to subsurface porosity, surface roughness plays a significant role in crack propagation [147]. Macroscopic analysis of fracture surfaces shows that large surface pores act as initiation sites for cracks. The presence of unmelted powder particles on as-built surfaces further contributes to early-stage crack initiation. This phenomenon aligns with findings in the literature, where surface defects and roughness are identified as major contributors to crack initiation and propagation in LPBF materials [2], [49], [157].

To further understand the cyclic deformation of the as-built B2 specimen, a detailed fractographic inspection was conducted (see Figure 5-12). The macro view of the fracture surface of the micro-tensile specimen in Figure 5-12 (a) provides a clear representation of the extremely rough outer surface, which is also evident in Figure 5-12 (e), (f). Figure 5-12 (c) highlights ratchet marks, indicating crack initiation and propagation on different planes, which helps to explain the severe plastic deformation. Severe plastic deformation due to ratcheting was also reported by Chen et al. [158], which aligns with the stress-displacement behaviour observed in Figure 5-11. These ratchet marks could have been initiated by surface features or material defects. The macro view of the fracture surface in Figure 5-12 (b) highlights important features on the fracture surface. For instance, Figure 5-12 (d) shows unmelted powder particles on the surface, which could have caused early-stage crack initiation, providing valuable insights into the failure mechanism. In addition, the as-built surface condition shown in Figure 5-12 (a) suggests a high level of surface roughness. Before conducting the tension-tension short crack test, an X-Ray CT scan was performed on the as-built B2 specimen. A qualitative representation of the roughness profile of the micro-tensile specimen is provided in Figure 5-12 (e), (f).

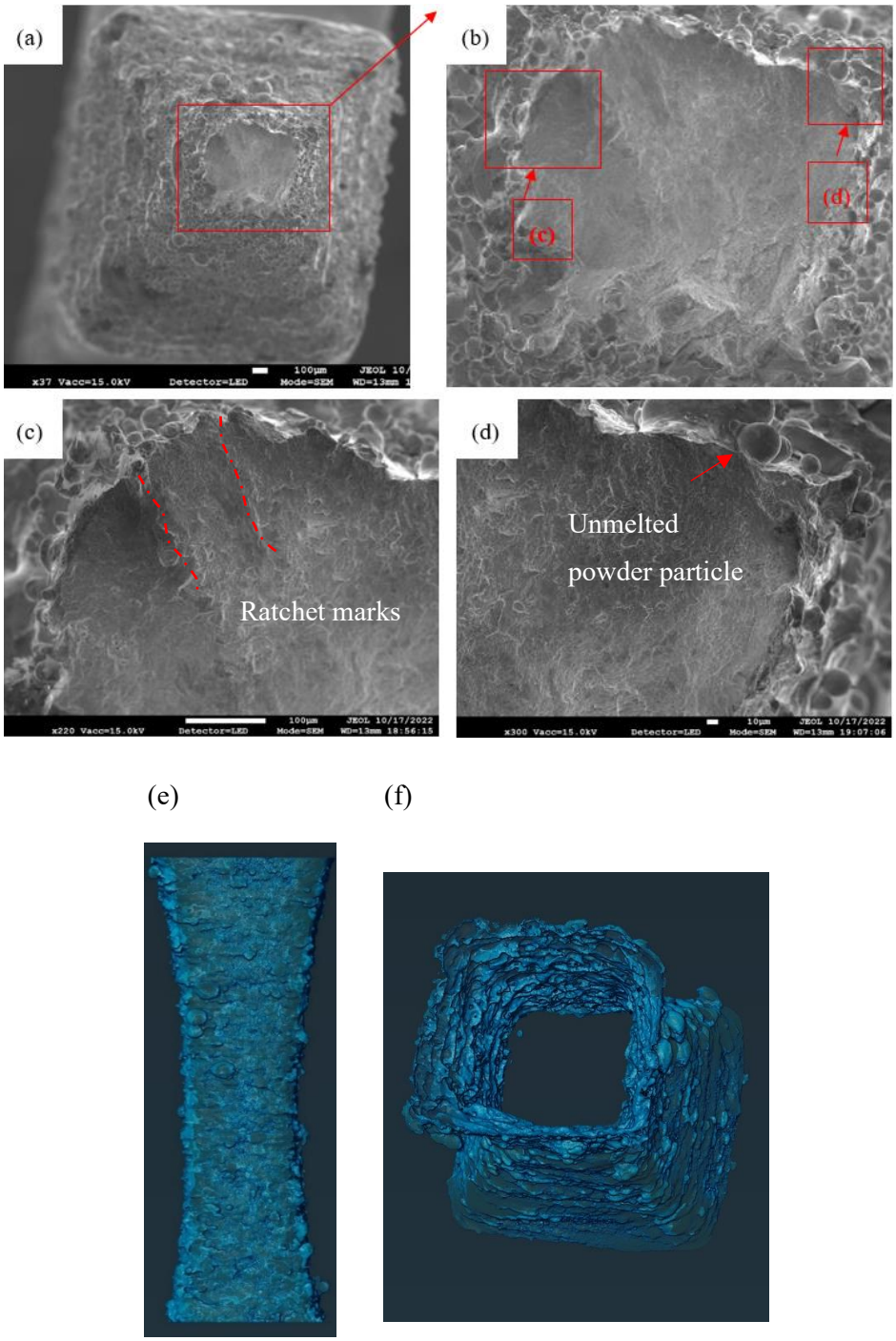

Figure 5-12: Fracture surface of B2 as-built micro tensile specimen under cyclic loading with $\sigma_{Max} = 523\ MPa$ *at R = 0.1;* N_f*= 13 cycle. (a) fractured micro tensile specimen (b) macro view of the fracture surface (c) ratchet marks resulting severe plastic deformation (d) unmelted powder particle at the surface. A qualitative representation of the surface roughness profile of the as-built micro tensile specimen (e) side view (f) isometric view.*

In contrast, the fracture surface of polished B2 specimen in shown in Figure 5-13, where several pores larger than 40 microns in diameter were observed. These pores played a critical role in controlling the fatigue behaviour of the micro-tensile specimen. The X-ray CT data in Figure 5-9 provided additional confirmation of the large defect/pore distribution throughout the gauge section of B2 micro tensile specimen. Ponticelli et al. [156] claimed in their research that high energy density leads to large defects during LPBF process. Increased VED results in greater layer thickness, which can cause less efficient consolidation and higher pore density.

In the fracture surface in the Figure 5-13 (a), the brittle fracture zones likely originated from such defects, which serve as stress concentrators. The fractography in the Figure 5-13 (b) showed crack initiation at the surface next to a large pore (45 μm), followed by simultaneous propagation from the pore. The river-lines indicate the direction of crack progression, while the coalescence of the cracks resulted in rapid propagation across the specimen's cross-section. The surface plane shift in Figure 5-14(c) is evident of the coalescence. These features, including spherical pores and other defects, were evident in various locations on the fracture surface in Figure 5-13 (c), (d) and (e).

In conclusion, subsurface pores, energy density, and surface roughness are all critical factors influencing the fatigue behaviour of AM components. These insights emphasise the need for controlling both pore formation and surface conditions to enhance the fatigue life of LPBF processed materials.

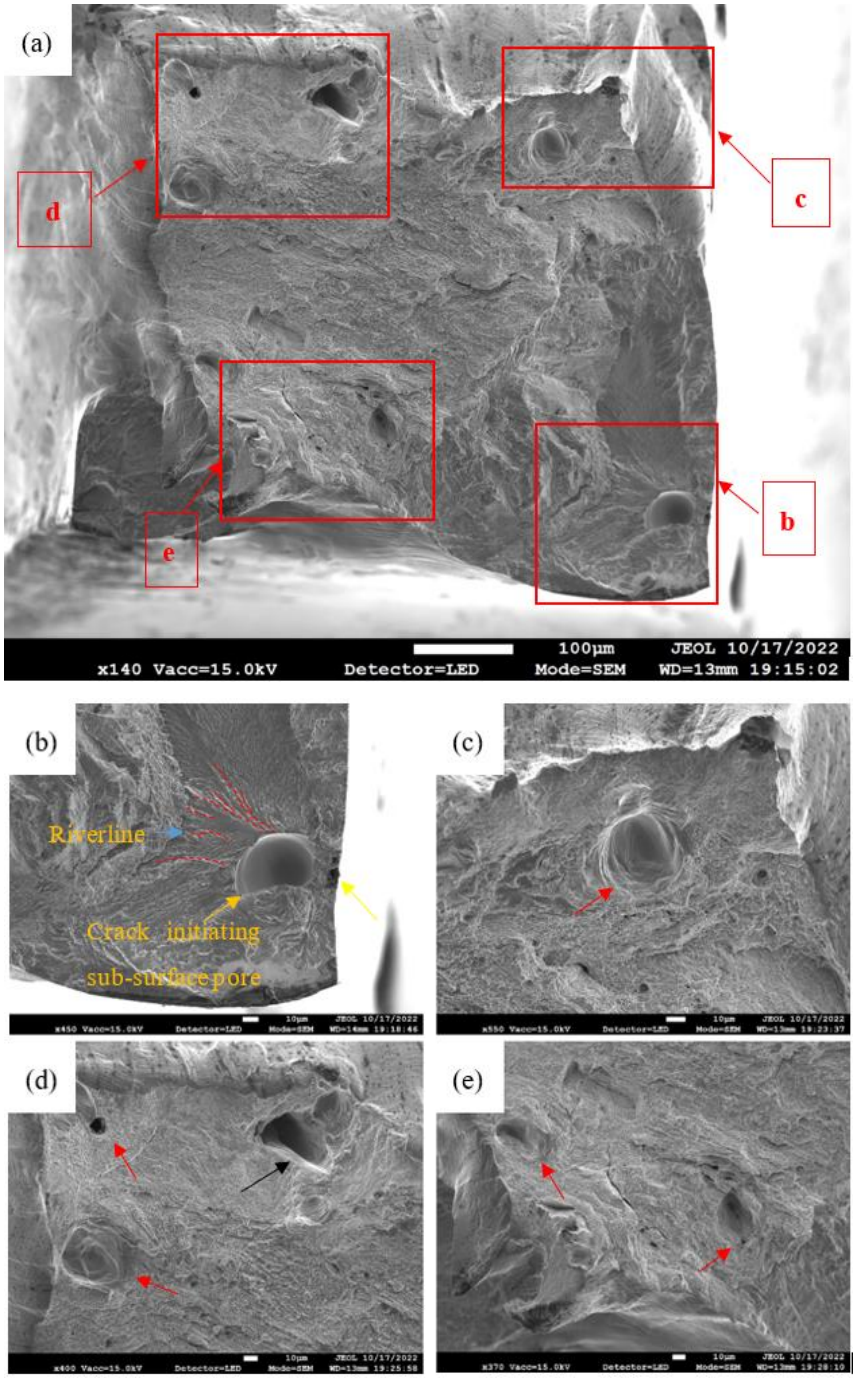

Figure 5-13: Fracture surface of 316L SS-B2 micro tensile specimen under cyclic loading at $\sigma_{Max} = 523\ MPa$ *at R=0.1;* N_f*= 80k cycle. The blue, yellow, orange, red and black arrow marks the riverline, crack initiated from slip band and pore, process induced pores and defect respectively.*

Another representation of the fracture surface can be seen in Figure 5-14, where the 3D surface profilometry indicates the final failure area. The final failure area for the as built and polished specimens are marked in Figure 5-14 (b) and (d) respectively. The final failure regions for as built and polished

specimen are 0.30 and 0.16 mm^2 respectively and they indicate 1335 MPa and 1422 MPa final failure stress respectively (indicative of likely true fracture stress).

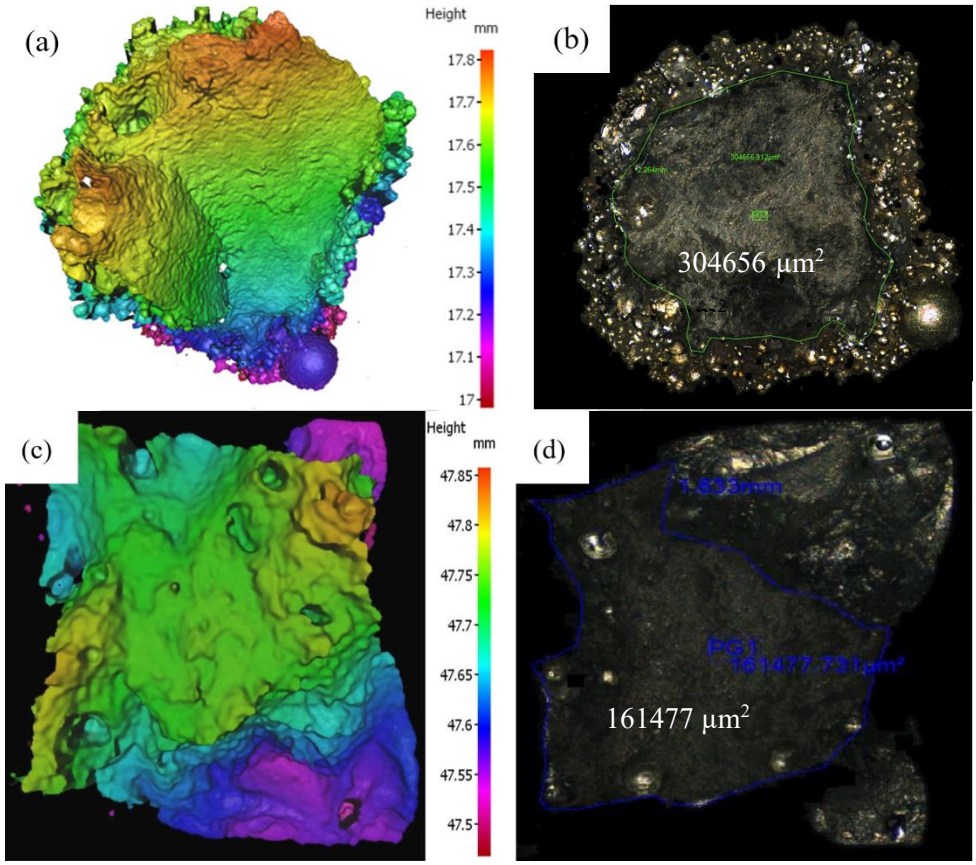

Figure 5-14:Fracture surface of B2 as-built specimen (a) 3D surface profile (b) failure region marked (0.30 mm^2); polished specimen (c) 3D surface profile (d) failure region marked (0.16 mm^2).

5.3.2 Effect of high (527 MPa) and low (484 MPa) stress on fatigue behaviour

In contrast to the B2 sample, the micro tensile specimen from B3 underwent through more plastic deformation at both stress levels (see Figure 5-15). Also, the recorded experimental data was not in good agreement with the simulated behaviour. The experimentally obtained data exhibited higher deformation for both cases compared to the simulated stress-displacement, especially at high stress amplitude. However, at higher stress amplitude, a sharp rise in deformation was observed at the beginning of the cycle. This is likely due to slipping of the specimen from the test fixtures.

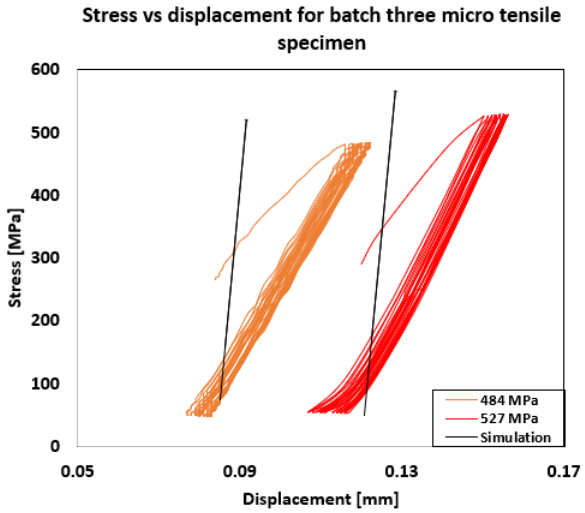

Figure 5-15: The comparison of stress-displacement data between experiment and simulation for B3 micro tensile specimen at 527 MPa and 484 MPa maximum nominal stress.

The fracture surface of the B3 micro-tensile specimen under low-stress conditions, as depicted in Figure 5-16, provides valuable insights into the failure mechanisms involved. The macroscopic overview of the fracture surface, shown in Figure 5-16 (a), highlights several regions of interest, which have been marked for closer examination. These regions reveal key features that are critical to understanding the crack initiation and propagation mechanisms that ultimately led to the specimen's failure.

The fracture surface indicates that the crack initiation occurred at a slip band rather than at a site of porosity, which suggests that the material failed through a mechanism of cyclic plastic deformation. This is supported by the observation that only four pores were identified within the final failure region, as shown in Figure 5-16 (b). These pores, while present, did not appear to play a significant role in the crack initiation, as the primary failure mechanism was related to dislocation movement along the slip band. Slip bands are indicative of localized plastic deformation, which is a common precursor to crack initiation in ductile materials under cyclic or tensile loading conditions. This finding aligns with existing

literature, which suggests that slip bands often act as sites of stress concentration and serve as precursors to fatigue crack initiation in metallic materials [62].

Further analysis of the crack initiation region, marked by river-lines in the top right corner of the macroscopic image, offers additional insights. These river-lines, magnified in Figure 5-16 (c), are indicative of the path along which the crack propagated after initiation. River-lines are typically observed in brittle fracture surfaces and signify the direction of crack growth. In this case, the presence of river-lines suggests that while the material initially experienced plastic deformation, the crack propagation mechanism involved more brittle characteristics, particularly as the crack length increased and approached critical dimensions. The crack appears to have propagated without interacting with any of the pores or other inherent defects in the material, which implies that the material was relatively homogeneous and free of significant inclusions or flaws. The absence of secondary crack initiation sites further supports the notion that a single crack was responsible for the ultimate failure of the specimen.

As the crack reached a critical length, the specimen experienced catastrophic failure. The final failure region, measuring 0.21 mm^2, corresponds to a failure stress of 1545 MPa, as shown in Figure 5-17. This stress value is indicative of the material's strength at the point of failure, and it aligns with the expected behaviour of 316L SS under tensile loading, where crack propagation accelerates rapidly once the crack reaches a critical size, resulting in fast fracture [159]. At this stage, the crack propagation would have transitioned from a slow, stable growth phase to an unstable growth phase, leading to final failure.

The presence of a ratchet mark, shown in Figure 5-16 (d), marks the transition zone between the stable crack growth region and the final failure region. Ratchet marks typically form when a crack propagates across different planes of material or when multiple cracks converge into a single failure point. In this instance, the ratchet mark highlights the region where the crack transitioned from its initial growth phase to the point of final failure. Finally, shear lip is visible in the Figure 5-16 (e), which confirms the area to be the final failure region.

Finally, the fracture surface exhibits a relatively smooth region, confirming that no secondary cracks were present. This smooth area suggests that the failure process was driven by a single dominant crack, which propagated steadily until it reached the critical crack length, leading to the specimen's ultimate failure. The absence of secondary initiation points supports the conclusion that the fatigue failure was not driven by multiple cracks, but rather by the progressive growth of a single, primary crack.

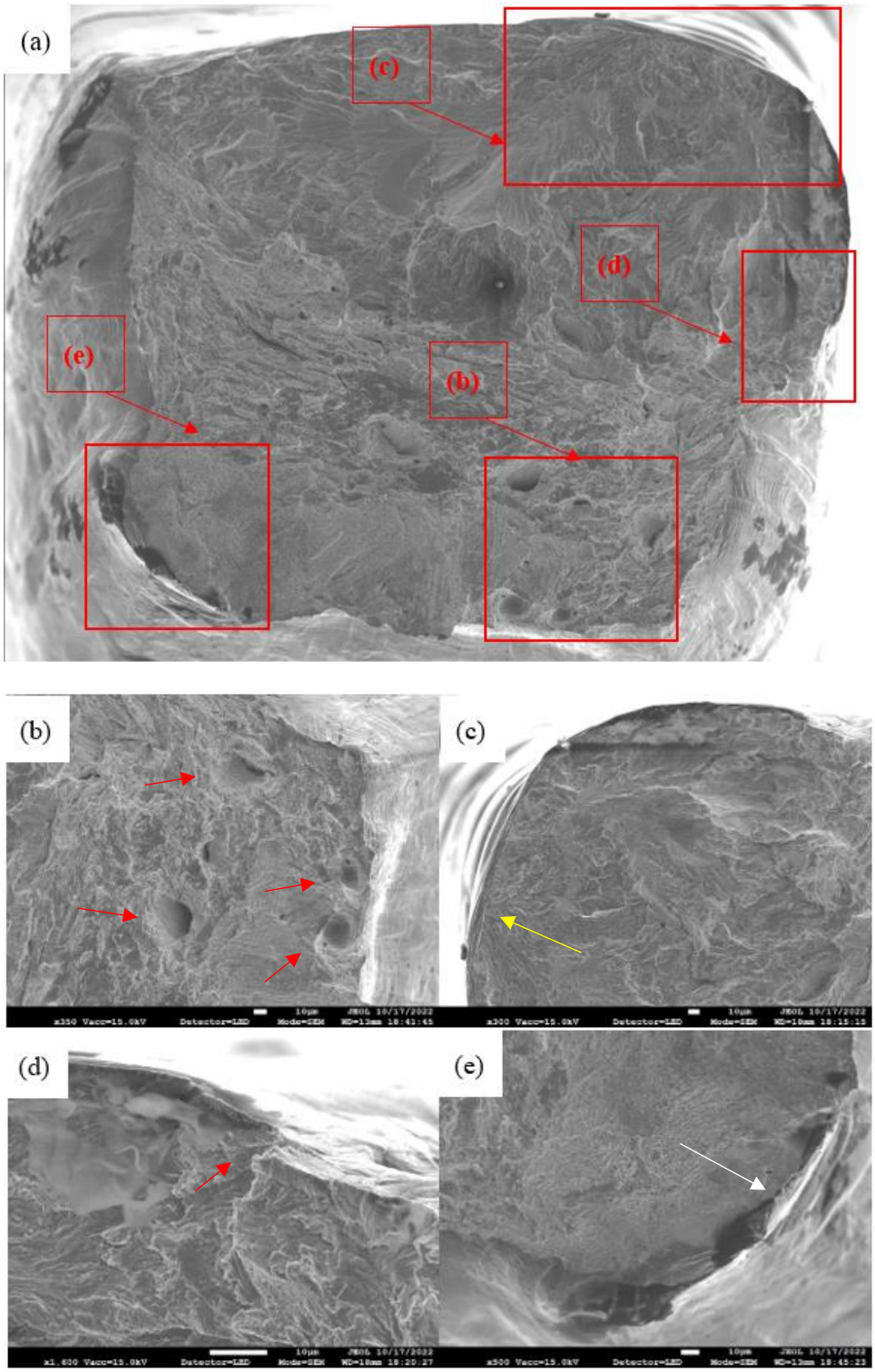

Figure 5-16: Fracture surface of B3 micro tensile specimen, which failed under cyclic loading with $\sigma_{Max} = 484\ MPa$ *at R=0.1;* N_f*=148k cycle (a) macroscopic view (b) pore on the final failure region highlighted with red arrow (c) crack initiation point highlighted with yellow arrow (d) ratchet mark indicating coalescence (e) shear lips on the final failure region is marked with white arrow.*

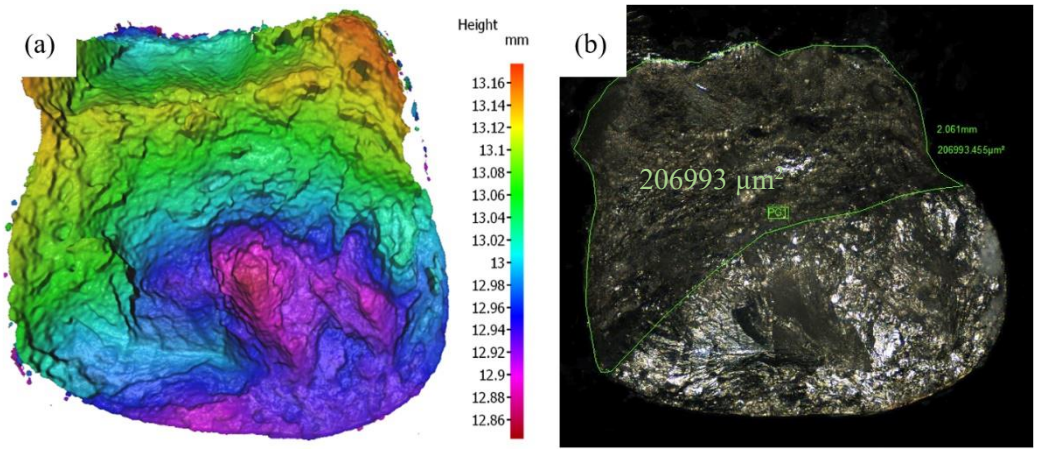

Figure 5-17: Fracture surface of B3 as-built specimen (a) 3D surface profile (b) failure region marked (0.21 mm^2). The maximum nominal stress applied was 484 MPa.

The fracture surface in Figure 5-18 (a) shows a combination of ductile and brittle fracture mechanisms. The rough surface with ridges is indicative of plastic deformation, characteristic of ductile behaviour, where the material undergoes significant deformation before failure. This type of fracture is consistent with the properties of 316L SS, known for its ductility and toughness. The red boxes in the Figure 5-18 (a) highlight crack initiation and transition regions.

Zooming into the localized fracture region in Figure 5-18 (c), we observe a brittle fracture morphology. The yellow arrow marks a smoother surface, contrasting with the rough, ductile regions. This is likely a result of localised defects, such as a lack of fusion or gas trapped porosity, common in LPBF-processed materials. This type of behaviour is further supported by studies [2], [13], [50], [160] that shows LPBF-induced defects can lead to brittle fracture, despite the inherent ductility of 316L SS. The green arrow in the Figure 5-18 (b) marks a pore on the fracture region, which is a characteristic feature of LPBF processed 316L SS.

In the case of the B3 micro tensile specimen, tested at higher stress (527 MPa), failure was driven by a single crack that originated from a slip band, as shown in Figure 5-18 (a), (c). The crack propagated without any interaction with pores, as no prominent pores were observed in the fracture surface in Figure 5-18 (a). However, two semi-elliptical pores were present in the final failure region marked with red arrow in Figure 5-18 (a). These pores, though not directly contributing to crack propagation, could act as stress concentrators in future loading cycles.

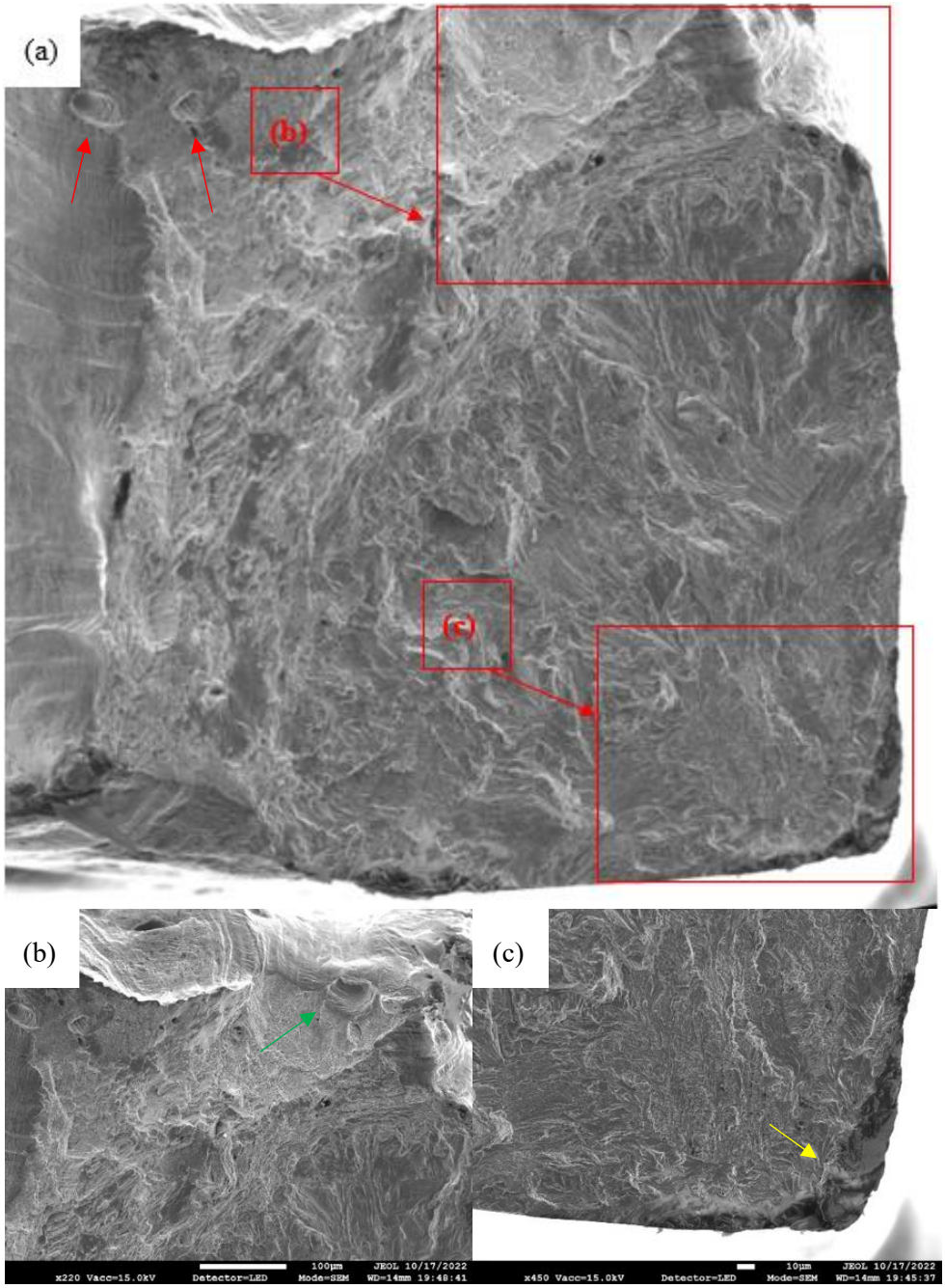

Figure 5-18: Fracture surface of B3 micro tensile specimen, failed under cyclic loading with $\sigma_{Max} = 527\ MPa$ *at R=0.1;* N_f*=260k cycle (a) macroscopic view (b) crack initiation point highlighted with yellow arrow and (c) pore on the final failure region highlighted with red arrow.*

The fracture surface area of the final failure region was calculated to be 0.19 mm², as shown in Figure 5-19 (b). From this, the final failure stress was estimated at 1510 MPa, significantly higher than the earlier applied stress. Despite different stress levels and varying fracture surface features, both B3 micro tensile specimens exhibited similar final failure stress values, indicative of the material's true fracture

stress. This suggests that even with variations in defect distribution, the material reaches a consistent stress threshold before catastrophic failure.

The final failure stress of the B3 micro tensile specimens, despite the presence of defects and differing stress levels, remained similar, with a value of 1510 MPa. This consistency in final failure stress suggests that the material reaches a critical stress level before failing, regardless of defect distribution or the presence of slip bands. The concept of true fracture stress is evident here, as both specimens showed the same threshold stress for failure. The presence of semi-elliptical pores in the final failure region, though not involved in crack propagation, further emphasizes the role of defects in determining the ultimate failure point of the material.

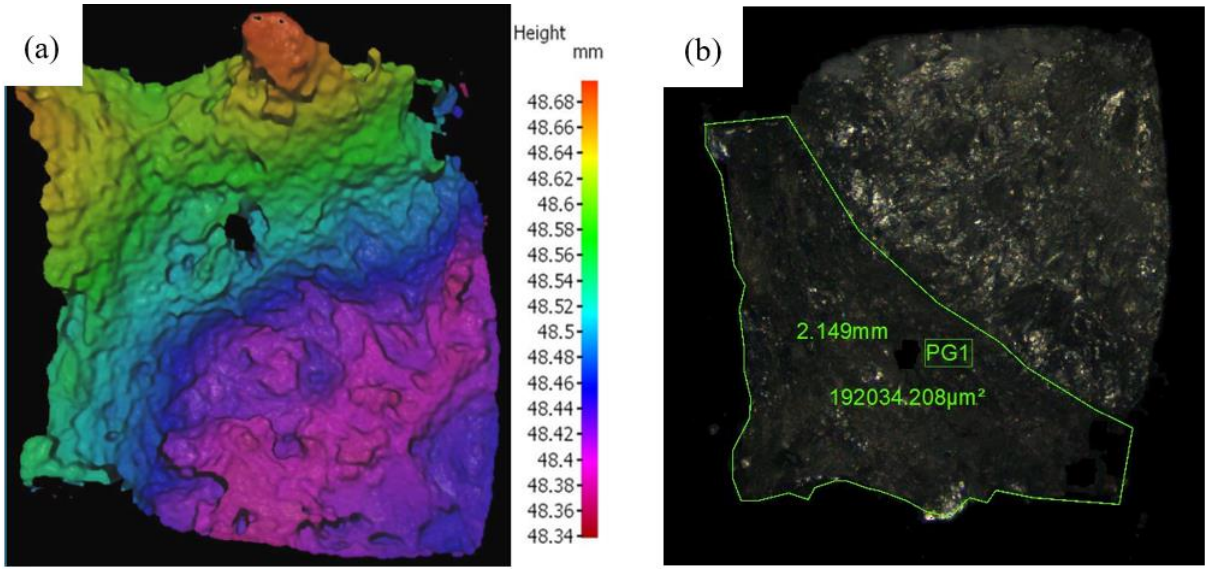

Figure 5-19: Fracture surface of B3 as-built specimen (a) 3D surface profile (b) failure region marked (0.19 mm^2). The maximum nominal stress applied was 527 MPa.

5.4 Discussion and conclusion

The examination of the short crack behaviour of micro tensile specimens required quite complex analysis. In this study, an approach was initially adopted to simulate the fatigue life behaviour through an experimentally derived constitutive material model, as detailed in Sections 3.4.2 and 4.2.1. The simulated stress-strain behaviour played a crucial role in determining the stress levels appropriate for the investigation. Subsequently, fatigue life tests were conducted on B2 and B3 micro tensile specimens, with a specific focus on independently exploring the roles of surface roughness and different stress states (i.e., uniaxial tension versus bend). Similar to the bend bar specimens, strain amplitude was found to be a reasonable representation of the controlling factor determining fatigue life; however, the micro tensile fatigue life was observed to be in general shorter than that of bend bar specimens (and below the expected lifetime based on the materials constitutive model). This is however much more likely to be linked to the importance of defect distributions in such small samples (see later discussion) than any sample volume effects or stress gradient differences between a large-scale bend bar sample and a small scale uniaxial tensile sample.

Chapter 3 reported that the gauge sections of the micro tensile specimens from B2 and B3 exhibited 12.6% and 47.5% recrystallization, respectively. It was reported by Zhang et al. that recrystallization induced by the Laser Powder Bed Fusion (LPBF) process was identified as a contributing factor to strain-sensitive areas, potentially initiating fatigue cracks and consequently shortening the overall fatigue life of micro tensile specimens, which contrast with Chapter 5 as B3 micro tensile specimen performed better compared to B2 micro tensile specimen under same stress state despite having higher percentage of recrystallised grain in the gauge section [161]. Despite the Finite Element (FE) model aligning well with the fatigue model of bend bar specimens, it was noted that the FE model (i.e., simply applying the established constitutive materials model within the uniaxial tensile stress state) overestimated the fatigue life of micro tensile specimens.

To independently investigate the impact of surface roughness on fatigue behaviour, two micro tensile specimens from B2 were examined. A qualitative representation of the 3D surface profile of the as-built micro tensile specimen revealed an extremely rough surface, detrimental to specimen life. The as built (high surface roughness) and polished specimens failed at 13 cycles and 80,000 cycles, respectively, under cyclic loading at the same nominal stress level. This huge disparity indicated the dominance of surface roughness (and very significant stress concentration features) in the fatigue crack initiation and propagation mechanism. This may also reflect the very different effective load bearing cross-section when surface roughness is effectively such a large proportion of the overall cross-section. Examination of the load-displacement response together with detailed fractography revealed coarse ratcheting occurred in the as-built specimen, indicative of high-stress concentrations leading to gross deformation

modes and possibly very high crack propagation rates, similar to monotonic tensile failure modes. Additionally, unmelted powder particles at the edge were identified as potential crack initiation points. However, for the polished specimen, subsurface porosity played a crucial role in crack propagation behaviour, and the presence of multiple large pores and defects on the final failure region further shortened the fatigue life of the specimen. Interestingly, these large pores and defects on the fracture surface closely resembled images obtained from CT-scan data. This indicates the likely increased dominance of defect distributions in such small gauge sections controlling the overall fatigue process in very different ways, dependent on the particular defect distributions in any small gauge section.

Conversely, two micro tensile specimens from B3 were subjected to micro tensile testing to investigate the role of stress state (and sample size) on fatigue crack initiation and propagation. In both cases, cracks appeared to initiate from slip bands, and no real interaction with existing pores/defects in the specimen gauge cross-section was observed. A few pores were seen on the fracture surface, but no other defects were identified. Specimens subjected to high (527 MPa) and low (484 MPa) stress levels failed at 260,000 cycles and 140,000 cycles, respectively. This non-intuitive result (shorter lifetime at the lower stress level) could be linked to differences in surface features related to polishing, which could have caused early crack propagation for the specimen with the unexpected shorter lifetime at a low-stress state. It should be noted that the polished B2 specimen showed a lower lifetime (~80k cycles) at a nominal stress of 523MPa which was linked to its propensity for surface or sub-surface porosity initiation of cracks.

Irrespective of the batch or stress state, the true failure stress calculated from the final failure area on the fracture surface for all specimens was found to be nearly twice the UTS value.

Overall, it seems as though the subtle materials microstructure differences produced due to very different heat flow characteristics during LPBF build of smaller features may affect the choice or identification of appropriate materials constitutive models that should be used in fatigue lifing. At these loading conditions, strain-life damage models seem most appropriate in predicting lifetime. However, the importance of defect distributions within the actual load bearing cross-section with respect to the mechanical fatigue behaviour of smaller features is likely to have a larger first order effect. It is evident that as-built surface roughness will have a highly significant effect, firstly in terms of the actual load-bearing area in such very small features, and then also the relative effect of the stress concentration effects from these relatively large-scale surface features on small load bearing regions needs to be considered. Even if surface roughness is removed (e.g., by surface polishing as in these tests) then the effect of surface or sub-surface porosity seems important to acknowledge (in the B2 sample near surface features appeared to initiate fatigue, whereas the B3 samples seemed to show slip band-initiated fatigue with internal porosity having little effect on performance).

Chapter 6 Overall discussion and remarks

The LPBF process is a relatively recent technology with various limitations, making it a highly active area of research. Current studies are being conducted on two parallel fronts: one aims to improve part quality through process optimisation, and the other seeks to understand the relationship between the resulting microstructure and mechanical properties. Process optimisation efforts focus on reducing porosity, surface roughness, and part distortion while increasing part strength. Meanwhile, studies on microstructure-linked mechanical properties explore the relationship between microstructural features (e.g., grain boundary distribution, recrystallisation, and crystallographic texture) and mechanical properties, especially tensile and cyclic fatigue properties of 316L SS material. While numerous studies [19], [33], [122], [162], [163], [164] have been conducted to investigate different aspects of the LPBF process and associated mechanical properties, few have comprehensively addressed the entire process-microstructure-properties relationship for LPBF-processed 316L SS.

This study was conducted to achieve three main objectives:

- Investigating the role of process parameters on LPBF-processed materials.
- Understanding the constitutive material and overall short-crack fatigue behaviour.
- Developing finite element (FE) and material models for both bend bar and micro-tensile specimens.

The objectives were achieved by first characterising the microstructure and mechanical properties of bend bars and micro-tensile specimens, processed in four different batches as described in Table 3-3. After the understanding of the process-property relationship became clearer in Chapter 3, the effects of process-induced defects/pores and tensile properties on three-point bending fatigue were thoroughly discussed in Chapter 4. Strain-life data and the constitutive material model from experiments were then used to validate the FE model, which had initially been used for load calculation for the tension-tension fatigue test of the micro-tensile specimen.

The microstructural analysis of the bend bar specimens in Chapter 3 revealed fine sub-structures in all batches, along with nickel and chromium-rich nanoparticles. These microstructural features are characteristic of AM 316L SS and have been reported in numerous studies [117], [122], [165]. Further analysis revealed grains that were elongated parallel to the build direction, while the grains appeared equiaxed and finer normal to the build direction, indicating anisotropy. Vertically built specimens exhibited stronger textures and larger elongated grains compared to horizontally built specimens. A broader analysis confirmed an inverse relationship between yield strength and average grain size, supporting the extended Hall-Petch effect, consistent with the findings of Salman et al. [40].

Additionally, a proportional increase in the standard deviation of average grain size was observed with yield strength.

Some of the key conclusions from Chapter 3 are as follows:

- Specimens built in the Z direction exhibit significantly larger columnar grains in the ZX plane compared to those built in other orientations, due to concentrated laser heat input and slower cooling in the Z direction. Additionally, Z-built specimens display a strong crystallographic texture in the <101> direction, attributed to prolonged heat exposure, which aligns with the findings of Leicht [166].
- Z-built specimens also demonstrate more pronounced anisotropy and a lower degree of recrystallisation compared to X and Y built specimens. This results in lower strength and ductility in Z-built specimens when loaded in tension along the build direction, likely due to material anisotropy. Hardness tests confirmed this anisotropy on XY and ZX planes for both horizontally and vertically built specimens, which is in agreement with Palmeri et al. [167].
- Consistently higher elongation to failure was observed in horizontally built (Y) specimens compared to their vertically built counterparts, confirming anisotropy, and aligning with the work of Ponticelli et al. and Wang et al. [156][168]. Wang et al. attributed the enhanced mechanical properties to a finer grain structure and increased dislocation density. The anisotropy observed in their study was linked to the presence of textured and columnar grains, consistent with the findings of Section 3.4.2.
- The vertically built specimen from B3 demonstrates higher strength and ductility, likely due to additional contour scanning, which distinguishes it from other vertically built specimens, agreeing with the work of Salman et al. [40]. The mechanical properties of vertically built specimens from B3 are comparable to horizontally built specimens from other batches.

From Chapter 3, it is clear that processing parameters such as energy density and build orientation can significantly influence the microstructure, as evidenced by the results from bend bar specimens. The energy density employed in the Laser Powder Bed Fusion (L-PBF) process plays a critical role in determining the grain size and overall microstructure of the produced material. According to Leicht [166], lower energy densities result in significantly smaller grain sizes, with a nearly fifty percent reduction observed in samples processed at the lowest energy density (58.0 J/mm^3) compared to those manufactured at higher energy densities, such as 203.1 J/mm^3.

During the L-PBF process, the heat generated in the melting stage is primarily dissipated through conduction towards the build plate, shaping the material's microstructure. This heat flow impacts a variety of structural features, ranging from millimetre-scale elongated grains separated by high-angle grain boundaries to nanometre-scale features such as melt pool boundaries, cellular sub-structures, and

precipitates. The rapid melting and high cooling rates (10^4 to 10^6 K/min) inherent in L-PBF promote the development of a fine cellular sub-structure morphology, with the thermal gradient playing a pivotal role in cell size. Faster heat transfer leads to finer cellular structures, while slower dissipation results in coarser cells. This phenomenon explains the geometry size-scale effect on the microstructure of micro tensile specimens, as illustrated in Figure 3-23. The restricted heat flow path in the micro tensile specimen created a "hot spot," resulting in slower cooling in the intermediate 5 mm² gauge section area. This caused the formation of a finer cellular structure and larger columnar grains compared to other areas (see Figure 3-19(a) and Figure 3-22(a)).

The micro tensile specimens exhibit a trend where the average grain size decreases with increasing cross-sectional area on the XY plane, due to varying heat transfer rates, as described by Equation 3-1. The largest grains are found in the intermediate gauge section, in the ZX plane (parallel to the build direction), where restricted heat flow triggered recrystallisation-driven grain growth. This trend is most pronounced in B2 specimens due to the high heat input. Recrystallisation-driven grain refinement and growth in L-PBF has been described by Sabzi et al. [169] as a three-step process. They deduced that the rapid cooling rate during solidification in the L-PBF process, particularly during the initial two thermal cycles, results in the formation of a highly deformed cellular microstructure. In the third thermal cycle, both discontinuous and continuous dynamic recrystallisation are activated, leading to grain refinement. During the fourth thermal cycle, dynamic recovery and grain growth occur. This is consistent with the refined grains and higher recrystallisation in the smallest gauge section area on the ZX planes.

The dynamic recrystallisation mechanism was reported by Pinto et al. [117], where both time and temperature were identified as critical factors in facilitating the dynamic recrystallisation process in LPBF 316L SS. Elevated temperatures provide the necessary atomic mobility and grain boundary movement, while the duration of annealing determines the extent of recrystallisation and nanoparticle coarsening, both of which influence the kinetics of the process. This also explains the high percentage of recrystallised grains in the critical gauge areas of the B2 (0.68 mm²) and B3 (0.28 mm²) micro tensile specimens. The low heat flow rate in this region is responsible for the high percentage of recrystallisation.

On the other hand, microstructural porosity was found to be linked with build orientation, with Z-built specimens exhibiting higher porosity (nearly 1%) compared to the horizontally built X and Y specimens (0.23% and 0.43%, respectively). This increased porosity in Z-built specimens, along with coarser grain and sub-grain microstructures, may explain their lower strength and ductility despite the usual correlation between these properties. A similar effect of build orientation on porosity has been reported in numerous studies [170][171], [172]. Fatemi et al. [171] and Beretta et al. [172] both claimed in their studies that build direction has a significant influence on fatigue properties, primarily due to orientation-

related factors. This is particularly evident in SLM steels, where lack of fusion defects and porosity are typically elongated in a direction perpendicular to the build orientation. Horizontally printed specimens were reported to exhibit a higher distribution of smaller-diameter porosities, resulting in superior fatigue properties compared to those printed vertically. However, as shown in Figure 4-15 and Figure 4-25, there were cases of larger singular defects in horizontally built specimens (X4), compared to the larger number of smaller spherical pores observed in the vertically built specimens.

As part of the continued material characterisation, the effect of tensile properties and porosity/defects on fatigue behaviour was investigated in Chapter 4, using a three-point bending setup with bend bars from two different batches (B1 and B2). After cyclically loading the bend bar specimens in the three-point bending setup at two primary stress states (maximum nominal stresses of 576 and 648 MPa), crack monitoring revealed intricate crack propagation and coalescence dynamics. Analysis of the distribution of surface porosity in Figure 4-7 showed a higher percentage of large pores and clustering behaviour in Z2 specimens, whereas X and Y built specimens exhibited smaller pores, with the exception of X4, which had a large lack of fusion porosity on the surface. This observation is consistent with the findings of Palmeri et al. [167], who reported that porosity percentage is highest in specimens manufactured with a vertical (90°) build orientation. In contrast, specimens produced at 0°, 15°, and 30° build orientations exhibited no porosity defects. Their study suggests that larger deposition surfaces and support structures at lower angles help mitigate edge effects and minimise porosity, which supports the porosity shape and distribution observed on the bend bar specimen surfaces.

After a thorough analysis of the fracture surfaces, the origins of crack initiation for specimens from B1 and B2 are summarised in Table 6-1. Notably, the horizontally built X4 and Y4 specimens exhibited a higher number of cracks initiated from pores and fewer from PSBs compared to the vertically built Z3 specimen, despite being subjected to a similar stress state (648 MPa). In all of the vertically built specimens, a greater number of cracks were initiated from PSBs than from open surface pores compared to horizontally built. This difference in initiation mechanism may explain the strain-life representation of the bend bar specimens (Figure 4-6 (b)), in which the fatigue life of most bend bar specimens can be reasonably explained except for Z2, Z3, and Z5. PSBs are formed due to localised plastic strain, which is linked to the material's yield strength. As shown in Figure 3-13, the yield strength of the material is inversely proportional to the average grain size. Vertically built specimens from batches B1 and B2 had larger grains and lower yield strength, and more crack initiations from PSBs, indicating that the microstructure has a direct influence on the crack initiation behaviour of the LPBF processed 316L SS.

The extended fatigue life observed in certain specimens can be attributed to the complex behaviour of crack propagation and coalescence. For instance, in the Z5 specimen, multiple cracks initiated simultaneously and in parallel, leading to significant crack stress shielding behaviour, which is detailed in Figure 4-31 using a fracture mechanics approach. Similarly, the Z2 specimen exhibited a total of

seventeen cracks on the top surface, many of which initiated simultaneously. Observations of crack propagation revealed intricate stress shielding and anti-shielding behaviour. Consequently, the fatigue failure behaviour of AM 316L SS bend bars can be considered highly complex.

Table 6-1: Numerical representation of crack initiation origin for different bend bar specimens.

Batch name	Specimen name	Applied maximum nominal stress, MPa	Number of cracks initiated from pores	Number of cracks initiated from PSBs
B1	X3	576	1	1
	X4	648	3	1
	Y3	576	2	0
	Y4	648	3	1
	Z2	648	11	6
	Z3	648	2	4
B2	Z5	576	2	8
	Z7	648	1	10

The fatigue performance of LPBF processed specimens is significantly influenced by factors such as surface roughness, porosity, and energy density. Following the investigation of the fatigue behaviour of the macro scale bend bar specimens, this study delved into the fatigue behaviour of the micro tensile specimens, examining critical aspects such as defect distribution, stress gradients, and sample size.

In an effort to simulate the fatigue life behaviour of these materials, a constitutive material model was employed, as detailed in the methodology in section 5.1. The model's predictions, however, were generally more accurate for larger bend bar specimens than for smaller micro tensile ones, highlighting the unique challenges posed by small-scale samples. This discrepancy in fatigue life predictions is attributed not to the sample volume or stress gradient differences but to the crucial role of defect distribution within smaller specimens. These defects, particularly subsurface pores and surface roughness can act as stress concentrators that accelerate crack initiation and propagation.

Specifically, in the case of micro tensile specimens, fatigue life was shorter compared to bend bar specimens, which is in agreement with Tridello et al. [148]. Batch B2 and B3 micro tensile specimens showed a significant reduction in fatigue life compared with bend bar specimens, which was linked to the role of defects, particularly under cyclic loading. In the B2 sample, two micro tensile specimens with different surface finishes (as built vs. polished) were tested. The as-built specimen, with its rough surface, failed at just 13 cycles, while the polished specimen endured up to 80,000 cycles under the same nominal stress. This significant disparity underscores the dominance of surface roughness in fatigue crack initiation. The rougher surfaces exhibited coarse ratcheting, a phenomenon indicative of stress concentration and gross deformation, leading to premature failure. Additionally, unmelted powder particles near the surface were identified as likely crack initiation points. In contrast, the polished B2 specimen, though it survived longer, ultimately failed due to subsurface porosity. The CT scan images revealed large pores near the fracture surface, pointing to the role of these defects in fatigue behaviour. This demonstrates that even with surface roughness reduced, the presence of internal defects, especially in small samples, remains a critical factor in determining fatigue life.

The microstructural variations within the material also played a significant role in the fatigue behaviour. B2 specimens exhibited 12.6% recrystallization in their gauge sections, while B3 specimens showed a much higher level of recrystallization at 47.5%. Zhang et al. [161]laimed that recrystallization, induced by the LPBF process, introduced strain-sensitive regions that were prone to crack initiation, thereby shortening the fatigue life which contrasts with the finding in Chapter 5. In general, smaller gauge sections, such as those in micro tensile specimens, are more sensitive to such microstructural differences, influencing their overall performance under fatigue loading.

Furthermore, B3 micro tensile specimens subjected to different stress states offered further insights into the fatigue mechanisms. When tested under both high (527 MPa) and low (484 MPa) stress levels, the specimens failed at 260,000 cycles and 140,000 cycles, respectively. Surprisingly, the lower stress specimen failed earlier, possibly due to differences in surface features that led to early crack propagation. Unlike B2, where porosity played a crucial role in failure, B3 specimens showed crack initiation from slip bands with minimal interaction with existing pores or defects. This may be attributed to the contour scanning around the perimeter of B3 specimens, which is known to reduce surface roughness, and was absent for B2 specimens. Nevertheless, the B3 specimen results suggest that surface characteristics, even in the absence of prominent defects, can significantly influence fatigue life.

Despite these variations in fatigue behaviour across different specimens and stress conditions, a common observation from the microtensile testing was the consistently higher failure stress relative to the material's Ultimate Tensile Strength (UTS). In all cases, the true failure stress calculated from the final fracture area was found to be nearly twice the UTS value. This phenomenon, observed across both

polished and as-built specimens, reflects the complex interplay between microstructure, surface roughness, and defect distribution in determining fatigue performance.

The findings from this study highlight several important considerations for improving the fatigue life of LPBF-manufactured components. First, surface roughness is a dominant factor in crack initiation and must be minimized to enhance fatigue performance, particularly in small features, supported by numerous studies [2], [49], [150], [157]. Even after polishing, however, subsurface porosity remains a significant concern, indicating the need for improved process control during the LPBF process to reduce internal defects which is in agreement with Sheridan et al [50] and Tammas et al [160]. Furthermore, the study illustrates those microstructural variations, such as recrystallization can affect fatigue crack initiation, particularly in smaller samples. Finally, while strain-life damage models remain a useful tool for predicting fatigue life, their accuracy can be compromised by the presence of defects and microstructural heterogeneity, especially in small, highly stressed regions.

In conclusion, this study demonstrates the significant impact of processing parameters on the mechanical properties and microstructure of LPBF-manufactured 316L stainless steel. Key factors such as build orientation, energy density, and cooling rates affect grain size, porosity, and recrystallisation, influencing fatigue behaviour. Vertical specimen Z2 from B1 exhibited larger columnar grains and greater porosity, leading to reduced mechanical properties compared to horizontal specimens. Additionally, surface roughness and internal defects, particularly in smaller specimens, were identified as critical contributors to premature fatigue failure. Further refinement of the LPBF process is necessary to enhance fatigue life.

Chapter 7 Summary and conclusion

To conclude, the examination of microstructures and mechanical properties in LPBF-processed specimens has provided valuable insights into the intricate relationship between laser parameters, specimen orientation, and geometry. Notably, the average grain size consistently displayed uniformity on the XY plane across all specimens, while the Z built on the ZX plane exhibited significantly larger columnar grains. This disparity is attributed to concentrated laser heat input, resulting in extended heat paths and slower conductive cooling. The Z built specimens additionally manifested a robust crystallographic texture in the <101> direction due to prolonged heat exposure, with both properties influenced by heat accumulation along the extended heat path. Moreover, an inverse relationship between average grain size and material strength, coupled with a direct correlation with grain size dispersion, was observed. Also, microstructural inhomogeneity was evident in vertically (Z) built specimens, showcasing stronger crystallographic texture and lower recrystallization percentages. These differences correlated with reduced strength and ductility, particularly when subjected to tension along the build direction, revealing anisotropy effects. Hardness testing confirmed high anisotropy in both XY and ZX planes for X and Z built specimens. The Z built specimen from B3, with additional contour scanning, exhibited enhanced strength and ductility, differentiating it from other Z built specimens. The average porosity of B1 Z built specimens was found to be significantly higher compared to X and Y built specimens.

Further investigation of mechanical properties led to the exploration of high-cycle fatigue for LPBF-processed 316L SS bend bars. Initially localised strain amplitude (which is microstructure dependent, essentially linking fatigue with process parameter influenced microstructure) was identified as a good representation of fatigue life but upon thorough investigation, intricate relationships between material defects, stress states, and fatigue lifetime were unfolded. The study further highlighted the importance of surface defect distribution, initiation events, and coalescence mechanisms in controlling fatigue behaviour.

On the other hand, micro tensile specimens, when analysed for grain size variation, demonstrated consistent trends, emphasizing the impact of heat flow restrictions in the intermediate gauge section. This effect-initiated recrystallization-driven grain growth processes, emphasizing the crucial role of complex thermal conditions in microstructure evolution. These findings underscore the intricate interplay of LPBF process parameters, orientation, and specimen geometry in shaping microstructures and properties. The study highlights that higher strength and ductility are associated with orientations featuring thicker layers and low energy density, while restricted heat flow influences the recrystallization process, potentially compromising material strength.

Further investigation of short crack behaviour in micro tensile specimens involved a complex analysis, employing an experimentally derived constitutive material model for simulating fatigue life behaviour. Despite aligning well with fatigue models for bend bar specimens, the finite element model overestimated the fatigue life of micro tensile specimens. Factors such as surface roughness, stress states, and defect distributions emerged as crucial contributors to fatigue behaviour. The investigation of micro tensile specimens emphasized the influence of surface roughness, stress states, and defect distributions on fatigue behaviour. Surface roughness emerged as a dominant factor, with as-built specimens exhibiting significantly shorter fatigue life than polished counterparts. Defect distributions played a crucial role in fatigue crack initiation and propagation. Subsequently, no strong evidence was found for the high recrystallization in the critical gauge section linked to strain-sensitive areas to potentially have resulted in crack initiation from persistent slip bank, owing to the effect of size scale of LPBF parts on microstructure.

In conclusion, this study contributes to our understanding of LPBF-processed material behaviour under cyclic loading conditions. for detailed considerations in fatigue lifing, examining the intricate interplay of material microstructure It underscores the need to fully assess defect distributions and surface conditions. The findings pave the way for more refined models and lifing techniques tailored to the specific challenges posed by LPBF components.

Chapter 8 Future work

The overarching goal of this project is to develop a fatigue life prediction approach tailored for complex structures, such as heat exchanger geometries that contain intricate small-scale features. This approach would be grounded in the insights gained from the aforementioned investigations. However, while the FE model in Chapter 5 contributes significantly to understanding fatigue behaviours in materials, it is important to recognize its limitations. One key limitation is its inability to account for combined cyclic hardening behaviour. The model does not integrate more advanced hardening frameworks, such as the combined Voce-Chaboche model, which has demonstrated superior predictive capabilities in scenarios involving complex loading. For instance, You [173] successfully applied this combined hardening model to simulate cyclic behaviour under variable loading conditions. Incorporating such advanced hardening models into the FE framework could improve the accuracy of fatigue life predictions across diverse loading paths, enhancing the model's applicability to practical, real-world conditions like those found in heat exchangers.

In addition, the current model does not consider critical factors such as porosity, surface defects, or surface roughness, all of which are well-known to significantly influence fatigue crack initiation and propagation. These imperfections, especially in additively manufactured metals, can act as stress concentrators that reduce the fatigue life of the material. The lack of these considerations renders the model limited, particularly when addressing components that undergo cyclic loading in harsh environments or those that are manufactured using processes prone to these defects. To rectify this, future work should incorporate techniques to model porosity and surface roughness explicitly. The inclusion of surface imperfections and microstructural features in the model would provide a more realistic prediction of fatigue life.

Furthermore, the current FE model only applies to uniaxial or sequential loading conditions, making it insufficient for multiaxial stress states, which are prevalent in many real-world applications such as heat exchanger and automotive components. The introduction of multiaxial fatigue models would extend the model's usability to a broader range of industries. Multiaxial fatigue is a dominant mode of failure in these fields, as components are frequently subjected to complex loading conditions that involve various stress components. Therefore, expanding the FE model to account for multiaxial loading would significantly increase its predictability in practical applications and thus could be useful for the industrial partner, Vestas Aircoil.

Another promising area of future research lies in advanced imaging techniques for microstructural analysis. For example, a 3D mapping of porosity in micro-tensile specimens using X-ray computed tomography (CT) could provide critical insights into the distribution and impact of internal defects on

fatigue behaviour. Interrupted fatigue tests combined with in-situ X-ray CT scanning would allow real-time observation of crack initiation and propagation, offering a more detailed understanding of the crack growth mechanisms in LPBF 316L stainless steel. Chatziathanasiou et al. [174] took an approach to map the porosity distribution in 3D space but could not investigate in-situ crack propagation behaviour for AlSi10Mg alloy. Qian et al.[175] attempted to employ similar approach to investigate crack propagation behaviour in composite material but their study had multiple limitations:

- The resolution of the micro-CT scans was constrained in their study, with a voxel size of 15.6 micron, which was inadequate for precise fibre tracing and detailed crack front analysis.
- The study was unable to perform 2D edge monitoring techniques to capture the 3D crack front effects, which further complicated their analysis, despite the improvements offered by in-situ micro-CT.

To address these limitations, future research should focus on enhancing the resolution of CT scans to enable more detailed analysis to fully capture crack propagation behaviour. The muVis facility at the university of Southampton offers a very high-resolution imaging with minimum of 0.7-micron voxel size. In fact, the micro-CT data presented in Figure 5-9, was scanned with 3-micron voxel size. Additional exploration into mode II and III effects could help clarify their influence on fracture behaviour.

In conclusion, the limitations of the current FE model provide clear directions for future work. The integration of more advanced hardening models, the inclusion of surface and internal defects, and the extension to multiaxial loading scenarios will significantly enhance the model's applicability and accuracy. Coupled with state-of-the-art imaging techniques like X-ray CT, these improvements will enable more accurate predictions of fatigue life, leading to a more reliable designs for applications such as exchangers, which was one of the initial objectives of the project.

Chapter 9 Appendix

9.1 Microstructure and mechanical properties

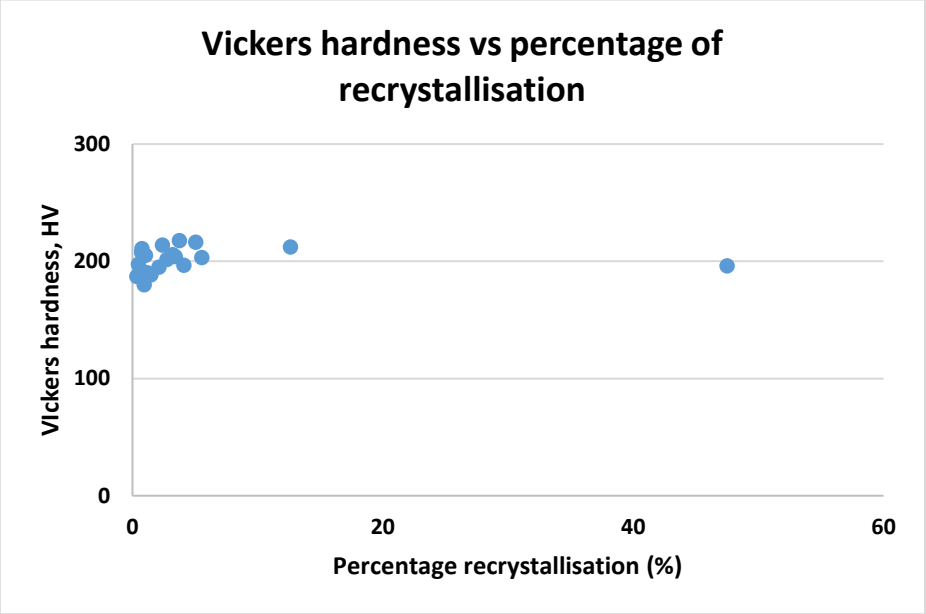

Figure 9-1: The relationship between hardness and percentage recrystallisation of grains for bend bar and micro tensile specimen.

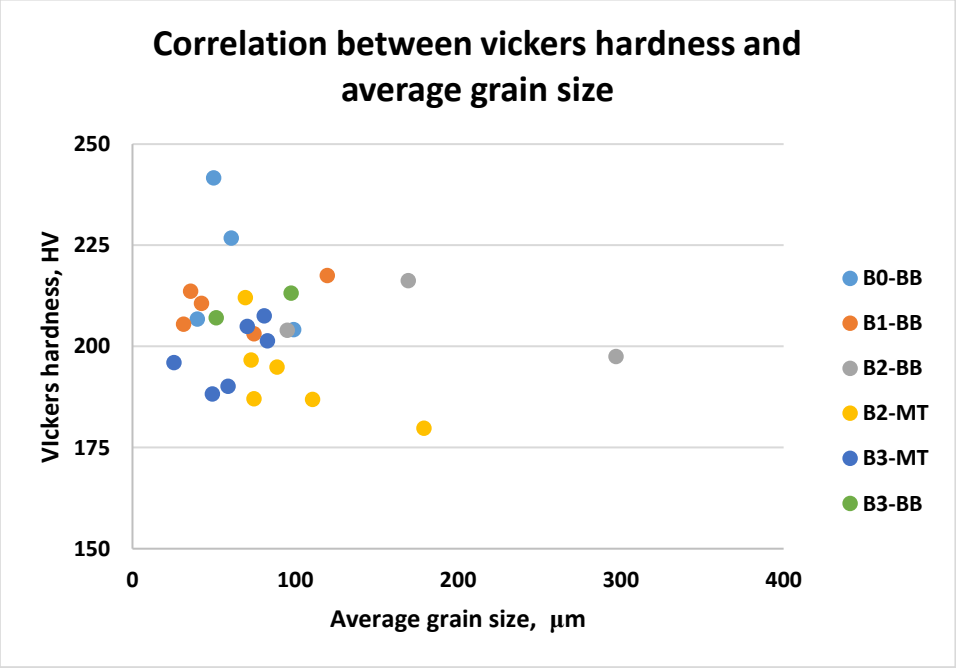

Figure 9-2: The relationship between hardness and average grain size for bend bar and micro tensile specimens.

9.2 Fracture surface characterisation of batch one specimen under high cyclic stress (σ_{max} = 648 MPa)

The analysis of fatigue crack growth across different specimens, specifically X4, Y4, Z2, and Z3 bend bar specimens from B1 provided valuable insights into the initiation, propagation, and interaction of cracks. Surface replica studies, supplemented by SEM imaging and fracture surface roughness profiles mentioned in Chapter 4, revealed detailed mechanisms of crack initiation and coalescence.

- **X4 Specimen**

The X4 specimen exhibited five distinct crack initiation sites, which were marked in Figure 4-15(a). Detailed images of two of these initiation points are provided, these cracks propagated and underwent multiple coalescence events. The fracture surface's roughness profile, displayed in Figure 9-3(a), shows sudden depth changes in the marked areas, indicating the coalescence of cracks. These coalescences are critical events in the fatigue life of the specimen. Two cracks are shown to have initiated at about 13% of the specimen's total lifespan, while the other cracks began around 50% of the lifespan. The four cracks led to two coalescence events in total.

- **Y4 Specimen**

In the Y4 specimen, a primary edge crack originated from an irregularly shaped subsurface defect, with additional cracks developing nearby. This primary edge crack eventually merged with a secondary crack and the corresponding roughness profile in Figure 9-3(b), shows a sudden depth change, indicating the occurrence of the coalescence event. The initial crack in the Y4 specimen began at approximately 18% of its total lifespan, which marks the beginning of a critical phase in the crack's growth.

- **Z3 Specimen**

The Z3 specimen displayed a unique crack growth behaviour, with four cracks initiating simultaneously at around 30% of the specimen's lifespan. Over time, these cracks underwent multiple coalescence events, leading to the progressive expansion of the edge crack. The roughness profiles provided in Figure 9-3(c) highlight two significant coalescence events.

- **Z2 Specimen**

The Z2 specimen had a total of seventeen crack initiation sites; most of the initiations were associated with surface porosity, particularly around clusters of pores, as shown in Figure 4-25(a). The first crack in Z2 was observed at around 27% of the specimen's total lifespan. Due to the high surface porosity, numerous secondary cracks developed. Throughout the specimen's lifespan, multiple coalescence events occurred with eleven prominent coalescence sites illustrated in Figure 9-3(d). The roughness profile in Figure 9-3(d) indicates changes in depth at several points, marking the locations of these

coalescences. Fluctuations in the crack growth rate, evident in Figure 4-26(a) and Figure 4-27(a), are likely due to the interactions between these cracks.

Overall Observations

Across all specimens, those subjected to higher stress levels exhibited a significantly greater number of crack initiation sites compared to specimens under lower stress, as indicated by the clustering of data points in the crack growth rate plots in Chapter 4. Early-stage cracks across high-stress specimens displayed a similar growth rate. The Z2 specimen, in particular, with its high number of initiation sites, underscores the critical impact of surface porosity on fatigue life. This highlights the strong correlation between porosity and fatigue behaviour, emphasising the importance of rigorous material evaluation in high-stress applications to ensure structural integrity and durability.

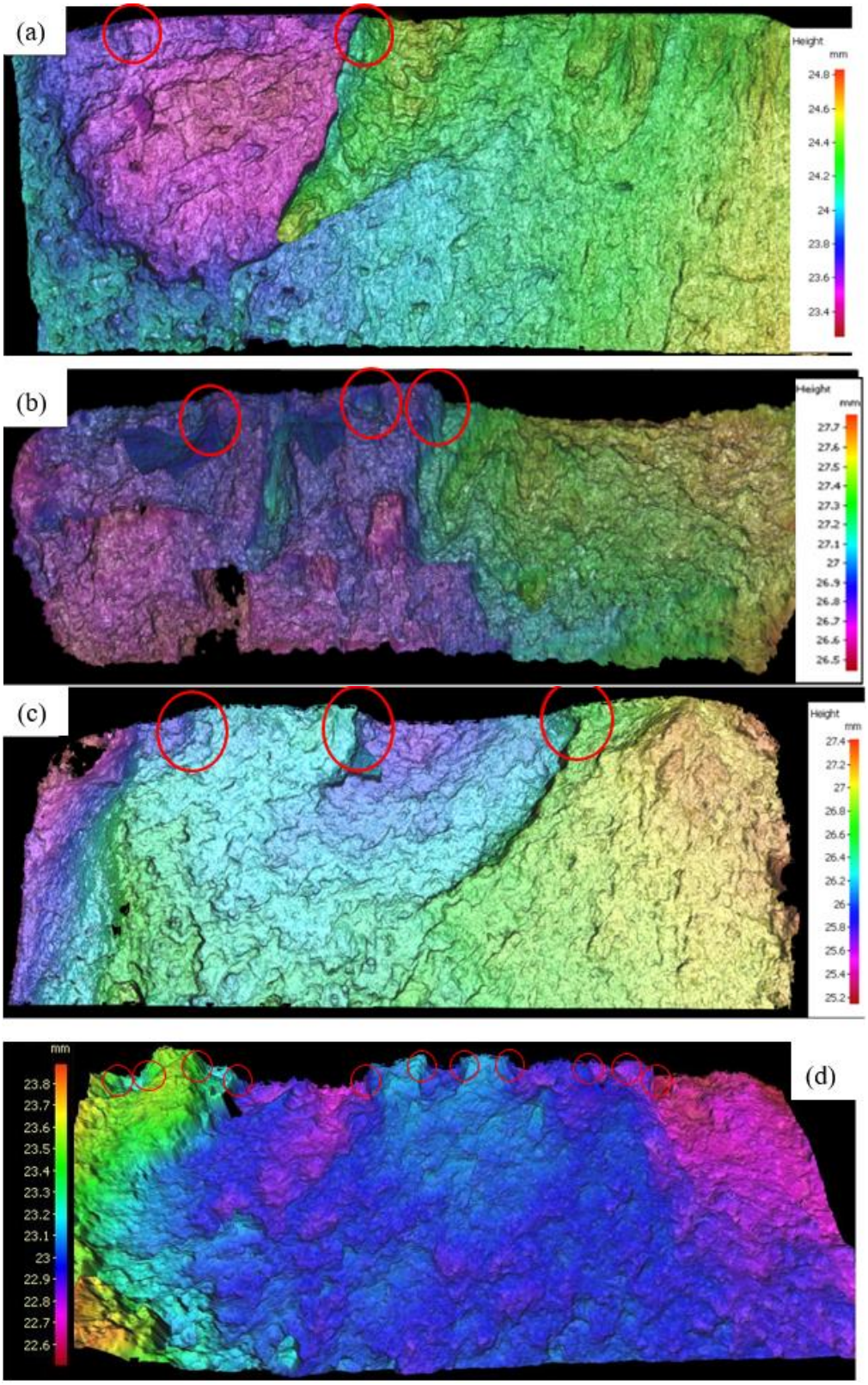

Figure 9-3: Fracture surface roughness profile of B1 bend bar specimens from high stress cyclic failure; (a) X4 ((b) Y4 (c) Z3 and (d) Z2 specimen.

9.3 Stress intensity factor calculation based on Scott and Thorpe's model for semi-elliptical crack

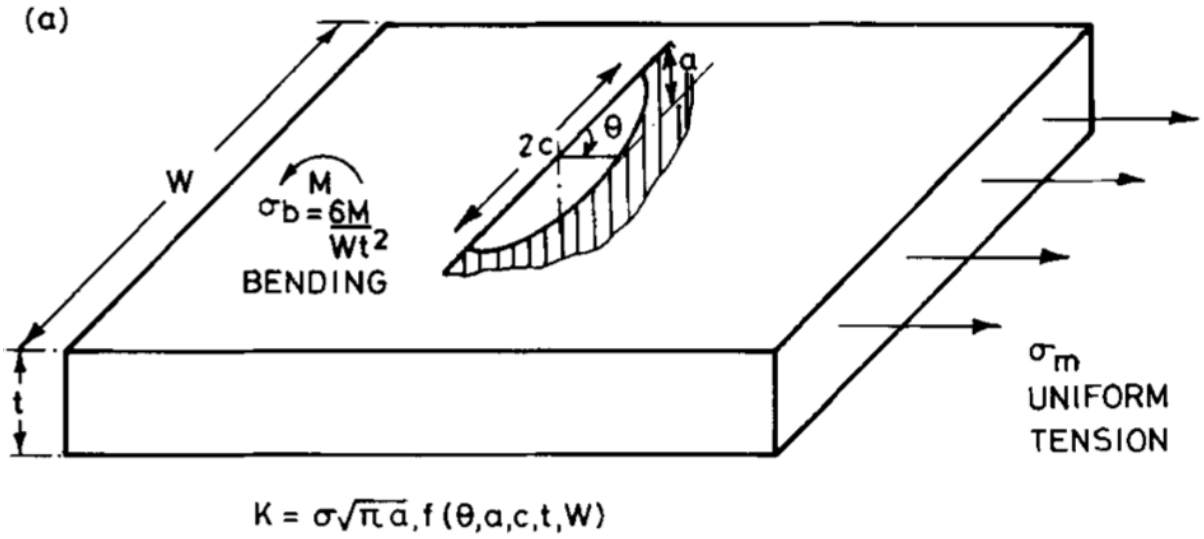

Figure 9-4: Semi-elliptical surface crack configuration from Scott and Thorpe model.

The stress intensity factor on the tip of the surface crack can be given in the A. 9-1.

$$K_I = M_{f(\frac{\pi}{2})}[1 - 1.36\left(\frac{a}{t}\right)\left(\frac{a}{t}\right)^{0.1}]\frac{\sigma_b}{E(K)}\sqrt{\pi a} \qquad \text{A. 9-1}$$

Here, $M_{f\left(\frac{\pi}{2}\right)}$ is the front face magnification factor

$$M_{f\left(\frac{\pi}{2}\right)} = 1.13 - 0.07\left(\frac{a}{c}\right)^{0.5} \qquad \text{A. 9-2}$$

And E(k) is the elliptic integral, and B_w is the finite area correction factor

$$\mathrm{E(K)} = [1 + 1.47\left(\frac{a}{c}\right)^{1.64}]^{0.5} \qquad \text{A. 9-3}$$

$$B_w = 1 + \frac{F\left(\frac{a}{c}\right)G\left(\frac{c}{w}\right)H\left(\frac{a}{t}\right)}{(0.2745)^2} \qquad \text{A. 9-4}$$

$F_{(\frac{a}{c})}$, $G_{(\frac{c}{w})}$ and $H_{(\frac{a}{t})}$ are polynomial function based on the specimen geometry.

$$F_{(\frac{a}{c})} = 0.38 - 0.141\left(\frac{a}{c}\right) - 0.366\left(\frac{a}{c}\right)^2 + 0.569\left(\frac{a}{c}\right)^3 - 0.246\left(\frac{a}{c}\right)^4 \quad \text{A. 9-5}$$

$$G_{(\frac{c}{w})} = -0.0239 + 0.1434\left(\frac{c}{w}\right) - 2.984\left(\frac{c}{w}\right)^2 + 7.822\left(\frac{c}{w}\right)^3 \quad \text{A. 9-6}$$

$$H_{(\frac{a}{t})} = 0.0113 - 0.323\left(\frac{a}{t}\right) - 0.749\left(\frac{a}{t}\right)^2 + 0.535\left(\frac{a}{t}\right)^3 \quad \text{A. 9-7}$$

The stress intensity factor at surface

$$K_I = (\frac{1+\gamma}{3+\gamma})\sigma_b\sqrt{\pi c} \quad \text{A. 9-8}$$

Considering poisons ratio for steel as 0.3, the equation shortens into the following

$$K_I = 0.394\sigma_b\sqrt{\pi c} \quad \text{A. 9-9}$$

With $\frac{a}{t}$ interpolation in eq

$$K_I = [\left[M_{f(0)}\left(1 - 0.3\frac{a}{t}\right)\left(1 - \left(\frac{a}{t}\right)^{12}\right)\right] + [0.394.E(k).\left(\frac{a}{t}\right)^{12}.\sqrt{\frac{c}{a}}]]\frac{\sigma_b}{E(k)}\sqrt{\pi a} \quad \text{A. 9-10}$$

$$M_{f(0)} = 1.21 - 0.1(\frac{a}{c} + 0.1\left(\frac{a}{c}\right)^4]\sqrt{\frac{a}{c}} \quad \text{A. 9-11}$$

9.4 Stress intensity factor calculation based on Newman and Raju's model for quarter-elliptical crack

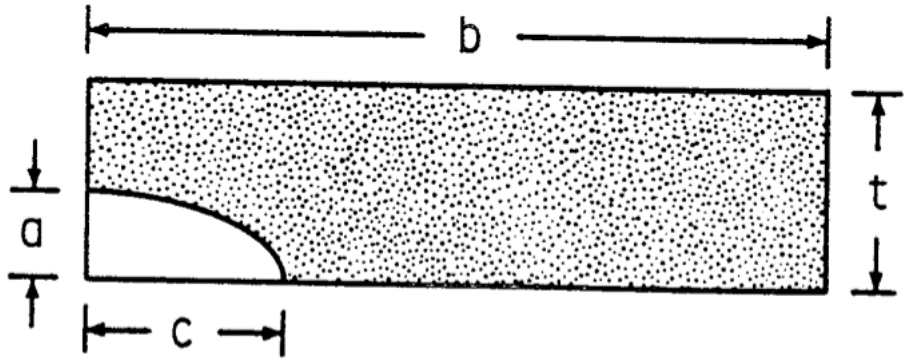

Figure 9-5: Corner crack configuration for Newman and Raju model

The crack tip stress intensity factor for quarter-elliptical corner crack in a finite plate can be expressed with the following equation for bending loads

$$K = (H_c S_b)\sqrt{\pi \frac{a}{Q} F_c\left(\frac{a}{c}, \frac{a}{t}, \frac{c}{b}, \phi\right)} \qquad \text{A. 9-12}$$

For 0.2<a/c<2, a/t<1 and 0< $\phi < \pi/2$ and c/b<0.5, the function for boundary correction factor, F_c is as following

$$F_c = [M_1 + M_2(\frac{a}{t})^2 + M_3(\frac{a}{t})^4] g_1 g_2 f_\phi f_w \qquad \text{A. 9-13}$$

For a/c < 1:

$$M_1 = 1.08 - 0.03(\frac{a}{c}) \qquad \text{A. 9-14}$$

$$M_2 = -0.44 + \frac{1.06}{0.03 + (\frac{a}{c})} \qquad \text{A. 9-15}$$

$$M_3 = -0.5 + 0.25\left(\frac{a}{c}\right) + 14.8(1 - \frac{a}{c})^{15} \quad \text{A. 9-16}$$

$$g_1 = 1 + [0.08 + 0.4(\frac{a}{t})^2](1 - sin\phi)^3 \quad \text{A. 9-17}$$

$$g_2 = 1 + [0.08 + 0.15(\frac{a}{t})^2](1 - cos\phi)^3 \quad \text{A. 9-18}$$

Here M_1, M_2, M_3, g_1 and g_2 are curve fitting function. The finite-width correction factor is given by

$$f_\phi = [(\frac{a}{c})^2\, cos^2\phi + sin^2\phi]^{\frac{1}{4}} \quad \text{A. 9-19}$$

$$f_w = 1 - 0.2\lambda + 9.4\lambda^2 - 19.4\lambda^3 + 27.1\lambda^4 \quad \text{A. 9-20}$$

Here λ is a width correction factor.

$$\lambda = \frac{c}{b}\sqrt{\frac{a}{t}} \quad \text{A. 9-21}$$

$$G_{21} = -1.22 - 0.12(\frac{a}{c}) \quad \text{A. 9-22}$$

$$G_{22} = 0.64 - 1.05(\frac{a}{c})^{0.75} + 0.47(\frac{a}{c})^{1.5} \quad \text{A. 9-23}$$

$$H_1 = 1 - 0.34\left(\frac{a}{t}\right) - 0.11\frac{a}{c}\left(\frac{a}{t}\right) \quad \text{A. 9-24}$$

$$H_2 = 1 + G_{21}\left(\frac{a}{t}\right) + G_{22}\left(\frac{a}{t}\right)^2 \quad \text{A. 9-25}$$

$$H_c = H_1 + (H_2 - H_1)sin^p\phi \quad \text{A. 9-26}$$

Here, H_c is the bending multiplier function.

Chapter 10 References

[1] F. Careri, R. H. U. Khan, C. Todd, and M. M. Attallah, "Additive manufacturing of heat exchangers in aerospace applications: a review," *Appl Therm Eng*, vol. 235, p. 121387, Nov. 2023, doi: 10.1016/j.applthermaleng.2023.121387.

[2] K. Solberg, S. Guan, S. M. J. Razavi, T. Welo, K. C. Chan, and F. Berto, "Fatigue of additively manufactured 316L stainless steel: The influence of porosity and surface roughness," *Fatigue Fract Eng Mater Struct*, vol. 42, no. 9, pp. 2043–2052, 2019, doi: 10.1111/ffe.13077.

[3] M. Zhang *et al.*, "Fatigue and fracture behaviour of laser powder bed fusion stainless steel 316L: Influence of processing parameters," *Materials Science and Engineering: A*, vol. 703, no. April, pp. 251–261, Aug. 2017, doi: 10.1016/j.msea.2017.07.071.

[4] R. Shrestha, N. Shamsaei, M. Seifi, and N. Phan, "An investigation into specimen property to part performance relationships for laser beam powder bed fusion additive manufacturing," *Addit Manuf*, vol. 29, p. 100807, Oct. 2019, doi: 10.1016/j.addma.2019.100807.

[5] J. Sienkiewicz, P. Płatek, F. Jiang, X. Sun, and A. Rusinek, "Investigations on the mechanical response of gradient lattice structures manufactured via slm," *Metals (Basel)*, vol. 10, no. 2, 2020, doi: 10.3390/met10020213.

[6] D. Wei *et al.*, "On microstructural homogenization and mechanical properties optimization of biomedical Co-Cr-Mo alloy additively manufactured by using electron beam melting," *Addit Manuf*, vol. 28, pp. 215–227, Aug. 2019, doi: 10.1016/j.addma.2019.05.010.

[7] J. P. Oliveira, A. D. LaLonde, and J. Ma, "Processing parameters in laser powder bed fusion metal additive manufacturing," *Mater Des*, vol. 193, p. 108762, 2020, doi: 10.1016/j.matdes.2020.108762.

[8] P. Hanzl, M. Zetek, T. Bakša, and T. Kroupa, "The influence of processing parameters on the mechanical properties of SLM parts," *Procedia Eng*, vol. 100, no. January, pp. 1405–1413, 2015, doi: 10.1016/j.proeng.2015.01.510.

[9] D. Gu and Y. Shen, "Processing conditions and microstructural features of porous 316L stainless steel components by DMLS," *Appl Surf Sci*, vol. 255, no. 5 PART 1, pp. 1880–1887, 2008, doi: 10.1016/j.apsusc.2008.06.118.

[10] S. Z. Hussain *et al.*, "Feedback Control of Melt Pool Area in Selective Laser Melting Additive Manufacturing Process," *Processes*, vol. 9, no. 9, p. 1547, Aug. 2021, doi: 10.3390/pr9091547.

[11] "What Is Powder Bed Fusion? Process Definition and Advantages," 2023. [Online]. Available: https://www.twi-global.com/technical-knowledge/faqs/what-is-powder-bed-fusion

[12] S. Kou, "Library," *MRS Bull*, vol. 28, pp. 674–675, 2003, doi: 10.1557/mrs2003.197.

[13] D. GERARD and D. KOSS, "The influence of porosity on short fatigue crack growth at large strain amplitudes," *Int J Fatigue*, vol. 13, no. 4, pp. 345–352, Jul. 1991, doi: 10.1016/0142-1123(91)90364-5.

[14] E. H. Valente, C. Gundlach, T. L. Christiansen, and M. A. J. Somers, "Effect of scanning strategy during selective laser melting on surface topography, porosity, and microstructure of additively manufactured Ti-6Al-4V," *Applied Sciences (Switzerland)*, vol. 9, no. 24, p. 5554, 2019, doi: 10.3390/app9245554.

[15] C. L. A. Leung, S. Marussi, R. C. Atwood, M. Towrie, P. J. Withers, and P. D. Lee, "In situ X-ray imaging of defect and molten pool dynamics in laser additive manufacturing," *Nat Commun*, vol. 9, no. 1, 2018, doi: 10.1038/s41467-018-03734-7.

[16] by Marie-Salomé Dani Duval-Chanéac and N. Gao Philippa Reed Raja Khan, "Microstructure properties and fatigue behaviour of multiple materials fabricated by Laser Powder Bed Fusion process," 2022.

[17] R. a. Covert and A. H. Tuthill, "Stainless Steels : An Introduction to Their Metallurgy and Corrosion Resistance," *Dairy, Food and Environmental Sanitation*, vol. 20, no. 7, pp. 506–517, 2000, [Online]. Available: https://www.nickelinstitute.org/media/1809/stainlesssteels_anintroductiontotheirmetallurgyandcorrosionresistance_14056_.pdf

[18] AZOM, "Stainless Steel 316L Properties," 2023. [Online]. Available: https://www.azom.com/article.aspx?ArticleID=2868

[19] G. Aktaş Çelik, S. Polat, S. H. Atapek, and G. N. Haidemenopoulos, "Microstructural and mechanical characterization of solidified austenitic stainless steels," *Archives of Foundry Engineering*, vol. 17, no. 3, pp. 163–167, 2017, doi: 10.1515/afe-2017-0110.

[20] K. Bartova, M. Domankova, and J. Janovec, "Influence of secondary phase precipitation on resistance to intergranular corrosion of AISI 316L austenitic stainless steel," *Communications - Scientific Letters of the University of Žilina*, vol. 12, no. 4, pp. 20–26, 2010, doi: 10.26552/com.c.2010.4.20-26.

[21] A. Gharehbaghi, “Precipitation Study in a High Temperature Austenitic Stainless Steel using Low Voltage Energy Dispersive X-ray Spectroscopy,” 2012. [Online]. Available: https://www.diva-portal.org/smash/get/diva2:560323/FULLTEXT01.pdf

[22] M. F. McGuire, *Stainless Steels for Design Engineers*. Asm International, 2008. doi: 10.31399/asm.tb.ssde.9781627082860.

[23] B. Sasmal, “Mechanism of the formation of lamellar M23C6 at and near twin boundaries in austenitic stainless steels,” *Metall Mater Trans A Phys Metall Mater Sci*, vol. 30, no. 11, pp. 2791–2801, 1999, doi: 10.1007/s11661-999-0116-7.

[24] T. Sourmail, “Precipitation in creep resistant austenitic stainless steels,” *Materials Science and Technology*, vol. 17, no. 1, pp. 1–14, 2001, doi: 10.1179/026708301101508972.

[25] Y. Yamamoto *et al.*, “Alloying effects on creep and oxidation resistance of austenitic stainless steel alloys employing intermetallic precipitates,” *Intermetallics (Barking)*, vol. 16, no. 3, pp. 453–462, 2008, doi: 10.1016/j.intermet.2007.12.005.

[26] H. J. Cross, J. Beach, L. S. Levy, S. Sadhra, T. Sorahan, and C. Mcroy, “Manufacture, Processing and Use of Stainless Steel: A Review of Health Effects,” 1999. [Online]. Available: https://www.worldstainless.org/Files/issf/non-image-files/PDF/1999HealthEffectsofStainlessSteels.pdf

[27] F. Bartolomeu *et al.*, “316L stainless steel mechanical and tribological behavior—A comparison between selective laser melting, hot pressing and conventional casting,” *Addit Manuf*, vol. 16, pp. 81–89, 2017, doi: 10.1016/j.addma.2017.05.007.

[28] S. Ramakumar, C. Deviannapoorani, L. Dhivya, L. S. Shankar, and R. Murugan, “Lithium garnets: Synthesis, structure, Li+ conductivity, Li+ dynamics and applications,” 2017. doi: 10.1016/j.pmatsci.2017.04.007.

[29] S. L. Sing, W. Y. Yeong, and F. E. Wiria, “Selective laser melting of titanium alloy with 50 wt% tantalum: Microstructure and mechanical properties,” *J Alloys Compd*, vol. 660, pp. 461–470, 2016, doi: 10.1016/j.jallcom.2015.11.141.

[30] H. Qu, J. Li, F. Zhang, and J. Bai, “Anisotropic cellular structure and texture microstructure of 316L stainless steel fabricated by selective laser melting via rotation scanning strategy,” *Mater Des*, vol. 215, Mar. 2022, doi: 10.1016/j.matdes.2022.110454.

[31] Y. Sun, A. Moroz, and K. Alrbaey, “Sliding wear characteristics and corrosion behaviour of selective laser melted 316L stainless steel,” *J Mater Eng Perform*, vol. 23, no. 2, pp. 518–526, Feb. 2014, doi: 10.1007/s11665-013-0784-8.

[32] L. Wang *et al.*, “Surface modification of biomedical AISI 316L stainless steel with zirconium carbonitride coatings,” *Appl Surf Sci*, vol. 340, pp. 113–119, 2015, doi: 10.1016/j.apsusc.2015.02.191.

[33] X. Yuan, L. Chen, Y. Zhao, H. Di, and F. Zhu, “Dependence of grain size on mechanical properties and microstructures of high manganese austenitic steel,” *Procedia Eng*, vol. 81, pp. 143–148, 2014, doi: 10.1016/j.proeng.2014.09.141.

[34] K. Saeidi, X. Gao, Y. Zhong, and Z. J. Shen, “Hardened austenite steel with columnar sub-grain structure formed by laser melting,” *Materials Science and Engineering: A*, vol. 625, pp. 221–229, 2015, doi: 10.1016/j.msea.2014.12.018.

[35] M. L. Pace *et al.*, “3D additive manufactured 316L components microstructural features and changes induced by working life cycles,” *Appl Surf Sci*, vol. 418, pp. 437–445, 2017, doi: 10.1016/j.apsusc.2017.01.308.

[36] Y. M. Wang *et al.*, “Additively manufactured hierarchical stainless steels with high strength and ductility,” *Nat Mater*, vol. 17, no. 1, pp. 63–70, 2018, doi: 10.1038/NMAT5021.

[37] J. C. Newman and I. S. Raju, “Stress-Intensity Factor Equations for Cracks in Three-Dimensional Finite Bodies.,” 1983. doi: 10.1520/stp37074s.

[38] S. Berbenni, V. Favier, and M. Berveiller, “Impact of the grain size distribution on the yield stress of heterogeneous materials,” *Int J Plast*, vol. 23, no. 1, pp. 114–142, Jan. 2007, doi: 10.1016/j.ijplas.2006.03.004.

[39] P. Lehto, H. Remes, T. Saukkonen, H. Hänninen, and J. Romanoff, “Influence of grain size distribution on the Hall-Petch relationship of welded structural steel,” *Materials Science and Engineering: A*, vol. 592, pp. 28–39, Jan. 2014, doi: 10.1016/j.msea.2013.10.094.

[40] O. O. Salman *et al.*, “Impact of the scanning strategy on the mechanical behavior of 316L steel synthesized by selective laser melting,” *J Manuf Process*, vol. 45, pp. 255–261, Sep. 2019, doi: 10.1016/j.jmapro.2019.07.010.

[41] D. Gu and Y. Shen, “Balling phenomena in direct laser sintering of stainless steel powder: Metallurgical mechanisms and control methods,” *Mater Des*, vol. 30, no. 8, pp. 2903–2910, Sep. 2009, doi: 10.1016/j.matdes.2009.01.013.

[42] Č. Donik, J. Kraner, I. Paulin, and M. Godec, “Influence of the Energy Density for Selective Laser Melting on the Microstructure and Mechanical Properties of Stainless Steel,” *Metals (Basel)*, vol. 10, no. 7, p. 919, Jul. 2020, doi: 10.3390/met10070919.

[43] Č. Donik, J. Kraner, I. Paulin, and M. Godec, "Influence of the Energy Density for Selective Laser Melting on the Microstructure and Mechanical Properties of Stainless Steel," *Metals (Basel)*, vol. 10, no. 7, p. 919, Jul. 2020, doi: 10.3390/met10070919.

[44] N. Haghdadi, M. Laleh, M. Moyle, and S. Primig, "Additive manufacturing of steels: a review of achievements and challenges," *J Mater Sci*, vol. 56, no. 1, pp. 64–107, Jan. 2021, doi: 10.1007/s10853-020-05109-0.

[45] A. Kumar Agrawal, G. Meric de Bellefon, and D. Thoma, "High-throughput experimentation for microstructural design in additively manufactured 316L stainless steel."

[46] A. LEICHT, "Laser powder bed fusion of 316L stainless steel : microstructure and mechanical properties as a function of process parameters, design and productivity." Accessed: Nov. 21, 2023. [Online]. Available: https://research.chalmers.se/publication/516336/file/516336_Fulltext.pdf

[47] A. K. Agrawal, G. Meric de Bellefon, and D. Thoma, "High-throughput experimentation for microstructural design in additively manufactured 316L stainless steel," *Materials Science and Engineering: A*, vol. 793, p. 139841, Aug. 2020, doi: 10.1016/j.msea.2020.139841.

[48] X. Wang, J. A. Muñiz-Lerma, O. Sánchez-Mata, M. Attarian Shandiz, and M. Brochu, "Microstructure and mechanical properties of stainless steel 316L vertical struts manufactured by laser powder bed fusion process," *Materials Science and Engineering: A*, vol. 736, pp. 27–40, Oct. 2018, doi: 10.1016/j.msea.2018.08.069.

[49] R. Shrestha, J. Simsiriwong, and N. Shamsaei, "Fatigue behavior of additive manufactured 316L stainless steel parts: Effects of layer orientation and surface roughness," *Addit Manuf*, vol. 28, pp. 23–38, Mar. 2019, doi: 10.1016/j.addma.2019.04.011.

[50] L. Sheridan, O. E. Scott-Emuakpor, T. George, and J. E. Gockel, "Relating porosity to fatigue failure in additively manufactured alloy 718," *Materials Science and Engineering: A*, vol. 727, pp. 170–176, 2018, doi: 10.1016/j.msea.2018.04.075.

[51] H. Jia, H. Sun, H. Wang, Y. Wu, and H. Wang, "Scanning strategy in selective laser melting (SLM): a review," *International Journal of Advanced Manufacturing Technology*, vol. 113, no. 9–10, pp. 2413–2435, 2021, doi: 10.1007/s00170-021-06810-3.

[52] C. Zhao, Y. Bai, Y. Zhang, X. Wang, J. M. Xue, and H. Wang, "Influence of scanning strategy and building direction on microstructure and corrosion behaviour of selective laser melted 316L stainless steel," *Mater Des*, vol. 209, p. 109999, Nov. 2021, doi: 10.1016/j.matdes.2021.109999.

[53] J. J. Marattukalam *et al.*, "The effect of laser scanning strategies on texture, mechanical properties, and site-specific grain orientation in selective laser melted 316L SS," *Mater Des*, vol. 193, p. 108852, Aug. 2020, doi: 10.1016/j.matdes.2020.108852.

[54] M. Rappaz, S. A. David, J. M. Vitek, and L. A. Boatner, "Analysis of solidification microstructures in Fe-Ni-Cr single-crystal welds," *Metallurgical Transactions A*, vol. 21, no. 6, pp. 1767–1782, Jun. 1990, doi: 10.1007/BF02672593.

[55] X. Zhou *et al.*, "Textures formed in a CoCrMo alloy by selective laser melting," *J Alloys Compd*, vol. 631, pp. 153–164, May 2015, doi: 10.1016/j.jallcom.2015.01.096.

[56] I. Yadroitsev, P. Krakhmalev, I. Yadroitsava, S. Johansson, and I. Smurov, "Energy input effect on morphology and microstructure of selective laser melting single track from metallic powder," *J Mater Process Technol*, vol. 213, no. 4, pp. 606–613, Apr. 2013, doi: 10.1016/j.jmatprotec.2012.11.014.

[57] ASTM, "Standard Test Method for Strain-Controlled Fatigue Testing," 2004.

[58] T. G. Spears and S. A. Gold, "In-process sensing in selective laser melting (SLM) additive manufacturing," 2016. doi: 10.1186/s40192-016-0045-4.

[59] Z. Sun, X. Tan, S. B. Tor, and C. K. Chua, "Simultaneously enhanced strength and ductility for 3D-printed stainless steel 316L by selective laser melting," *NPG Asia Mater*, vol. 10, no. 4, pp. 127–136, 2018, doi: 10.1038/s41427-018-0018-5.

[60] E. Malekipour and H. El-Mounayri, "Common defects and contributing parameters in powder bed fusion AM process and their classification for online monitoring and control: a review," *International Journal of Advanced Manufacturing Technology*, vol. 95, no. 1–4, pp. 527–550, 2018, doi: 10.1007/s00170-017-1172-6.

[61] A. M. Roach, B. C. White, A. Garland, B. H. Jared, J. D. Carroll, and B. L. Boyce, "Size-dependent stochastic tensile properties in additively manufactured 316L stainless steel," *Addit Manuf*, vol. 32, p. 101090, Mar. 2020, doi: 10.1016/j.addma.2020.101090.

[62] S. Suresh, *Fatigue of Materials*. Cambridge University Press, 1998. doi: 10.1017/CBO9780511806575.

[63] A. Risitano, *Fatigue of Materials*. Cambridge Univ. Pr, 2020. doi: 10.1201/9781439895313-9.

[64] H. Gerber, "Bestimmung der zulassigen Spannungen in Eisen-konstructionen," *Zeitschrift des Bayerischen Architecketen und Ingenieur-Vereins 6*, vol. 6, pp. 101–110, 1974.

[65] J. Goodman and G. P. Sendeckyj, *Mechanics Applied To Engineering*, vol. 23, no. 4. Longmans, Green, 1904.

[66] C. R. Soderberg, “Factor of Safety and Working Stress,” *J Fluids Eng*, vol. 52, no. 2, pp. 13–21, 1930, doi: 10.1115/1.4057307.

[67] T. Topper, “14 . Smith , K . N ., Watson , P . and Topper , T . H ., " ’ A StressStrain Function for,” vol. 5, no. March, 1970.

[68] O. H. Basquin, “The exponential law of endurance tests,” *Proceedings of the American Society for Testing and Materials*, vol. 10, pp. 625–630, 1910.

[69] M. H. Aliabadi, *Fundamentals of metal fatigue analysis*, vol. 9, no. 3. Prentice Hall, 1992. doi: 10.1016/0955-7997(92)90114-m.

[70] S. K. VISVANATHA, “A Study on the Use of Neuber’s Rule in Fatigue Crack Initiation Predictions,” 1998. [Online]. Available: https://curve.carleton.ca/69b6aab8-64dc-4b85-af5b-15161ace2ea0

[71] N. H., *Theory of notch stresses*. University Microfilms, 1958. [Online]. Available: https://scholar.google.co.uk/scholar?start=420&q=translation+theory&hl=en&as_sdt=0,5#18

[72] G. Massing, “Vortrags-Auszüge / Zürich, ETH, 12. - 17. September 1926 = Resumés des conférences / 2ième Congrès International de Mécanique Appliquée = Abstracts of lectures / 2nd International Congress for Applied Mechanics,” *Worldcat.org*, 1926, [Online]. Available: http://worldcat.org/identities/viaf-128696577/

[73] W. Ramberg and W. R. Osgood, “Description of stress-strain curves by three parameters,” *National Advisory Committee For Aeronautics*, p. Technical Note No. 902, 1943, [Online]. Available: http://hdl.handle.net/2060/19930081614

[74] P. Kelly, “Strain Hardening, Solid Mechanics Part II: Engineering Solid Mechanics – small strain,” *Solid Mechanics Part II: Engineering Solid Mechanics – small strain*, pp. 299–313, 2012, [Online]. Available: http://homepages.engineering.auckland.ac.nz/~pkel015/SolidMechanicsBooks/index.html

[75] ASTM, “E1049 (1985),” *Asme*, vol. 85, no. Reapproved, pp. 1–10, 2015.

[76] P. Heuler and W. Schütz, “Assessment of concepts for Fatigue Crack initiation and propagation life prediction,” *Materwiss Werksttech*, vol. 17, no. 11, pp. 397–405, 1986, doi: 10.1002/mawe.19860171105.

[77] J. C. Newman, E. P. Phillips, and M. H. Swain, “Fatigue-life prediction methodology using small-crack theory,” *Int J Fatigue*, vol. 21, no. 2, pp. 109–119, 1999, doi: 10.1016/S0142-1123(98)00058-9.

[78] U. Krupp, “Fatigue crack propagation in metals and alloys,” *Materials Today*, vol. 10, no. 7–8, p. 53, 2007, doi: 10.1016/s1369-7021(07)70180-3.

[79] P. J. E. Forsyth, “A Two Stage Process of Fatigue Crack Growth Royal Aircratt Establishment,” *Proceedings of the Crack Propagation Symposium*, vol. 1, pp. 76–94, 1961.

[80] B. Kuṅkler, O. Duber, P. Köster, U. Krupp, C. P. Fritzen, and H. J. Christ, “Modelling of short crack propagation - Transition from stage I to stage II,” *Eng Fract Mech*, vol. 75, no. 3–4, pp. 715–725, 2008, doi: 10.1016/j.engfracmech.2007.02.018.

[81] D. Kwon, H. Lahodny, and A. Brückner-Foit, “Limitations of growth regimes for cracks initiated in smooth fatigue specimens,” *Theoretical and Applied Fracture Mechanics*, vol. 16, no. 1, pp. 63–71, 1991, doi: 10.1016/0167-8442(91)90041-H.

[82] P. Mu and V. Aubin, “Microcrack initiation in low-cycle fatigue of an austenitic stainless steel,” *Procedia Eng*, vol. 2, no. 1, pp. 1951–1960, 2010, doi: 10.1016/j.proeng.2010.03.210.

[83] H. D. Carlton, A. Haboub, G. F. Gallegos, D. Y. Parkinson, and A. A. MacDowell, “Damage evolution and failure mechanisms in additively manufactured stainless steel,” *Materials Science and Engineering: A*, vol. 651, pp. 406–414, 2016, doi: 10.1016/j.msea.2015.10.073.

[84] W. Wang, T. Liu, X. Cao, Y. Lu, and T. Shoji, “In-situ observation on twin boundary evolution and crack initiation behavior during tensile test on 316L austenitic stainless steel,” *Mater Charact*, vol. 132, pp. 169–174, 2017, doi: 10.1016/j.matchar.2017.08.020.

[85] C. A. Zapffe and C. O. Worden, “Fractographic registrations of fatigue,” *Transactions of the American Society of Metals*, vol. 43, pp. 958–969, 1951.

[86] P. J. E. Forsyth and D. A. Ryder, “Fatigue Fracture: Some Results Derived from the Microscopic Examination of Crack Surfaces,” *Aircraft Engineering and Aerospace Technology*, vol. 32, no. 4, pp. 96–99, 1960, doi: 10.1108/eb033233.

[87] C. Laird and G. Thomas, “On fatigue-induced reversion and overaging in dispersion strengthened alloy systems,” *International Journal of Fracture Mechanics*, vol. 3, no. 2, pp. 81–97, 1967, doi: 10.1007/BF00182687.

[88] C. Laird and G. C. Smith, “Crack propagation in high stress fatigue,” *Philosophical Magazine*, vol. 7, no. 77, pp. 847–857, 1962, doi: 10.1080/14786436208212674.

[89] M. -Y He, A. Bartlett, A. G. Evans, and J. W. Hutchinson, “Kinking of a Crack out of an Interface: Role of In-Plane Stress,” *Journal of the American Ceramic Society*, vol. 74, no. 4, pp. 767–771, 1991, doi: 10.1111/j.1151-2916.1991.tb06922.x.

[90] K. Palaniswamy and W. G. Knauss, “on the Problem of Crack Extension in Brittle Solids Under General Loading.,” *Mech Today*, vol. 4, pp. 87–148, 1978, doi: 10.1016/b978-0-08-021792-5.50010-0.

[91] F. Erdogan and G. C. Sih, “On the crack extension in plates under plane loading and transverse shear,” *Journal of Fluids Engineering, Transactions of the ASME*, vol. 85, no. 4, pp. 519–525, 1963, doi: 10.1115/1.3656897.

[92] C. M. Suh, J. J. Lee, Y. G. Kang, H. J. Ahn, and B. C. Woo, “a Simulation of the Fatigue Crack Process in Type 304 Stainless Steel At 538°C,” *Fatigue Fract Eng Mater Struct*, vol. 15, no. 7, pp. 671–684, 1992, doi: 10.1111/j.1460-2695.1992.tb01305.x.

[93] C. M. Suh, J. J. Lee, and Y. G. Kang, “Fatigue Microcracks in Type 304 Stainless Steel At Elevated Temperature,” *Fatigue Fract Eng Mater Struct*, vol. 13, no. 5, pp. 487–496, 1990, doi: 10.1111/j.1460-2695.1990.tb00619.x.

[94] A. Bataille and T. Magnin, “Surface damage accumulation in low-cycle fatigue: Physical analysis and numerical modelling,” *Acta Metallurgica Et Materialia*, vol. 42, no. 11, pp. 3817–3825, 1994, doi: 10.1016/0956-7151(94)90447-2.

[95] Y. Z. Wang, K. Ebtehaj, D. Hardie, and R. N. Parkins, “The behaviour of multiple stress corrosion cracks in a Mn-Cr and a Ni-Cr-Mo-V steel: I-Metallography,” *Corros Sci*, vol. 37, no. 11, pp. 1651–1675, 1995, doi: 10.1016/0010-938X(95)00037-K.

[96] Y. Ochi, A. Ishii, and S. K. Sasaki, “an Experimental and Statistical Investigation of Surface Fatigue Crack Initiation and Growth,” *Fatigue Fract Eng Mater Struct*, vol. 8, no. 4, pp. 327–339, 1985, doi: 10.1111/j.1460-2695.1985.tb00431.x.

[97] J. Stolarz, “Multicracking in low cycle fatigue - A surface phenomenon?,” *Materials Science and Engineering: A*, vol. 234–236, pp. 861–864, 1997, doi: 10.1016/s0921-5093(97)00408-5.

[98] P. J. E. Forsyth, “A unified description of micro and macroscopic fatigue crack behaviour,” *Int J Fatigue*, vol. 5, no. 1, pp. 3–14, 1983, doi: 10.1016/0142-1123(83)90002-6.

[99] F. L. E. Poulain, M. Touzet, M. Puiggali, and I. Aubert, “Mechanical behaviour of a solid with many stress corrosion growing cracks,” *J Mater Sci*, vol. 40, no. 7, pp. 1731–1741, 2005, doi: 10.1007/s10853-005-0676-x.

[100] Y. Z. Wang, J. D. Atkinson, R. Akid, and R. N. Parkins, “Crack interaction, coalescence and mixed mode fracture mechanics,” *Fatigue Fract Eng Mater Struct*, vol. 19, no. 1, pp. 51–63, 1996, doi: 10.1111/j.1460-2695.1996.tb00931.x.

[101] M. Kamaya and T. Haruna, “Influence of local stress on initiation behavior of stress corrosion cracking for sensitized 304 stainless steel,” *Corros Sci*, vol. 49, no. 8, pp. 3303–3324, 2007, doi: 10.1016/j.corsci.2007.01.011.

[102] M. Kamaya and M. Itakura, “Simulation for intergranular stress corrosion cracking based on a three-dimensional polycrystalline model,” *Eng Fract Mech*, vol. 76, no. 3, pp. 386–401, 2009, doi: 10.1016/j.engfracmech.2008.11.004.

[103] M. Kamaya and N. Totsuka, “Influence of interaction between multiple cracks on stress corrosion crack propagation,” *Corros Sci*, vol. 44, no. 10, pp. 2333–2352, 2002, doi: 10.1016/S0010-938X(02)00039-2.

[104] P. T. Quinn, “Evaluation of the metal additive manufacturing process through the study of the recyclability of metal powder and in-situ metrology.,” 2019. [Online]. Available: https://www.researchgate.net/publication/332565453_Evaluation_of_the_metal_additive_manufacturing_process_through_the_study_of_the_recyclability_of_metal_powder_and_in-situ_metrology

[105] M. Kamaya, “Influence of the interaction on stress intensity factor of semielliptical surface cracks,” *Journal of Pressure Vessel Technology, Transactions of the ASME*, vol. 130, no. 1, pp. 0114061–0114067, 2008, doi: 10.1115/1.2826424.

[106] E. Uhlmann, C. Fleck, G. Gerlitzky, and F. Faltin, “Dynamical Fatigue Behavior of Additive Manufactured Products for a Fundamental Life cycle Approach,” *Procedia CIRP*, vol. 61, pp. 588–593, 2017, doi: 10.1016/j.procir.2016.11.138.

[107] A. B. Spierings, T. L. Starr, and K. Wegener, “Fatigue performance of additive manufactured metallic parts,” *Rapid Prototyp J*, vol. 19, no. 2, pp. 88–94, 2013, doi: 10.1108/13552541311302932.

[108] M. Free, “The Difference Between Ra and Rz,” 2022. [Online]. Available: https://www.productionmachining.com/blog/post/the-difference-between-ra-and-rz#:~:text=“Rz is calculated by measuring

[109] T. M. Mower and M. J. Long, “Mechanical Behavior of Additive Manufactured Layered Materials, Part 2: Stainless Steels*,” 2015. Accessed: Feb. 21, 2021. [Online]. Available: https://pdfs.semanticscholar.org/29a6/6b7f9f031501d2e296faaa45453e82719cb4.pdf

[110] A. Avanzini, “Fatigue Behavior of Additively Manufactured Stainless Steel 316L,” *Materials*, vol. 16, no. 1, p. 65, Dec. 2022, doi: 10.3390/ma16010065.

[111] Carpenter Additive, "Powder Range 316L," pp. 1–7, 2000, [Online]. Available: https://f.hubspotusercontent10.net/hubfs/6205315/Resources/Data Sheets/20201112-CT-PowderRange-316L-AM-DataSheet_Revs.pdf

[112] D. Kim, R. Jiang, I. Sinclair, and P. Reed, "Microstructural influences on fatigue crack initiation and early propagation in Ni-based superalloy," *Materials Science and Technology*, vol. 38, no. 14, pp. 1081–1094, Sep. 2022, doi: 10.1080/02670836.2022.2070336.

[113] S. M. Yusuf, Y. Chen, R. Boardman, S. Yang, and N. Gao, "Investigation on porosity and microhardness of 316L stainless steel fabricated by selective laser melting," *Metals (Basel)*, vol. 7, no. 2, 2017, doi: 10.3390/met7020064.

[114] H. Jia, H. Sun, H. Wang, Y. Wu, and H. Wang, "Scanning strategy in selective laser melting (SLM): a review," *International Journal of Advanced Manufacturing Technology*, vol. 113, no. 9–10, pp. 2413–2435, 2021, doi: 10.1007/s00170-021-06810-3.

[115] A. Hadadzadeh, F. Mokdad, M. A. Wells, and D. L. Chen, "A new grain orientation spread approach to analyze the dynamic recrystallization behavior of a cast-homogenized Mg-Zn-Zr alloy using electron backscattered diffraction," *Materials Science and Engineering: A*, vol. 709, 2018, doi: 10.1016/j.msea.2017.10.062.

[116] A. Ayad, N. Allain-Bonasso, N. Rouag, and F. Wagner, "Grain orientation spread values in if steels after plastic deformation and recrystallization," in *Materials Science Forum*, 2012. doi: 10.4028/www.scientific.net/MSF.702-703.269.

[117] F. C. Pinto, L. S. Aota, I. R. Souza Filho, D. Raabe, and H. R. Z. Sandim, "Recrystallization in non-conventional microstructures of 316L stainless steel produced via laser powder-bed fusion: effect of particle coarsening kinetics," *J Mater Sci*, vol. 57, no. 21, pp. 9576–9598, 2022, doi: 10.1007/s10853-021-06859-1.

[118] C. Zhao, Y. Bai, Y. Zhang, X. Wang, J. M. Xue, and H. Wang, "Influence of scanning strategy and building direction on microstructure and corrosion behaviour of selective laser melted 316L stainless steel," *Mater Des*, vol. 209, p. 109999, Nov. 2021, doi: 10.1016/j.matdes.2021.109999.

[119] D. Wei *et al.*, "On microstructural homogenization and mechanical properties optimization of biomedical Co-Cr-Mo alloy additively manufactured by using electron beam melting," *Addit Manuf*, vol. 28, pp. 215–227, Aug. 2019, doi: 10.1016/j.addma.2019.05.010.

[120] S. Y. Liu, H. Q. Li, C. X. Qin, R. Zong, and X. Y. Fang, "The effect of energy density on texture and mechanical anisotropy in selective laser melted Inconel 718," *Mater Des*, vol. 191, 2020, doi: 10.1016/j.matdes.2020.108642.

[121] D. Kong *et al.*, “About metastable cellular structure in additively manufactured austenitic stainless steels,” *Addit Manuf*, vol. 38, no. September 2020, p. 101804, 2021, doi: 10.1016/j.addma.2020.101804.

[122] S. Wang, L. Wang, J. Liu, R. Yang, J. Li, and G. Wang, “Effects of laser energy density on morphology features and microstructures of the single molten track in selective laser melting,” *Front Mater*, vol. 10, no. February, pp. 1–9, 2023, doi: 10.3389/fmats.2023.1110844.

[123] P. M. SCOTT and T. W. THORPE, “a Critical Review of Crack Tip Stress Intensity Factors for Semi-Elliptic Cracks,” *Fatigue Fract Eng Mater Struct*, vol. 4, no. 4, pp. 291–309, 1981, doi: 10.1111/j.1460-2695.1981.tb01127.x.

[124] Q. (Zong) Tseng, “PIV (Particle Image Velocimetry) --- ImageJ plugin - ImageJ plugins by Qingzong TSENG.” [Online]. Available: https://sites.google.com/site/qingzongtseng/piv

[125] A. B. Spierings, M. Schneider, and R. Eggenberger, “Comparison of density measurement techniques for additive manufactured metallic parts,” *Rapid Prototyp J*, vol. 17, no. 5, pp. 380–386, 2011, doi: 10.1108/13552541111156504.

[126] B. Stokes, N. Gao, K. K. Lee, and P. A. S. Reed, “Effects of carbides on fatigue characteristics of austempered ductile iron,” *Metall Mater Trans A Phys Metall Mater Sci*, vol. 36, no. 4, pp. 977–988, 2005, doi: 10.1007/s11661-005-0291-0.

[127] Y. Murakami, “Material defects as the basis of fatigue design,” *Int J Fatigue*, vol. 41, pp. 2–10, 2012, doi: 10.1016/j.ijfatigue.2011.12.001.

[128] S. Suresh, C. F. Shih, A. Morrone, and N. P. O’Dowd, “Mixed-Mode Fracture Toughness of Ceramic Materials,” *Journal of the American Ceramic Society*, vol. 73, no. 5, pp. 1257–1267, 1990, doi: 10.1111/j.1151-2916.1990.tb05189.x.

[129] I. Kumar and A. Bakshi, “Effect of Empirical Constant of Ramberg-Osgood Relation on the Buckling Strength of Transformer Inner Winding,” *IEEE Transactions on Power Delivery*, vol. 39, no. 2, pp. 1307–1309, Apr. 2024, doi: 10.1109/TPWRD.2024.3356254.

[130] S. K. Pandey, M. K. Samal, and S. S.D, “A new approach to evaluate Ramberg-Osgood parameters for SS316LN using different types of specimens,” *Procedia Structural Integrity*, vol. 60, pp. 3–12, 2024, doi: 10.1016/j.prostr.2024.05.026.

[131] A. Yanchukovich, A. Ahola, T. Björk, and C. M. Sonsino, “Comparison of analytical and numerical methods for estimating notch strains**,” *Materwiss Werksttech*, vol. 55, no. 6, pp. 719–732, Jun. 2024, doi: 10.1002/mawe.202300095.

[132] B. Salehnasab and S. Hashem-Sharifi, “Low cycle fatigue behavior and life prediction of a directionally solidified alloy,” *Journal of Design Against Fatigue*, vol. 2, no. 1, Mar. 2024, doi: 10.62676/ygye8n63.

[133] S. Wu, J. Liu, J. Lu, Y. Wang, and W. Kou, “Fatigue life evaluation of notched components affected by multiple factors,” *Archive of Applied Mechanics*, vol. 94, no. 7, pp. 1871–1889, Jul. 2024, doi: 10.1007/s00419-024-02607-4.

[134] M. V. Borodii, “Prediction of Strain Hardening and Durability Based on the Calculated Non-Proportional Cyclic Hardening Coefficient,” *Strength of Materials*, vol. 56, no. 2, pp. 271–280, Mar. 2024, doi: 10.1007/s11223-024-00646-4.

[135] Y. Ma, P. Li, T. Su, Q. Yuan, J. Wang, and L. Xia, “Fatigue life and experimental study of high-temperature bellows based on the improved Manson-Coffin equation,” *International Journal of Pressure Vessels and Piping*, vol. 209, p. 105216, Jun. 2024, doi: 10.1016/j.ijpvp.2024.105216.

[136] S. Paul, P. Roy, A. Chatterjee, P. Pandit, R. Mukherjee, and M. Ghosh, “Design and Analysis of Automotive Vehicle Components with Composite Materials Using ANSYS 18.1,” *Journal of The Institution of Engineers (India): Series D*, Jan. 2024, doi: 10.1007/s40033-023-00627-y.

[137] J. Krmela and V. Krmelová, “Computational Simulation of Biaxial Loading of Polymer Composites in ANSYS,” 2024, pp. 65–81. doi: 10.1007/978-3-031-60920-6_6.

[138] I. Urcelay Oca, B. L. V. Bak, A. Turon, and E. Lindgaard, “An ANSYS user cohesive element for the modelling of fatigue initiation and propagation of delaminations in composite structures,” *Eng Fract Mech*, vol. 308, p. 110337, Sep. 2024, doi: 10.1016/j.engfracmech.2024.110337.

[139] B. Michael and D. Cunningham, “EXTENDING FATIGUE LIFE OF INDUSTRIAL LOW-PRESSURE FV566 TURBINE BLADES: EFFICACY OF A LIFETIME EXTENSION STRATEGY TO EXTEND SERVICE LIFE THESIS FOR THE DEGREE OF DOCTOR OF PHILOSOPHY,” 2022, doi: 10.5258/SOTON/T0044.

[140] M. S. Haque and C. M. Stewart, “The Stress-Sensitivity, Mesh-Dependence, and Convergence of Continuum Damage Mechanics Models for Creep,” *J Press Vessel Technol*, vol. 139, no. 4, Aug. 2017, doi: 10.1115/1.4036142.

[141] S. Gross-Hardt, F. Boehning, U. Steinseifer, T. Schmitz-Rode, and T. A. S. Kaufmann, “Mesh Sensitivity Analysis for Quantitative Shear Stress Assessment in Blood Pumps Using Computational Fluid Dynamics,” *J Biomech Eng*, vol. 141, no. 2, Feb. 2019, doi: 10.1115/1.4042043.

[142] S. Sakata, Y. Chan, and Y. Arai, “On accuracy improvement of microscopic stress/stress sensitivity analysis with the mesh superposition method for heterogeneous materials considering geometrical variation of inclusions,” *Int J Numer Methods Eng*, vol. 121, no. 3, pp. 534–559, Feb. 2020, doi: 10.1002/nme.6233.

[143] C. You, M. Achintha, K. A. Soady, and P. A. S. Reed, “Low cycle fatigue life prediction in shot-peened components of different geometries – part II: life prediction,” *Fatigue Fract Eng Mater Struct*, vol. 40, no. 5, pp. 749–760, May 2017, doi: 10.1111/ffe.12542.

[144] Y. H. Zhao *et al.*, “Influence of specimen dimensions and strain measurement methods on tensile stress–strain curves,” *Materials Science and Engineering: A*, vol. 525, no. 1–2, pp. 68–77, Nov. 2009, doi: 10.1016/j.msea.2009.06.031.

[145] W. Liu *et al.*, “Study of pore defect and mechanical properties in selective laser melted Ti6Al4V alloy based on X-ray computed tomography,” *Materials Science and Engineering: A*, vol. 797, p. 139981, Oct. 2020, doi: 10.1016/j.msea.2020.139981.

[146] C. Meier, R. W. Penny, Y. Zou, J. S. Gibbs, and A. J. Hart, “THERMOPHYSICAL PHENOMENA IN METAL ADDITIVE MANUFACTURING BY SELECTIVE LASER MELTING: FUNDAMENTALS, MODELING, SIMULATION, AND EXPERIMENTATION,” *Annual Review of Heat Transfer*, vol. 20, no. 1, pp. 241–316, 2017, doi: 10.1615/AnnualRevHeatTransfer.2018019042.

[147] W. Beard, R. Lancaster, N. Barnard, T. Jones, and J. Adams, “The influence of surface finish and build orientation on the low cycle fatigue behaviour of laser powder bed fused stainless steel 316L,” *Materials Science and Engineering: A*, vol. 864, p. 144593, Feb. 2023, doi: 10.1016/j.msea.2023.144593.

[148] A. Tridello, C. B. Niutta, F. Berto, and D. S. Paolino, “Size-effect in Very High Cycle Fatigue: A review,” *Int J Fatigue*, vol. 153, p. 106462, Dec. 2021, doi: 10.1016/j.ijfatigue.2021.106462.

[149] N. Sanaei and A. Fatemi, “Defects in additive manufactured metals and their effect on fatigue performance: A state-of-the-art review,” *Prog Mater Sci*, vol. 117, p. 100724, Apr. 2021, doi: 10.1016/j.pmatsci.2020.100724.

[150] H. Masuo *et al.*, “Influence of defects, surface roughness and HIP on the fatigue strength of Ti-6Al-4V manufactured by additive manufacturing,” *Int J Fatigue*, vol. 117, pp. 163–179, Dec. 2018, doi: 10.1016/j.ijfatigue.2018.07.020.

[151] A. Tridello, J. Fiocchi, C. A. Biffi, M. Rossetto, A. Tuissi, and D. S. Paolino, “Size-effects affecting the fatigue response up to 109 cycles (VHCF) of SLM AlSi10Mg specimens produced

in horizontal and vertical directions," *Int J Fatigue*, vol. 160, p. 106825, Jul. 2022, doi: 10.1016/j.ijfatigue.2022.106825.

[152] S. Invernizzi, F. Montagnoli, and A. Carpinteri, "Experimental Evidence of Specimen-Size Effects on EN-AW6082 Aluminum Alloy in VHCF Regime," *Applied Sciences*, vol. 11, no. 9, p. 4272, May 2021, doi: 10.3390/app11094272.

[153] A. Carpinteri, F. Montagnoli, and S. Invernizzi, "Scaling and fractality in fatigue resistance: Specimen-size effects on Wöhler's curve and fatigue limit," *Fatigue Fract Eng Mater Struct*, vol. 43, no. 8, pp. 1869–1879, Aug. 2020, doi: 10.1111/ffe.13242.

[154] M. Tang and P. C. Pistorius, "Anisotropic Mechanical Behavior of AlSi10Mg Parts Produced by Selective Laser Melting," *JOM*, vol. 69, no. 3, pp. 516–522, Mar. 2017, doi: 10.1007/s11837-016-2230-5.

[155] A. B. B. Spierings, T. L. L. Starr, and K. Wegener, "Fatigue performance of additive manufactured metallic parts," *Rapid Prototyp J*, vol. 19, no. 2, pp. 88–94, Mar. 2013, doi: 10.1108/13552541311302932.

[156] G. S. Ponticelli, R. Panciroli, S. Venettacci, F. Tagliaferri, and S. Guarino, "Experimental investigation on the fatigue behavior of laser powder bed fused 316L stainless steel," *CIRP J Manuf Sci Technol*, vol. 38, pp. 787–800, Aug. 2022, doi: 10.1016/j.cirpj.2022.07.007.

[157] J. Lai, H. Huang, and W. Buising, "Effects of microstructure and surface roughness on the fatigue strength of high-strength steels," *Procedia Structural Integrity*, vol. 2, pp. 1213–1220, 2016, doi: 10.1016/j.prostr.2016.06.155.

[158] X. Chen, X. Chen, D. Yu, and B. Gao, "Recent progresses in experimental investigation and finite element analysis of ratcheting in pressurized piping," *International Journal of Pressure Vessels and Piping*, vol. 101, pp. 113–142, Jan. 2013, doi: 10.1016/j.ijpvp.2012.10.008.

[159] T. L. Anderson and T. L. Anderson, *Fracture Mechanics*. CRC Press, 2005. doi: 10.1201/9781420058215.

[160] S. Tammas-Williams, P. J. Withers, I. Todd, and P. B. Prangnell, "The Influence of Porosity on Fatigue Crack Initiation in Additively Manufactured Titanium Components," *Sci Rep*, vol. 7, no. 1, 2017, doi: 10.1038/s41598-017-06504-5.

[161] H. Zhang, M. Xu, Z. Liu, C. Li, and Y. Zhang, "Role of local recrystallization behavior on fatigue performance of SLMed 304L austenitic stainless steels," *Mater Charact*, vol. 177, p. 111159, Jul. 2021, doi: 10.1016/j.matchar.2021.111159.

[162] A. Evangelou *et al.*, “Effects of process parameters and scan strategy on the microstructure and density of stainless steel 316L produced via laser powder bed fusion.” [Online]. Available: https://ssrn.com/abstract=4369397

[163] A. K. Agrawal *et al.*, “High-throughput experimentation for microstructural design in additively manufactured 316L stainless steel,” *Materials Science and Engineering: A*, vol. 793, p. 139841, Aug. 2020, doi: 10.1016/j.msea.2020.139841.

[164] A. Leicht, U. Klement, and E. Hryha, “Effect of build geometry on the microstructural development of 316L parts produced by additive manufacturing,” *Mater Charact*, vol. 143, pp. 137–143, Sep. 2018, doi: 10.1016/j.matchar.2018.04.040.

[165] U. Scipioni Bertoli, B. E. MacDonald, and J. M. Schoenung, “Stability of cellular microstructure in laser powder bed fusion of 316L stainless steel,” *Materials Science and Engineering: A*, vol. 739, pp. 109–117, Jan. 2019, doi: 10.1016/j.msea.2018.10.051.

[166] A. LEICHT and ALEXANDER LEICHT, “Laser powder bed fusion of 316L stainless steel : microstructure and mechanical properties as a function of process parameters, design and productivity,” 2020. Accessed: Nov. 14, 2023. [Online]. Available: https://research.chalmers.se/publication/516336/file/516336_Fulltext.pdf

[167] D. Palmeri, G. Buffa, G. Pollara, and L. Fratini, “Sample building orientation effect on porosity and mechanical properties in Selective Laser Melting of Ti6Al4V titanium alloy,” *Materials Science and Engineering: A*, vol. 830, p. 142306, Jan. 2022, doi: 10.1016/j.msea.2021.142306.

[168] H. Wang, P. Jiang, G. Yang, and Y. Yan, “An Investigation of the Anisotropic Mechanical Properties of Additive-Manufactured 316L SS with SLM,” *Materials*, vol. 17, no. 9, p. 2017, Apr. 2024, doi: 10.3390/ma17092017.

[169] H. E. Sabzi *et al.*, “Grain refinement in laser powder bed fusion: The influence of dynamic recrystallization and recovery,” *Mater Des*, vol. 196, Nov. 2020, doi: 10.1016/j.matdes.2020.109181.

[170] M. Gabilondo, X. Cearsolo, M. Arrue, and F. Castro, “Influence of Build Orientation, Chamber Temperature and Infill Pattern on Mechanical Properties of 316L Parts Manufactured by Bound Metal Deposition,” *Materials*, vol. 15, no. 3, p. 1183, Feb. 2022, doi: 10.3390/ma15031183.

[171] A. Fatemi *et al.*, “Fatigue behaviour of additive manufactured materials: An overview of some recent experimental studies on <scp>Ti-6Al-4V</scp> considering various processing and loading direction effects,” *Fatigue Fract Eng Mater Struct*, vol. 42, no. 5, pp. 991–1009, May 2019, doi: 10.1111/ffe.13000.

[172] S. Beretta and S. Romano, “A comparison of fatigue strength sensitivity to defects for materials manufactured by AM or traditional processes,” *Int J Fatigue*, vol. 94, pp. 178–191, Jan. 2017, doi: 10.1016/j.ijfatigue.2016.06.020.

[173] C. You, “Fatigue lifing approaches for shot peened turbine components,” 2017.

[174] T. Chatziathanasiou, J. Soete, J. Vanhulst, D. Carrella-Payan, L. Gorbatikh, and M. Mehdikhani, “In-situ X-ray computed tomography of mode I delamination in carbon-epoxy composites: The effect of the interface ply orientation,” *Compos B Eng*, vol. 260, p. 110761, Jul. 2023, doi: 10.1016/j.compositesb.2023.110761.

[175] W. Qian *et al.*, “In situ X-ray imaging of fatigue crack growth from multiple defects in additively manufactured AlSi10Mg alloy,” *Int J Fatigue*, vol. 155, p. 106616, Feb. 2022, doi: 10.1016/j.ijfatigue.2021.106616.